The role of microalloying on tuning the mechanical performance of Cu-Zr based Shape Memory Alloys

Abdurauf K M Younes

PhD

A thesis submitted in partial fulfilment of the requirements of the University of Northumbria at Newcastle for the degree of Doctor of Philosophy

Research undertaken in the Faculty of Engineering and Environment

December 2021

Abstract

Shape Memory Alloys (SMAs) are an interesting class of materials that possess sensing and actuation functions due to Shape Memory Effect (SME). Although SME is observed in NiTi where high recoverable stress-strain is observed, there are limitations associated with implementation of NiTi such as high cost compared to cost-effective elements (i.e., Cu) and the inability to observe SME at temperatures above ~100^{o}C. Therefore, a cost-effective and temperature-adaptive replacement (CuZr-based SMAs) may replace NiTi in sensing and actuation applications.

The tribological performance of CuZr-based SMAs is investigated by wear and hardness tests at Room Temperature (RT) and high temperature. CuZr-based SMAs are obtained by rapid solidification and the microstructure is examined using X-ray Diffraction (XRD), Scanning Electron Microscopy (SEM) and Transmission Electron Microscopy (TEM). Due to poor SME of $Cu_{50}Zr_{50}$ at.% SMA compared to NiTi, a microalloying element (i.e., Co) is introduced in place of Cu at different at.% in order to promote martensitic transformation, leading to enhanced mechanical performance. This research found that microalloying with $Co_{0.5}$ at.% at RT decreased mass loss by 46% compared to $Cu_{50}Zr_{50}$. However, when operating at 100^{o}C, mass loss of the same alloy only decreased by 10%.

Additionally, other microalloying elements such as Fe and Mn were investigated to improve the wear performance of CuZr-based SMAs, it was found that partial replacement of Cu by 0.5 at.% Fe, results in a lifetime enhancement of about 30.5% while for 0.5 at.% Mn the lifetime enhancement is about 21%. Microalloying is therefore an efficient strategy to develop CuZr-based SMAs as temperature adaptive shaft seals for engines.

The synergistic effect of cooling rate control and concentration of microalloying element on mechanical performance of CuZr-based SMAs is also novel. In the case of fast cooling rate, 0.5 at.% Fe addition promotes formation of B19’ martensite upon wear testing, hence improving wear resistance. However, for slower cooling rate of the same alloy, relatively large volume fraction of B33 martensite is formed resulting in reduction of wear resistance.

Acknowledgements

First and foremost, I would like to thank Almighty Allah for giving me the courage and determination to conduct this work.

I would like to express my appreciation to my supervisor Dr Sergio Gonzalez Sanchez for his continuous support over the duration of my research.

Special thanks go to the laboratory technicians Simon Neville, Sam Hutchinson, Phil Donnelly, Pietro Maiello and Rebecca Payne for their invaluable support and guidance throughout my research. I would also like to express my gratitude to the researchers who have helped me throughout my research:

- Paul Nnamchi and Victor Villapun for their technical and literature support in my first year.
- James Watson and Matthew Unthank for their support in conducting DSC scans at low temperatures at Northumbria university.
- Royce institute and their TEM facility in Sheffield University for their support in conducting TEM analysis together with Dr John Nutter.
- National Physical Laboratory in Teddington and François de Luca for performing nano-indentation tests at high temperature.

My biggest thanks go to my parents for their unconditional support and encouragement through all these years.

Finally, I would like to thank Northumbria University for their financial support.

Declaration

I declare that no outputs submitted for this degree have been submitted for a research degree of any other institution. I also confirm that this work fully acknowledges opinions, ideas, and contributions from the work of others. The contribution of other authors in my published work and in this thesis is listed in bullet points in my acknowledgment section.

Any ethical clearance for the research presented in this commentary has been approved by the Faculty Ethics Committee/ University Ethics Committee on 14/5/2018

I declare that the word count is 44,366 words

Name: Abdurauf Younes

Signature:

Date: 23/12/2021

Table of Contents

List of abbreviations and symbols

Abbreviation	Meaning
SMA	Shape Memory Alloy
SME	Shape Memory Effect
NOL	Naval Ordnance Laboratory
T_g	Glass Transition Temperature
A_s	Austenite start
A_f	Austenite finish
M_s	Martensite start
M_f	Martensite finish
BCC	Body Centered Cubic
FCC	Face Centered Cubic
HCP	Hexagonal Close Packed
M_t	twinned martensite
M_d	detwinned martensite
SFE	Stacking Fault Energy
TTT	Time Temperature Transformation
XRD	X-ray Diffraction
MD	Molecular Dynamics
GFA	Glass Forming Ability
d_p	Droplet diameter
GMR	Gas-To-Melt Mass Flow Ratio
FFA	Free-Fall Atomisation
HTSMA	High temperature Shape Memory Alloy
BMGC	Bulk Metallic Glass Composites
CRSS	Critical Resolved Shear Stress
MEMS	Micro-Electro Mechanical Systems
CASTEP	Cambridge Serial Total Energy Package
SEM	Scanning Electron Microscopy
FEM	Field Emission Gun

TEM	Transmission electron microscopy
PIPS	Precision Ion Polishing System
DSC	Differential Scanning Calorimetry
DMA	Dynamic Mechanical Analysis
R_a	Surface Roughness

List of Figures

--

List of Tables

Chapter 1 – Introduction

1.1. Overview

Shape memory alloys (SMAs) are a unique class of materials that “remember” its original shape (i.e., when heated up they can return to their original shape) [1]. This ability of returning to original shape after deformation is called Shape Memory Effect (SME). SMAs have the ability to produce high stress, work output and actuation strain due to the nature of its phase transformation. SMAs are also considered robust, lightweight and some SMAs are biocompatible and environmentally friendly. SMAs possess excellent properties that make them suitable for sensing, damping, actuation and vibrating applications [1].

The SME phenomenon relates to how the transformation occurs in the SMAs from B2 austenite into B19’ martensite in what is called martensitic transformation and vice versa [2]. In solid state, two possible transformations can occur: diffusional and displacive. In a diffusional transformation, atoms randomly move to form a new phase, this movement happens over a relatively long distance. This type of transformation is governed by temperature and time and therefore atomic movement is required to achieve diffusional transformation. However, displacive transformation “do not require such long range movements; in these cases atoms are cooperatively rearranged into a new, more stable crystal structure, without changing the chemical nature of the matrix” [3]. Martensitic transformation is considered a displacive transformation as a metastable phase transforms into a more stable crystal structure, for example, in the case of CuZr SMAs that is known as transformation from B2 CuZr austenite into B19’ CuZr martensite. [3].

1.2. Research background and history of materials

Towards the end of the nineteenth century, martensite phase was named after scientist Adolf Martens who discovered it. Martensite is a crystalline phase that is stable at low temperatures. Similarly, austenite is named after physicist Charles Austen, who found the phase to be stable at higher temperature than martensite [4]. In the first stages of discovering the shape recovery phenomenon, terms such as pseudo-elasticity were used to describe the recovery behaviour. Pseudo-elasticity or sometimes called super-elasticity,

is a reversible elastic response to an applied stress, caused by a phase transformation between the austenitic and martensitic phases of a crystal. In 1932, Olander [5] noticed that Au-Cd alloy exhibited what he referred to as “rubber like effect”. Furthermore, Greninger and Mooradian reported a thermoelectricity behaviour in 1938 [6] when investigating Cu-Zn alloy. The main difference between the two phenomenon is that pseudoelasticity relates to a material recovering its deformation, this can reach 10% and more after yielding, whilst thermoelasticy indicated the functional dependence of the recoverable strain on thermal conditions [4].

In 1951, Chang and Read were the first ones to report the term “shape recovery” when studying the Au-Cd alloy system of 1:1 at.% ratio [7]. In 1954 Basinki and Christian [8] also discovered SME in indium-thallium (In-Tl) alloy system. All these findings by the mentioned researchers were vital in the study of SMAs. However, there is one highly significant alloy that led to outburst of scientific interest in this type of materials. In 1965 U.S. Naval Ordnance Laboratory (NOL) received a United States patent [9] for observing SME in Ni-Ti alloys, also referred to as Nitinol, in reference to the laboratory in which it was discovered. The chemical compound consists of 50-52 at.% Nickel to 48-50 at.% Titanium and therefore the alloy is equiatomic. Following the 1965 discovery, SME phenomenon was observed in several alloy systems including Cu-based SMAs (see section 2.3.3 for more details) [4] and Fe-based SMAs [4]. These two in particular have attracted attention due to their potential use in different applications and the low economic cost. Over the last few decades, certain alloy systems were widely investigated due to their SME. For example, to name a few of Cu-based, such as Cu-Mn [10], Cu-Al [11] and Cu-Zn [12] alloys. Similarly, for Fe-based alloys, Fe-Ni, Fe-Pt, Fe-Ni-Nb, Fe-Ni-C and Fe-Ni-Co-Ti have all exhibited SME [13]. In the following years, SME was observed in more than 25 binary, ternary or quaternary alloy systems [14]. The scope of this research is directed towards Cu-based SMAs, however, more information regarding Fe-based SMAs can be found in the literature [15-17].

Despite the long time since its discovery, NiTi is still the alloy with best recovery ratio compared to other alloy systems [18, 19]. The combination of its excellent resistance to corrosion and biocompatibility makes NiTi the primary SMA choice for many industries,

such as in implantation in human bodies. Nevertheless, NiTi-based SMAs are more expensive than Fe and Cu-based SMAs. **Table 1.1** lists the cost of pure bulk Ti, Cu, Ni and Fe per 100g in United States Dollars (USD), noting that the prices given [20] are a representative for the date taken (Oct 2012) and therefore the market value of these elements may slightly change with time. The difficulty to melt and elaborate is also considered an issue when dealing with Ti since its melting point is around 1668^{o}C, higher than Cu and Fe, which are around 1085^{o}C and 1538^{o}C, respectively [21].

Table 1. 1. Cost of pure Ti, Cu, Ni and Fe per 100g [20].

Element	Cost, pure per 100g	Atomic number	Melting point (^{o}C)
Ti	£535	22	1668
Cu	£6.23	29	1085
Ni	£7.90	28	1455
Fe	£5.82	26	1538

Despite the high cost of NiTi SMAs since its discovery, it has been used for various applications due to its unique properties. The demand for strong and light materials with tailored properties that address both stringent structural requirements and provide additional engineering functionality (*for example, actuation and sensing*) has shed light on a new branch of materials called multifunctional/active materials [22]. These include magnetostrictive ceramics, piezoelectric polymers, piezoelectric ceramics, shape memory alloys and magnetic shape memory alloys [22].

The suitability of an active material for actuation applications depends on actuation frequency of the material and actuation energy density (work output per unit volume). Ideally, an active material would have high actuation frequency (Hz) and high actuation energy density (J/kg). "**Figs. 1.1 and 1.2** compare the actuation energy densities and the actuation frequencies, respectively, of some common materials. The actuation energy density is denoted in **Fig. 1.1** by the dotted lines and is defined as the product of the actuation strain (related to the stroke of an actuator) with the actuation stress, assuming here that the active material is operating under constant stress. The specific actuation

energy density (work output per unit mass) for a specific active material can be calculated from **Fig. 1.1** by dividing the actuation energy density by the mass density" [22].

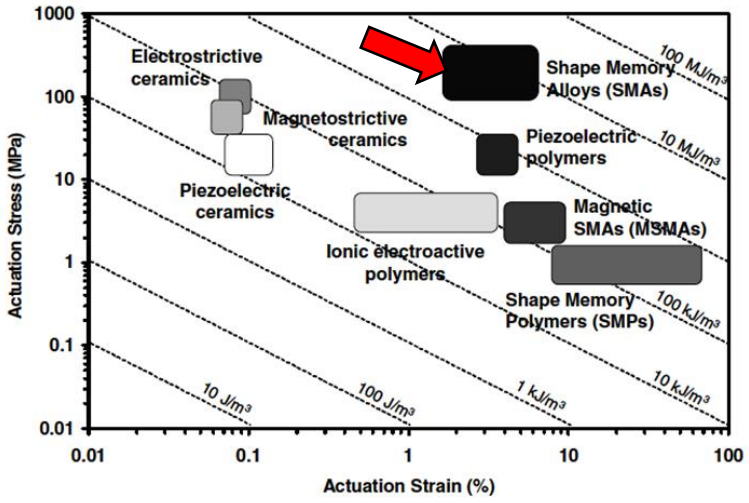

Fig. 1. 1. Actuation energy density diagram indicating typical ranges of actuation stress, actuation strain, and the actuation energy densities of different materials [22].

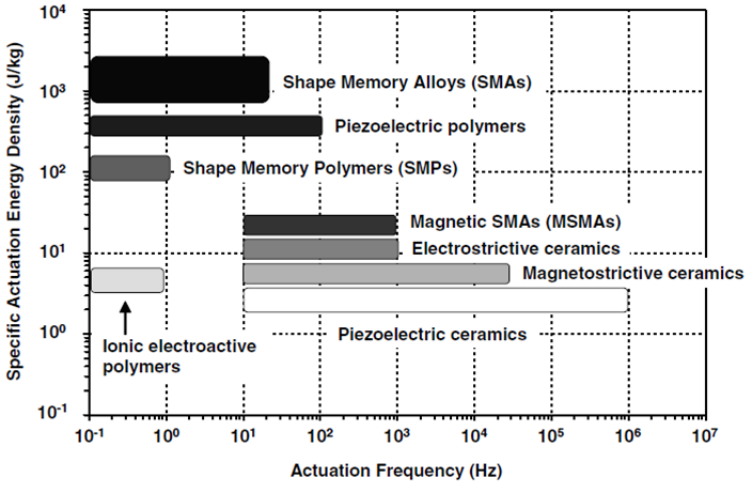

Fig. 1. 2. Actuation frequency diagram comparing the actuation frequency ranges of different materials [22].

An increase in temperature results in shape recovery for SMAs even under high loads, hence resulting in high actuation energy densities as can be seen in **Fig. 1.1**. These unique properties of SMAs make this branch of materials popular for actuation and sensing applications.

Summary:

- NiTi alloys provide the **best recovery ratio** of known SMAs.
- **CuZr-based** SMAs also exhibit SME, however, the recovery ratio is reported to be lower than that of NiTi.
- CuZr-based SMAs would be favourable if SME is improved due to **cost effectiveness** compared to NiTi.
- The SME of CuZr-based SMAs can be **altered** by **changing the composition**.
- SMAs provide **high actuation stress** and **high actuation strain**.

1.3. Research questions

Since the discovery of SME in NiTi SMAs in the last century, researchers have tried to understand the mechanisms responsible for phase transformation, factors effecting it and ways of enhancing the transformation from soft austenite into hard martensite in order to obtain favourable mechanical properties. In recent years, researchers have started to investigate alternative SMAs with lower cost than NiTi [23].

The research questions mainly investigated in this study are the following:

- What is the role and importance of microalloying element in altering the Stacking Fault Energy (SFE) and consequently promoting the martensitic transformation?
- Does the microalloying element impact the operating temperature range of SMAs?
- What microalloying element can lower SFE the most, therefore promote martensitic transformation and enhance tribological performance?
- What is the role of cooling rate control in determining microstructure of rapidly solidified CuZr SMAs and its effect on presence of intermetallic phases?

1.4. Research aims and objectives

The main aim of this work is to enhance the tribological and mechanical performance of novel cost-effective CuZr SMAs to replace costly NiTi SMAs. $Cu_{50}Zr_{50}$ at.% SMAs are reported to have SME similar to that of NiTi SMAs, however, the performance of $Cu_{50}Zr_{50}$ at.% is considerably worse than that of NiTi. For this purpose, it is necessary to implement a strategy to enhance $Cu_{50}Zr_{50}$ SMAs in order to be viable and used in tribological and

mechanical applications. To accomplish this aim, a thorough analysis has been carried out to accomplish several objectives.

- Understanding the effect of 0.5 and 1 at.% **Co** as microalloying element entering $Cu_{50}Zr_{50}$ at.% in solid solution on decreasing SFE and therefore promoting martensitic transformation of $Cu_{50}Zr_{50}$ at.%. The concentration of Co entering $Cu_{50}Zr_{50}$ austenite B2 phase in solid solution plays a crucial role in enhancing the **tribological performance** of CuZr SMAs. Additionally, an investigation on the extent of the improvement at high temperature compared to RT is conducted. **See Chapter 4**.
- Evaluate the effect of **Ni** and **Co** as microalloying element in $Cu_{50}Zr_{50}$ at.% SMAs in terms of **mechanical performance**. The recovery ratio measured for these alloys pre and post addition of microalloying elements is examined by nanoindentation experiments to assess the viability of introducing Ni and/or Co as microalloying element in $Cu_{50}Zr_{50}$ SMAs. Once again, this investigation also considers the concentration at which microalloying elements are introduced (i.e. 0.5 and 1 at.%). **See Chapter 5**.
- Implementing a **screening method** Cambridge Serial Total Energy Package (CASTEP) electronic structure and materials properties package) to anticipate the potential of some elements in lowering SFE of B2 austenite CuZr and therefore enhancing wear resistance and tribological performance through density-based function calculations. **Mn and Fe** were chosen due to atomic number being close to Co and Ni, which have been investigated in chapters 4 and 5, respectively. Results obtained from wear testing are examined and compared with the nominal composition $Cu_{50}Zr_{50}$ at.%. **See Chapter 6**.
- The **synergistic effect** of combining cooling rate control and optimisation of microalloying element concentration is also novel and potentially leads to the ability of altering the properties of SMAs. The change of cooling rate may influence the ability of microalloying element entering in solid solution, formation of intermetallic phases as well as the nature of wear mechanism occurring when wear testing a pin of novel $Cu_{50}Zr_{50}$ at.% based SMAs against steel for 1h. For this chapter,

microalloying with cost-effective Fe (0.5 and 1 at.%) is investigated at different cooling rates (2 and 4mm diameter rods). **See Chapter 7**.

1.5. Novelty and contribution to knowledge

SMAs possess sensing and actuation functions due to SME making them an interesting candidate for various engineering applications. Although SME in NiTi SMAs is well investigated as NiTi provides maximum recoverable stress-strain, there are few limitations associated with the implementation of NiTi. First, the cost associated with NiTi is considerably higher than lower cost elements such as Cu and NiTi alloys inability to be implemented in applications where temperatures surpass 100^{o}C is considered another drawback. Therefore, Cu-Zr based SMAs are investigated in this thesis as potential replacement SMA due to cost effectiveness and potential ability to be used at higher temperatures in what is referred to as HTSMAs. Additionally, the contribution of microalloying elements is to be investigated based on the element's ability in lowering SFE in order to enhance martensitic transformation. The process of element selection is based on density-based function calculations (CASTEP) that highlights potential elements that can lower SFE, these finding are further examined by experimental testing to assess the contribution of each alloying element. Furthermore, the synergistic effect of combining cooling rate control and concentration of alloying elements entering in solid solution in B2 CuZr austenite phase is novel.

Other researchers such as Kim et al [24] investigated the effect of cooling rate and composition on Sn-Zn-Bi alloys. However, the alloy system investigated is completely different to that of CuZr. Also, the main factor investigated in my research is the effect of cooling rate control and microalloying on the crystalline phases where martensitic transformation from B2 austenite to B19' martensite occurs. It is important to differentiate between improvement of mechanical performance due to martensitic transformation and formation of intermetallic phases in place of amorphous phase. Furthermore, in order to emulate NiTi SMAs in actuation applications, tribological performance (i.e. pin-on-disc) testing is performed which is completely different to tensile testing provided by Kim et al [24]. Additionally, in 2018, Wang [25] worked with Cu-Zr-Al alloys which are predominantly amorphous. As will later be explain in section 2.3.3, CuZr-based SMAs are

very sensitive to composition change, a small variation in at.% from the predominately crystalline $Cu_{50}Zr_{50}$ at.% results in formation of amorphous phase that will directly impact the wear performance at RT and high temperature. The presence of amorphous phase (i.e. metallic glasses) has a different effect to that coming from martensitic transformation that occur in the B2 austenite crystals transforming them into B19' martensite and therefore providing the SME. Additionally, in Wang [25], the investigation focuses on the tensile and compressive strength of Cu-Zr-Al, however, this research investigates the tribological performance due to the need of implementing CuZr SMAs in actuation applications.

1.6. **Thesis structure**

- Chapter 1 provides an introduction to SME phenomenon that has been observed in NiTi and CuZr as well as highlighting research aims and objectives, novelty and contribution to knowledge.
- Chapter 2 presents a comprehensive review of the studies that are relevant to the current research topic. The review focuses on the reversible diffusion-less phase transformation in solids from austenite to martensite and vice versa. It also focuses on the methods used to obtain CuZr SMAs using various rapid solidification techniques. Moreover, this chapter discusses common metallic SMAs such as NiTi Fe-based SMAs and Cu-based SMAs as well as providing important current market needs and cost analysis.
- Chapter 3 presents the materials and methodology used throughout this research from early stages such as sample preparation to mechanically wear testing and nanoindentation as well as highlighting the post-testing analysis techniques such as Scanning Electron Microscopy (SEM) and Transmission Electron Microscopy (TEM).
- Chapter 4 investigates the importance of microalloying with Co on the wear performance of $Cu_{50}Zr_{50}$ SMA at RT and 100^{o}C. This approach is chosen in order to improve the wear performance of $Cu_{50}Zr_{50}$ SMA to emulate the wear performance of NiTi SMA. Testing was carried out at two different temperature

ranges in order to investigate the temperature impact on mechanical performance and martensitic transformation.

- Chapter 5 investigate the role of alloying and microalloying on mechanical performance of $Cu_{50}Zr_{50}$ SMA. In this chapter, alongside Co, Ni was also investigated due to its wear resistance characteristics and its promising ability in promoting martensitic transformation. Method of investigation for this chapter was done using nanoindentation testing in order to investigate the recovery ratio of the different alloys.
- Chapter 6 focuses on the wear performance of $Cu_{50}Zr_{50}$ SMA when microalloyed with Mn and Fe at different at.% concentrations. The atomic number of Mn and Fe falls in line with previously used microalloying elements that enhanced wear performance and therefore with the use of CASTEP electronic structure and materials properties package, it is possible to predict potential performance of chosen elements that can enhance wear performance of CuZr SMAs. Results obtained were validated with practical wear testing.
- Chapter 7 focuses on the synergistic effect of composition change as well as cooling rate control on wear performance of CuZr SMAs as it is an important factor that influences the microstructure of CuZr SMAs. alongside the effect of microalloying mentioned in previous chapters, this chapter takes into consideration the role of cooling rate control (~1000 k/s and ~250 k/s) on the microstructure and therefore its impact on the overall tribological performance.
- Chapter 8 summarises the major findings and proposes recommendations for future investigations.

Chapter 2 – Literature review

2.1. Martensitic transformation and shape memory effect

First, the idea of martensitic transformation and SME highlighted in **section 1.1** is not exclusive to alloys. The SME is also found in **ceramics and polymers** [26]. The SME known for alloys comes from the recovery to original shape after apparent deformation, however, in the case of ceramics the phase transition is referred to as ferroelectricity and this has been studied and observed by Reyes-Morel et al. [27] when studying $Ce0_2$-

stabilized tetragonal zirconia (ZrO_2) polycrystal. After a series of uniaxial compressive tests, it was found that heating produces gradual recovery to original shape in a similar manner to SME of alloys. The temperatures at which this transformation takes place is governed by the ceramics tested and in the case of Reyes-Morel study ferroelectric transition started at around 60^{o}C, however, the strain recovery was minor up to 186^{o}C in which around 95% of ferroelectric transition takes place.

The SME is also found in certain polymers, the mechanism of SME in polymers is entirely different from SME of alloys. The best way to describe the SME mechanism in polymers is the example of rubber behaviour under stress. When stress is applied, rubber elongates to a certain length, once the stress is removed, the rubber reverts to original shape. This behaviour is bound by elasticity of rubber at RT. However, when temperature drops below glass transition temperature (T_g), the elastic behaviour of rubber is lost, and the deformed shape remains stiff without reverting to original shape. When temperature is increased above T_g, the strain is released and therefore deformed frozen polymer reverts to original shape. Despite their low cost, ease of control and light weight, the practical use of shape memory polymers is limited due to low strength and lack of recovery stress. For example, recovery stress of shape memory polymers is 10-30 kgf/cm^2 while it is 1500-3000 kgf/cm^2 for shape memory metal alloys [26].

In terms of metal alloys, a brief background is given in **section 1.1**. In greater details, Otsuka and Wayman referred to martensitic transformation [26] as a diffusion-less phase transformation in solids, where atoms are moved in a shear-like manner. The transformation from B2 austenite into B19' martensite cannot be characterised by a single value of stress and/or temperature [4]. A slight composition change can lead to a change in the transformation stress needed and temperature at which the transformation occurs. Noting that the transformation process occurs at a range of temperature, in fact, the transformation process is characterised by four temperatures:

Austenite start (A_s) refers to the temperature at which austenitic transformation from martensite into austenite, which starts taking place at A_s.

Austenite finish (A_f) refers to the temperature at which austenitic transformation from martensite into austenite, which starts taking place and end at A_f and for which B19' has fully transformed into B2 stable austenite.

Martensite start (M_s): refers to the temperature at which martensitic transformation from austenite into martensite, which taking place at M_S.

Martensite finish (M_f) refers to the temperatures at which martensitic transformation from austenite into martensite, which ends at M_f and for which B2 austenite has fully transformed into B19' stable martensite.

The martensitic transformation mechanism is the same for different alloys that includes the widely known NiTi, Cu-based SMAs and Fe-based SMAs. The transformation temperature may differ from one alloy system to the other, however, the mechanism responsible for the transformation is the same. **Fig. 2.1.** shows a schematic of martensitic transformation of CuZr, starting from the simple cubic unit cell of CuZr one can construct a new tetragonal unit cell as indicated by the dashed lines. Shuffling of the (110) lattice plane along the [11-0] direction transforms the B2 lattice into a B19 structure. Shearing of the (001) plane along the [11-0] direction finally leads to B19' CuZr" [28]

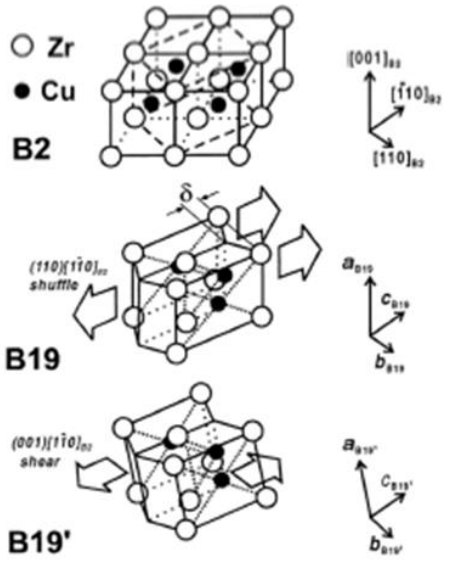

Fig. 2. 1. Martensitic transformation in NiTi and CuZr from B2 to B19' structure [28].

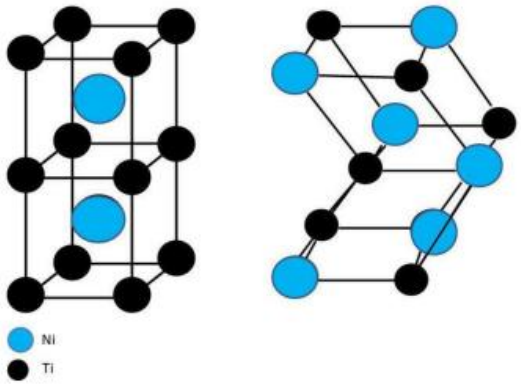

Fig. 2. 2. Crystallography: (left) austenitic phase (B2), (right) martensitic phase (B19') [29].

The interest in investigating SMAs comes from their special ability to **remember their original shape**. Once a SMA is subjected to a stress high enough to cause permanent plastic deformation in the metastable austenite to transform into martensite, the alloy afterwards is able to revert to the original shape after heating up beyond certain temperature (i.e. A_f), the process in which martensite is reverted to austenite due to heating process is known as austenitic transformation [30]. This fascinating characteristic accompanied by the typical peculiarities of metals such as, stiffness, workability, resistance, etc, makes SMAs a very interesting topic for investigation [4].

The SME emerges from a phase shift (rearrangement of atoms), in which a crystal structure is rearranged according to the stability of crystalline phases. Their stability is governed by the temperature at which they exist. The phase stable at low temperature is also referred to as martensite and it is known to be crystalline and harder than austenite [31, 32]. On the other hand, the phase stable at higher temperature than martensite is referred to as austenite and it has Body Centered Cubic (BCC) structure geometry for NiTi.

The stability of the phase is better illustrated in **Fig. 2.3** where the austenitic and martensitic transformations are shown. The peak during the heating process (heating curve) shows how the austenitic transformation occur starting from A_s to A_f. A_f marks the end of the transformation process and attains a stable austenite structure at a particular temperature. That temperature varies from one alloy system to another. Upon cooling (cooling curve), the fully stable austenite at high temperature is cooled down to below the

transformation curve, leading to martensitic transformation from austenite into martensite M_s to M_f, the result of that is fully stable martensite at low temperature.

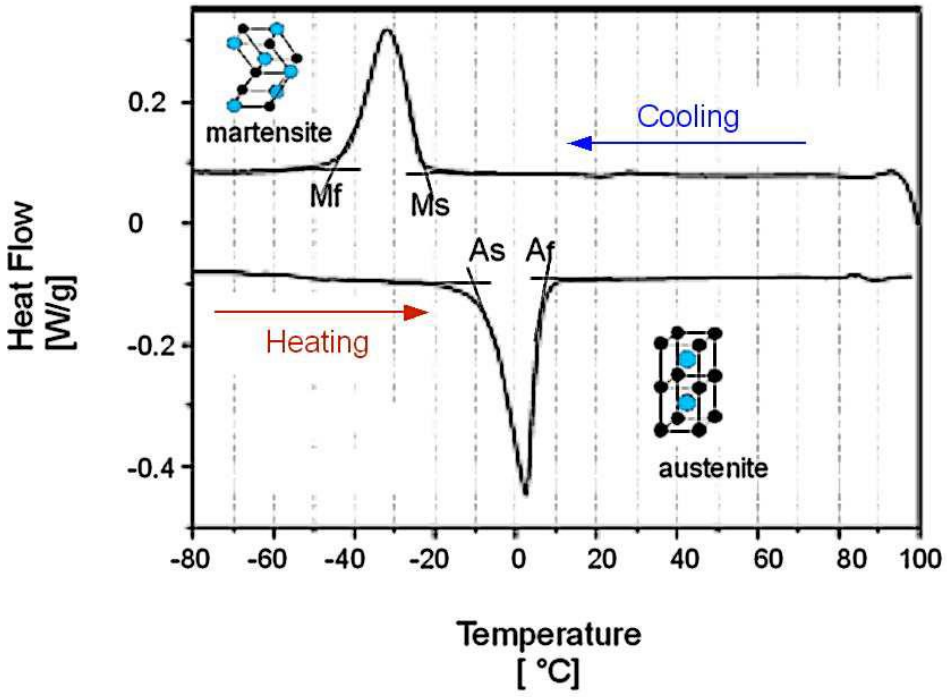

Fig. 2. 3. Typical DSC scan showing austenitic and martensitic transformations [33].

The martensitic transformation occurs due to **deformation twinning process** that is responsible for transforming B2 austenite into stress-induced B19' martensite. Before going into details in explaining deformation twinning in detail, a brief explanation of plastic deformation in metals is given first.

Plastic deformation in metals can be split into **slip dislocation and twinning**. **Slip** is the most common mechanism of plastic deformation in metals. It involves movement of dislocations along crystalline planes leading to plastic deformation. During **twinning**, the atoms in each successive plane in a block move through different distances proportional to their distance from twinning plane. Slip dislocation is commonly observed in BCC and Face Centered Cubic (FCC) metal structure, on the other hand, twinning is commonly observed in Hexagonal Close Packed (HCP) metals. A distinctive difference between the two deformations is related to the stress required to cause plastic deformation, slip dislocation requires relatively low stress compared to twinning [34].

Table 2. 1. Deformation by slip dislocation and twinning [35].

Slip	twin
Orientation across the slip plane is same	Orientation across the twin plane is different
Atomic movements are equal to atomic distances	Atomic movement are less than atomic distances
Atoms are moving in only one plane (slip plane)	Atoms are moving in all planes in the region of twin
Takes place at low strain rates	Takes place at high strain rates

The process of martensitic transformation occurs through the motion of twin boundaries that results in twinning of the microstructure. This re-orientation of the austenite structure results in transformation of the phase into martensite. The twinning and de-twinning process is responsible for the SME and this makes SMAs unique [36].

When a material is subjected to stress levels beyond its yield point in a martensite state, dislocations start to generate and are responsible for plastic deformation due to surpassing the yield point. On the other hand, in a SMA, the dislocations generated when the yield point is surpassed are insignificant because the critical stress needed to start a detwinning process is lower than the stress required for dislocations. This leads to a full or partial reversible phase transformation [37]. The plastic deformation associated with martensite in SMAs is accredited to the detwinning process. In fact Ashby [38] claims this plastic deformation can reach around 6% strain without any significant increase in dislocation density and that is what differs SMAs to other materials [39].

Each martensitic crystal in a SMA can have a different orientation direction, also called “variant” [39]. These variants may assemble in two ways, first in a twinned martensite (M_t) which consists of a combination of self-accommodated martensitic variants. Second is detwinned martensite (M_d) where a specific variant is dominant [39]. Therefore, when a stress is applied, martensite transforms through twinning process that transforms variants to different variants where it can accommodate maximum strain. The principle that governs which variant transforms into the other depends on the direction of the applied

force [40]. In the contrary, austenite has only one possible orientation, this explains why SMAs are able to recover their original undeformed shape. SMAs are different from one to another in terms of magnitude of shape recovery, factors such as dislocation generation and detwinning are responsible for the macroscopically observed deformation [22].

The present interest in the phenomenon of **twinning arose from its importance to simultaneously improve the strength and ductility of traditional materials such as steel and aluminium alloys**. This idea has been recently applied as a strategy to improve the ductility of more new materials such as CuZr and NiTi based alloys [41]. These alloys combine the improved ductility, fracture toughness and plasticity of shape memory crystalline phase because the dispersed particles of B2 austenitic phase **undergo stress-induced martensitic transformation thus resulting in work-hardening** and therefore can delay catastrophic failure [39].

Deformation twins have long been identified in BCC, HCP and in lower symmetry metals and alloys, and more recently have been observed in many FCC metals and alloys [42-45], and other intermetallic compounds [46], in elemental semiconductors [47] and compounds [48], in other non-metallic compounds such as calcite and sodium nitrate and even in complex minerals and crystalline polymers [49]. An example of deformation twinning in a BCC alloys was observed in Fe-Cr-Co alloy system [50]. Additionally, deformation twinning in FCC was also reported in Co-Fe alloy [50].

Twinning does not form readily in FCC or BCC because they have sufficient slip systems unlike HCP that possess only 3 slip systems. However, twinning has been observed in FCC Al-Mg alloys which according to conventional theory, should not twin since Stacking Fault Energy (SFE) of aluminium is too high. This is possible in certain circumstances such as high strain rates and low temperatures [51].

Consider the interface between a twin and the parent crystal. The atomic arrangement at a **twin boundary** in an FCC metal is shown in **Fig. 2.4**. This diagram assumes that the twin interface is exactly parallel to the twinning plane. In this structure, the two lattices (twin and parent) match perfectly at the interface. Atoms on either side of the boundary have the normal interatomic separation expected in an FCC lattice. [52]

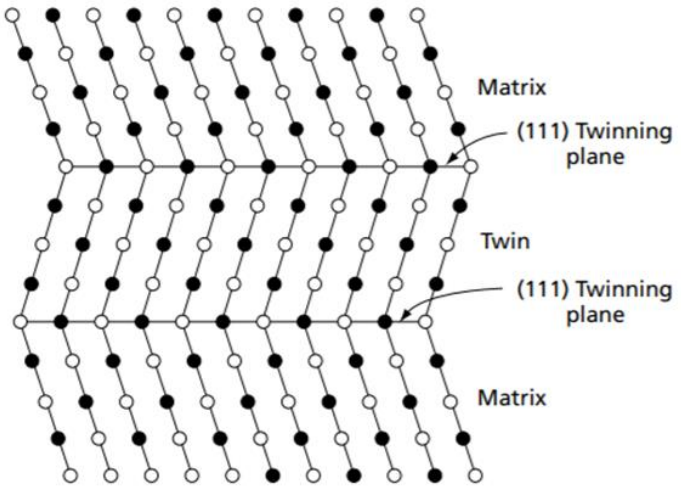

Fig. 2. 4. Atomic arrangement at the twinning plane in a face-centered cubic metal. Black and white circles represent atoms on different levels (planes) [52].

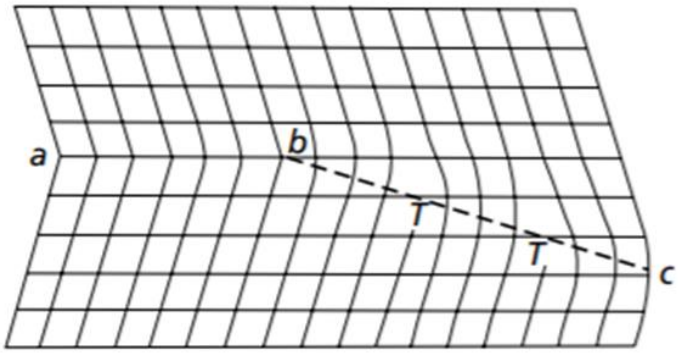

Fig. 2. 5. The difference between a coherent twin boundary ab and an incoherent twin boundary bc. Notice the dislocations in the incoherent boundary [52].

The interfacial energy of the boundary is very small. In the case of copper, it has been determined to be 0.044 J/m^2 [52], which is very much smaller than the surface energy of a Cu-Cu grain boundary, which is 0.646 J/m^2 [52]. Barrett has drawn similar diagrams to that of **Fig. 2.4** for {10-12} twins in hexagonal metals and {112} twins in BCC metals. He shows that in both cases a reasonable match between twin and parent lattices can be made across twinning plane. However, atoms on both sides of the interface are displaced small distances from their normal lattice positions. Because atomic bonds are strained in these twin interfaces, they must possess higher interfacial energies than the {111} twin boundary of FCC metals. **However, these energies are still much smaller than those of normal grain boundaries**. The fact that deformation twins invariably form on planes

of low indices may be explained in terms of the surface energy associated with the interface between twins and parent crystals. In general, **the higher the surface energy, and the lower the probability of twin formation**. A **twin boundary** that parallels the twinning plane is said to be a coherent boundary. Most twins start as thin narrow plates that become more and more lens shaped as they grow. The average twin boundary is, accordingly, incoherent. In a coherent boundary it is usually quite possible to match the two lattices without assuming the presence of dislocations in the boundaries. (**See Fig. 2.4**.) In an actual boundary where it is not coherent, it is generally accepted that a dislocation array is necessary in order to adjust the mismatch between lattices of parent and twin. This is demonstrated in **Fig. 2.5**, **where it is shown schematically segments of both a coherent boundary and an incoherent boundary** [52].

So far in this thesis, **martensitic transformation** is referred to as the transformation of B2 CuZr austenite phase into B19' CuZr twinned phase **caused by stress-induced martensitic transformation**. This superior mechanical and tribological performance of B19' twinned martensite phase in terms of work hardening makes it centre of attention in terms of martensitic transformation. This transformation was first revealed by Nicholls et al. [53]. However, it was also found that an unknown structure having Cm space group was also found and later referred to as **B33 CuZr phase** [54] therefore, based on studies [55], B19' is a monoclinic martensite phase with a basic structure of ($P2_1/m$) and B33 is the superstructure of the former with a doubling of lattice parameter along the a and b axes (Cm). The lattice parameters of both are the following [56]:

B19'
a = 0.3278 nm
b = 0.4161 nm
c = 0.5245 nm
β = 103.88°

B33
a = 0.6316 nm
b = 0.8562 nm
c = 0.5331 nm
β = 105.27°

Fig. 2.6 shows a schematics of a) austenite, b) basic monoclinic martensite and c) superstructure martensite with the associated crystallographic relation [56].

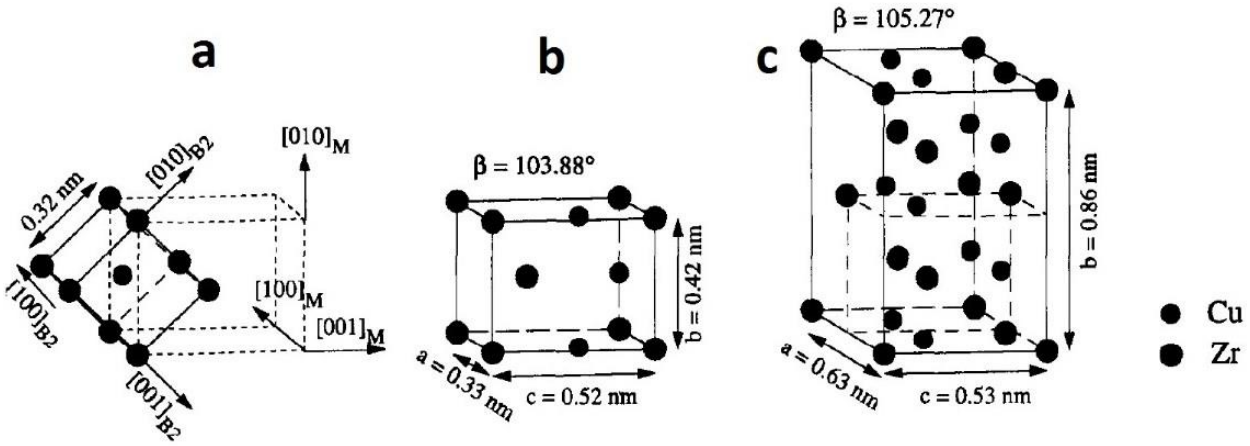

Fig. 2. 6. Schematics of a) austenite, b) basic monoclinic martensite and c) superstructure martensite with the associated crystallographic relation [57].

Despite the lack of research about the mechanical performance of B33 phase, it is important to highlight that B33 phase may exist in CuZr SMAs and therefore contribute towards tribological and mechanical performance. The tribological performance and contribution of B33 phase in CuZr SMAs will be investigated in this thesis.

Summary:

- The martensitic transformation process is characterised by four temperatures: **A_s, A_f, M_s and M_f.**
- Martensitic transformation is a **diffusion-less phase transformation in solids**, where atoms move in a shear-like manner.
- During martensitic transformation, an alloy transforms from B2 austenite (stable at high temperature) to B19' martensite (stable at low temperature).
- **Twinning** process (commonly observed in HCP metal structure) improves strength, ductility of SMAs through process of **work-hardening** and thus delays catastrophic failure.
- During martensitic transformation, SMAs **exhibit deformation twinning** that is responsible for transforming B2 austenite into stress-induced B19' martensite.
- B2 austenite can also transform to B33 martensite phase and not only to stress-induced B19' martensite.

2.2. **Rapid solidification**

Rapid solidifcation is described as the rapid extraction of thermal energy from molten metal to solidify it. Rapid solidification processes offer an alternative to conventional casting methods for the fabrication of SMAs. These processes have a high solidification rate and can result in large deviations under which equilibrium diagrams such as **Fig. 2.7** are obtained offering significant advantages including: extension of the solid solubility, formation of nonequilibrium or metastable crystalline phases, microsegregation free solidification and a host of other microstructural effects (i.e. refinement of grain size and shape) [58].

One of the reasons for using rapid solidification technqiues is promote the presence of microalloying elements in solid solution and thus avoid element segregating to grain boundaries from the crystalline phase. One way of doing so is to increase the cooling rate since this will not allow time for microalloying element to segregate. Ciftci et. al. [59] referred to any solidication process with cooling rate ranging from 10^3-10^6 K/s is considered rapid solidification.

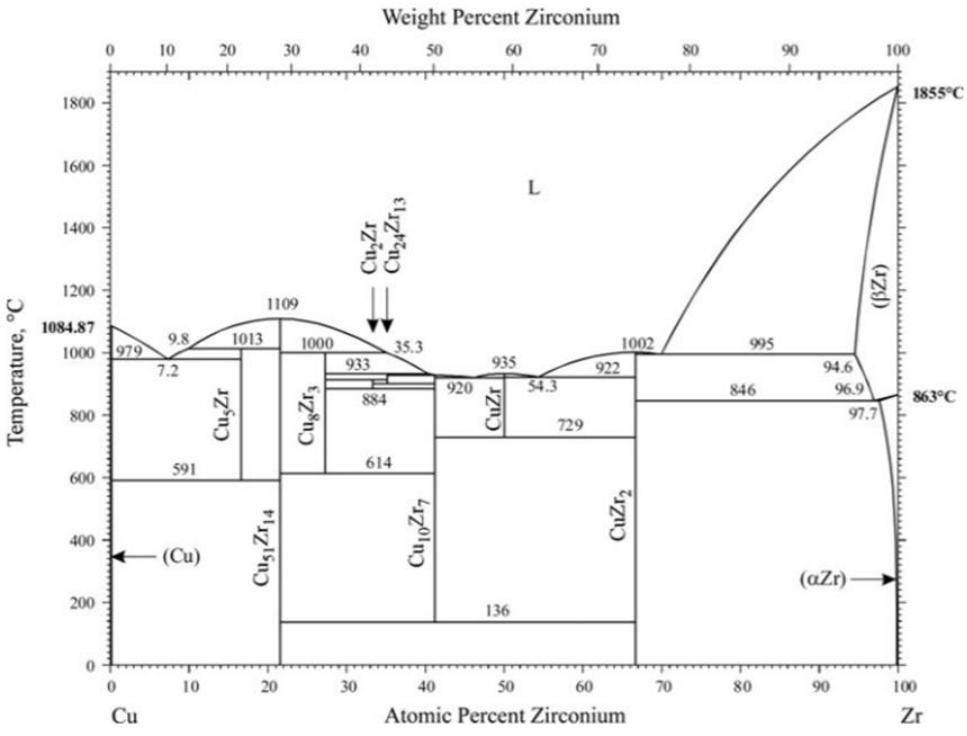

Fig. 2. 7. Phase diagram of Cu-Zr binary alloy [60].

Stable binary CuZr diagrams give an idea of what intermetallic compounds are expected (e.g., Cu_8Zr_3, $CuZr_2$, $Cu_{10}Zr_7$, etc…) during the solidification process “infinitely slow”, however, in rapid solidification, the cooling rate is much faster. A faster cooling rate **promotes** twinning of CuZr phase during solidification process due to the presence of microalloying element in solid solution creating an obstacle and preventing slip dislocation. Therefore, Time Temperature Transformation (TTT) diagrams are introduced as they provide information about the different microstructures that are formed depending on the cooling rate.

Fig. 2.8 shows a schematic TTT diagram of CuZr-based SMA and the role of rapid solidification on the phase formation of the cooled alloy. As explained in **Fig. 2.7** if the cooling rate is infinitely slow, $Cu_{50}Zr_{50}$ at.% decomposes into equilibrium phases $CuZr_2$, $Cu_{10}Zr_7$. However, when rapidly solidification the molten metal, the solidification process follows the trend shown in **Fig. 2.8**. R is cooling rate where the molten metal (liquid state) cools down at a certain cooling rate from above T_{liq} crossing the B2 phase, $CuZr_2$, $Cu_{10}Zr_7$ and M_s lines. However, when the cooling rate is at or below R_{B2} (critical cooling rate), the formation of intermetallic compounds namely $CuZr_2$, $Cu_{10}Zr_7$ is prevented. Furthermore, if the cooling rate is even faster reaching R_c, the obtained cooled alloy is fully amorphous. Additionally, **Fig. 2.8** shows that addition of microalloying element (Co in this case) shifts the nose of the graph towards the left and increases thermal stability of B2 phase as well as shifting the eutectoid reaction (B2 decomposing into $CuZr_2$, $Cu_{10}Zr_7$) towards lower temperatures. This and more will be highlighted in detail in **section 2.4.1**.

The above explanation shows and how metallic glasses are formed relating to the critical cooling rate of alloys. For SMAs, our point of interest is on the crystalline phase which contains the SME and according to our results in chapters 4-7 shows that from X-ray Diffraction (XRD) results of multiple samples casted at different times, the crystallinity of the alloys is clear from major peaks (B2 CuZr) in particular and interestingly the amorphous halo associated to the amorphousness of a given materials is barely visible. TTT diagram is very useful in terms of understanding the influence of cooling rate as our rapidly solidified materials do not follow a stable equilibrium binary diagram because that

require an extremely low cooling rate to ensure full crystallisation and stabilisation of all phases.

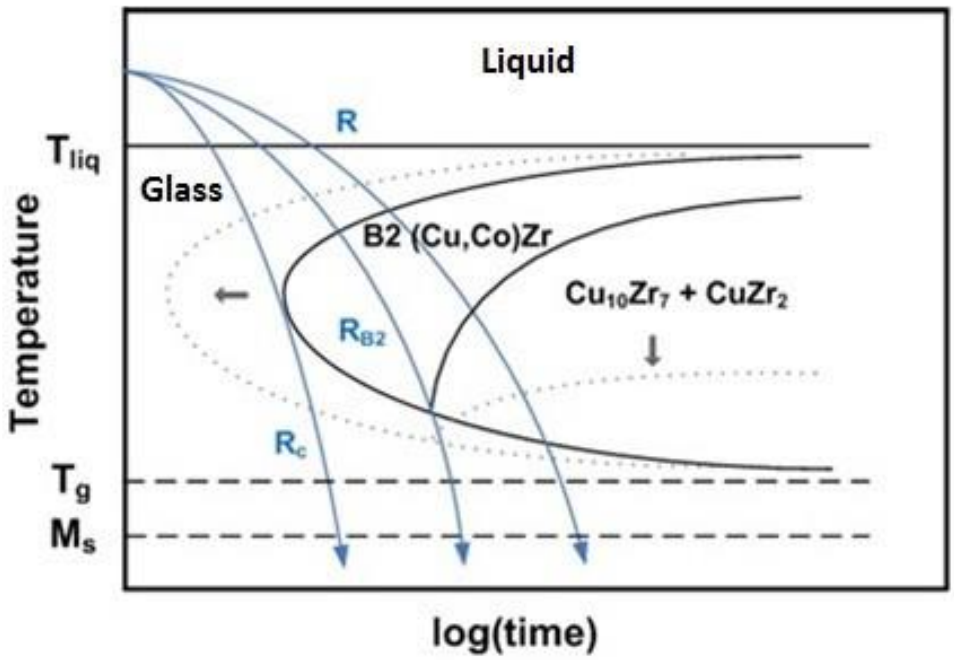

Fig. 2. 8. A schematic TTT diagram of CuZr-based SMA during rapid solidification. R_{B2} is the critical cooling rate to supress the decomposition of B2 CuZr austenite to $CuZr_2$ + $Cu_{10}Zr_7$ intermetallic phases and R_c is the critical cooling rate to obtain a fully amorphous structure [57].

Unlike eutectoid steel, the TTT diagrams of $Cu_{50}Zr_{50}$ at.% are not widely popular due to researchers only recently focusing their interest on this alternative type of SMAs to replace NiTi. Sato et al. [61] proposed TTT diagram and critical cooling rates of $Cu_{50}Zr_{50}$ and $Cu_{20}Zr_{80}$ at.% alloy using Molecular Dynamics (MD) simulation. MD is promising tool to achieve a theoretical prediction. However, direct MD prediction continues to be challenging due to the time-scale limitation of MD. This approach is important to understand how sensitivity to composition change and Glass Forming Ability (GFA) impact the phase stabilisation and obtained microstructure after rapid solidification. **Fig. 2.9** shows how a change in composition shifts the nose to the left and increases thermal stability of B2 phase. This is in agreement with [62] where it was found that even smaller composition change (±2 at. % Cu) can lead to dramatic change of microstructure (crystalline to amorphous volume fraction) [63].

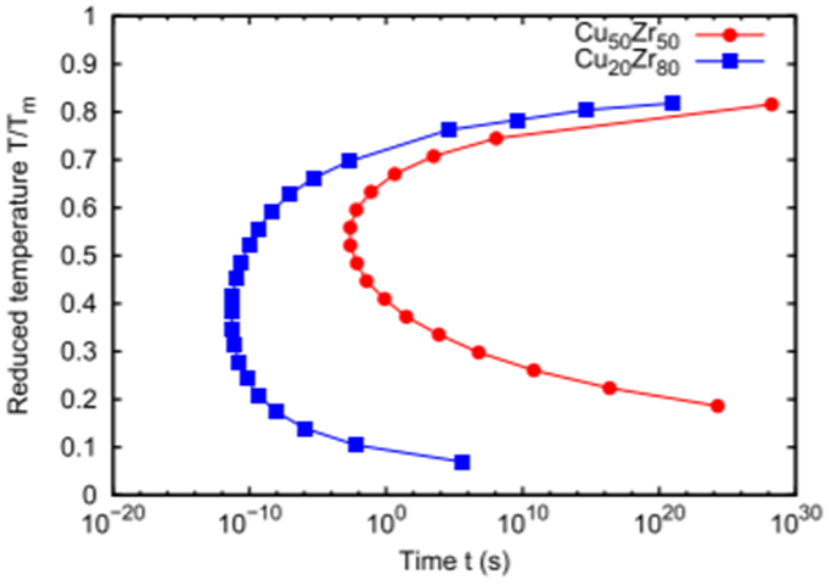

Fig. 2. 9. TTT diagrams of $Cu_{50}Zr_{50}$ and $Cu_{20}Zr_{80}$ at.% [61].

2.2.1. **Rapid solidification techniques**

A number of methods are used for the production of SMAs. While most of the conventional methods yield the alloys in large quantities, some of the recent techniques are not amenable for their large-scale production. Moreover, these techniques require capital investment and are expensive to use. Some of the methods that are used for the production and processing of SMAs are given below.

While some of these methods use bulk Ni and Ti to produce the alloys, certain others make use of Ni and Ti powder for the synthesis. Some of the techniques that are used for making thin films and foams make used of the raw materials in the form of powder. Accordingly, we can classify the production methods as casting methods, powder metallurgy, methods, thin film methods and metal foam processes. While some methods yield bulk solids, certain others yield porous solids. The alternative routes to ingot metallurgy have been resorted to overcome the problems arising during melting and subsequent processing/machining. Most of mechanical properties and shape memory characterisation that are not achievable in alloys made using the conventional methods can be achieved in alloys made using non-conventional methods.

2.2.1.1. **Melt spinning**

Melt spinning is a process used for producing amorphous metal and metallic glassy alloys in the form of thin strips (called ribbons) [64]. This approach, which was introduced by Duwez and his group in 1960 [65], has led to synthesizing several hundred binary, ternary and multicomponent amorphous and metallic glassy systems during the last five decades [66-69]. **During melt spinning, a molten metal is subjected to very rapid cooling rate that reaches 10^4-10^6 K/s** [64]. Details related to the exact details of production of amorphous materials is found in [70]. In melt spinning process, 5-100g of small pieces of alloy are placed in a boron nitride or quartz glass crucible surrounded by induction coil.

Applying high current leads to increase in the temperature of the alloy inside the crucible, therefore it melts. Then the molten metallic drops are ejected by Ar-pressurization through a fine nozzle onto a fast-rotating copper wheel, which usually rotates at 5,000-7,000 rpm. Such high-rotation rate offers the rapid solidification rates (10^5 -10^6 K/s) required to freeze the atoms of the liquid phase (molten metal) into solid amorphous state. It is worth mentioning that melt spinning of molten metallic system does not only lead to the formation of amorphous and metallic glassy alloys, but also leads to the formation of other nonequilibrium phases, such as nanocrystalline [71], quasi-crystalline phases [72, 73], and supersaturated solid solution [74]. More detailed information on the formation of bulk metallic glassy alloys was reported by Suryanarayana and Inoue [69].

Estimations of the cooling rate in melt spinning is reported in the literature between 10^4-10^6K/s [75], depending on number of parameters [76, 77]. However, it is inappropriate to assign a single value to the cooling rate for any chill block casting since the cooling rate can vary dramatically through the thickness of the ribbon [78]. This is critically important when producing ribbons in systems where critical cooling rate and effective cooling rate are close. In this situation results in ribbons that are crystalline on the free side and amorphous on the wheel side. This can be seen in XRD analysis.

The variation of ribbon thickness and cooling rate of melt spun material depends on the wheel speed. Earlier in this chapter, it was mentioned that the cooling rate for melt spinning varies in range of 10^4-10^6K/s as there are factors that govern the cooling rate achieved [79]. The melt layer is directly influenced by the speed of which the wheel is

rotating hence reducing the ribbon thickness. When the melt layer on the wheel surface is thinner, the entire layer will be undercooled resulting in high cooling rate through the entire transverse cross section of the ribbon. Whereas, for a thicker melt layer, solidification at the contact surface starts before the entire layer is undercooled and the crystallization heat absorbed by the remaining melt will decrease its cooling rate. For instance, Nithya Christopher et al. [79] found that ribbons with thickness of 126μm show a cooling rate of ($3x10^6$ K/s), on the other hand, ribbons with thickness of 17μm show a cooling rate of ($2x10^7$ K/s). From **Equation 2.1** the cooling rate can be determined.

$$\mathbf{dT/dt\ [K/s] = (h.\ \Delta T) / (s.\ \rho.\ Cp)} \qquad \mathbf{(2.1)\ [79]}$$

where,

dT/dt: Cooling rate [K/s];

h: heat transfer coefficient [W/m^2K];

ΔT: difference between melt temperature and temperature of copper wheel [K];

S: thickness of the melt spun ribbon [m^2];

ρ: density of the material [kg/m^3];

Cp: specific heat of the material [J/Kg.K].

2.2.1.2. **Melt atomisation**

Melt atomisation is the most common method used to produce alloy powders from Ti, Cu, Al, Fe, Ni, and other alloys because high production rates favour economies of scale. Atomisation process involves the energetic disintegration of a liquid into micro-meter-sized droplets [80]. The process of melt atomisation consists of a molten metal forced through an orifice at moderate pressures. It is important to stream the molten metal at moderate pressures to ensure disintegration into droplets by the impingement of high-energy jets of a particular fluid medium, which may be either gas or liquid, such as inert gas, water, or oil. Gas atomisation is usually the favourable method of atomisation for production of alloy powders, the reason for that is control of powder cleanliness, powder size distribution and powder chemistry can be controlled. The melt is delivered to an atomizer nozzle where it is fragmented into micro-meter-sized droplets by means of

energetic jets. The ligaments and other irregular shapes that form first during disintegration, and subsequently during interactions with aerodynamic forces, are spheroidized, a process that is driven by the high surface energy that is typical of molten metals. The molten spheres subsequently experience solidification into powder particles during flight. Particles are collected normally in the lower region of the atomisation chamber, frequently via a cyclone separator device [80].

The powder particles' size resulting from atomisation enables cooling rates many orders of magnitude above those in casting processes, ranging from **10^2 to 10^6 K/s** [80], which is known as rapid solidification, a non-equilibrium process. **The cooling rate of the droplets depends on several process parameters**, such as gas pressure, gas composition, gas/melt mass flow ratio, and atomizer design, etc. The cooling rates depend on the heat exchange between the atomized particles and the surrounding medium via two mechanisms: convection into the cooling gas and radiation towards the atomizer chamber. The former is the predominant mechanism, given the temperature gradient and flow conditions that are typical of melt atomisation. **As the cooling rate experienced by the atomized particles depends on their size, amorphous and well-developed microstructures** can be found in a gas atomisation batch with an appropriate composition [81].

The cooling rate strongly depends on the droplet diameter (d_p) and on gas-to-melt mass flow ratio (GMR). The GMR and the initial gas temperature T_{G0} are not independent of each other, meaning that a change in T_{G0} results in different GMR values. A mathematical correlation was developed based on heat flow considerations for molten metal gas atomisation. The following atomizer equation is proposed [59]:

$$\mathbf{dT/dt\ [K/s] = a_o .\ d_p^{-1.55}\ (\dot{m}_G/\dot{m}_L)^{0.18}} \qquad \mathbf{(2.2)}$$

where,

dT/dt: Cooling rate [K/s];

a_o: pre-exponential factor describing the material and gas properties;

d_p: Droplet diameter [µm];

$\dot{m}_G$: Gas mass flow rate [kg/s];

$\dot{m}_L$: Melt mass flow rate [kg/s].

Note that, a_o depends on the atomizer configuration as well as the material and gas properties. For instance, in Cifti et. al study [59], where Cu-6 wt.% Sn alloy was gas-atomized using close-coupled (CCA) and free-fall atomisation (FFA), a_o was 3.73 x 10^6 for CCA and 2.79 x 10^6 for FFA, respectively. In addition, it should be noted that this equation is valid for particle sizes from 25 to 250 µm, a GMR ($\dot{m}_G/\dot{m}_L$) from 1.3 to 8.3 and gas temperatures from 293 to 571 K (atomized under argon atmosphere).

2.2.1.3. **Vacuum arc melting and suction casting**

In vacuum arc melting process [82] theoeritically, if the elements were thoroughly cleaned, there is less possibility for contamination of the molten metal with carbon since a water-cooled copper crucible is used for melting instead of a graphite crucible in the case of vacuum induction melting where graphite crucibles are used instead of carbon. Moreover, the alloy produced has to be repeatedly remelted, five to six times to bring about chemical homogeneity which can be later analysed in detail using SEM-EDX technique [82].

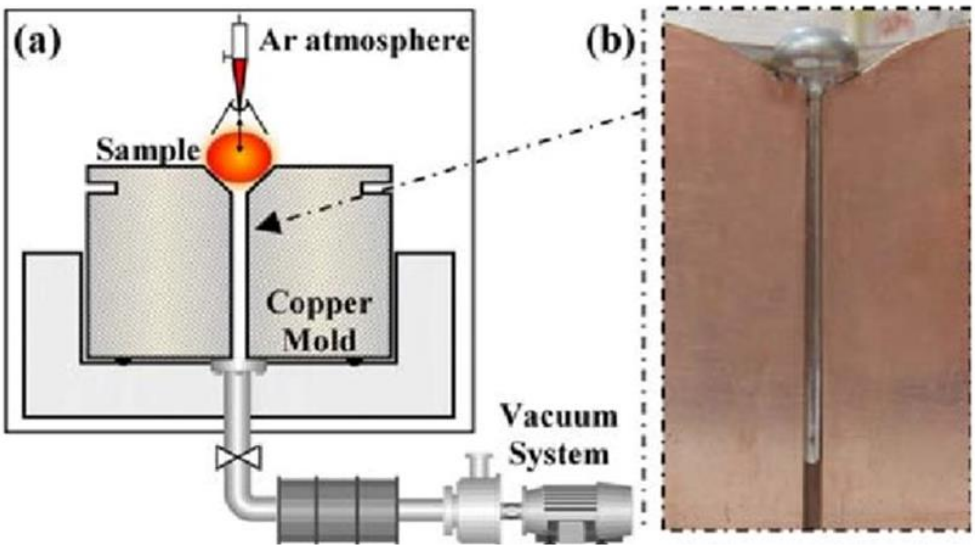

Fig. 2. 10. (a) Schematic of suction casting process and (b) a sample in copper mould [83].

Rapid solidification techniques are used to prevent segregation, e.g., melt spinning is considered the fastest technique where cooling rate reaches around 1million K/s [64]. Despite wanting a high cooling rate to preserve the microalloying element in solid solution

and prevent segregation, however, such high cooling rate prevents the ability to produce bulk material. Therefore, melt spinning is usually used to produce thin ribbons, Arc melting on the other hand, enables the production of bulk samples more than 1mm thickness due to its slightly lower cooling rate compared to melt spinning. **Copper mould suction casting cooling rate is reported by Lin and Johnson to be around 10^5 K/s** [84]. Additionally, atomisation has the slowest cooling rate.

The effect of cooling rate on the properties of metals is well documented [85]. Hardening of steel can be altered by modifying the cooling rate to promote the formation of certain phases and ability to allow certain elements to enter in solid solution during the process of solidification. This is no different to the case of SMA where the target is to cool down fast enough to have microalloying element preserved in austenite grains, and in the meantime not cooled so fast to still have a mostly crystalline material rather than an amorphous material. XRD results and analysis will shed light to the volume fraction of casted materials in Chapters 4-7.

Following melting the material using arc melter in vacuum conditions, it is possible with this technique to produce rods of metallics alloys at different dimensions. The variation of the diameter size of the Cu cast mould where molten metal is casted has a significant effect on mechanical properties of the alloy. Therefore, Lin and Johnson [84] proposed the following relationship Equation 2.3 between the total cooling time, sample dimension (radius) and thermal diffusivity [84]

$$T \sim (R^2 / \kappa) \qquad (2.3)$$

where,

T: Total cooling time (to RT), R: Radius of sample (cm), κ: Thermal diffusivity. κ is given as K/C where K is thermal conductivity and C is heat capacity per unit volume. This relationship shows that an increase of radius of casted material results in two orders of magnitude increase in total cooling time. Bearing in mind that an increase of cooling time means slower cooling rate.

Lin and Johnson [84] derived Equation 2.4 showing the cooling rate achieved will be of the order of [84]

$$dT/dt = (T_m - T_g) / T = K(T_m - T_g) / CR^2 \qquad (1.4)$$

Typical values for molten alloys were taken by Lin and Johnson [84] T_m-T_g~400K, K~0.1 W/cm s^{-1} K^{-1} and C~4 J/cm^3 K^{-1}, which gives [86]

$$\mathbf{dT/dt\ (K/s) = 10/R^2\ (cm)} \qquad \mathbf{(5)}$$

It is worth mentioning that this formula is derived for bulk metallic glasses, hence the temperature difference is between the melting point and the glass transition temperature T_g. However, this process is similar to the technique used to produce CuZr based alloys for this study using Compact Arc Melter MAM-1, that is capable of producing metallic glasses too. The point of interest in this thesis is regarding SME in CuZr based alloys, therefore the crystalline phase (where SME exists) is the focus point of this study.

Summary:

- Theoretically speaking, a molten metal cools down infinitely slow to provide equilibrium diagrams (refer to Fig. 1.9), however, in the case of rapid solidification, heat is extracted rapidly resulting in deviation from equilibrium diagrams.
- Rapid solidification provides range of advantages such as: solid solubility, formation of nonequilibrium or metastable crystalline phases and grain refinement.
- When the **cooling rate** ranges from **10^3-10^6 K/s**, it is considered rapid solidification [56].
- Rapid solidification is essential to **ensure microalloying element entering in solid solution** in B2 austenite phase in order to create an obstacle to slip dislocation, therefore promote twinning and enhance martensitic transformation.
- **Melt spinning** (**fastest** cooling rate $\approx$**10^4-10^6K/s**) is a well-known process used to produce metallic glassy alloys in the form of **ribbons**.
- **Melt atomisation** is the dominant method used to produce alloy **powders** with cooling rate ranging from **10^2-10^6 K/s**.
- Vacuum arc melting and suction casting is used to **produce bulky material**.
- Despite cooling rate being lower in suction casting compared to melt spinning, suction casting technique is fast enough to **ensure microalloying** element entering into **solid solution** (preventing segregation).
- Elements entering in solid solution creates **obstacles** that **prevent** dislocations slip and can also decrease the stacking fault energy and thus **promote twinning**.

2.3. Common metallic shape memory alloy systems

It is well known that NiTi has attracted the most public interest in recent decades due to stability, practicability, high recovery ratio and superior thermo-mechanical performance [87]. With the increased demand for SMAs in a variety of applications, research have started to investigate other potential SMA systems with lower cost and potential energy output that can match NiTi SMA systems. SMAs are classified as Ni-based SMAs, Cu-based and Fe-based SMAs [88, 89].

2.3.1. NiTi and NiTi based shape memory alloys

NiTi SMAs exhibits SME in a similar manner as explained in section 1.1, the high temperature phase B2 austenite has a BCC structure while B19' martensite phase is stable at low temperatures and has a monoclinic lattic structure [14]. This monoclinic lattice structure can be treated as a distorted HCP structure. In binary NiTi alloys, the thermally induced SME and the pseudoelasticity only occur in a narrow chemical composition range. Only around the stoichiometric composition (1:1), the intermetallic phase NiTi (B2) can exist in the absence of other phases under equilibrium conditions (see gray area of the binary phase diagram shown in **Fig. 2.11**).

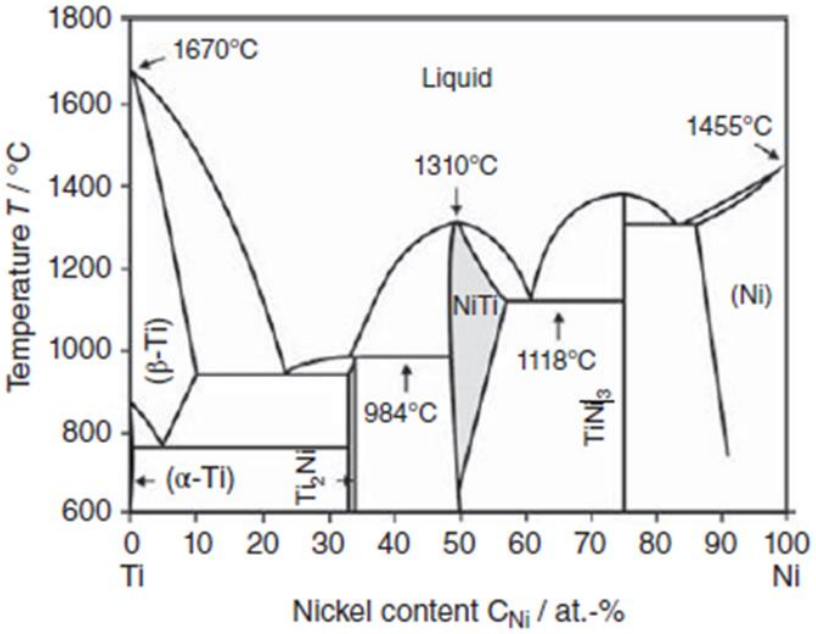

Fig. 2. 11. Phase diagram of the system nickel–titanium. The single-phase NiTi (B2) is shaded; important temperatures are highlighted [14].

In addition, from the phase diagram in **Fig. 2.11**, it is evident that NiTi phase has a limited solubility for Ti for less than 51% independt of temperature [14]. Therfore, in these Ti-rich compositions and in almost equiatomic balances, the NiTi phase is stable even at low temperatures. On the other hand, The maximum nickel content of the NiTi phase cannot exceed 57 at.%. Below 1118 ^{o}C, the solubility limit of Ni in NiTi phase decreases with decreasing temperature. At temperatures below 1118 ^{o}C, this overstoichiometric balance of the B2 phase does not exist. However, by rapid solidification from this overstoichiometric balance, the Ni-rich composition of the B2 phase can be frozen in a metastable state without decomposing to secondary intermetallic phases. If this metastable phase is afterwards subjected to heat, it will reach a state of thermodynamic equilibrium by complex diffusion and precipitation processes [90].

Depending on the temperature and the aging time, a two-phase state of the phase NiTi and Ni-rich precipitations will be formed. This results in a depletion of Ni in the B2 phase due to precipitation of Ni-rich intermetallic phases. **Fig. 2.12a** shows a section of the binary phase diagram; in **Fig. 2.12b**, the precipitation kinetics for Ni-rich NiTi ($Ni_{52}Ti_{48}$) are shown. In the beginning, at low temperatures and short aging, metastable precipitates of type Ni_4Ti_3 form. With longer durations and higher temperatures, metastable Ni_3Ti_2 precipitates are formed. Precipitation of stable Ni_3Ti only occurs at very long aging treatments. The Ni_4Ti_3 phase has a significant influence on the martensitic phase transformation.

It is important to understand that with the formation of these intermetallic phases, stress fields arise in the crystal structure, which can lead to a multistage phase transformation. For example, Ni_4Ti_3 phase acts as nucleation sites for the martensite, and therefore, its existence reduces the critical stress to start the transformation. Additionally, the presence of Ni_4Ti_3 phase, obstructs the disclocation movement and their hardening effect leads to higher anticipated yield stresses.

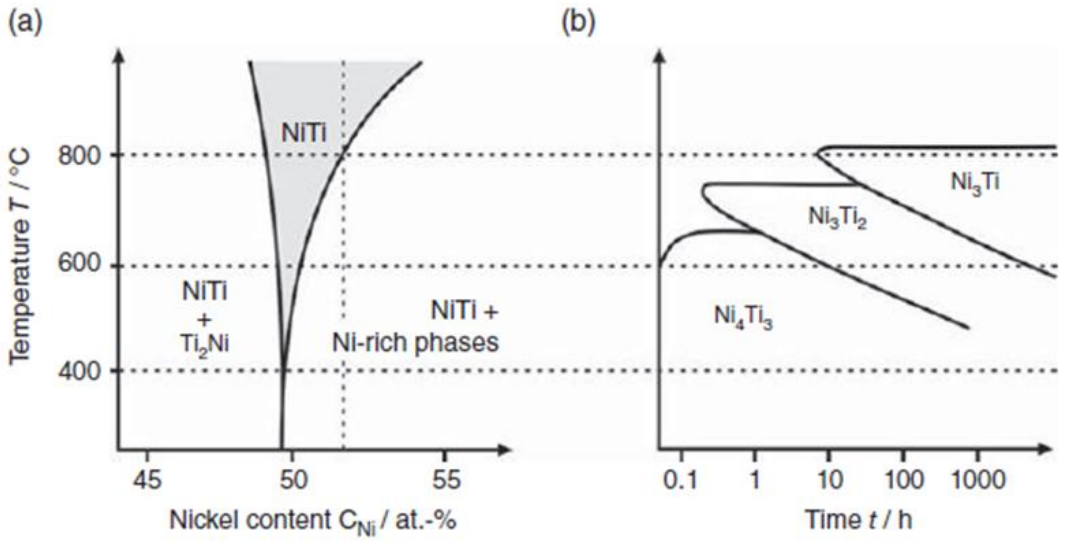

Fig. 2. 12. (a) Section of the phase diagram of the system nickel–titanium. (b) Isothermal transformation diagram of a $Ni_{52}Ti_{48}$ alloy [90-92].

In this metastable state, the phase transformation temperatures of NiTi SMA strongly depend on the Ni-Ti ratio of the B2 austenite matrix [93-95]. This relationship is shown in **Fig 2.13** for both M_s, the martensite start temperature, and T_0, temperature of the thermodynamic equilibrium of the B2 austenite phase and the B19' martensite phase. Binary NiTi SMAs with a sub-stoichiometric nickel content, where NiTi and Ti-rich phases (Ti_2Ni, i.e., $Ti_4Ni_2O_X$) are in the thermodynamic equilibrium, show no significant effect (see range 1 in **Fig. 2.13**). On the other hand, for nickel contents higher than 49.7 at. %, both temperatures continuously decrease with increasing nickel content (see range 2 in **Fig. 2.13**). This dependence can be used to adjust the phase transformation temperatures by the Ni-Ti ratio. Alloys can thus be produced, which show either a thermal or pseudoelastic memory effect in the ambient temperature.

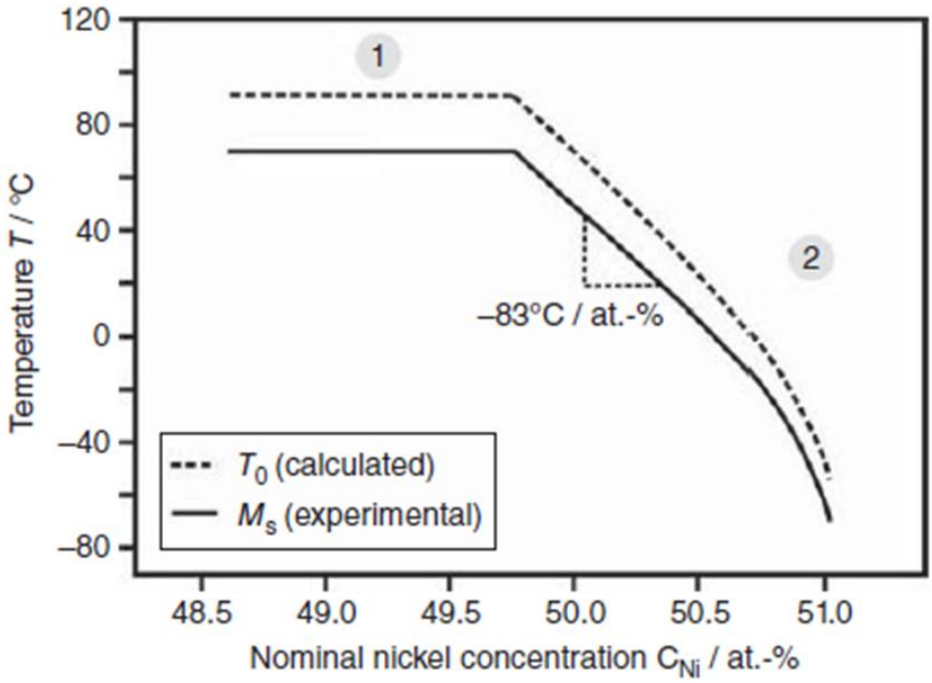

Fig. 2. 13. Influence of nominal nickel concentration on martensite start and thermodynamic equilibrium temperature [96].

NiTi SMAs are used in actuation applications due to their compact nature, lightweight, high force-to-weight ratio and large displacement, making it useful to implement them and replacing piezoelectric materials, magnetostrictive materials and electrostrictive materials in DC motors and solenoids [14]. However, certain disadvantages also have to be mentioned such as slow actuation cycle due to longer cooling time, low energy efficiency due to conversion of heat to mechanical energy and challenging motion control due to hysteresis, nonlinearities, parameter uncertainties and difficulties in measuring state variables such as temperature. **The shape recovery strain** value for NiTi alloys is around **8%** that is significantly higher than that of Cu-based SMAs where shape recovery strain reaches around 4-5% **[88]**.

The mechanical properties of NiTi SMAs tend to differ when operating at higher temperature e.g., 100^{o}C, this is highlighted by Duerig et al. [3] when comparing the ability of NiTi SMAs to Cu-based SMAs in actuation applications, describing the cyclic stability of Cu-based SMAs superior for high temperature applications.

Summary:

- In NiTi, B2 austenite has a **BCC** structure while B19' martensite has a **monoclinic** lattic structure.
- The **shape recovery strain** for **NiTi** alloys is around **8%** while for **Cu-based** SMAs it is around **4-5%**.
- **NiTi** is considered a **costly SMA,** and researchers are investigating replacements with similar shape recovery values (i.e., more cost-effective).

2.3.2. **Fe and Fe based shape memory alloys**

The principle of SME that occurs in Fe based SMAs remains the same as mentioned in **section 2.3.1** for NiTi based SMAs with A_s, A_f, M_s and M_f governing the transformation processes from austenite into martensite and vice versa. However, the NiTi SMAs with such phase transformation process have been used in such fields as aerospace and the medical industry. **Due to expensive cost of production and raw material it is not feasible for them to be used in civil structures which require large and stable recovery stresses for active control, damping, and pre-stressing strengthening material** [16, 97-100]. In 1982, Sato discovered SME in Fe-30Mn-1Si alloy [8], the significance of this discovery stems from the low cost of production compared to NiTi SMAs. Furthermore, Fe-based SMAs have wide transformation hysteresis and high stiffness and strength [99-104].

Using the principle of SME, **Fig. 2.14** illustrates how concrete can be pre-stressed using SMA reinforcements. SMA elements are pre-strained and then embedded in concrete. Once the concrete has cured, the SMA elements are heated, that can be achieved using electric resistive heating, their deformation is constrained in the concrete and a prestress develops in the SMA. Hence, a compressive stress develops in the concrete. This effect can be applied to pre-stress various reinforced concrete (RC) elements, such as building constructions, bridge girders or slabs. Compared to conventional pre-stressing steel tendons, the advantage of this technique lies in elimination of use of ducts, duct injections, oil hydraulic jacks. Additionally, no pre-stress force loss due to friction occurs during pre-stressing, so the application of SMAs is promising also for reinforcing strongly curved structures [104].

If a metal is being deformed and the elastic deformations are exceeded, dislocations in the atomic structure begin to move, resulting in plastic deformations. Dislocations are defects such as stacking faults in the atomic structure. When the dislocations move, bindings between the atoms are fractured, and new bindings are formed. In such cases, the atoms movements (dislocations) correspond to the complete spacing between the atoms, so the crystal lattice remains the same.

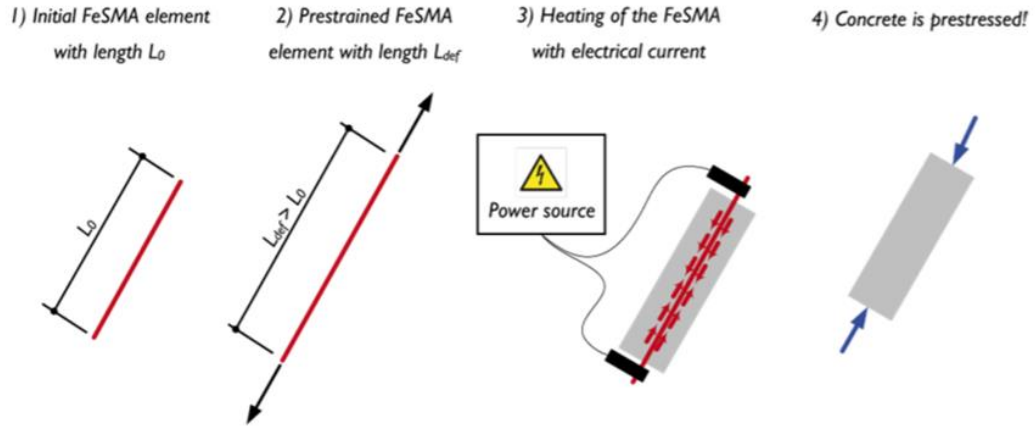

Fig. 2. 14. Schematic description of the prestressing procedure of concrete using Fe based SMA reinforcement [105].

Once Fe-based SMAs is produced and cooled down to RT, they have an atomic crystal structure called **'austenite γ-phase'**. This phase has an **FCC** crystal structure. **Fig. 2.15 shows a model of an FCC crystal**, with an atom in each corner and in the middle of each face. If an Fe-based SMA in the austenite γ-phase is deformed, **'martensite ε-phases'** develop. The main point to understand is that the atom movements in this transformation do not correspond to the complete dislocation (spacing) between the atoms but only to a partial dislocation (a so-called partial Shockley dislocation). Due to this partial dislocation, a new crystal lattice develops and is called 'martensite ε-phase'. Martensite ε-phase has an **HCP** crystal structure. **Fig. 2.16 presents a photo of a model of an HCP crystal**. The change (i.e., martensitic transformations or partial dislocations) between the two phases is **reversible**. When temperature increases above the temperature A_s, atoms rearrange themselves to develop austenite phase again as austenite has a lower free enthalpy (driving power of a reaction) than martensite. [101]

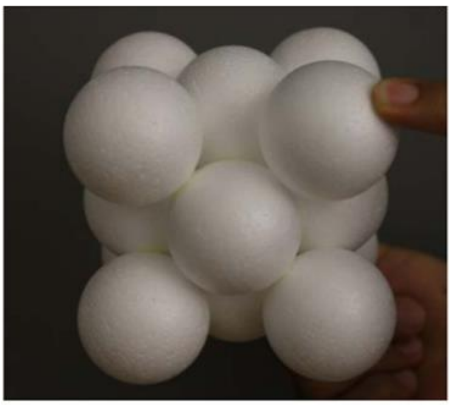

Fig. 2. 15. Crystal lattice Face-Centered-Cubic (FCC) model of the austenite γ-phase [105].

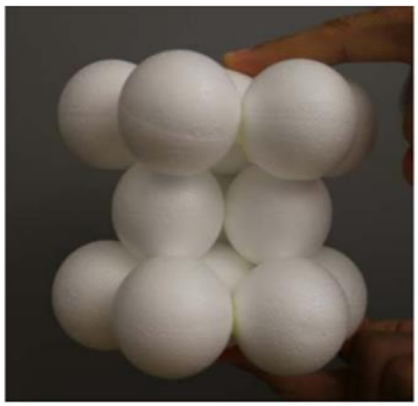

Fig. 2. 16. Cristal lattice Hexagonal-Close-Packed (HCP) model of the martensite ε-phase [105].

Initially discovered Fe-SMAs, including **Fe-Pt, Fe-Pd, and Fe-Ni-Co**, showed a transformation hysteresis caused by the phase transformation from the γ-austenite phase that is stable in high temperature to the ε-martensite phase that is stable in low temperature [16]. However, not only did this transformation hysteresis narrow thermal hysteresis, but also the dissolution and homogenization processes were complicated, and cyclic heating treatment known as “training” was required to improve the SME [101, 102, 106, 107]. On top of those limitations, the increased cost of production made Fe SMAs challengeable in civil engineering applications [97, 98, 108]. Later, Fe-SMAs processing a wide transformation hysteresis with different precipitates were discovered. In 2001, Kajiwara et al. and Farjami et al. discovered fine NbC and VN precipitates in the microstructure that enhanced the SME of Fe-SMAs without any training process [109, 110]. Dong et al. and Leinenbach et al. improved the SME of Fe-17Mn-5Si-10Cr-4Ni-1(V,C) and Fe-16Mn-5Si-10Cr-4Ni-1(V,N) by mass fraction [111, 112]. The developed SME, high stiffness, high strength, and low production cost of these Fe-SMAs prompted international research into its application in such civil engineering fields as damping, active control, and pre- or post-stressing tensioning of structures [99, 102, 113-118].

In 2014, Czaderski et al. reported that **recovery stresses of Fe based SMAs used in near surface mounted reinforcement ranged from 250 MPa to 300 MPa** when heating to 160 ◦C, which demonstrated the general feasibility of the Fe SMA strips [98].

In order to further investigate Fe based SMAs capability of being used in civil engineering applications, in 2018, Czaderski [105] produced Fe–17Mn–5Si–10Cr–4Ni–1 (mass%). The produced SMA can be activated at temperatures between 100 and 160°C, which is feasible in combination with concrete without crucial damage in the concrete due to the elevated temperatures. **It was found that the developed alloy exhibited corrosion resistance superior to conventional reinforcement steels**. It can be produced on the industrial scale under atmospheric conditions without the need for expensive, high vacuum processing facilities. For different applications, it can be formed into different shapes such as wires, strips, foils, bars, etc.

Fe-based SMA are relatively low cost and therefore can be used in civil engineering structures. This implies that new markets can be developed. Possible applications for Fe-based SMA rebars, strips or wires are as follows [105]:

- prestressing of strongly curved structures, e.g., shells
- prestressing of new, very slender structures (no anchor heads necessary), e.g., façade elements
- prestressed short fibre concrete
- prestressed confinement of columns or silos
- prestressed near surface mounted reinforcement
- prestressed shotcrete for strengthening existing RC structures

The potential of Fe-based SMAs of being used extensively in civil structures remains under investigation. However, thus far, the shape recovery of Fe based SMAs remain lower than that of NiTi. In a study conducted by Maruyama and Kubi [15] on Fe-Mn-Si system applied in the industrial field as the material of a joint for pipes and rails, **the shape recovery is around 4%.** That is significantly less than that of NiTi (8%) mentioned in **section 2.3.1.**

Summary:

- Fe-SMAs is favourable in civil engineering applications due to the low cost of Fe compared to Ni and Ti.
- Shape recovery of Fe-based SMA is around 4% compared to 8% in the case of NiTi.
- In the case of Fe-based SMAs, austenite FCC crystal structure transforms into martensite HCP through martensitic transformation.
- Fe-SMAs are mainly used in civil structures where large volumes of material is required. Therefore, despite the lower shape recovery of Fe-based SMAs compared to NiTi, the cost difference plays a major role.

2.3.3. **Cu and Cu based shape memory alloys**

The discovery of Cu-based alloys goes back to 1950s [119, 120], this alloy system is an interesting alternative for NiTi alloys due to its lower cost, ease of fabrication and its relatively good properties. In addition, Cu is widely available and can be easily produced and machined to almost any shape required. However, the drawbacks associated with Cu mainly relates to brittleness [4].

SME has been well-defined in Cu-Al, however, the transformation temperatures are too high making it not useful for a number of applications. This withdraw may be overcome by the introduction of a third element, Cu-based SMA systems such as CuZnAl, CuAlNi, CuAlMn and CuAlBe have been investigated [4] in order to manipulate the transformation temperatures to allow the usage of alloys in hydraulic fittings and civil pipe coupling. Certain Cu-based alloys have also been used in thermal actuators, sensor systems and mechanical dampers [121-124].

The research focus on improvement on the mechanical properties of Cu-based alloys led to their usage in early 1990s. One of the first applications of these alloys was setting up a heat engine [125], this particular task was already performed by NiTi but at much higher economic cost. For example, Witting and Cozzarelli [126] conducted low-frequency experiments aimed at getting twisting, bending and tension characterisation of CuAlBe and CuZrAlNi alloy systems. Additionally, Gillet [127] investigated the long-term damping performance of Cu-based alloys using one-dimensional model. Along with other

researchers work, these were the basis of the development of Cu-based alloys as energy dissipation devices for civil engineering structures [128].

A particular Cu-based alloy that was **extensively commercially exploited** [129-131] is **CuZnAl**. The reason behind that is that its SME is accompanied by low cost, wide availability, and ease of fabrication of Cu, Zn and Al. Also, the presence of Zn restricts the transformation temperatures to a range of -100 to 100^{o}C, which is very desirable to various applications. **The maximum recoverable strain for this alloy is around 5% [4] and improvement of results is highly dependent on the Al percentage added to the nominal composition**, bearing in mind the strict limitations associated with the third elements e.g. Al in order not to affect the internal stability of the chemical structure and therefore the shape memory of CuZn. Drawbacks related to long term cycling at RT that results in increasing the transformation temperatures and stabilisation of martensite as well as the degradation of SME [132, 133]. in addition, when exposed to high temperatures e.g., in this case >100^{o}C, the alloy system decomposes, which eventually makes its economic advantage is not significant enough given the mentioned disadvantages related.

CuAlNi alloys have also been extensively investigated. Similarly to Zn, the element Ni is also adopted as a valid alternative due to its low cost and ease processing. Transformation temperatures range between 80 to 200^{o}C in CuAlNi when composition at.% is made of $Cu_{83}Al_{13}Ni_{4}$ at.% [4] unlike CuZnAl, the percentage added of Al in CuAlNi has a negligible affect workability, therefore, hot working is the only fabrication process for CuAlNi. Therefore, cooling rate control is essential as it is responsible for various attributes such as transformation temperatures. This added process increases the cost associated with CuAlNi to be more expensive than CuZnAl but still less expensive than NiTi. Also, transformation temperature range is smaller than that of CuZnAl [4]. In a more recent study [134], it was observed that transformation temperature range can be decreased by increasing Hf content in CuAlNi alloys and therefore impacting the phase transformation from austenite into martensite [134].

The shape memory properties in Cu-based SMAs are very sensitive to the compositional change and addition of alloying element/s. This change results in changes in the

transformation temperatures and therefore of the alloy performance. This presents a good opportunity to investigate certain elements that contribute towards low-transformation stresses as Alkan et al [135] found when studying CuZnAl SMA. The experimental results show that the Critical Resolved Shear Stress (CRSS) for austenite to slip is in excess of 200 MPa in CuZnAl alloy, which far exceeds the transformation stress level varying from 25 MPa to 60 MPa depending on the crystal orientation. Introduction of crystallographic disorder in simulations resulted in an increase of the transformation energy barrier from 68 to 86–96 mJ/m^2 as well as increasing the critical transformation stress from 25 MPa to 33 MPa for the sample under tension.

Deformation twinning has been studied in Cu-based SMAs for years, for example **Cu-Zn** [12], **Cu-Mn** [10] and **Cu-Al** [11] have all exhibited deformation twinning. In fact, deformation twinning was found to be the dominant mechanism in Cu-Al alloys with high content of Al. Lui et al reported synchronous improvement of strength and plasticity (SISP), that is similar to (TWIP) reported in steels. The others attributed the improvement of strength and plasticity to constructive interaction between deformation twins and dislocations. Moreover, the authors have also studied the effect of addition of Mn from 5-20 at. % on Cu-Mn alloys. They observed that with the increase of Mn in Cu-Mn alloys, the alloys exhibited higher SFEs and displayed dislocation-cells to planar-slip structures. Interaction between these dislocation slip structures with deformation-twins enhances the strain-hardenability, causing an improved strength and ductility. The enhanced deformation twining in both Cu-15 at. % Mn and Cu-20 at. % Mn alloys, can improve the strength by increasing the work-hardening rate through the effect of TWIP, similar to TWIP steels, TWIP Cu-Al alloys and Cu-Zn alloys [39].

Researchers have been investigating Cu-based SMAs for a number of years as a potential replacement of NiTi in various applications. In fact, Cu-based SMAs have been in the forefront of recent developments in the field of shape memory alloys [136]. The range of applications in which Cu-based SMAs is investigated and potentially implemented has increased in recent years, notably, marine and aerospace industries and to a lesser degree medical industry. Traditionally, actuation and sensors are the most conventional use of Cu-based SMAs, however, the recent developments of SMAs in

general is governed by three driving factors and they are cost, portability, and the need to achieve small internal volume. It is expected that the areas of application of SMAs will also increase with better materials [136].

Despite the advantages that Cu-based SMAs have in terms of low cost, it is important to understand that it comes with rather poor SME compared to the widely used NiTi. **Recovery %** gives a clear idea of how effective the SME in various alloys [30]. Recovery % of NiTi-based SMAs varied from **90-100%**, that included NiTi-Pb, NiTi-Pt and NiTi-Zr. On the other hand, CuZr SMA exhibited **44%** recovery percentage, which leads us to the next part, discussing how can recovery % be improved for low-cost temperature adaptive SMAs.

Summary:

- Cu-based SMAs are a potential replacement of NiTi due to its lower cost.
- The **SME** in Cu-based SMAs is **lower** than that of NiTi.
- The SME of Cu-based SMAs can be improved by introduction of microalloying elements and composition change.
- **Recovery percentage %** of **NiTi**-based SMAs generally varies from **90-100%** whilst **CuZr** SMA generally smaller around **44%** recovery.
- CuZr based SMAs are **high temperature SMAs** meaning they can **operate at high temperatures** before transforming into soft austenite. Unlike NiTi where the transformation temperatures are much lower compared to CuZr.

2.4. Cu-Zr based alloys

CuZr-based SMAs have attracted considerable attention recently due to their potential use as **high temperature SMA** [137-141]. In addition to **cost effectiveness** compared to costly NiTi and **ease of processing**, CuZr based SMAs are considered a potential replacement for NiTi in two ways, first being a replacement in applications where operating temperatures are below 100^{o}C and that is purely due to cost effectiveness since NiTi SME provides optimum shape recovery, second is replacing NiTi in applications where operating temperatures are above 100^{o}C, this is important since NiTi work output diminishes significantly above 300^{o}C [142].

High temperature SMAs (HTSMAs) including CuZr display the austenitic transformation (martensite to austenite) at relatively high temperatures. This is a significant factor since it allows CuZr SMAs to be implemented in transport (aerospace, automobile), oil industry and robotics. where temperature can rise up to and beyond 100^{o}C. This high potential is relatively still **held back** due to lower SME effect for binary CuZr, significant shifting of transformation temperatures with minor change of composition, decomposition of the matrix phase, oxidation and brittleness and plasticity problems [142].

Recent advancements in CuZr based alloys come at the intersection between SMAs and metallic glasses [143-145]. For $Zr_{48}Cu_{47.5}Al_4Co_{0.5}$ Bulk Metallic Glass Composites (BMGC), the strain hardening rate was enhanced and plastic instability was suppressed due to a martensitic transformation of B2 austenite to B19′ martensite which is associated with SME [146]. From a BMGC point of view, there are some reports about how to improve the GFA and the mechanical properties [147, 148]. However, fewer research about the crystalline phase and martensitic transformation are reported, in this thesis, the interest revolves around the SME, therefore the focus will be regarding martensitic transformation. In the case of CuZr, **B2 CuZr austenite structure can transform into two martensite structures (one is B19' CuZr martensite monoclinic structure with P2/m symmetry and the other with a superstructure with Cm symmetry [10,11])**. The superstructure is later referred to in Zhou and Napolitano as B33 martensite [54, 141].

The introduction of a third element in the composition or altering the cooling rate in order to alter the volume fraction of the crystalline to amorphous phase all have been under various studies. The compositional change and altering of cooling rate are ways of enhancing the performance of CuZr SMAs. However, one single limitation that remains true for CuZr SMAs is their brittle mode of failure that highly limits its use in various applications.

In order to understand CuZr alloy system better, **Fig. 2.17** shows the phase diagram and potential intermetallic phases (Cu_8Zr_3, $Cu_{51}Zr_{14}$, , $Cu_{10}Zr_7$, $CuZr_2$) that stabilises upon cooling of the molten metal [57]. As can be seen from **Fig. 2.17**, Upon rapidly cooling and when reaching 1208 K, the shape memory phase B2 CuZr starts to decompose into low temperature stable phases $Cu_{10}Zr_7$ (C2ca) and $CuZr_2$ (I4/mmm) if the system is given

enough time to equilibrate during cooling. However, when enough time is not given (i.e., rapidly cooling), the high temperature phase B2 CuZr austenite becomes metastable at low temperatures as there is no time to decompose into stable $Cu_{10}Zr_7$ and $CuZr_2$ phases. This process is very similar to that of NiTi explained in **section 2.3.1**.

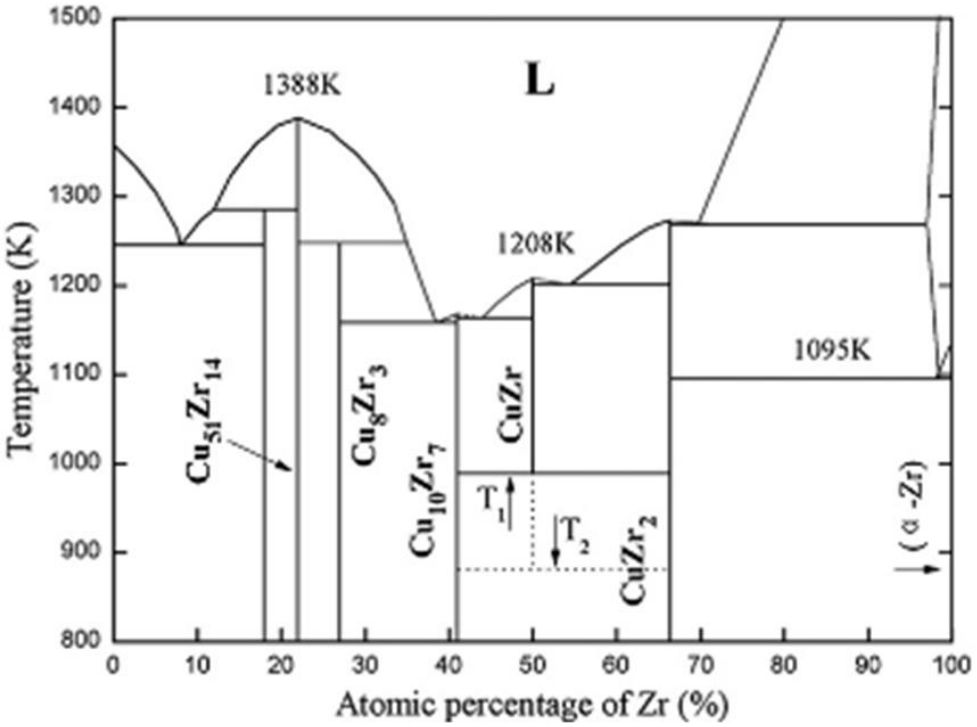

Fig. 2. 17. Phase diagram of Cu-Zr binary alloy [149].

After mentioning that potential of CuZr SMAs in range of low and high temperature applications, it is important to understand that the limitation associated with the implementation of CuZr SMAs come from RT brittleness and performance and work output point of view. Researchers have tried to overcome this issue by introducing alloying element into CuZr SMAs in various concentrations.

It is important to note that addition of microalloying elements into CuZr SMAs may impact its ability to perform in high temperature environment as HTSMA. For instance, in a recent study conducted by Biffi et al. [150], despite improvements in mechanical properties of CuZr when microalloyed with Al at different at.%, it was found that the addition of Al significantly lowers transformation temperatures therefore eliminates any possibility of using CuZrAl in HTSMAs.

Summary:

- Despite the lower SME of CuZr SMAs, they are considered a potential replacement of NiTi in various applications due to low cost and ability to exhibit martensitic transformation at higher temperatures compared to NiTi.
- The SME of CuZr can be improved by introducing a microalloying element and/or adjustment of cooling rate.
- A major pitfall in implementing CuZr SMAs in engineering applications is related to RT brittleness and performance work output. These can be overcome by introduction of microalloying element.

2.4.1. **Alloying effect on mechanical properties of CuZr based SMAs**

The idea of introducing an alloying element into B2 CuZr austenite phase comes from its effect in enhancing martensitic trasformation. As discussed in **section 2.4**, the stress-induced martensitic transformation of B2 CuZr austenite makes the alloy work-harden (i.e. plastic deformation) therefore delaying yield point and enhance the ductility. The introduction of certain alloying element at certain concentrations may make this martensitic transformation process easier to occur [151].

In 2012, Wu et al. [151] studied the SFE of B2 CuZr austenite phase and the possiblity to lower that by introduction of microalloying elements using density function theory [151]. Among all possible lattice planes, the minimum SFE occurred along the (011)[100] slip system, meaning that the energy barrier required for stacking fault formation is the lowest along (011)[100] slip system. In fact, the energy barrier for stacking fault formation of B2 CuZr ausntite along this particular slip system is **381 mJ/m^2**. After that, Wu et al [151] proposed a range of elements that may lower SFE therefore enhance twinning propensity which effectively enhances martensitic transformation of B2 CuZr austenite phase. These elements are Ti, Cr, Fe, Co, Ni, Ag, Ga, Hd, Ta and Nb. It was found that of 0.5 at.% addition of Cr, Fe, Co, Ni or Ag in place of Cu have lowered SFE to levels below what is required to transform B2 austenite into B19' martensite. To be precise, Co in particular greatly decreased SFE to **75 mJ/m^2** [151]. It is important to highlight that the mentioned elements substitute Cu sites in B2 CuZr in order to lower SFE, when the alloying elements replace Zr sites, the SFE increases makes it even more difficult to promote twinning and martensitic transformation.

The illustration of stacking fault structure of CuZr SMAs is presented in **Fig 2.18** [152].

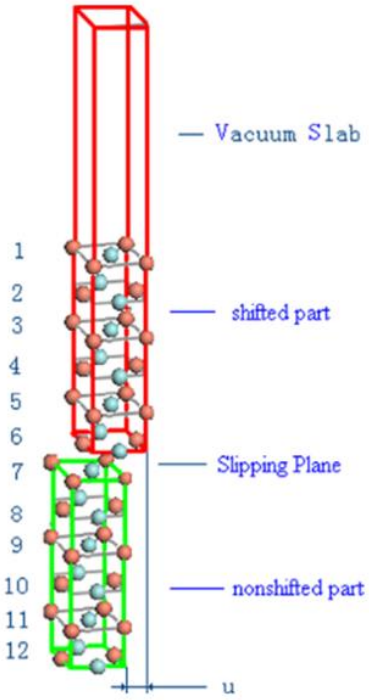

Fig. 2. 18. Schematic illustration of a stacking fault structure. u is rigid shift vector and the red and blue balls represent Cu atoms and Zr atoms, respectively [152].

Fig. 2.19a shows that the lowest SFE of **381 mJ/m^2** is obtained along (011)[100] slip system, while other slip systems shown in **Fig. 2.19a** show higher SFE, highest being **966 mJ/m^2** along (001)[100]. These findings are in agreement with [151].

Considering Co lowered SFE the most for [151] and based on experimental data, Co addition to CuZr SMAs enhances work hardening. It is important to consider the effect of Co addition in place of Cu in CuZr alloy for each slip system. This is shown in **Fig. 2.19b**, where the trend follows a similar trend to that of base B2 CuZr with lowest SFE obtained along (011)[100] slip system.

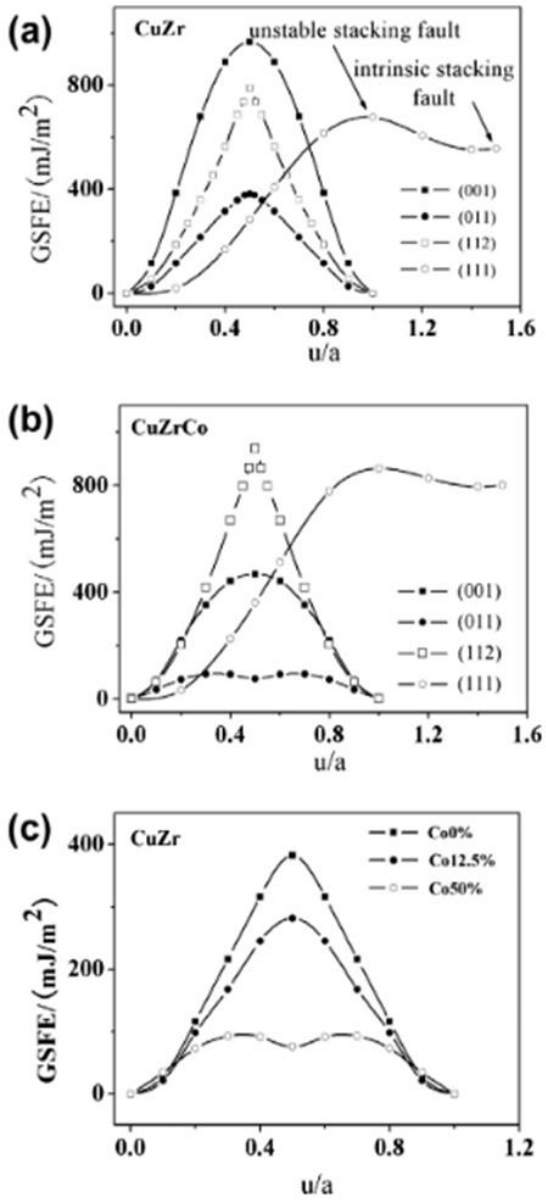

Fig. 2. 19. (a) GSFE curves for the (001)[100], (011)[100], (111)[11-2] and(112)[11-1] slip systems in B2-CuZr, (b) GSFE curves for the (001)[100],(011)[100], (111)[11-2] and (112)[11-1] slip systems in B2-CuZr with addition of Co on the stacking fault plane, and (c) GSFE curves for the (011)[100] slip systemin B2-CuZr with different concentration of Co at the stacking fault plane [152].

The amount of the Co atoms at the stacking fault plane also has a significant influence on the SFE (see **Fig. 2.19c**). When the concentration of the Co atoms at the stacking fault plane changed from 0%,12.5% to 50%, the lowest SFE is calculated to be 381, 281 and 75 mJ/m^2, respectively, showing a decreasing trend with Co contents. Similarly, effects

of other solute atoms including Ta, Ni, Fe, Hf, Ga, Y, Cr, Ti, and Ag, were also investigated, as demonstrated in **Fig. 2.20a**.

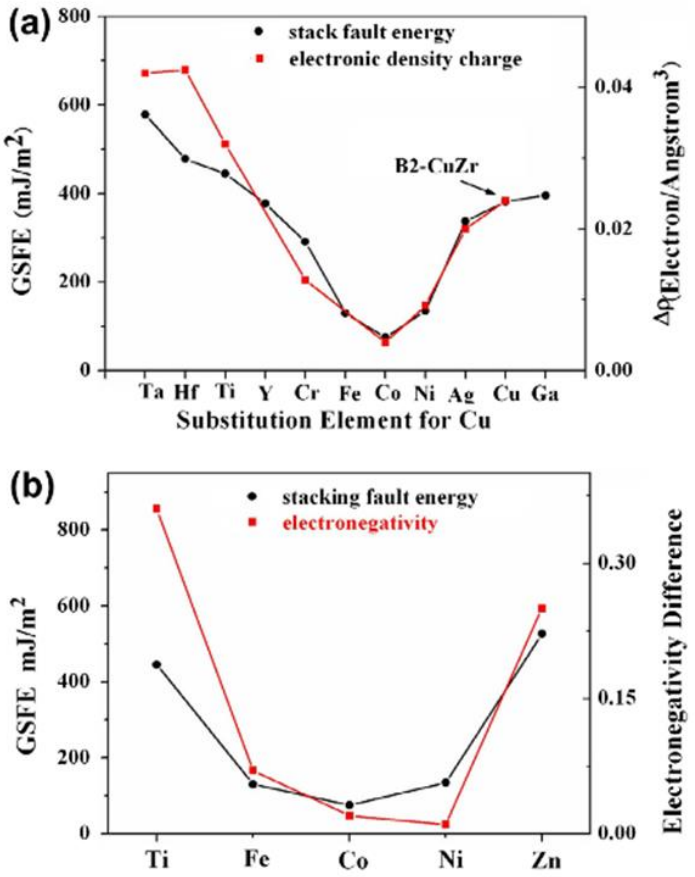

Fig. 2. 20. (a) SFE and charge density redistribution on the (011)[100] slip system of B2-CuZr substituted with different elements, and (b) the SFE value for the (001)[100] slip system in B2-CuZr doped with different solutes and the corresponding electronegativity difference between each solute atom and Cu [152].

It is clear to see in **Fig. 2.20** that Fe, Co, and Ni in particular are three elements that can dramatically decrease SFE of B2 CuZr austenite phase and enhance martensitic transformation.

2.5. Problems associated with shape memory alloys

The main issue of concern of the potential offered by the thermomechanical properties of SMAs is the long-term predictability of the material behaviour and the fatigue lifetime of the macrostructural elements [136]. Repeated use of the shape memory effect may lead to a shift of the transformation temperatures [153]. This effect is referred to as functional

fatigue, as it is closely related with a change of microstructural and functional properties of the material.

Experimental studies on the fatigue life of SMA bars at room and high temperatures were conducted by Casciati et al. [154] on a cylindrical specimen of Cu-based alloy of diameter 3.5 mm, which preliminarily underwent a heat treatment consisting of heating at 850 °C for 10 min, followed by cooling at room temperature, and finally reheating at 100 °C for 2 h. After that, the specimen is tested in tension with strain values measured using extensometer that is attached to the specimen. The test is conducted in span control during the loading, and in load control during the unloading. Ten cycles at room temperature up to the strain of 2% are applied for performing the so-called “mechanical training”. They are followed by four series of three cycles each, again up to the maximum strain of 2%, at the temperatures of 30 °C, 60 °C, 90 °C, and 120 °C, respectively. Test results in terms of stress-stress curve obtained at different temperatures indicate that stress and the residual strain increase as the temperature increases, while the width of the hysteretic loop of the transformation temperatures decreases. These results indicate that Cu-based SMAs present an advantage in avoiding creep, this capability is achieved by preliminarily performing a suitable heat treatment.

2.6. Industrial applications for conventional and high temperature SMAs

2.6.1. Conventional-temperature SMAs

Since the discovery of the SME, NiTi has been the most commonly used SMA due to its maximum recoverable strains and low brittleness compared to Cu-based SMAs as discussed in section 2.3.3. Fe-based SMAs remain to have a significantly lower recoverable strains compared to NiTi and Cu-based SMAs [155] but their cost is lower. The recoverable strains for NiTi range from 3% near the [001] direction to approximately 10% for directions close to [011] and [-111] [156].

Various types of microactuator devices have been reported in the literature, including microvalves, micropumps, optical switches, imaging displays and microrelays [156]. Each of these devices used one of a variety of integrated actuator mechanisms based on piezoelectric, magnetic, electrostatic, bimetallic or thermopnuematic phenomena. Many applications require an integrated microactuation mechanism that is compatible with

microfabrication, and able to provide a large displacement and a large actuation energy density. None of these microactuator technologies is capable of simultaneously satisfying these requirements.

An example of industrial use of SMAs at RT applications is the use of NiTi thin films microvalve developed by Busch and Johnson in 1990 [157]. This device used pneumatic pressure bias to deform a NiTi diaphragm positioned over an outlet orifice and thereby close the valve. The transformation from martensite phase to austenite phase was achieved by passing a current through the thin film, therefore causing temperature to rise, at which diaphragm became flat and the valve opened to allow the fluid to flow. This device used a mechanical bias to close the device in the martensite state and therefore enabled the valve to have repeatable characteristics under cyclical use.

The latest version of the microvalve employs a microfabricated single crystal silicon spring is presented in **Fig. 2.21**. In the unpowered position (**Fig. 2.21a**) the silicon micro-spring bends the martensitic NiTi film downward, causing the film to press the boss against the orifice opening, hence preventing the fluid from flowing. However, when heated to certain temperature (**Fig. 2.21b**), the austenitic NiTi film becomes flat, deflecting the silicon micro-spring upward, lifting the boss away from the orifice and allowing fluid to flow. This microvalve exhibits an on/off flow rate ratio of 1000:1 for water flows of 0.9 ml min^{-1}.

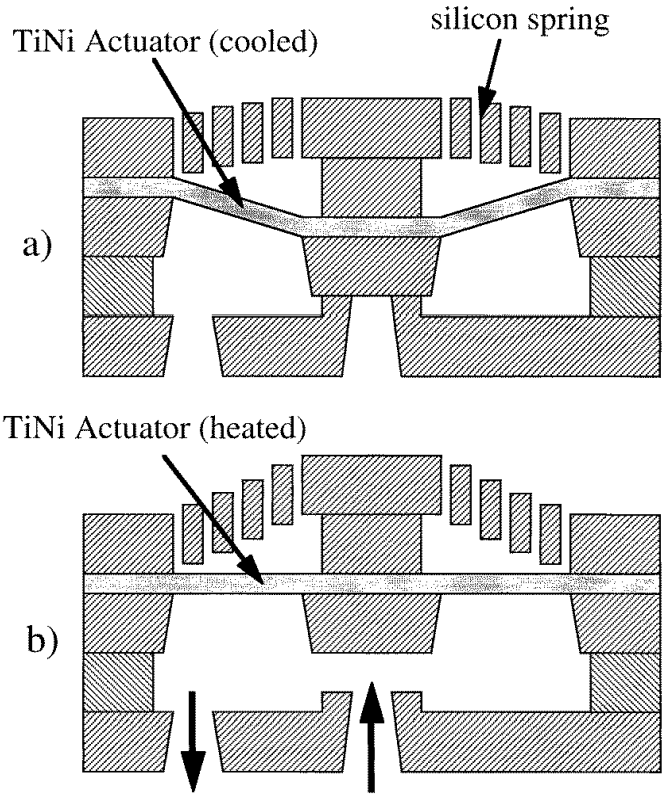

Fig. 2. 21. Schematic cross-sectional drawings of a TiNi-actuated microvalve in the (a) closed and (b) open positions [156].

Despite the advantages mentioned related to the usage of NiTi in various engineering and industrial applications, **its inability to perform at a significantly high temperatures is considered one of the drawbacks of its implementation**. NiTi SMAs have low transformation temperatures (generally A_f below 100^{o}C [142, 158]) depending on treatment, meaning that its impractical to use in applications exposed to high temperature since the SME will take place at an undesired time. Instead, HTSMAs are used for this exact reason.

2.6.2. **High-temperature SMAs**

SMAs with high transformation temperatures can enable simplifications and improvements in operating efficiency of many mechanical components designed to **operate at temperatures above 100^{o}C**, potentially impacting the automotive, aerospace, manufacturing, and energy exploration industries. Also, industrial electric motors can reach about 100^{o}C and surfaces under full sunlight in space can go beyond that

temperature, therefore, understanding the transformation temperature of SMAs is crucial to maximise the SME.

SMAs have been successfully demonstrated in Micro-Electro Mechanical Systems (MEMS) applications such as microactuators and micropumps. In MEMS applications, strict dimensional limits often make SMA actuation one of the very few viable options in a device. For example, Liu et al [159] used a magnetron sputtered Ti–Ni–Pd thin films with M_s of 150^{o}C in a micro valve, as seen in **Fig. 2.22**. The valve was actuated by resistance heating and was capable of operating at temperatures up to 120^{o}C. The shape memory valve could supply up to 75 mN of actuation force and was able to stop the flow of 70 kPa gas pressure with less than 0.1% leakage. Also, due to the high cooling rates through the thin film, a minimum response time of 22 ms or maximum actuation frequency of 30 Hz was obtained. Compared to binary NiTi microvalves of the same design, a greater amount of power was required for operation, but faster response time was possible with Ti–Ni–Pd valves.

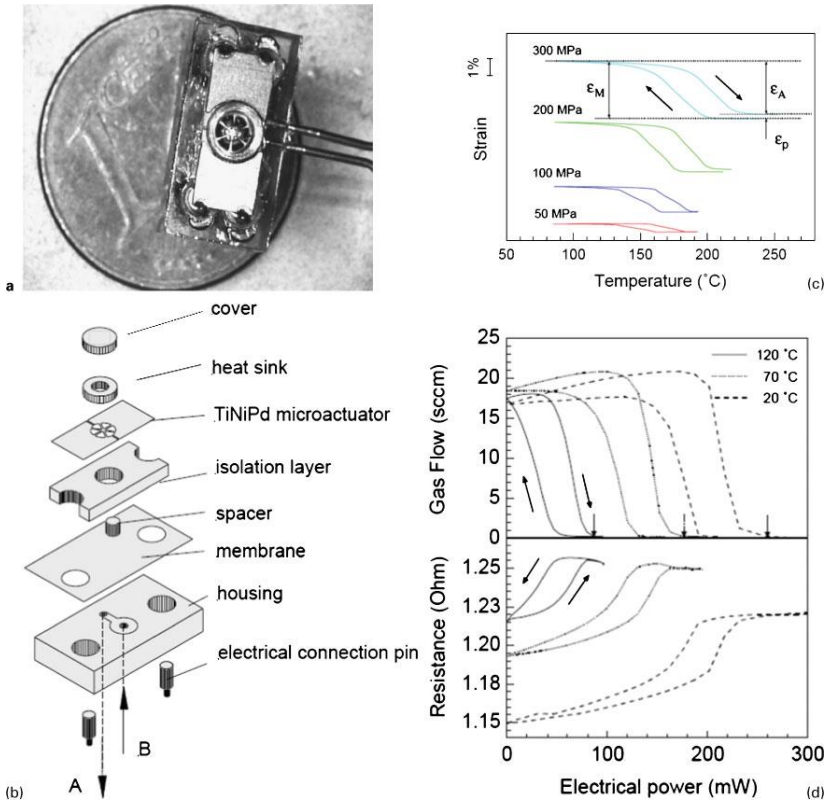

Fig. 2. 22. Illustration of a $Ti_{50}Ni_{30}Pd_{20}$ at.% thin film microvalve. (a) Size of the completed assembly, (b) exploded view of the microvalve, (c) shape memory response of the thin film

under constant stress heating cooling experiments, maximum recoverable strain of ~ 3.2% can be achieved under 200–300 MPa and (d) performance of the actuator for gas flow at a fixed pressure difference of 70 kPa [137].

The transformation temperatures for most common SMA systems are relatively well known along with the basic mechanisms for manipulating the transformation temperatures through compositional control, heat treatment, and thermomechanical processing. Of course, the functional capability of high temperature SMAs clearly depends on much more than simply a high transformation temperature. In addition to the intricate microstructural and thermomechanical issues associated with shape memory behaviour, high temperature SMAs face similar challenges to those of traditional high temperature structural alloys. The abundance of thermal energy at higher temperatures promotes many rate-dependent processes that are otherwise inactive at room temperature and creates a series of tough challenges related to thermal and microstructural stability, deformation and creep resistance, recovery and recrystallisation, and environmental resistance.

In the case of micropumps in MEMS applications, the fluid pumping (actuation) is realized through the periodically oscillating diaphragm acting upon the chamber with fluid [160]. As such, the micropump performance depends strongly on the achievable deflection of the diaphragm, that is, the higher deflection leads to the larger flow rate. Diaphragms that utilize the SME in the NiTi SMA have a high force to volume ratio, large strain recovery, and are biocompatible [161].

2.7. **Market needs for shape memory alloys**

Shape Memory Alloys Market size was estimated over USD 9 billion in 2018 and the industry will grow by a Compound Annual Growth Rate (CAGR) of more than 12% up to 2025. Rapid growth in the global biomedical, aerospace & defence and automotive industries will be the major growth drivers for the market. This expected growth is attributed mainly to emerging aerospace markets such as Japan, Russia, UK, China, Germany, India France. Moreover, the increasing investment in defence sector of developed and developing countries is likely to increase the demand of SMAs in the near future [162].

Table 2.2 shows the SMA market report coverage in 2018:

Table 2. 2. SMAs market report coverage [162]

SMA market report	Details
Market size	$9 billion
Forecast period	2019 to 2025
Forecast period 2019 to 2025 CAGR	12%
2025 valuation projection	$20 billion
Growth drivers	• Booming global biomedical sector • Increasing product demand in aerospace and defence industry • Growing automobile industry in Asia Pacific region
Pitfalls and challenges	Volatility in raw material prices

As can be seen in Table 2.2, a critical challenge that faces the industry with the expected growth in near future is coming from the fluctuating of raw material prices which may hinder the growth prospect of SMAs market share during the forecast period despite the enormous demand for flourishing automotive and biomedical industry as well as better healthcare services.

In order to better assess the SMAs market, it is important to split it into market by product and market by end-user. Market by product is mainly segmented into NiTi and Cu-based SMAs. Other SMAs also contribute towards the global market share however the majority comes from NiTi and Cu-based SMAs. In fact, NiTi occupies the largest market share and will grow by a CAGR of around 12% in the forecast timeframe. NiTi is superior to other alloy systems due to its stability, excellent thermo-mechanical properties and practicability as compared to other SMAs. In the coming years, it is expected to implement other SMA systems such as Ni-Fe-Ga and Fe-Mn-Si in wider applications. These alloy systems are currently being used in pipe-joint for steel pipes and fishplate for crane rail [162].

Based on end-user, the market is segmented into biomedical, aerospace & defence, automotive, home appliances and others. Biomedical is the main end-user segment and is likely to gain by more than 11% CAGR during the forecast period. Extensive application of the product for dental implants, stents and catheters will drive its growth. Additionally, surging biomedical industry in the developing countries will also propel the shape memory alloys market demand over the forecast period.

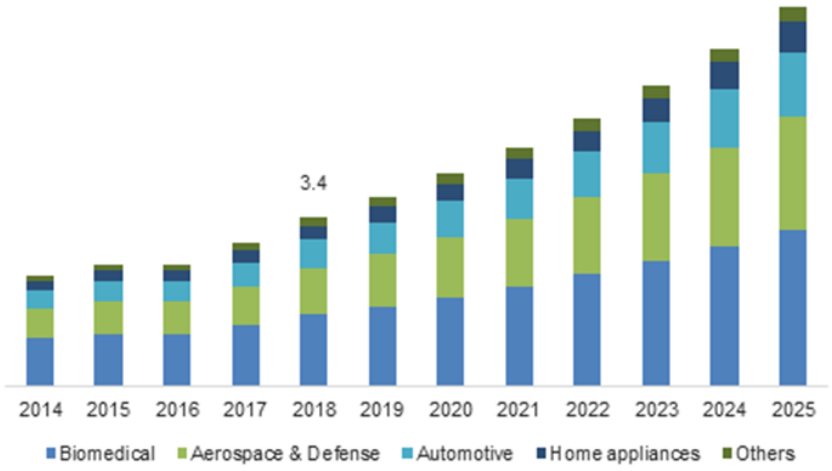

Fig. 2. 23. US SMAs market size by end-user, 2014-2025 ($ Billion) [162]

Home appliance end-user segment had a share of approximately 10% of the overall market in 2018. The product is extensively used for gas-water heaters, subfloor vents, regulator valves, etc. Rising disposable income, robust economic growth, urbanization and increasing demand of home appliances will propel the usage of shape memory alloys in home appliance.

The global market is currently dominated by North America, which accounted for approximately one third of the market share in 2018. This dominance is attributed to the regions high production capacity, large number of product manufacturers coupled with the presence of an established automotive and biomedical industry. The North America SMAs market is likely to grow at a CAGR of over 12% in coming years. Meanwhile, Asia Pacific region is the fastest growing SMAs market and is likely to exhibit a CAGR of more than 14% during the forecast timeframe. Rising population, economic progress and improving government expenditure on infrastructure development are some of the factors for the high growth in the region [162].

2.8. Cost analysis for NiTi and CuZr shape memory alloys

Cost analysis for $Ni_{50}Ti_{50}$ and $Cu_{50}Zr_{50}$ is needed to justify using CuZr as an alternative to NiTi in various engineering applications.

Table 2.3 lists the cost of the pure elements of Ti, Cu, Ni and Zr per 100g along with density at RT (kg/m^3). Cost analysis of $Ni_{50}Ti_{50}$ and $Cu_{50}Zr_{50}$ alloys are performed in order to justify the selection of CuZr for MEMS applications.

Table 2. 3. Cost of pure Ti, Ni, Cu and Zr per 100g [20, 21]

Element	Cost, pure per 100g [20]	Atomic number	Density at RT (kg/m^3) [21]
Ti	£535	22	4500
Ni	£6.23	28	8900
Cu	£7.90	29	8960
Zr	£127	40	6520

The processing conditions at laboratory scale for $Ni_{50}Ti_{50}$ and $Cu_{50}Zr_{50}$ are the same and therefore the costs would be roughly the same. The difference comes from the cost of raw elements where it is mentioned in Table 2.3 that cost of NiTi is more expensive than CuZr. The cost values are converted into pounds according to the exchange rate of April 26, 2022.

Upon addition of cost of raw elements, the total cost of each alloy is the following:

- Cost of raw elements $Ni_{50}Ti_{50}$ is £541.2 per 100g = £5412 per 1kg
- Cost of raw elements $Cu_{50}Zr_{50}$ is £134.9 per 100g = £1349 per 1kg

Using the rule of mixtures, the density in kg/m^3 for $Ni_{50}Ti_{50}$ and $Cu_{50}Zr_{50}$ is 6707 and 7725 kg/m^3, respectively.

Cost of transportation of the alloys is taken as £1.37 per km according to [163] therefore in order to transport $1m^3$ volume of $Ni_{50}Ti_{50}$, the following calculations have to be performed:

(£5412/kg x 6707kg/m^3 x $1m^3$) = £$36x10^6$

That is cost of $Ni_{50}Ti_{50}$ per $1m^3$

In order to add the transportation cost (e.g., 10000km):

(£36x10^6) + (6707kg/m^3 x 1m^3 x £1.37/1kg.km x 10000km) = £128x10^6

Table 2.4 lists longer distances and the calculations for $Cu_{50}Zr_{50}$ at the same distances measured for $Ni_{50}Ti_{50}$.

Table 2. 4. Cost of 1m^3 of $Ni_{50}Ti_{50}$ and $Cu_{50}Zr_{50}$ as a function of distance. Cost of transport is taken £1.37 per km according to [163].

Distance (km)	cost $Ni_{50}Ti_{50}$ (£million) per 1m^3	cost $Cu_{50}Zr_{50}$ (£million) per 1m^3
0	36.30	15.21
10000	128.18	121.04
12500	137.37	131.63
15000	146.56	142.21
17500	155.75	152.79
20000	164.94	163.38
22500	174.13	173.96
25000	183.32	184.54
27500	192.50	195.13
30000	201.69	205.71

Fig. 2.24 shows that with increase of distance, the cost of NiTi and CuZr increases. Since the density of CuZr alloys is higher than NiTi, the cost of transportation increases by a bigger amount for CuZr. However, as Fig. 2.24 shows, it is still cheaper to purchase CuZr despite the transportation cost due to the high initial cost of NiTi.

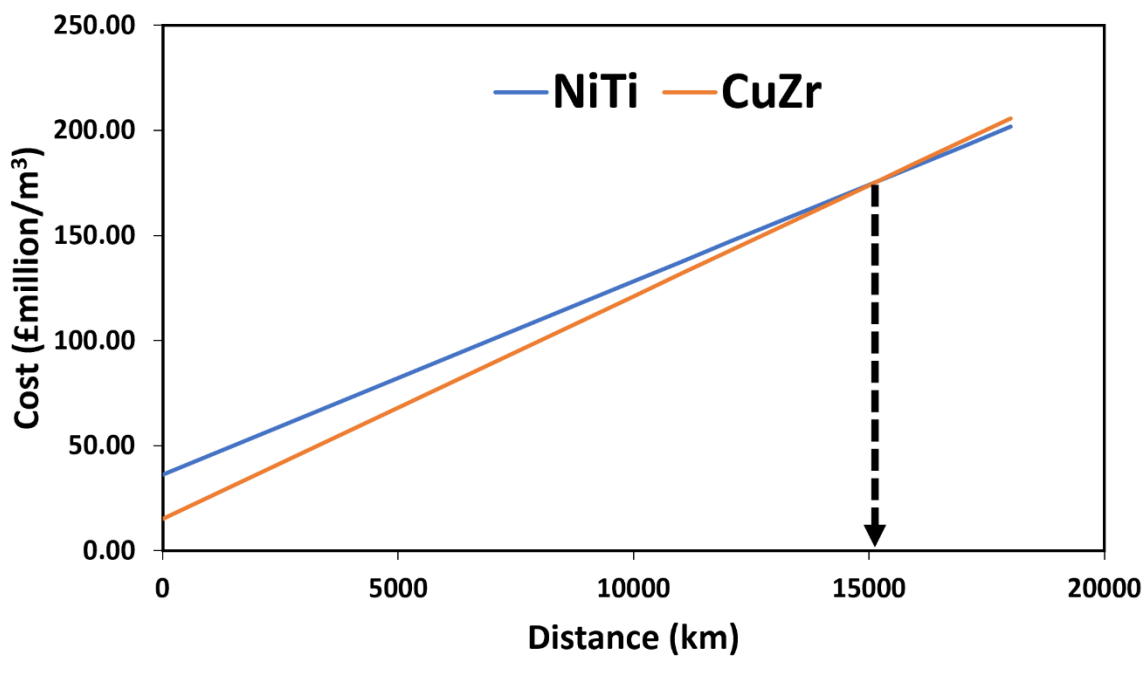

Fig. 2. 24. Cost of transportation of $1m^3$ of $Ni_{50}Ti_{50}$ and $Cu_{50}Zr_{50}$ as a function of distance

The two lines which correspond to $Ni_{50}Ti_{50}$ (blue line) and $Cu_{50}Zr_{50}$ (orange line) alloys intersect at around 15,000km. This point of intersection corresponds to the break-even point in which the total cost of raw elements and transportation costs is equal for both alloys. For any distance less than 15,000km in which $1m^3$ of $Ni_{50}Ti_{50}$ and $Cu_{50}Zr_{50}$ are transported for, the total cost is lower for $Cu_{50}Zr_{50}$. However, if the distance transported is more than 15,000km, it is more cost-effective to purchase $Ni_{50}Ti_{50}$.

Chapter 3 – Materials and methods

In this chapter all materials, methods and equipment required to carry out the work in this thesis will be described.

3.1. Sample preparation

Multiple compositions were investigated in this work, the main one of them is $Cu_{50}Zr_{50}$ at.% in different diameters (e.g. 2, 3 and 4mm). Other alloys such as; $Cu_{50-x}Zr_{50}Co_x$ ($0 \leq x0 \leq 1$), $Cu_{50-x}Zr_{50}Fe_x$ ($0 \leq x0 \leq 1$), $Cu_{50-x}Zr_{50}Ni_x$ ($0 \leq x0 \leq 1$) and $Cu_{50-x}Zr_{50}Mn_x$ ($0 \leq x0 \leq 1$) at.% were also investigated after being obtained using the same casting technique. All elements had purities of 99.9% or higher as listed in **Table 3.1**. After working out the weight needed for each element to achieve the required composition, elements were ground mechanically using silicon carbine (SiC) grinding papers with grit size ranging from (P1200 to P4000). The process of getting the exact measurements may require numerous grinding which therefore leaves residues of SiC attached to the surface of the sample, hence all samples were thoroughly cleaned inside an ethanol beaker using ultrasound bath for 3 mins and left to dry at room temperature, before finally measuring the weight of the elements using an analytical balance (Fisherbrand™ Analytical Balance, ±0.1 mg).

Table 3.1. elements of different purities supplied by Alfa Aesar in different shapes

Table 3. 1. Elements of different purities supplied by Alfa Aesar in different shapes.

Element	Purity at.%	Shape provided by supplier
Copper	≥99.9	Shot
Zirconium	≥99.9	Plate
Cobalt	≥99.9	Pieces
Manganese	≥99.9	Pieces/Flakes
Iron	≥99.9	Wire

In order to be able to measure the weight of pure elements in wt.% to achieve the desired at.%, Avogadro's number is used. Avogadro's number is a proportion that relates molar mass on an atomic scale to physical mass on a human scale. Avogadro's number is

defined as the number of elementary particles (molecules, atoms, compounds, etc.) per mole of a substance. It is equal to 6.022×1023 mol-1 and is expressed as the symbol NA.

It is worth noting that there is more than a single technique to produce metallic alloys by rapid solidification, one of those is melt spinning, where molten metal is casted onto a rotating copper wheel that is cooled internally. The rotating wheel continuously removes the rapidly solidified material in order to allow continues production. The description of this technique is only very brief as it was not used in this work, for the interest of the reader, refer to section 2.2.1.1.

3.2. Suction casting

All samples in this study were produced using Compact Arc Melter MAM-1 Edmund Bühler. A schematic diagram of the casting equipment is drawn in **Fig. 3.1** [26] and a picture of Compact Arc Melter MAM-1 Edmund Bühler in 2.2.

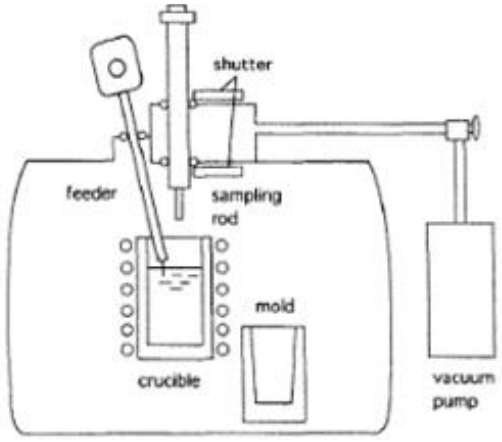

Fig. 3. 1. Simple schematic of fabrication at vacuum condition [26].

Fig. 3. 2. Compact Arc Melter MAM-1 Edmund Bühler equipment.

The chamber pressure was raised to atmospheric pressure by allowing air in order to be able to place the elements in the melting crucibles. After that, using rotary pump, pressure inside the chamber was evacuated to below $5x10^{-2}$ mbar. Below this certain pressure, the rotary pump is no longer used, and turbo pump is used instead to further decrease the pressure inside the chamber to $4x10^{-4}$ mbar, which is the recommended pressure set by the manufacturer to start the melting process. The final step of the process includes re-melting all samples at least three times in a Ti-gettered/Zr-gettered high purity argon atmosphere to attain good chemical homogeneity, all performed in similar way using arc intensity of level 4 and applying the arc melter on top of the molten metal for 5 seconds, however when casting, arc intensity was raised to level 5 and applied to the sample for 5-10 seconds. This is crucial to ensure consistency in obtaining all samples in similar conditions and minimise variation of temperature raised during the melting process and duration of melting as there is no way of controlling the temperature of the melt inside the

chamber. Furthermore, the water-cooling system is set to 20ºC during casting the molten metal into copper mould and producing 2,3 or 4mm diameter and 35mm long rods.

3.3. X-ray diffraction (XRD)

The microstructure of all samples was analysed by X-ray diffraction (XRD) using two equipment. First, Bruker D8 diffractometer with monochromated Cu-Kα radiation (λ =1.54184 Å) at 40kV and 40mA, in the 2θ range of 10º-90º, step size of 0.02º and scanning speed of 0.02º/s. Second, SmartLab Rigaku XRD diffractometer with monochromated Cu-Kα radiation (λ =1.54184 Å) at 40kV and 40mA, in the 2θ range of 10º-90º, step size of 0.02º and scanning speed of 0.02º/s. All samples were prepared in the same way by cutting a 1mm thickness regardless of the diameter of the sample. This measurement is achieved by cutting the master alloy into slices of slightly longer than 1mm using low-speed precision sectioning saw that uses diamond wafering blades. After that, the samples are manually ground to thickness of 1mm using SiC grinding papers (P1200, P2500 and P4000) in that order. Subsequently, all samples are cleaned in ultrasound using ethanol for 3 mins. The XRD peaks detected in the diffractogram are identified and analysed using SmartLab software which is provided with the XRD equipment. Considering all the samples are CuZr based and the effect of minor addition of microalloying elements does not have an effect on the peak identification as will be discussed in Chapter 4, therefore Table 3.2 lists all crystallographic phases detected during this work.

Table 3. 2. Crystalline phases detected in the analysis of all samples.

Chemical formula	Crystal system	Space group	a (Å)	b (Å)	c (Å)	α (º)	β (º)	γ (º)
B2 CuZr	Cubic	Pm-3m	3.2562	3.2562	3.2562	90.00	90.00	90.00
B19' CuZr	Monoclinic	P21/m	3.2370	4.1380	5.4490	90.00	105.19	90.00
$Cu_{10}Zr_7$	Orthorhombic	Aba2	9.3470	9.3130	12.6750	90.00	90.00	90.00
Cu_8Zr_3	Orthorhombic	Pnma	7.8686	8.1467	9.9770	90.00	90.00	90.00
$CuZr_2$	Tetragonal	I4/mmm	3.2204	3.2204	11.1830	90.00	90.00	90.00

3.4. Hot mounting press

After cutting rod samples into slices of 2-4mm thickness and analysing it in the XRD, each sample is mounted in bakelite in order to make it easier to handle and protect the sample. Ideally, this step should be performed before XRD analysis, however, due to the small size of disc being analysed, it was decided to handle the samples with extra care during the XRD process and not mount it to make sure no signal is picked from the bakelite in XRD analysis.

A pre-defined programme on mounting press equipment was set for all samples to be mounted in the same. Samples are placed inside a cylinder with 15ml of resin added to cover the sample with the intended surface for analysis facing downwards. The process starts by heating the sample to 180^{o}C and pressure of 250 bar for 7-8 mins. The sample is cooled down afterwards by means of cold water circulating around the hot cylinder for 4 mins before being able to withdraw the sample embedded in resin. The temperature and duration of heating set for this programme are not high enough to have any significant on the microstructure of the CuZr based SMAs.

3.5. Chemical Etching

Chemical etching is a destructive technique used to reveal the microstructure. Etching can be performed in several ways, in this study, a common metallographic etchant Kroll's Reagent which consists of 92% distilled water, 6% Nitric acid and 2% Hydrofluoric acid [164] is used to reveal the microstructure and grain boundaries of CuZr SMAs. The etching takes place by swabbing on the surface of the sample for 15 seconds using a cotton swab then rinsing the alloy with water. Due to lack of literature on how to etch CuZr alloys, the 15-second time limit was chosen after multiple trials of revealing the microstructure. The high acidity of kroll's reagent means if the sample is over-etched the microstructure cannot be seen under the microscope.

3.6. Microscopy

3.6.1. Optical microscopy

After the process of grinding the sample using SiC grinding papers in this sequence (P1200, P2500 and P4000), all samples were analysed under the optical microscope to

ensure the number and magnitude of the scratches are as small as possible and consistent finish across the surface of the sample using X20 and X50 magnification. Once that is achieved, fine polishing using 3µm then 1µm polycrystalline diamond Suspension (Beuhler MetaDi Supreme Suspension) for 5-10 times. After that, samples are cleaned thoroughly with ethanol using ultrasound equipment and dried at room temperature.

Optical microscope is also used after chemically etching the samples with Kroll's Reagent. Despite the limitations in terms of high magnifications associated with optical microscope compared to Scanning Electron Microscope (SEM). However, the etching effect can still be visible and reveal the microstructure of the etched sample. This is particularly helpful, as etching is a highly damaging technique and having optical microscope to use straight after etching help in determining the correct duration needed for etching.

3.6.2. **Scanning Electron Microscopy**

Prior to any analysis in SEM and EDS, samples are mounted in a conductive phenolic mounting resin (CONDUCTO-MOUNT, MetPrep Ltd.) and ground using SiC in the same way mentioned before (P1200, P2500 and P4000), followed by 3µm then 1µm polycrystalline diamond Suspension.

With a mirror-finish surface “P4000”, the samples are investigated in Tescan Mira3 SEM equipped with Field Emission Gun (FEG) shown in **Fig. 3.3** which enables high resolution performance 1.0 nm at 30kV. In addition, EDS acquisition and analysis can be performed on an Oxford Instruments X-Max 150 EDS detector shown in **Fig. 3.3**.

Fig. 3. 3. TESCAN Mira3 SEM and EDS Oxford instruments detector.

3.6.3. **Transmission Electron Microscopy**

Transmission electron microscopy (TEM) was done using JEOL JEM-F200 TEM high throughput 200kV S/TEM with Cold FEG and dual Silicon Drift Detectors. The samples for TEM are initially ground to thickness of 300μm using P2500 SiC papers and then to thickness of 50-100μm using P4000 grit papers. After that, a hole is made in the middle of the sample using Buehler PoliMat-2 & METALTHIN Twin Jet and the area surrounding the hole is made progressively thin and electron-transparent by ion-milling using Gatan Precision Ion Polishing System (PIPS II) that uses focused gas ion beams to remove material from a sample of interest. The duration of ion-milling depends on the thickness of the sample and therefore the amount of material to be removed, however on average the duration is 2-3 h.

3.7. Thermal and thermomechanical properties

3.7.1. **Differential Scanning Calorimetry (DSC)**

Prior to the investigation of the thermal behaviour, samples were ground down to discs with thickness of 1mm using the same technique mentioned before then thoroughly

cleaned in ethanol in ultrasound before measuring the weight of sample using (Fisherbrand™ Analytical Balance, ±0.1 mg).

The thermal behaviour of the samples was studied using two differential scanning calorimetry equipment. First equipment is (DSC, SETARAM C131 EVO) which was used at a constant heating rate of 5 K/min up to 550 ^{o}C and natural cooling down the samples inside the furnace to room temperature as the equipment does not enable accurate control of cooling rate. Aluminium pans were used to house the samples of 1mm thickness. Despite austenitic transformation may be occurring at relatively high temperature for some alloys, that temperature should always be monitored as Aluminium pans are susceptible to high temperature.

Second equipment is (DSC Mettler DSC-3+) and it was used at constant heating rate of 20Km/min up to 350 ^{o}C and cooling rate of 20K/min down to -50^{o}C to ensure detecting martensitic transformation peak of CuZr SMAs. The variation of heating rate is believed to have a significant effect in shifting of the transformation peak (austenitic or martensitic) towards higher values as heating rate increases.

3.7.2. **Dynamic Mechanical Analysis (DMA)**

The dynamic mechanical analysis (DMA) studies were performed in a temperature range of 30– 420 °C/420–20 °C with a heating and cooling rate of 10 °C/min. The ratio of the loss to the storage (tan δ) is often called damping and was measured as a function of temperature using a dynamic thermal mechanical analyser (TA InstrumentsDMAQ800) equipped with a liquid nitrogen cooling system. Measurements were conducted with a continuous heating rate of 5 °C/min in the 30–100 °C temperature range and with a frequency of 0.2 Hz. Samples were subjected to flexural loading in the three-point bending configuration (with a low-friction, self-adjusting three-point bending clamp) at a strain amplitude of 0.03%.

3.8. Alicona surface roughness

The roughness profiles were measured and analysed using an Alicona InfiniteFocus 3D profilometer. The measurements of surface roughness (R_a) were taken as an average

measurement after drawing 10 straight lines perpendicular to the direction of grooves of worn samples.

3.9. Mechanical testing

The shape memory behaviour of the samples was investigated by mechanically testing the samples using pin on disc equipment (i.e., wear test) as the primary method in this investigation. Other mechanical testing methods were performed to supplement and validate the shape memory behaviour of CuZr based shape memory alloys such as nanoindentation.

3.9.1. **Wear test**

Dry sliding wear experiments were conducted using a pin-on disc (DUCOM Micro POD) in air at room temperature and at 100^{o}C following the ASTM-G99. Reason for choosing this high temperature is that it is similar to temperatures reached in microactuators in engineering applications e.g., microactuators for satellites and motors. The pins were made using the as-casted rods and their surfaces were mirror surface polished using 4000 grit paper prior to wear testing against a counterbody disc of 60 HRC hardened SS304 stainless steel of 0.6 mm (Ra) surface roughness provided by the company DUCOM. SS304 stainless steel was chosen because of its excellent corrosion resistance considering pin-on-disc are carried out at RT and high temperatures (> 100^{o}C). Tests were performed at increasing loads of 5, 10 and 15 N at a sliding velocity of 0.5 m/s for a sliding distance of 1800 m. The loads used refer to previous studies in which the transformation effect appear to take place at and around these pressures/loads [32]. The mass loss was obtained by measuring the weight of the pins before and after the wear tests using an analytical balance (Fisherbrand™ Analytical Balance, ±0.1 mg).

3.9.2. **Nanoindentation**

Nanoindentation were performed with a high temperature vacuum nanoindentation system (NanoTest Xtreme, Micro Materials, UK). Indents were made in ambient conditions at a loading rate of 50 mN s_1 and a maximum load of 1 mN, using a diamond Berkovich indenter. To get an average and representative value, at least 5 valid indents (contained within the phase of interest) were made per composition on individual B2-CuZr

austenite grains. As a result of sample quenching, the austenite grains exhibit a dendritic shape. SEM observation and selection of large dendrites allowed for identification of suitable location to carry out indentation. In order to confine the plastic field generated by the indenter within the austenite phase, indents were made in portion of dendrites wider than 1 mm, at least 20 times the maximum depth reached during indentation.

2.9.3. **Indentation**

Indentation was performed using WILSON VH1150 test instrument with an indentation load of 3 N and a holding time of 10 s to measure Vickers hardness. The hardness values were the average of at least 5 measurements.

Chapter 4 – Effect of microalloying with Co on $Cu_{50}Zr_{50}$ at.% SMA and wear performance at RT and 100°C

Overview of the approach

The literature provided and highlighted throughout this thesis, shows that CuZr SMAs have high potential to replace costly NiTi in various applications, however, the SME is still worse than that of NiTi SMAs as explained in chapter 2.3. One way of tackling such an issue is the addition of microalloying element that enables CuZr based SMAs to work harden during wear testing. This is attributed to the fact that certain microalloying elements lower SFE which facilitate deformation twinning to initiate and thus stimulate martensitic transformation (B2 CuZr austenite to B19' CuZr martensite). This accelerated transformation makes the alloy harder and improves tribological and mechanical performance. However, the process of substituting B2 CuZr austenite phase with an element is not straight forward.

The SFE, which represents the energy cost per unit area incurred by relative displacement of two parts of a crystal through a shift vector across a certain slip plane, governs the deformation twinning event [151]. For the BCC B2 CuZr austenite phase, ab initio calculations of the SFE were performed by rigidly shifting the lattice across the {100}, {110}, and {111} planes at an interval of 0.1a along the possible slip directions, where a is the B2 CuZr austenite lattice constant. Among all possible lattice planes investigated, the minimum SFE occurred along the (011)[100] slip system, which corresponds to the most favourable slip direction [151].

The SFE value of the stoichiometric CuZr phase in **Fig. 4.1** illustrates a maximum of 381 $mJ=m^2$ at a=2, which corresponds to the energy barrier for the stacking fault formation. The addition of Co in place of Cu on the (011)[100] slip plane dramatically reduces the SFE to 75 $mJ=m^2$.

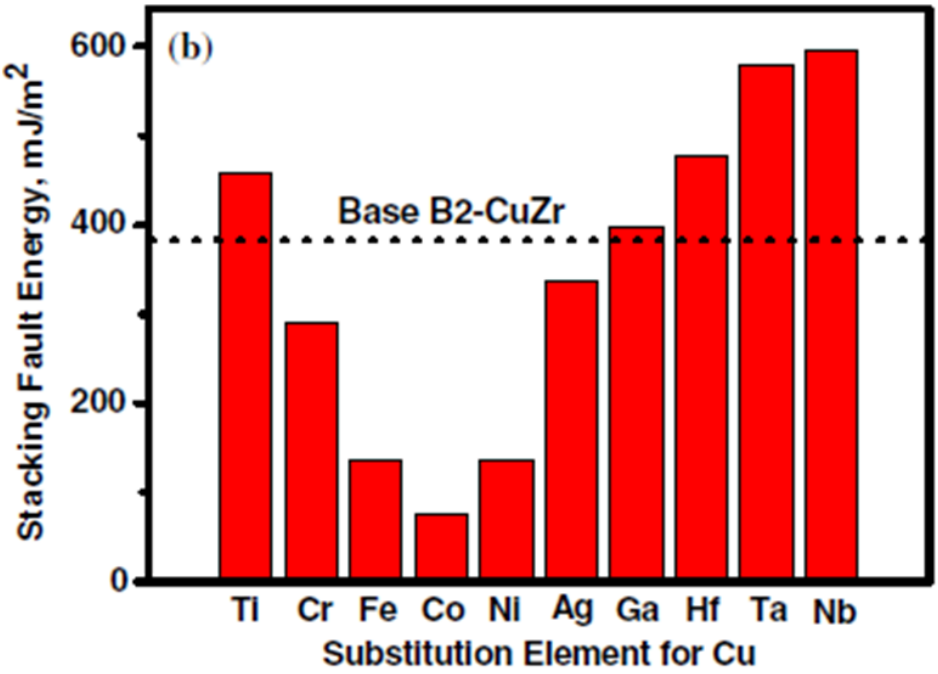

Fig. 4. 1. stacking fault energy of the B2-CuZr phase substituted with different elements [151]

These findings highlight that 0.5 at.% addition of microalloying element can significantly alter SFE and therefore promote martensitic transformation of B2 CuZr phase. It is important to highlight that the alloying elements should **only substitute Cu** in CuZr structure in order to achieve the beforementioned outcome. In fact, when microalloying **elements substitute Zr in CuZr** structure, the potential energy of the system sharply increases, thereby not energetically favourable.

Despite the ability of Co to significantly decrease SFE and promote martensitic transformation, the operating temperature range at which this effect is valid in terms of promoting martensitic transformation has not been studied before, therefore, the wear performance at RT and 100^{o}C and operating temperature range of microalloyed $Cu_{50}Zr_{50}$ SMA is investigated next.

In this section, the **effect of addition of Co as microalloying element and its concentration** on $Cu_{50}Zr_{50}$ SMAs is investigated in terms of **wear performance**. Although there are several studies highlighting the performance of CuZr-based SMAs, the wear performance at RT and high temperature is scarce. This is important since CuZr-based SMA engineering components **can be used in engineering applications where**

temperature vary during work period. It is important to improve the tribological performance of CuZr-based SMAs, in the meantime it is also important to understand the **limitations** at which these changes may not be beneficiary. For example, industrial electric motors **can reach about 100ºC** and surfaces under full sunlight in space **can go beyond that temperature**.

For this reason, the wear behaviour of suction casted 3mm diameter rods of CuZr and CuZr-based SMAs have been investigated at RT and 100ºC. This study shed light the tribological performance of SMAs in micro-actuators for satellites and motors.

4.1. Microstructural characterisation of the as-cast pins

Fig. 4.2 shows the XRD patterns for $Cu_{50}Zr_{50}$, $Cu_{49.5}Zr_{50}Co_{0.5}$ and $Cu_{49}Zr_{50}Co_1$ at. % alloys. The crystalline phases detected are orthorhombic $Cu_{10}Zr_7$ (a = 0.9347 nm, b = 0.9347 nm, c = 1.2675 nm), orthorhombic Cu_8Zr_3 (a = 0.78686 nm, b = 0.81467 nm, c = 0.9977 nm), austenite B2 CuZr (a = 3.2562 nm, b = 3.2562 nm, c = 3.2562 nm), monoclinic martensite B19' CuZr (a = 0.3237 nm, b = 0.4138 nm, c = 0.5449 nm) and tetragonal $CuZr_2$ (a = 0.3220 nm, b = 0.3220 nm, c = 1.1183 nm). In addition, the small overlapping halo indicates the presence of a fine microstructure, which is consistent with the TEM analysis (see **section 4.6**). The main peak at around $2\theta = 39.4^o$ corresponds to B2 CuZr austenite and its intensity is smaller for the alloys containing Co (**Fig. 4.2a, 1b and 1c**). Multiple peaks associated with martensite are detected at around 36.5^o and 56.5^o, while other peaks overlap with peaks corresponding to the intermetallic phases (Cu_8Zr_3, $Cu_{10}Zr_7$ and $CuZr_2$). Consequently, a mixture of austenite, martensite and intermetallic phases are present in different proportions upon quenching for the three compositions. The small halos detected between 35 and 45 ºC corresponds to the overlapping of XRD peaks associated to a fine microstructure as can be observed in **section 4.6**.

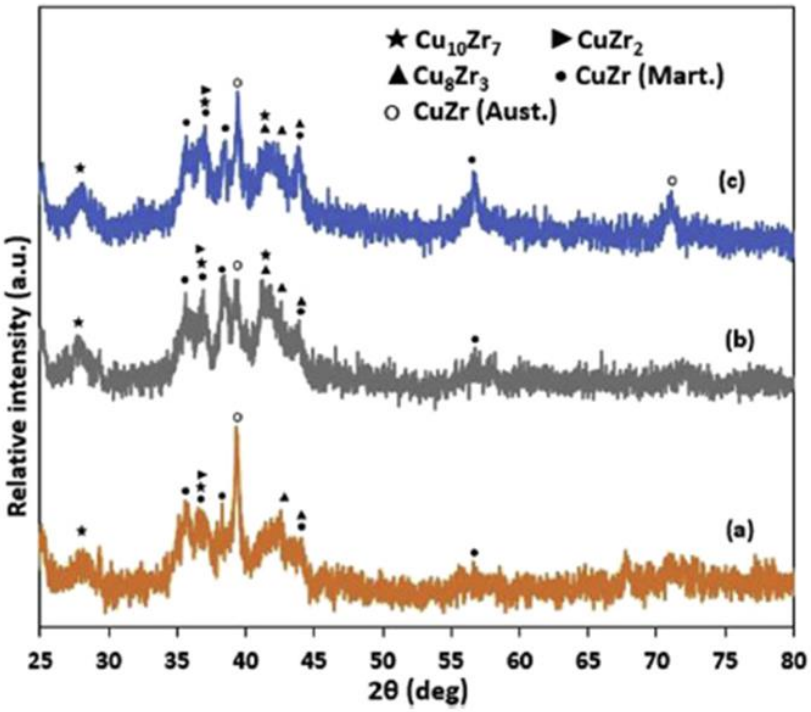

Fig. 4. 2. XRD scan of as cast (a) $Cu_{50}Zr_{50}$, (b) $Cu_{49.5}Zr_{50}Co_{0.5}$ and (c) $Cu_{49}Zr_{50}Co_1$ alloys.

To understand the mechanical behaviour of $Cu_{50}Zr_{50}$, $Cu_{49.5}Zr_{50}Co_{0.5}$ and $Cu_{49}Zr_{50}Co_1$ alloys at RT and at 100 ºC, wear tests will be conducted at both temperatures (**see section 4.2**) and therefore their thermal behaviour will be first studied by DSC (**Fig. 4.3**). Upon heating, a large exothermic peak associated with the transformation of martensite into austenite is detected and the temperatures at which the transformation starts A_s and ends, A_f, are listed on **Table 4.1**. This peak shifts towards lower temperatures with increasing Co content: Co_0 (curve a: A_s = 256.3 and A_f = 340.7 ºC), $Co_{0.5}$ (curve b: A_s = 235.2 and A_f = 312.3 ºC) and Co1 (curve c: A_s = 218.8 and A_f = 268.9 ºC), indicating that addition of Co tends to stabilize the formation of austenite [165] thermodinamically upon cooling [166, 167]. When the molten alloy starts to cool down during the casting process, certain phases stabilize at different temperatures [149], in this case, the addition of Co in solid solution tend to stabilize B2 CuZr austenite [168]. It is well known that martensite is harder and more wear resistant than austenite and therefore it is of interest to prevent the temperature to surpass A_s. For this reason, it is important for engineering components subjected to wear to work within the operational temperature range, As-RT, and in this

work the range decreases from 236.3 ºC for Co_0 to 215.2 ºC for $Co_{0.5}$ and 198.8 ºC for Co_1 alloy (see **Table 4.1**).

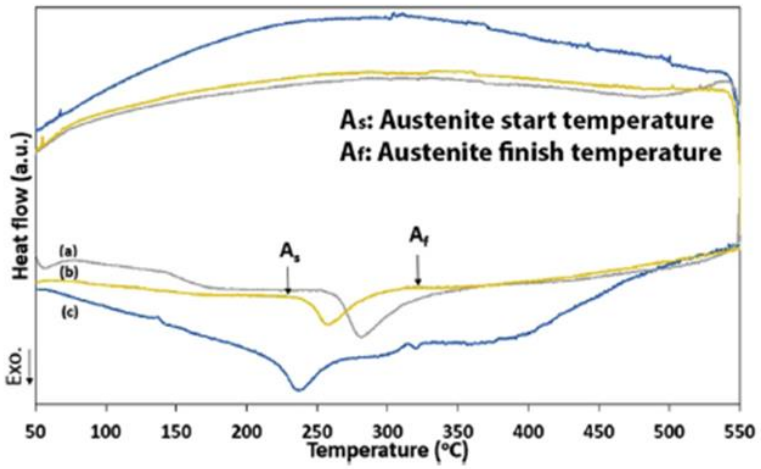

Fig. 4. 3. DSC curves for (a) $Cu_{50}Zr_{50}$, (b) $Cu_{49.5}Zr_{50}Co_{0.5}$ and (c) $Cu_{49}Zr_{50}Co_1$ heated up at 5K/min up to 550 ºC and left to cool down naturally in the DSC.

Table 4. 1. Transformation temperatures for the three compositions and operational temperature range.

Composition (at.%)	A_s (ºC)	A_f (ºC)	Operating temperature range A_s-RT (ºC)
$Cu_{50}Zr_{50}$	256.3	340.7	236.3
$Cu_{49.5}Zr_{50}Co_{0.5}$	235.2	312.3	215.2
$Cu_{49}Zr_{50}Co_1$	218.8	268.9	198.8

4.2. Wear tests

Fig. 4.4 shows the evolution of the mass loss for 3 mm diameter $Cu_{50}Zr_{50}$, $Cu_{49.5}Zr_{50}Co_{0.5}$ and $Cu_{49}Zr_{50}Co_1$ (at. %) rods tested at 5, 10 and 15 N load for 1h at two different conditions, room temperature (RT) (**Figs. 4.4a**) and 100 ºC (**Fig. 4.4b**).

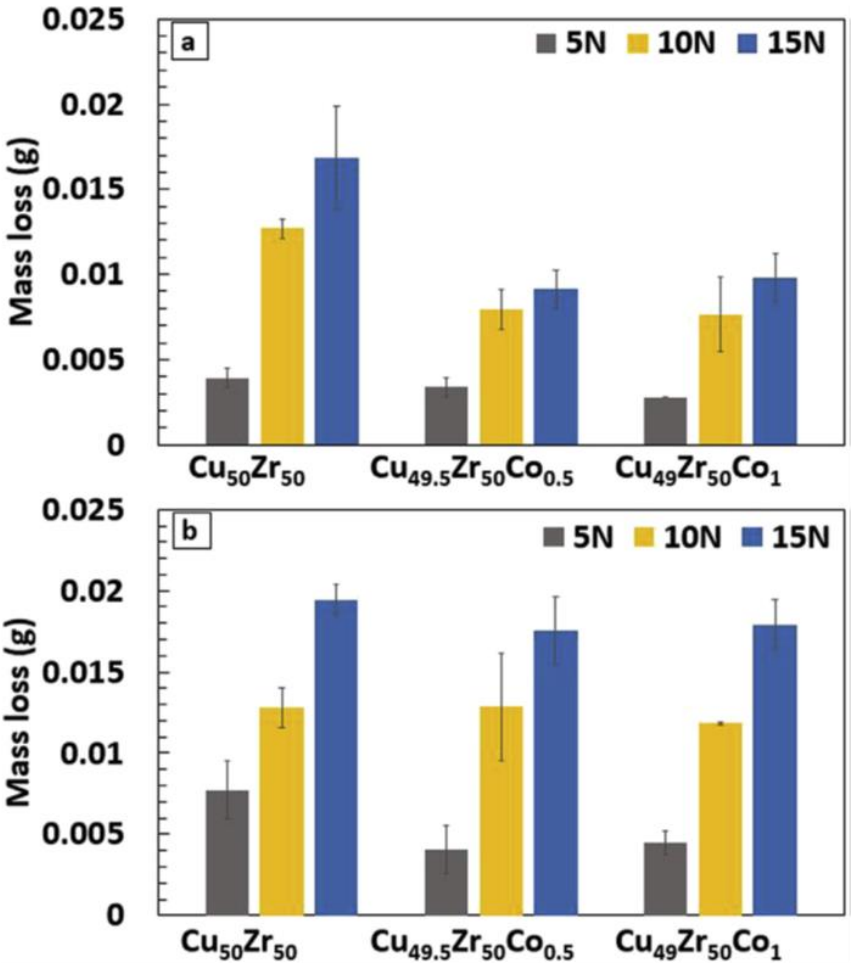

Fig. 4. 4. Mass loss for $Cu_{50}Zr_{50}$, $Cu_{49.5}Zr_{50}Co_{0.5}$ and $Cu_{49}Zr_{50}Co_1$ alloys tested at 5, 10 and 15 N load for 1 h at a) room temperature and b) 100 ^{o}C.

These tests have been coded according to the composition and testing conditions (load and temperature) as listed in **Table 4.2**.

Table 4. 2. Code for the different compositions and testing conditions of load and temperature.

Code for the different compositions and testing conditions of load and temperature						
Load (N)	Composition (at.%)					
	$Cu_{50}Zr_{50}$		$Cu_{49.5}Zr_{50}Co_{0.5}$		$Cu_{49}Zr_{50}Co_{1}$	
	Room Temperature (RT)	100ºC	Room Temperature (RT)	100ºC	Room Temperature (RT)	100ºC
5	$5NCo_0RT$	$5NCo_0100ºC$	$5NCo_{0.5}RT$	$5NCo_{0.5}100ºC$	$5NCo_1RT$	$5NCo_1100ºC$
10	$10NCo_0RT$	$10NCo_0100ºC$	$10NCo_{0.5}RT$	$10NCo_{0.5}100ºC$	$10NCo_1RT$	$10NCo_1100ºC$
15	$15NCo_0RT$	$15NCo_0100ºC$	$15NCo_{0.5}RT$	$15NCo_{0.5}100ºC$	$15NCo_1RT$	$15NCo_1100ºC$

For RT tests, a clear trend of mass loss increase with increasing load is observed, and it is maximum for $Cu_{50}Zr_{50}$ at. % ranging from about 0.0039 g for 5 N to about 0.0169 g for 15 N. The average mass loss has increased about 33% when the load increases from 10 N ($10NCo_0RT$) to 15 N ($15NCo_0RT$). Smaller mass losses are detected for the Co-containing alloys than for $Cu_{50}Zr_{50}$ at. % and especially at 15 N load for the alloy with 0.5 at. % Co since the mass loss for $Co_{0.5}$ (0.0091 g) is smaller than for Co_0 (0.017 g) and Co_1 (0.0098 g). At 100 ºC (**Fig. 4.4b**), the mass loss is generally higher than at RT, especially at high loads for the Co-containing alloys. The effect of the composition seems less significant than for tests at RT since similar increases in mass loss are found for the three compositions when the applied load is increased. The mass loss increases by 52%, 36 and 51%, when the applied load is raised from 10 to 15 N for Co_0, $Co_{0.5}$ and Co_1, respectively. The mass loss difference is slightly more noticeable at 15 N, with a maximum mass loss of about 0.0194, 0.0175 and 0.0179 g for Co_0, $Co_{0.5}$ and Co_1, respectively. The mass loss values are higher at 100 ºC than at RT while the evolution of the mass loss with increasing Co content is more noticeable at RT than at 100 ºC. This suggests that any mechanism responsible for the deformation associated with microalloying (i.e., twinning propensity) has little effect at 100 ºC. In fact, for 15 N load, the decrease in mass

loss from 15NCo$_0$RT to 15NCo$_{0.5}$RT is about 46% while it is only about 10% between 15NCo$_0$100 ^{o}C and 15NCo$_{0.5}$100 ^{o}C. It should be noted that the mechanism responsible for stabilization of austenite with Co addition upon cooling (see DSC in **Fig. 4.3**), is different from the mechanism responsible for stress-induced martensitic transformation. Microalloying with Co$_{0.5}$ is shown to promote stress-induced martensitic transformation due to the fact that the newly formed B2 CuZr with Co in solid solution has lower stalking fault energy than that of the parent alloy [151].

4.3. Microstructural analysis after wear tests

In order to understand the evolution of the wear performance on the surface of tested samples, In-beam Secondary Electron (SE) SEM images have been taken for all the compositions at 10 and 15 N at RT and 100 ^{o}C as shown in (**Fig. 4.5**).

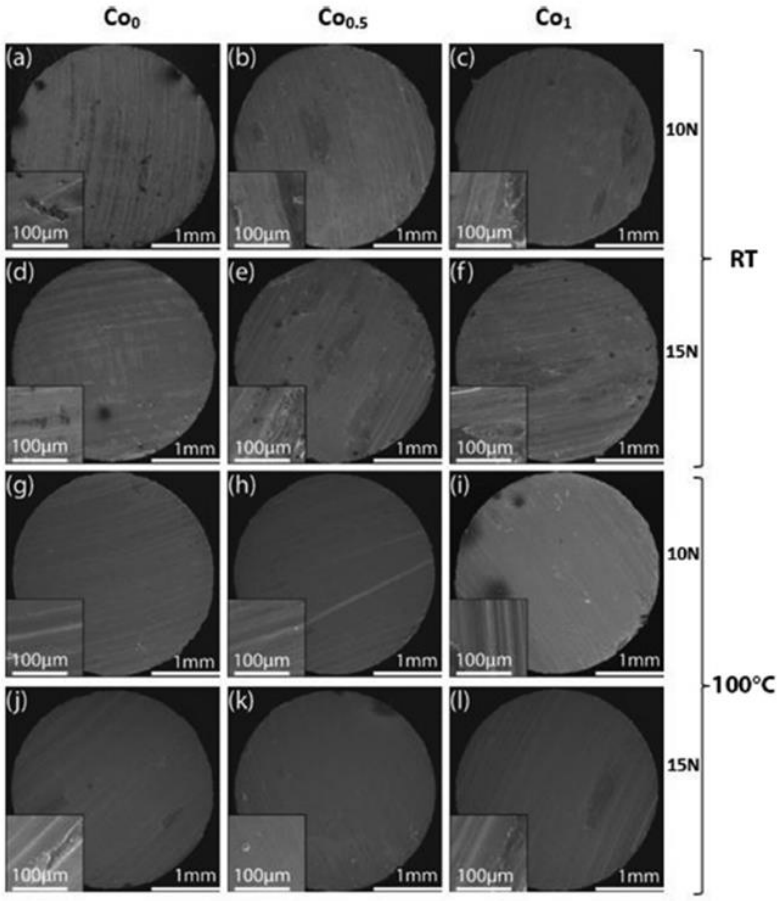

Fig. 4. 5. In-beam Secondary electron (SE) SEM images for a) 10NCo$_0$RT, b) 10NCo$_{0.5}$RT, c) 10NCo$_1$RT, d) 15NCo$_0$RT, e) 15NCo$_{0.5}$RT, f) 15NCo$_1$RT, g) 10NCo$_0$100 ^{o}C, h) 10NCo$_{0.5}$100 ^{o}C,

i) $10NCo_1100$ ^oC, j) $15NCo_0100$ ^oC, k) $15NCo_{0.5}100^oC$, l) $15NCo_1100$ ^oC pin samples. Insets: magnified

The surface finish for samples tested at RT show surface features and grooves originated from the wear process with the disc, this clear pattern of grooves is not as clear for samples tested at 100 ^{o}C. At higher temperature, the oxidation rate is increased, which leads to a thicker oxide layer that covers up the substrate pattern and features (**see Fig. 4.5 g-l**). The thicker oxide that was built at 100 ^{o}C, leads to higher removal rate as brittle oxides can easily get fragmented and detached, which could explain the higher mass loss for 100 ^{o}C compared to the behaviour at RT (**Fig. 4.4**). This is in line with the thickness of oxide layer study (**see section 4.5**). In order to investigate the different features in more detail, high magnification SEM images (see insets of **Fig. 4.5**) have been shown. All the surfaces show the presence of continuous grooves with material displaced to the lateral sides, thus suggesting that ploughing is the mechanism responsible for abrasive wear. The surface finish of tested samples contains different features that can be studied, samples tested at 100 ^{o}C exhibit abrasive wear and higher oxidation compared to samples tested at RT. For this reason, these features have been observed when testing at 100 ^{o}C (i.e., SEM images of **Fig. 4.6a and 4.6b** for $15NCo_0100$ ^{o}C). **Fig 4.6** shows the SEM images and corresponding EDX scans of two different representative areas from the surface of $15NCo_0100$ ^{o}C sample. An elongated smeared patch of 500 mm long oriented along the groove direction is observed (**Fig. 4.6a**).

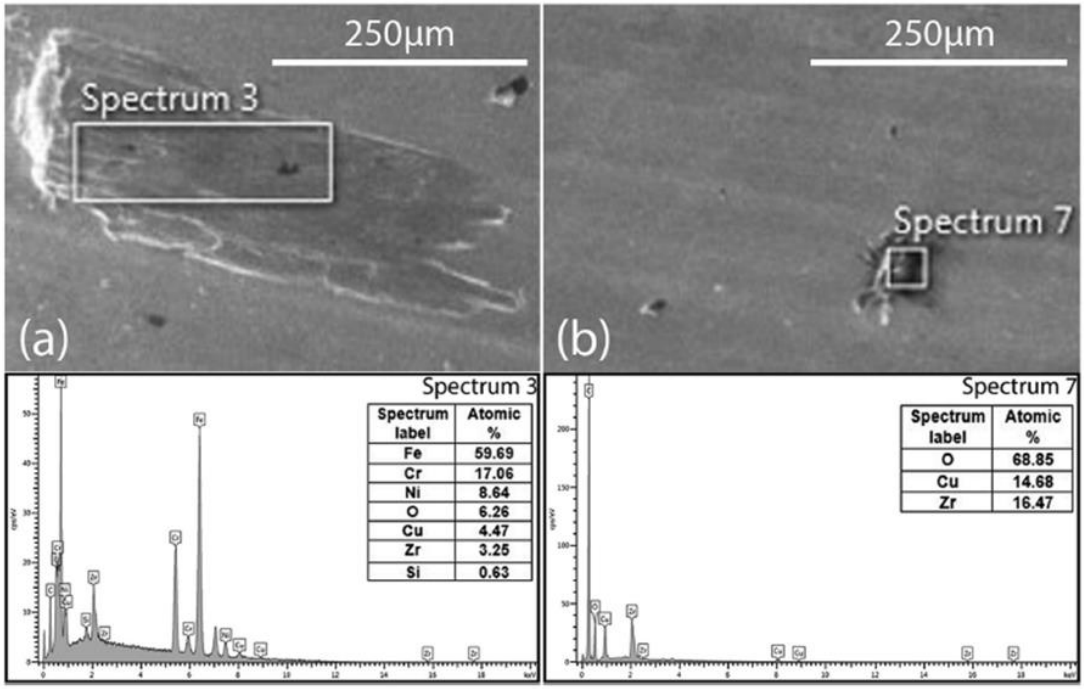

Fig. 4. 6. SEM images and corresponding EDX scans showing two selected areas a) and b) from the surface of 15NCo$_0$100 ^{o}C sample.

According to EDX analysis the composition of these patches is 59.69 at. % Fe, 17.06 at. % Cr, 8.64 at. % Ni, 6.26 at. % O, 4.47 at. % Cu, 3.25 at. % Zr, 0.63 at. % Si, very rich in iron, oxygen, nickel, and chromium and therefore could correspond to the steel transferred from the disk onto the surface of the pin. Along with the patches there are small particles of dark tonality of about 44 mm (**Fig. 4.6b**) distributed homogeneously across the surface of the samples. EDX analysis of the particles indicate that their composition is 68.85 at. % O, 14.68 at. % Cu, 16.47 at. % Zr and therefore could be attributed to an oxidized debris released from the pin during the wear tests.

The wear behaviour of the alloys not only depends on their as cast microstructure and composition but also on the changes that take place on the surface of contact with the disc and microstructural changes over the wear test time. Considering that the Co$_1$ alloy is the most critical since it decreases the operating temperature range the most, the XRD scans for this alloy have been performed (**Fig. 4.7**) for the as-cast sample (**Fig. 4.7a**), for 15NCo$_1$100 ^{o}C from the bulk (**Fig. 4.7b**) and after annealing at 400 ^{o}C for 1 h (**Fig. 4.7c**). XRD after annealing at 400 ^{o}C show that all martensite has transformed into austenite since the temperature is well beyond A_f = 268.9 ^{o}C. The relative intensity of austenite

peaks from the bulk of 15NCo$_1$100 ^{o}C **(Fig. 3.7b**) is intermediate between that in the as-cast condition (**Fig. 3.7a**) and after the transformation (A_f) (**Fig. 3.7c**) and therefore partial isothermal transformation from martensite into austenite has taken place.

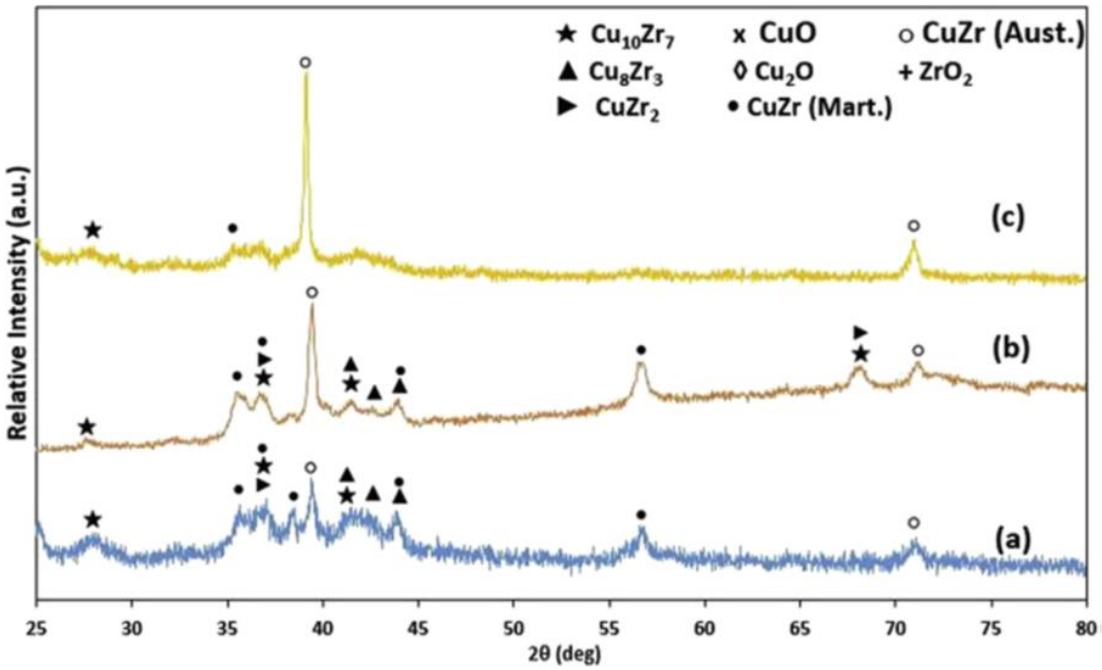

Fig. 4. 7. XRD scans for the $Cu_{49}Zr_{50}Co_1$ alloy a) in the as-cast condition, b) after 15NCo$_1$100 ^{o}C wear test and (c) annealed at 400 ^{o}C for 1 h.

4.4. Estimation of temperature rise at the pin-disc contact surface

The presence of oxides clearly suggests that friction between pin and disc can rise the temperature. The temperature rise at the centre of contact area between the pin and the disk can be estimated using the following friction temperature (ΔT_{max}) equation [169]

$$\Delta T_{max} = \frac{1.32 b \mu p V}{\sqrt{\pi}(K_2\sqrt{1.2344+Pe_1}+K_2\sqrt{1.2344+Pe_2})} \qquad (4.1)$$

where b, μ, p, V, K and Pe are the contact radius, friction coefficient, normal pressure, sliding velocity, thermal conductivity and the Peclet number respectively and assuming that material 1 is the rotating steel disk while material 2 is the stationary pin. Some of these parameters are calculated using the **equations (4.3-4.8)** given by [169] and these values have been subsequently substituted into **Equation (4.1).**

$$b = \left(\frac{3wr}{4E'}\right)^{1/3} \qquad (4.2)$$

$$E' = \frac{1-v_1^2}{E_1} + \frac{1-v_2^2}{E_2} \quad (4.3)$$

$$r = \left(\frac{1}{R_{pin}} + \frac{1}{R_{disc}}\right)^{-1} \quad (4.4)$$

$$Pe_1 = \frac{V_1 b \rho_1 1 C_1}{2K_1} \quad (4.5)$$

$$Pe_2 = \frac{V_2 b \rho_2 1 C_2}{2K_2} \quad (4.6)$$

$$p = \frac{w}{\pi b^2} \quad (4.7)$$

Where b, w, r, E' and p are the radius of contact circle, normal load, effective radius, effective modulus and pressure. The mechanical properties of the different alloys has been estimated using the rule of mixtures [170] given by:

$$M^{-1} = \sum f_i . {M_i}^{-1} \quad (4.8)$$

Table 4.3 lists mechanical properties of Cu, Zr, Co, steel disk, $Cu_{50}Zr_{50}$, $Cu_{49.5}Zr_{50}Co_{0.5}$ and $Cu_{49}Zr_{50}Co_1$ as well as the surface temperature at the centre of contact area between the pin and disk for the different loads (i.e. 5, 10 and 15 N). For tests conducted at RT (20 ^oC) and at 100 ^oC, the temperature rise ΔT_{max} has been added. Values of r, K and C for Cu, Co and SS304 were taken from [171], K and C for Zr from Ref. [172] while r for Zr was interpolated from Ref. [173] using the rule of mixtures (see **Equation (4.9)**).

Young's modulus E and Poisson's ratio n for Cu and Zr was taken from [32] and for Co and SS304 from [174, 175] respectively. The value of E at 100 ^oC can be calculated from [176]:

$$\frac{E}{E_o} = \left(1 - a\left(\frac{T}{T_m}\right)\right) \quad (4.9)$$

Where E is the Young's modulus at temperature T, E_0 is the modulus at 0 K and T_m is melting temperature. The constant "a" relates to the proportionality constant, which is around 0.5 due to the linear decrease of modulus from 0 K to melting temperature [176]. In addition, Poisson's ratio change with temperature is minimal [177] and practically has

no effect in the estimation of temperature. From all these values, the friction temperatures (ΔT_{max}) have been calculated, added to the testing temperatures (RT or 100 ^{o}C) and the resultant contact surface temperatures obtained and listed (**Table 4.3**). Additionally, the temperature measured experimentally using a thermocouple attached to the other side of the pin recorded a slightly lower temperature. This difference in temperature is attributed to the fact that contact surface temperature at the centre of the interaction between pin and disc is higher than the temperature measured at the other side of the pin despite the alloy being a very heat conductive. The contact temperature increases with increasing load, as expected, due to the increase in friction temperature and achieve maximum values for 15 N at RT with 81 ^{o}C for Co_0 and $Co_{0.5}$ while for Co_1 it is 78 ^{o}C. For 15 N load at 100 ^{o}C the contact surface temperatures are 153 ^{o}C for Co_0, 154 ^{o}C for $Co_{0.5}$ and 155 ^{o}C for Co_1 alloys. These results indicate that the contact surface temperature is always below the austenitic transformation temperature A_s (**Fig. 4.3** and **Table 4.1**). These are, however, estimated values since there are uncertainties for calculation of ΔT_{max}, especially when obtaining the thermal conductivity for the three alloys. Thermal conductivity K of each individual element (i.e., Cu, Zr and Co) is well-known, however, several studies disagree on the value of thermal conductivity of the alloys, for example, Touloukian et al. [178] reported a value of 216 W/mK for CuZr alloy while Yamasaki et al. [179] obtained 5.02 W/mK for $Zr_{55}Cu_{30}Al_{10}Ni_5$. For the studied $Cu_{50}Zr_{50}$, $Cu_{49.5}Zr_{50}Co_{0.5}$ and $Cu_{49}Zr_{50}Co_1$ alloys we could not measure experimentally the thermal conductivity and experimental results are not available in the literature. For this reason, it was estimated using the rule of mixtures since they led to reasonable values close to 216 W/mK and even error value of 20% would all result in an estimated surface temperature below the start of the austenitic transformation peak (**Fig. 4.3**).

Table 4. 3. Properties of elements and alloys at RT and 100 ºC and estimated contact surface temperature as a function of load and temperature (RT and 100 ºC).

	Mechanical properties					Contact surface temperature (ºC)		
	E (GPa) RT|100ºC	ρ (Kg/m³) RT|100ºC	ν[j] RT|100ºC	K (W/mK) RT|100ºC	C (Nm/KgK) RT|100ºC	5N RT|100ºC	10N RT|100ºC	15N RT|100ºC
Cu	130[b]|112[g]	8930[c]|8890[c]	0.34[b]	400[c]|395[c]	385[c]|397[c]	-	-	-
Zr	68[b]|62[g]	6520[e]|6488[e]	0.34[b]	21[d]|20[d]	285[d]|295[d]	-	-	-
Co	209[h]|187[g]	8862[c]|8827[c]	0.31[h]	99[c]|89[c]	424[c]|452[c]	-	-	-
Steel disk	210[i]|187[g]	8020[c]|8000[c]	0.29[i]	15[c]|16[c]	480[c]|500[c]	-	-	-
$Cu_{50}Zr_{50}$	99[a]|87[a]	7725[a]|7689[a]	0.34[a]	216[f]|224[f]	335[a]|346[a]	37[a]|117[a]	90[a]|120[a]	81[a]|153[a]
$Cu_{49.5}Zr_{50}Co_{0.5}$	99[a]|87[a]	7725[a]|7689[a]	0.34[a]	216[f]|224[f]	335[a]|346[a]	40[a]|122[a]	66[a]|125[a]	78[a]|154[a]
$Cu_{49}Zr_{50}Co_{1}$	100[a]|88[a]	7724[a]|7688[a]	0.34[a]	216[f]|224[f]	335[a]|347[a]	39[a]|118[a]	68[a]|139[a]	81[a]|155[a]

[a] Material properties (calculated)
[b] [V.M. Villapún, J. Medina, P. Pérez, F. Esat, F. Inam, S. González. Strategy for preventing excessive wear rate at high loads in bulk metallic glass composites. Materials and Design 135 (2017) 300-308]
[c] [Mills, K.C., 2002. Recommended values of thermophysical properties for selected commercial alloys. Woodhead Publishing.]
[d] [Fink, J.K. and Leibowitz, L., 1995. Thermal conductivity of zirconium. Journal of Nuclear Materials, 226(1-2), pp.44-50.]
[e] [Valencia, J.J. and Quested, P.N., 2013. Thermophysical properties]
[f] [Touloukian, Y.S., 1970. Thermal conductivity-metallic elements and alloys. Thermophysical properties of matter, 1, 985-987]
[g] [Courtney, T.H., 2005. Mechanical behaviour of materials. Waveland Press.]
[h] [G.V. Samsonov (Ed.) in Handbook of the physicochemical properties of the elements, IFI-Plenum, New York, USA, 1968.]
[i] Engineering Properties of Steels, Philip D. Harvey, editor, American Society for Metals, Metals Park, OH, (1982).
[j] Poisson's ratio variation with form RT to 100ºC is very small that makes it insignificant in terms of temperature estimation.

4.5. Oxidation

Figs. 4.8 and **4.9** show backscattered SEM images of the oxide layer for $15NCo_0RT$ and $15NCo_0100$ ºC, respectively.

The tonality of the oxide layer differs from the substrate due to the different atomic mass of elements. Also, the oxide layer is split into different layers of darker/brighter tonalities indicating that the nature of each layer is different from one another. In order to investigate the formation of oxides on the worn surface of the samples tested at $15NCo_0RT$ and $15NCo_0100$ºC conditions, the cross-section of the samples have been investigated by backscattered and elemental mapping SEM analysis (**Figs. 4.8 and 4.9**). For $15NCo_0RT$, the oxide layers are thinner than for $15NCo_0100$ºC.

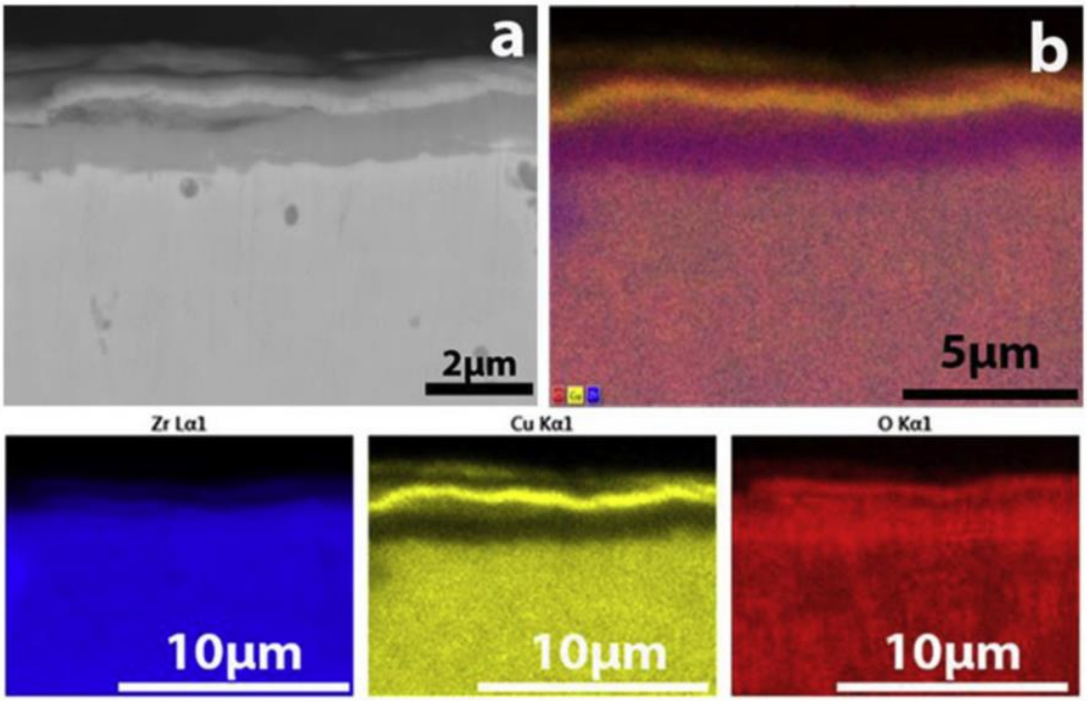

Fig. 4. 8. a) Backscattered SEM and b) SEM-EDS elemental mapping for 15NCo$_0$RT.

The backscattered image for 15NCo$_0$RT (**Fig. 4.8**) shows that the deepest oxide layer of dark tonality, in contact to the substrate is rich in Zr and oxygen with a composition of 25.81 at. % Zr, 17.94 at. % Cu and 56.26 at. % O and thus could be attributed to ZrO_2. The high propensity in the formation of ZrO_2 is consistent with the high negative enthalpy of mixing [180]. The second layer closer to the surface is of bright tonality and the concentration of Cu ranges from 49.66 to 67.48 at. % while for oxygen ranges from 20.44 to 28.80 at. % and thus could be attributed to Cu_2O.

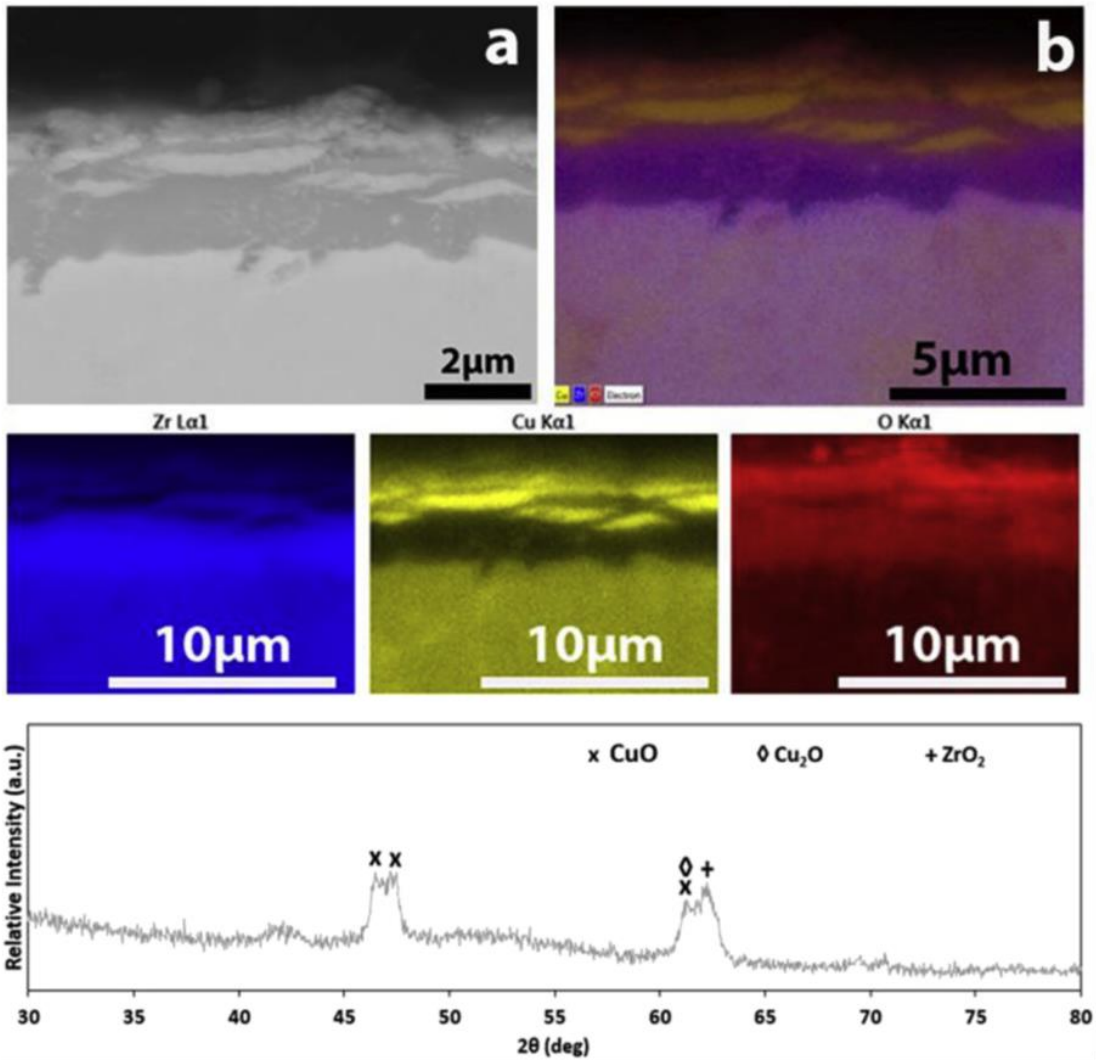

Fig. 4. 9. a) Backscattered SEM, b) SEM-EDS elemental mapping for 15NCo$_0$100 ^{o}C along with the XRD scan from the top view (Fig. 4.5j).

The outermost layer is of darker tonality and has similar ratio of Cu to oxygen and thus can be attributed to CuO. These same oxides have been detected by XRD from the surface of the tested pins as shown in (**Fig. 4.9c**). For 15NCo$_0$100 ^{o}C (**Fig. 4.8**) the composition of the oxide layers is very similar to those observed at RT and thus could be attributed to ZrO_2, Cu_2O and the outer layer to CuO. However, in this case, the Cu_2O layer is fractured into multiple fragments while for RT tests the fracturing is very limited and this can be attributed to the fact that the oxide layers at 100 ^{o}C are thicker and thus the brittle oxide layer is more prone to be fractured than at RT. This is consistent with the Weibull modulus that describes the variability in the measured material strength [181], where under identical testing conditions, the failure of brittle specimens is related to the

distribution of physical flaws and weak points, which is in this case the cracks and voids within the body of the oxide layer [182]. As the material wears out the ZrO_2 is formed again from the surface of the Cu_2O thus resulting in a multilayered-like structure. The Cu_2O fragments get more broken when closer to the surface, which could be expected due to the high shear forces during the test. As observed at 100 ^oC, the oxide layer is thicker than at RT and thus more prone to get easily detached from the pin substrate, especially when subjected to shear stress [183, 184], which could be attributed to the mechanical stress generated between this oxide layer and the surface beneath [185]. The brittle oxides detached from the pin surface during the wear test can act as abrasive particles and therefore promote material removal from the pin thus resulting in higher mass loss, as observed at 100^oC for 15 N load. As mentioned in **section 4.3**, the dominant type of wear is abrasive, which is characteristic in shape memory alloys with high crystallinity [186] while the mechanism by which the material is removed is by displacement during ploughing process. On the worn surface, multiple features can be observed, including spot-like oxides, material transfer (see **Fig. 4.6**) and formation of a brittle oxide layer (see **Figs. 4.8 and 4.9**), these features play a major role in the evolution of mass loss. **Fig. 4.10** shows the roughness profile (arithmetic average: Ra) of the three alloys wear tested at 5, 10 and 15 N load at RT (**Figs. 4.10a**) and 100 _C (**Fig. 4.10b**). Two factors mostly determine the roughness profile, and they are the following:

I. Oxidation

The roughness follows similar trend for $Cu_{50}Zr_{50}$, $Cu_{49.5}Zr_{50}Co_{0.5}$ and $Cu_{49}Zr_{50}Co_1$ at RT and 100^oC. However, the average variation of roughness with load at RT is higher (i.e., from 0.92 mm to 1.8 mm) than for 100^oC (i.e., from 1.3 mm to 1.6 mm) due to the excessive oxidation effect at 100 ^oC that tends to mask the changes taking place on the underlying substrate.

II. Martensitic transformation

For either austenite or martensite, an increase in load results in an increase of surface roughness because the removal of material increases with the increase of load. However, when the transition load (i.e., stress) for which austenite transforms into martensite is

reached, the surface roughness drops rapidly since martensite is harder than austenite and thus martensite cannot be worn out so easily.

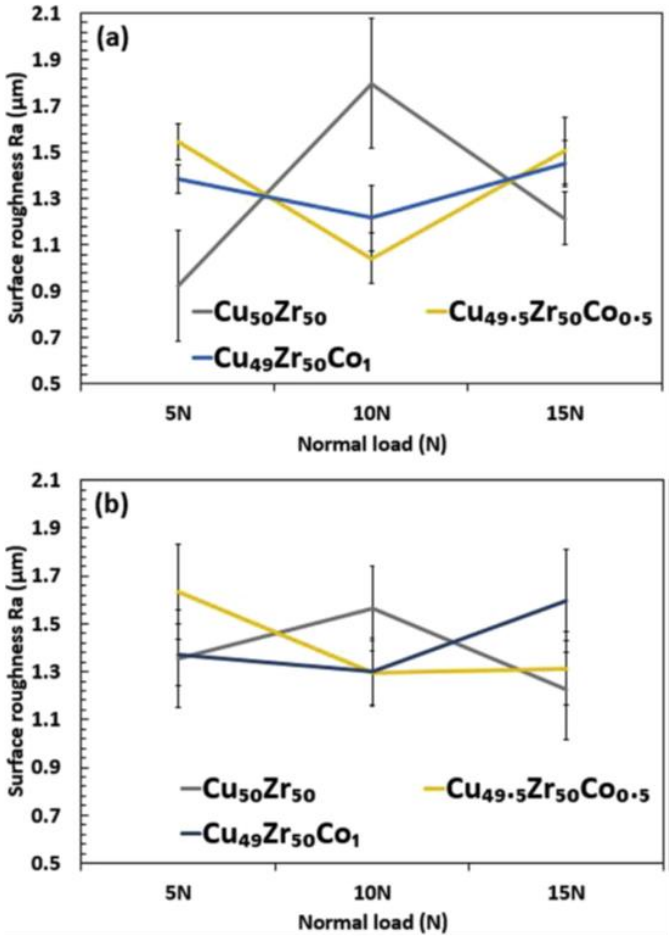

Fig. 4. 10. Roughness profile of the $Cu_{50}Zr_{50}$, $Cu_{49.5}Zr_{50}Co_{0.5}$ and $Cu_{49}Zr_{50}Co_1$ alloys for 5, 10 and 15 N load applied a) at room temperature and b) at 100 ^oC.

Since the trend for RT and 100 ^oC is similar but more noticeable at RT, the discussion will be only done for RT (see **Fig. 4.10a**). For $Co_{50}Zr_{50}$, Ra increased from 0.92 mm (for $5NCo_0RT$) to 1.8 mm (for $10NCo_0RT$) and then decreased to 1.22 mm, this could be attributed to martensitic transformation having a clear effect in limiting mass loss at 15 N load. In this case, 10 N load was not high enough to transform B2 austenite into B19 martensite. These findings are in agreement with the mass loss results (see **Fig. 4.4a**) where mass loss increase from 10 N to 15 N is less dramatic than from 5 N to 10 N. For the Co-containing alloys, the mass loss increase (**Fig. 4.4a**) from 5 N to 10 N for $Co_{0.5}$ and Co_1 is clearly lower than that for Co0 indicating that martensitic transformation is

already taking place at 10 N. This happens because addition of Co promotes martensitic transformation and thus decreases the load required to initiate the transformation [9]. However, once the transformation has taking place, further increase in load (i.e., at 15 N) results in further removal of material and thus the roughness increases.

4.6. SEM and TEM analysis

In order to analyse the wear performance of the three different compositions tested at RT and at 100ºC, the microstructure has been analysed under a SEM and TEM. The backscattered SEM images of (**Fig. 4.11**) for $Cu_{50}Zr_{50}$, $Cu_{49.5}Zr_{50}Co_{0.5}$ and $Cu_{49}Zr_{50}Co_1$ alloys show that the microstructure for the parent alloy and with 1 at. % Co is very similar but different from the alloy with 0.5 at. % Co, which is consistent with the XRD scans.

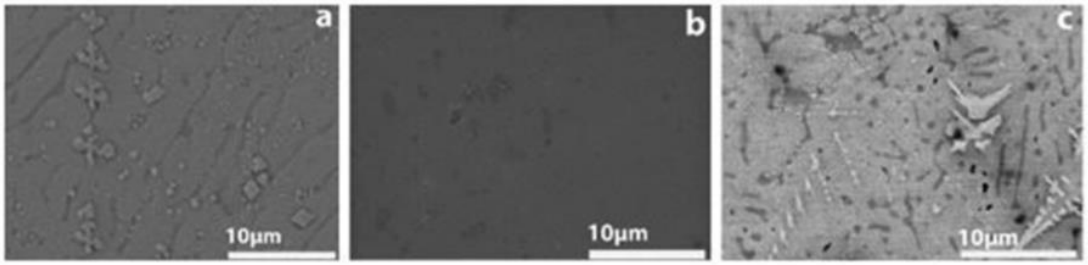

Fig. 4. 11. Backscattered SEM images for as-cast a) $Cu_{50}Zr_{50}$, b) $Cu_{49.5}Zr_{50}Co_{0.5}$ and c) $Cu_{49}Zr_{50}Co_1$ alloys.

For Co_0 and Co_1 alloys the microstructure consists of clear tonality precipitates from about 1 mm (polygonal) to 5 mm (dendritic shape) size dispersed within a matrix of large dendrites of grey tonality surrounded by a dark phase at the interphases. From EDX, the composition of the precipitates ranges from 34.05 to 37.78 at. % Cu and 65.95-62.22 at. % Zr and therefore would correspond to $CuZr_2$. The composition of the dendrites is about 50.36-50.88 Cu and 49.12-49.64 at. % Zr, similar content of Cu and Zr and therefore would correspond to austenite/martensite. Finally, the approximate composition of the dark area between interphase could be associated to $Cu_{10}Zr_7$ at. % since the concentration of Cu and Zr ranges from 57.55 to 57.70 at. % Cu and 42.30-42.45 at. %, respectively. Considering that the microstructures are so fine that could not be easily identified by SEM, have performed TEM analysis. The microstructures for the three compositions are very similar as deduced from XRD (**Fig. 4.2**) and SEM (**Fig. 4.11**) and therefore we have focused our analysis on the $Co_{0.5}$ alloy since it exhibits the highest

twinning propensity and thus lower mass loss. **Fig. 4.12** shows representative TEM images from the surface of the pin in contact with the steel disc after being tested at RT and 15 N load.

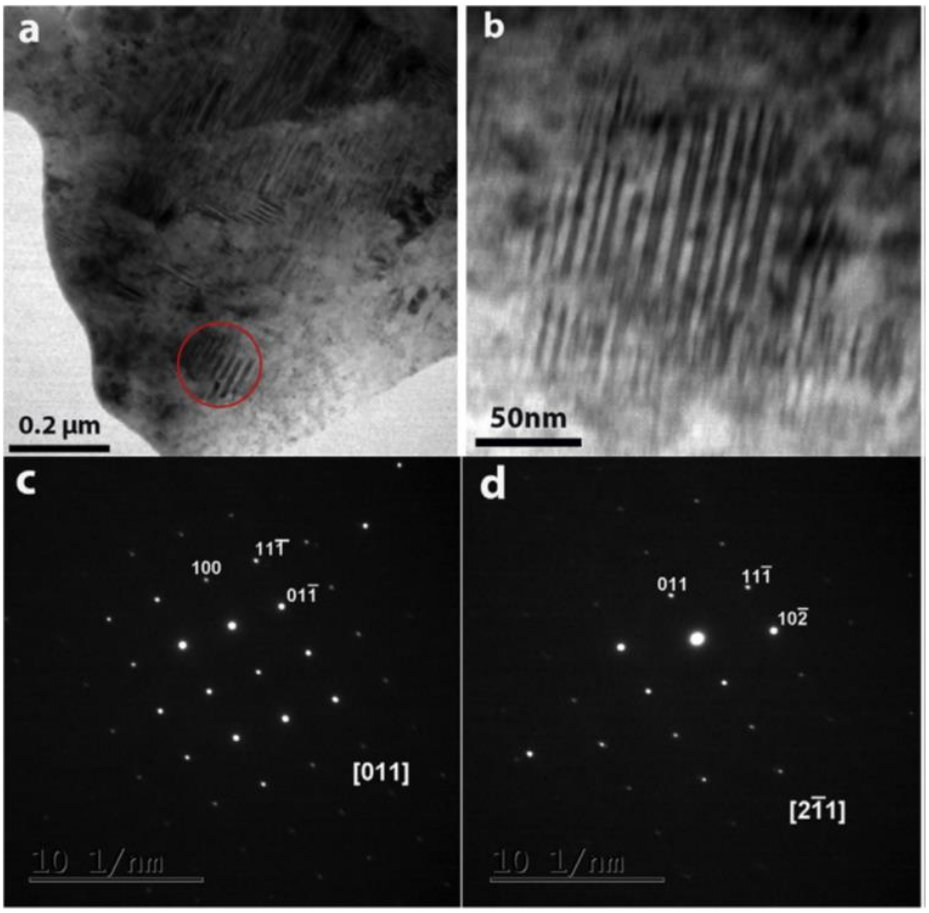

Fig. 4. 12. (a) Bright field TEM image of $Cu_{49.5}Zr_{50}Co_{0.5}$ alloy tested at 15 N and RT, (b) magnified twinned phase and (c) corresponding SAED patterns (B = [011] and B = [2-11]) of the B19' martensite twinned phase.

The microstructure consists of grains where most of them have a plate structure and about 0.2 mm size. EDX analysis from the highlighted circle in (**Fig. 4.12a**) indicate that the concentration of Cu ranges from 50.92 to 51.99 at. % and Zr from 46.32 to 47.51 at. % it therefore would correspond to $Cu_{50}Zr_{50}$ at. %. A magnified image of the grain inside the highlighted circle is shown in **Fig. 4.12b**, which has a clear twinned structure typical of martensite. To identify the nature of the crystalline phase, SAED patterns have been obtained. They can be effectively identified as [011] (**Fig. 4.12c**) and [2-11] (**Fig. 4.12d**) zone axes of B19' martensite phase respectively. To understand the difference in

performance when the samples are wear tested at 100 ^{o}C, TEM images of the $Co_{0.5}$ sample at 15 N load have been studied. A representative area from the sample was shown in (**Fig. 4.13**).

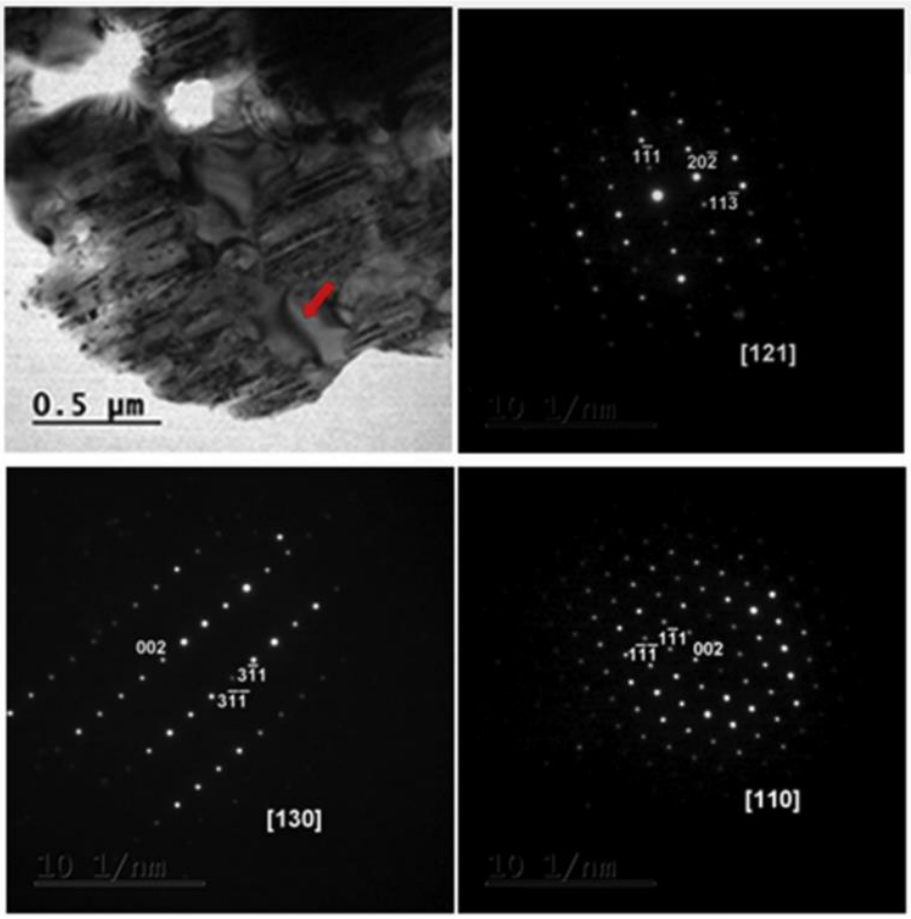

Fig. 4. 13. (a) Bright field TEM image of $Cu_{49.5}Zr_{50}Co_{0.5}$ alloy tested at 15 N and 100 ^{o}C, (b, c, and d) SAED patterns (B = [121], B = [130] and B = [110] respectively) of a grain without stripes corresponding to Cu10Zr7 (see red arrows).

Although some twinned grains (**Fig. 4.13a**) are observed, larger areas do not contain twinned grains as shown in the representative image of (**Figs. 4.13a and 4.14**) show that the microstructure consists of grains with plate structure, and they have similar concentration of Cu and Zr and small Co content. Grains without stripes (see red arrow) of 59 at. % Cu, 41% at. Zr could be associated to the intermetallic $Cu_{10}Zr_7$ as can be proven from the SAED patterns of **Fig. 4.12b, c and d**.

In order to assess the volume fraction of the crystalline phases present and considering the limitations of TEM (i.e., local technique), the analysis has been done from XRD results (**Fig. 4.7**). After testing with 15 N load at 100ºC for 1 h (**Fig. 4.7b**), the intensity of the austenite peak increases indicating the volume fraction of austenite has increased due to an isothermal effect. In fact, volume fraction of austenite to martensite for as cast sample (**Fig. 4.7a**) is 1.4:1 and after testing at 100ºC (**Fig. 4.7b**) is 2.6:1. Additionally, after annealing at 400ºC (**Fig. 4.7c**) volume fraction of austenite to martensite is 7.1:1.

In addition, Cu-rich particles of different morphologies, including trapezoidal shape (see red arrow in **Fig. 4.14**) particles are present. These particles have a concentration of Cu ranging from 83.52 to 88.01 at. %, Zr from 7.22 to 12.38 at. % and Co from 2.1 to 3.37 at. %, and thus could identified as Cu_8Zr_3 compound with Co in solid solution. **Fig. 4.14** shows a bright field TEM image of the microstructure containing these particles and the corresponding SAED patterns of the one with trapezoidal shape, which confirm the existence of Cu_8Zr_3 particles. It can be noticed that due to their small size, these particles were not detected by SEM.

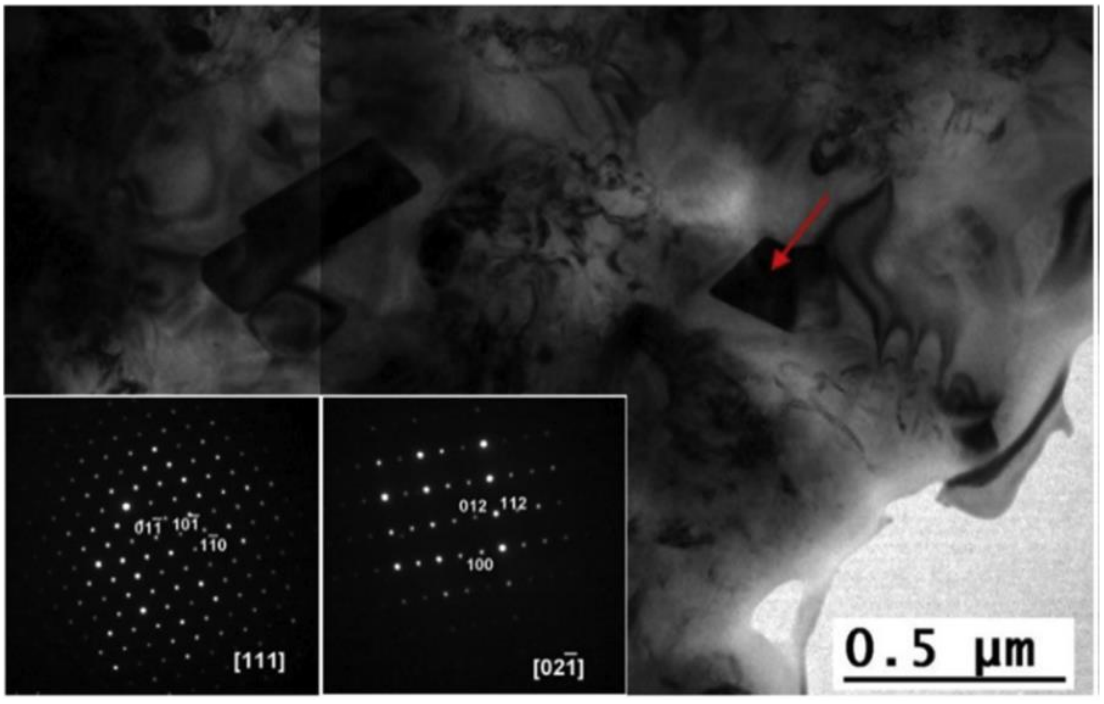

Fig. 4. 14. (a) Bright field TEM image of $Cu_{49.5}Zr_{50}Co_{0.5}$ alloy tested at 15 N and 100 ºC. Inset: SAED patterns (B = [111] and B = [02-1]) of a trapezoidal shape particle (red arrow).

In summary, these results show that for tests performed at RT and 15 N load the twinned grains of B19' martensite are present and contributing towards low mass loss and enhanced wear behaviour. However, when testing at 100 ^{o}C and 15 N load, some of the grains are not twinned, which is consistent with (1 h testing) partial isothermal transformation of martensite into austenite (**Figs. 4.7b and 4.13**). This chapter shows that although microalloying with Co promotes the martensitic transformation and thus it is a good strategy to prevent high mass loss at room temperature (**Fig. 4.4a**), it is not very useful to prevent mass loss if the surface contact temperature is close to As (**Fig. 4.4b**). In this latter case, when testing at 100 ^{o}C, the mass loss of the $Co_{0.5}$ and Co_1 alloys are very similar to the parent Co_0 alloy and it is about twice the mass loss of $Co_{0.5}$ and Co_1 at RT. Moreover, addition of Co shifts the A_s temperature from 256.3 ^{o}C for Co0 to 218.8 ^{o}C for Co_1 thus reducing the operating temperature range.

This chapter highlights the importance and limitations when selecting microalloying elements to enhance the wear resistance of CuZr based SMAs. An engineering component of $Cu_{50}Zr_{50}$ working at 100 ^{o}C in friction contact with SS304 steel would exhibit about double mass loss (about half lifetime) than while working at RT. The outcomes of this PhD research could be useful for selecting CuZr SMAs for engineering components and points out the need of using microalloying elements that can also extent the operating temperature (shifting A_s to higher temperatures) to prevent early failure associated to excessive mass loss.

4.7. Conclusions

In this chapter, the effect of temperature on the tribological performance of CuZr-based SMA has been studied by investigating wear behaviour and mass loss of $Cu_{50}Zr_{50}$, $Cu_{49.5}Zr_{50}Co_{0.5}$ and $Cu_{49}Zr_{50}Co_1$ at RT and 100 ^{o}C. The combined effect of oxidation and martensitic transformation determined the overall mass loss achieved at 5, 10 and 15 N at RT and 100 ^{o}C and the following conclusions can be made:

- The Mass loss at RT is the lowest for $Co_{0.5}$ due to the effect of the microalloying element in promoting martensitic transformation (i.e., the material hardens).
- The mass loss at 100^{o}C is higher than at RT and similar for the three compositions (Co_0, $Co_{0.5}$ and Co_1) thus indicating that the martensitic transformation is not as

effective as at RT. This could be attributed to the fact that the contact temperature is close to the start of the austenite peak and thus stress-induced martensite partly reverts into austenite via an isothermal process (see **Fig. 4.7**). In addition, the material is more prone to oxidation and therefore it develops a thick oxide layer that tends to detach easily (**Fig. 4.9**) thus resulting in an increase of mass loss.

- Addition of a microalloying element, such as Co, which promotes the martensitic transformation, is a good strategy to improve the wear resistance at room temperature of CuZr-based alloys. However, it is not useful at 100^{o}C, and this could be partly improved by microalloying using elements that can shift the austenitic transformation peak As to higher temperatures to increase the operating temperature range (i.e., A_s-RT) to prevent the stress-induced martensite revert into soft (i.e., low wear resistant) austenite.
- This chapter highlights through a critical analysis the importance of wise selection of microalloying elements in shape memory alloys since addition of an element that can effectively enhance the wear resistance at RT may decrease the operating temperature range to such an extent that for relatively low temperatures of 100^{o}C, microalloying would have practically no benefit in enhancing the durability.

Chapter 5 – The role of microalloying and co-microalloying with Ni and Co in $Cu_{50}Zr_{50}$ at.% SMA

Overview

After investigating the role of Co in $Cu_{50}Zr_{50}$ SMA, in this section, the effect of microalloying with Ni is also investigated along with Co. Ni is chosen due to its wear resistance characteristics and its promising ability in decreasing SFE in CuZr alloy systems (see Fig. 4.1). Similarly to Chapter 4, the introduction of microalloying element comes in place of Cu and opens the possibility to achieve cost-effective CuZr alloys to replace costly NiTi. The addition of microalloying element of Ni and Co is minimal in this study in order to ensure microalloying element entering in solid solution, therefore, due to small amount of microalloying element, the added cost of replacing Cu with Co and/or Ni is negligible.

Methods of investigating the mechanical performance includes nanoindentation experiments and analysis of recovery ratio post heat treatment in order to observe the alloys' ability to recover its pre-deformed shape. $Cu_{50}Zr_{50}$, $Cu_{49}Zr_{50}Ni1$, $Cu_{49}Zr_{50}Co_{0.5}Ni_{0.5}$ and $Cu_{49}Zr_{50}Co_1$ samples of 4mm diameter size were obtained by suction casting.

5.1. Overview of recovery ratio

The shape memory behaviour of the different samples was assessed by means of recovery ratio (RR: ability of a material to recover permanent strains), measuring indent change of depth upon annealing at 400 ^oC for 5 min. Prior to annealing the sample were indented to a load of 8 mN, at a loading rate of 400 mN s^{-1}. The residual indent depth after indentation, and prior to annealing ($h_{ind\text{-}b}$), was measured by acquiring a 3D topographic scan (5 by 5 mm) of the sample surface, using the same Berkovich tip, at a load of 1 mN and a resolution step of 30 nm. Annealing of the samples was also conducted within the indenter chamber under vacuum (10^{-7} mbar, $[O_2]$ = 2.5 0.10^{-3} ppm), without moving the relative position and orientation of the sample to the indenter. The sample was heated to 400^oC using the hot stage of the high temperature indenter, controlling the temperature of the sample with a thermocouple mounted on its surface.

The residual indent depth after annealing ($h_{ind\text{-}a}$) was measured following the same scanning procedure, at RT. The recovery ratio (RR) was defined as:

$$RR(\%) = \frac{\boldsymbol{h}ind(b) - \boldsymbol{h}ind(a)}{\boldsymbol{h}ind(b)}\ x\ 100 \qquad (5.1)$$

Where $\mathbf{h}_{ind(b)}$ and $\mathbf{h}_{ind(a)}$ are the depth of the indent marks before and after heating, respectively.

5.2. Nanoindentation tests and recovery ratio

The mechanical behaviour of the studied alloys (i.e., $Cu_{50}Zr_{50}$, $Cu_{49}Zr_{50}Ni1$, $Cu_{49}Zr_{50}Co_{0.5}Ni_{0.5}$ and $Cu_{49}Zr_{50}Co_1$ at. %) were investigated by means of 5-10 nanoindentation, performed on different austenite dendrites [187-189]. The size of the indents was about 500 nm wide, much smaller than the dendrite size, as shown in the representative SEM micrograph of an indented austenite dendrite presented in **Fig. 5.1**.

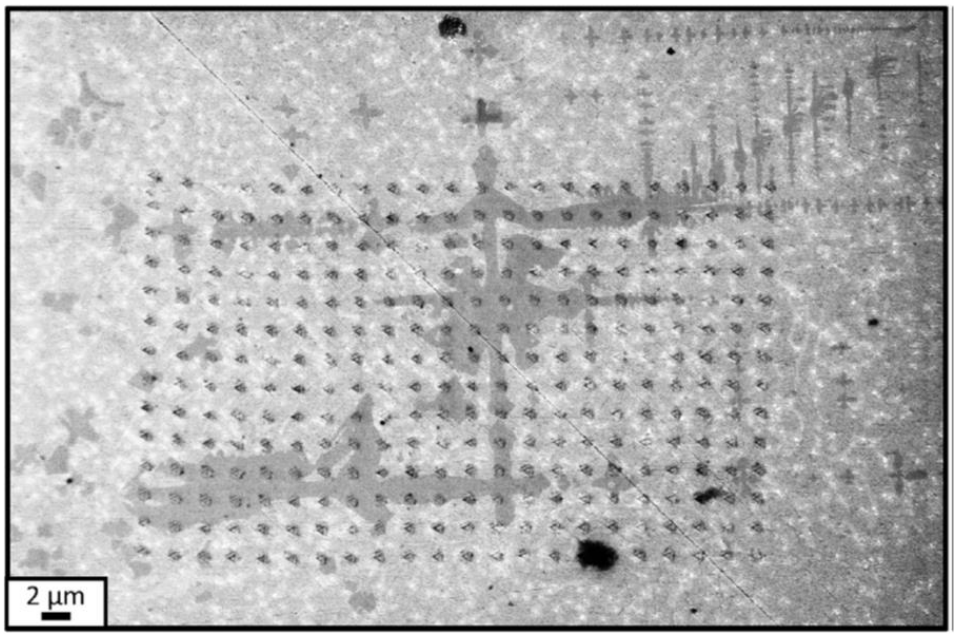

Fig. 5. 1. SEM micrograph of a dendrite indented with a grid of indents (14 x 22 - spacing of 2µm) - $Cu_{49}Zr_{50}Co_{0.5}Ni_{0.5}$ alloy.

In order to prevent any influence of the grain boundaries and surrounding amorphous phase, indents fully contained within the dendrite and at least 500 nm away from the nearest edge of the dendrite (maximum depth of 50 nm, at 1 mN) were considered valid. **Fig. 5.2a, c, e and g** show the load-displacement (P-h) curves obtained from the indentation of the austenite dendrites of $Cu_{50}Zr_{50}$, $Cu_{49}Zr_{50}Ni1$, $Cu_{49}Zr_{50}Co_{0.5}Ni_{0.5}$ and

$Cu_{49}Zr_{50}Co_1$ at. %, respectively. These results are the most representative from the statistical study of multiple nanoindentations performed on each sample. The curves show the presence of displacement bursts, called pop-ins, starting at a very early stage of the loading segment, as highlighted by arrows on the (P-h) curve. In addition, the slopes of the (P/h)-h plots for $Cu_{50}Zr_{50}$ (**Fig. 5.2b**), $Cu_{49}Zr_{50}Ni1$ (**Fig. 5.2d**), $Cu_{49}Zr_{50}Co_{0.5}Ni_{0.5}$ (**Fig. 5.2f**) and $Cu_{49}Zr_{50}Co_1$ (**Fig. 5.2h**) at. % were calculated from **Fig. 5.2a, c, e, and g**, respectively.

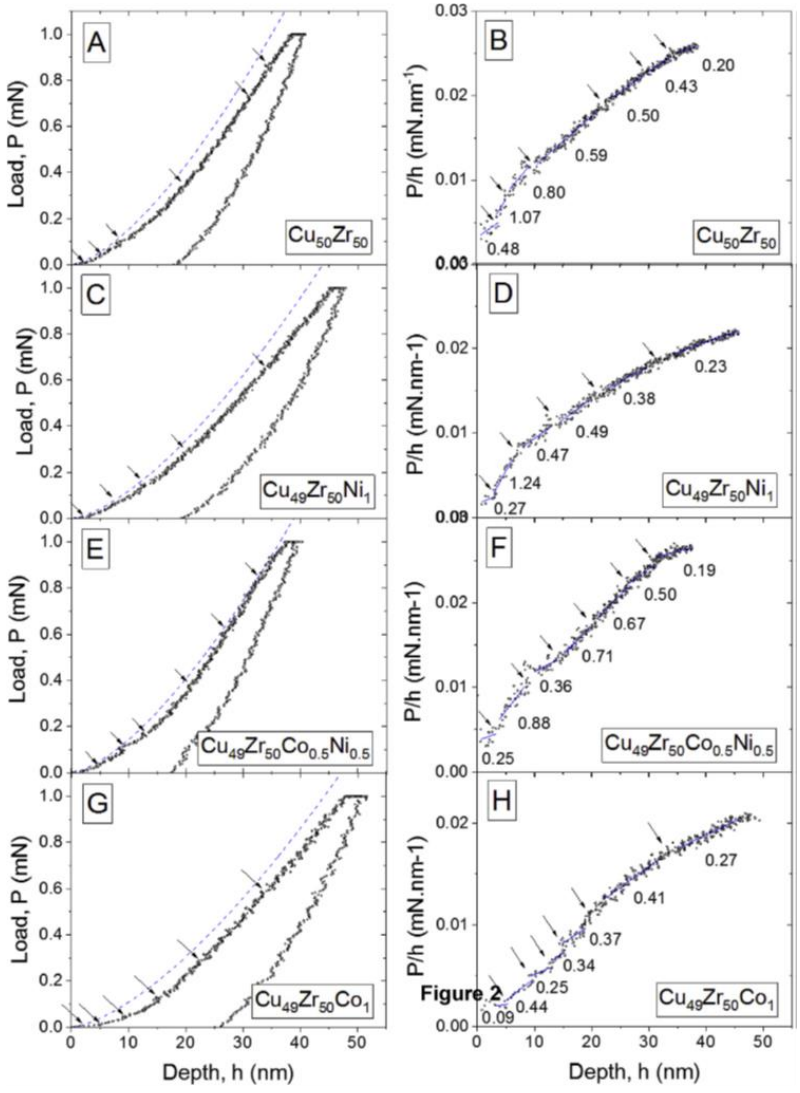

Figure 2

Fig. 5. 2. Load-displacement (P-h) curves obtained from indentation in the austenitic phase of CuZr alloys with varying composition (A, C, E and G) and the associated (P/h)-h curves (B, D, F and H). For each composition, an Hertzian solution was fitted to the (P-h) curves (dashed lined).

Although the slopes are different for each composition, they all follow a similar trend; at an early stage, prior to the first pop-in, the slope is low and rapidly steepens as P/h increases. For $Cu_{50}Zr_{50}$, the slopes of the (P/h)-h curve increase from 0.48 to 1.07 $mNnm^{-2}$, past the second pop-in. The largest slope increase, after the second pop-in, was observed for the alloy containing 1 at. % Ni, with a rise from about 0.27 to 1.24 $mNnm^{-2}$. On the other hand, the alloy containing 1 at. % Co exhibits an increase in slope from 0.09 to 0.44 $mNnm^{-2}$, with a second slope lower than that of the $Cu_{50}Zr_{50}$ parent alloy. For the co-microalloying composition of $Cu_{49}Zr_{50}Co_{0.5}Ni_{0.5}$, the slope

increases from 0.25 to 0.88 $mNnm^{-2}$, with the second slope ranging between that of $Cu_{49}Zr_{50}Ni_1$ and $Cu_{49}Zr_{50}Co_1$. The change in slope, from the first to second pop-in, arises from the change in predominant deformation mode, namely, from dislocation slip to martensitic transformation [188], in agreement with other studies on shape memory materials such as Fe-28Mn-6Si-5Cr alloy [188]. Since martensite is harder than austenite, higher (P/h)-h slope relates to more effective martensitic transformation [190]. In other words, alloys undergoing martensitic transformation are more prone to work-hardening. The improvement in the stress-induced martensitic transformation of alloys, where 1 at. % of Cu in B2 CuZr structure have been replaced by either Ni (microalloying) or Ni and Co (co-microalloying), can be attributed to the reduction in the Stacking Fault Energy (SFE) [151]. However, the substitution of Cu by solely Co appears to decrease the propensity of the transformation since (P/h)-h slope is lower than for $Cu_{50}Zr_{50}$ at. % alloy.

The first and second pop-in events provide relevant information regarding the deformation mode occurring at the early stage of plasticity. Hence, the relationship between the critical load, P_c, and the corresponding excursion depth, Δh, at the first pop-in (P_{c1} - Δh_1) and second pop-in (P_{c2} - Δh_2), was studied for all the different compositions (**Fig. 5.3a and Fig. 5.3b**, respectively).

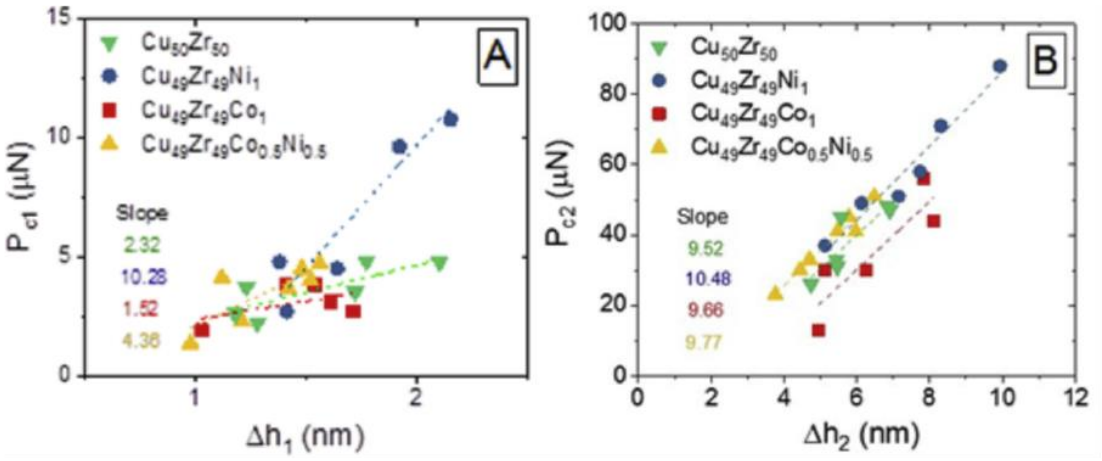

Fig. 5. 3. Relationship between the critical load P_c and the excursion depth Δh for the first and second pop-in (A and B, respectively).

The first pop-in event can be associated to the transition in deformation mode from purely elastic to elastic-plastic (shift from the Hertzian solution, presented in **Fig. 5.2**), with plasticity occurring through dislocation slip. At higher load, the second pop-in highlight further change in the deformation mode, namely from dislocation slip to martensitic transformation. At the first pop-in (**Fig. 5.3a**), the maximum excursion depth for all alloy compositions is smaller than 3 mm, similar to that of Fe-28Mn-6Si-5Cr alloy [188]. The slope of the parent $Cu_{50}Zr_{50}$ alloy was measured about 2.32 and increased to about 10.28 for $Cu_{49}Zr_{50}Ni_1$ alloy due to the substitution of 1% at of Cu by Ni microalloying element. On the other hand, the use of Co as microalloying element was found to decrease the slope to about 1.52. For the co-microalloying $Cu_{49}Zr_{50}Ni_{0.5}Co_{0.5}$ alloy, the slope was measured about 4.36, ranging between that of $Cu_{49}Zr_{50}Co_1$ and Cu49Zr50Ni1 (**Fig. 5.3a**). Differences in slope among the different alloy compositions (**Fig. 5.3a**) can be attributed to their different stacking fault energy (SFE). Higher SFE involves smaller dislocation core size and, therefore, dislocations can come closer to each other, enabling a larger accumulated number of dislocations in each slip plane [191]. Lower SFE results in larger dislocation core size, making dislocations less mobile and, therefore, a limited number of dislocations can be accumulated on a slip plane. The excursion depth at the first pop-in event, can be linked to the magnitude of the Burgers vector, /b/, through the following equation [188]:

$$\Delta h = n \mid b \mid \qquad (5.2)$$

where n is the number of geometrically necessary dislocations, linearly proportional to the displacement of the pop-in event. According to **equation (5.2)** and **Fig. 5.3a**, compositions with higher $dP_{c1}/d\Delta h_1$ values than the parent alloy, i.e. $Cu_{49}Zr_{50}Ni_1$ and $Cu_{49}Zr_{50}Co_{0.5}Ni_{0.5}$, are those for which microalloying has decreased the SFE and, therefore, lowered the number of dislocations in a slip plane. On the other hand, the incorporation of 1 at % Co micro-alloying elements in $Cu_{49}Zr_{50}Co_1$ appears to have increased the SFE, leading to a greater number of dislocations in slip plane. Differences in slope among the four compositions (**Fig. 5.3a**) can be indirectly attributed to their different SFE.

Fig. 5.3b shows the relationship between the critical load, P_{c2}, and the excursion depth, Δh_2, for the second pop-in. These pop-in events occur when the stress-induced martensite reaches a critical size, larger than the contact area between the indenter tip and sample [192].

The length of the excursion depth of the second pop-ins (Δh_2) is proportional to the thickness increase of twinned martensite plate (Δth), as described in the following equation [192]:

$$\Delta h_2 = 0.12\ \Delta th \qquad (5.3)$$

According to **equation (5.3)** and **Fig. 5.3b**, for the same thickness increase of twinned martensite, the critical load P_{c2} for the alloys containing 1 at. % Ni and 0.5Co0.5Ni at. % is higher and therefore the slope $dP_{c2}/d\Delta h_2$ is higher than for the parent alloy and the alloy containing 1 at. % Co. The slope increases from about 9.52 for the parent $Cu_{50}Zr_{50}$ at. % alloy to about 10.48 for $Cu_{49}Zr_{50}Ni_1$ at. % while that of $Cu_{49}Zr_{50}Co_1$ at. % decreased to 9.66, indicating that the stress-induced martensitic transformation is best promoted with 1 at. % of Ni micro-alloying element.

5.3. Plasticity index and residual indent depth

In order to assess the influence of microalloying elements on the relative plastic/elastic deformation behaviour of B2 austenite, the plastic index, ζ, was measured for all compositions [193] as follow:

$$\zeta = \frac{A_1}{A_1 + A_2} \qquad (5.4)$$

where A_1 and A_2 are the plastic deformation area and the elastic recovery area under the unloading segment of the P-h curves, respectively. The plastic index of a material can vary from $\zeta = 0$, for a purely elastic behaviour, to $\zeta = 1$ for purely plastic. Additionally, the mechanical properties of a crystalline phase can be correlated to the plastic index through the following equation [194]:

$$\zeta = \frac{E}{H}\left(\frac{\sigma}{R}\right)^{1/2} \qquad (5.5)$$

where E is the elastic modulus, H the hardness, σ the root-mean square surface roughness and R the average radius of curvature of asperities. Because all the different samples were polished and indented following the exact same procedure, the plastic index can directly be related to the mechanical properties of the crystalline phase. **Fig. 5.4** shows the plastic index for the different alloy compositions. A reduction of plasticity was observed for $Cu_{49}Zr_{50}Ni_1$ as compared to $Cu_{50}Zr_{50}$, with an average measured plastic index of 0.49 and 0.52, respectively. The incorporation of 1 at. % Ni favoured the martensitic transformation upon nanoindentation loading, promoting work hardening. On the other hand, addition of 1 at. % Co led to an increase in the plastic index, to a value of 0.54, result of a less effective martensitic transformation. For the alloy containing Co and Ni, the plastic index is approximately intermediate between that of the alloys containing only Co or Ni. Although, there is no information in the current state of literature about the plastic index of shape memory alloys, including the CuZr systems, the results seem reasonable considering that they are similar to those measured in other metallic alloys [195-197].

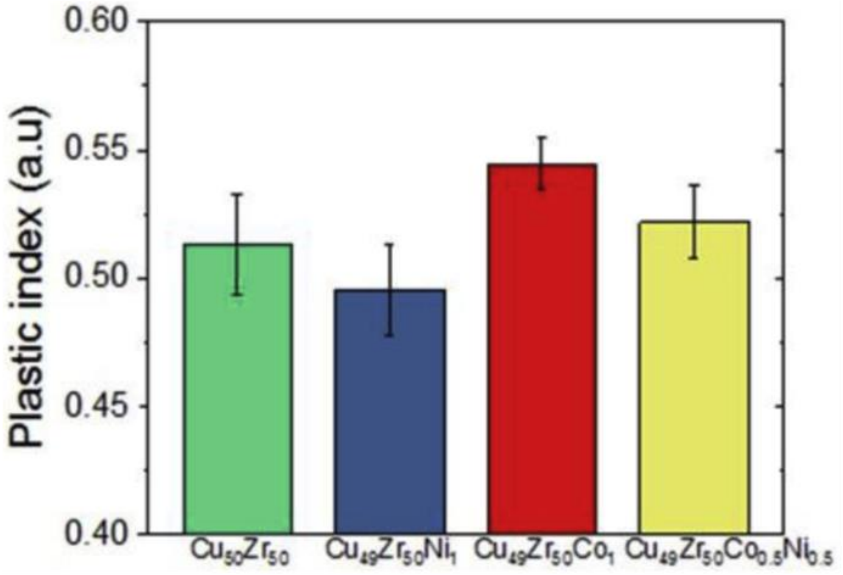

Fig. 5. 4. Plasticity index of the alloys compositions extracted from indentation at 1mN load, in ambient conditions.

The shape memory behaviour was characterized by calculating (see **equation (5.1)** in Methods) the recovery ratio (RR) obtained from measuring the value of the deepest point of residual indents (indent depth) before ($h_{ind\text{-}b}$) and after annealing ($h_{ind\text{-}a}$) at 400^{o}C for 5 min. No significant change in surface roughness or oxidation was detected after annealing. **Fig. 5.5** shows the 3D image of residual indents, made at a load of 8 mN, before and after annealing at 400^{o}C for 5 min in vacuum for $Cu_{50}Zr_{50}$ and $Cu_{49}Zr_{50}Co_{1}$ at. % alloys. These results are summarised in **Fig. 5.5e**, where the residual indent depth before and after annealing along with the recovery ratio (%) for the four compositions are presented. At the same 8mN indent load, the initial residual indent depth ranges from about 60 nm for $Cu_{50}Zr_{50}$ to about 116 for $Cu_{50}Zr_{50}Co_{1}$ at. %, respectively, but decreases after annealing. From both values and **equation (5.1)**, a recovery ratio of 15.6% has been obtained for the $Cu_{50}Zr_{50}$ parent alloy, while a maximum value of 19.5% is obtained for the alloy with 1 at. % Ni. These results confirm that for the Ni-containing SMA, a larger volume fraction of martensite induced upon loading has transformed into martensite.

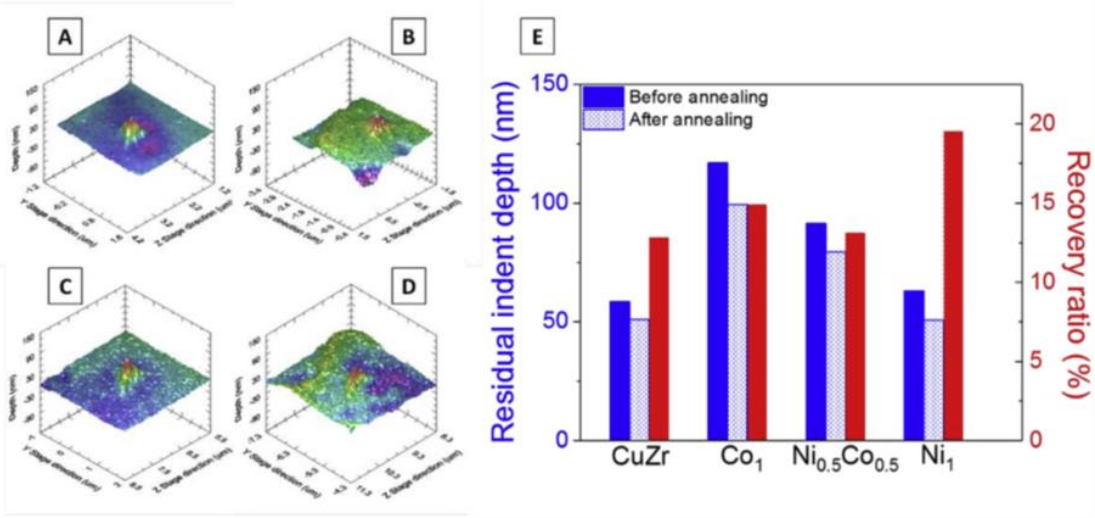

Fig. 5. 5. 3D image of residual indents, made at 8 mN, for $Cu_{50}Zr_{50}$ and $Cu_{49}Zr_{50}Co_1$ before (A and C, respectively) and after annealing (B and D, respectively) at 400 ^oC for 5 min in vacuum. e) Graph plotting the residual indent depth and recovery ratio (%) for the four compositions.

For NiTi, which is known to exhibit the best shape memory performance among all alloy systems, the recovery ratio obtained from Vickers tests was measured about 30% independently of the load applied [198]. As far as the authors are concerned, no information for the shape memory CuZr system has been published. We have shown that despite the relatively poor performance of $Cu_{50}Zr_{50}$ alloy with a recovery ratio of 15.6%, it can be increased to 19.5% with only 1 at. % Ni addition. These results are promising and open-up the possibility to develop more cost-effective commercial CuZr alloys than traditional costly NiTi alloys.

In order to assess the reliability of the results obtained at the nanoscale and, therefore, confirm whether they are representative of the sample bulk behaviour, the thermal behaviour of the as-cast samples and the microstructural changes upon compression for the different alloy compositions were investigated. The thermal behaviour of the $Cu_{50}Zr_{50}$, $Cu_{49}Zr_{50}Ni1$, $Cu_{49}Zr_{50}Co_{0.5}Ni_{0.5}$ and $Cu_{49}Zr_{50}Co_1$ at. % samples was studied by running DSC scans heating up to 400 ^oC and cooling down (**Fig. 5.6**).

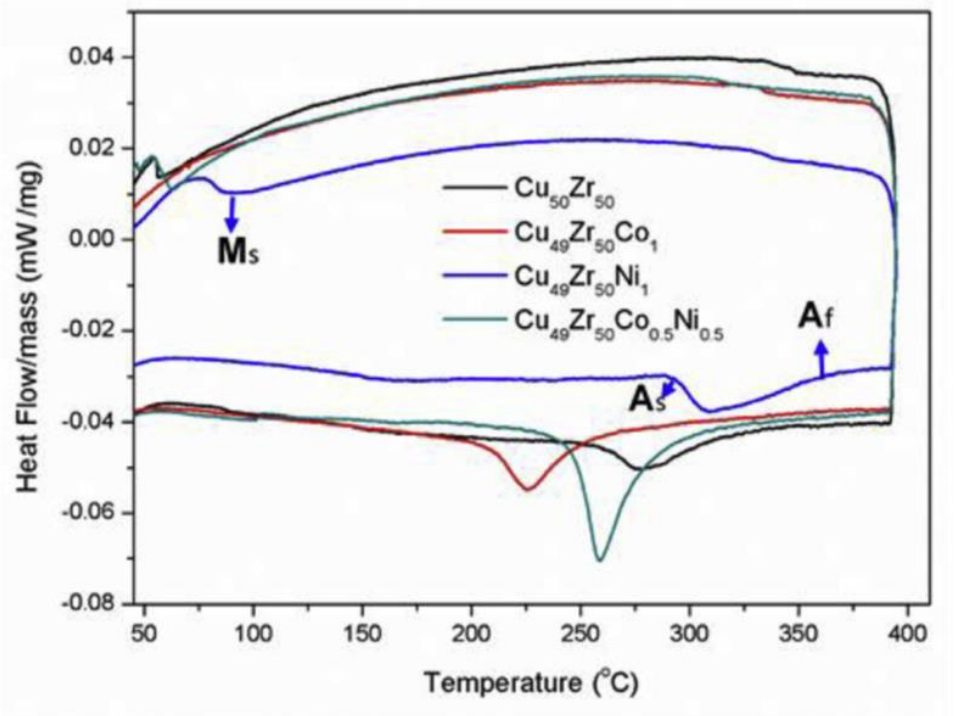

Fig. 5. 6. DSC scans at 20 _C/min for the CuZr alloys of different composition - heating and cooling scans.

The temperatures at which martensite starts and finishes to transform into austenite (A_s and A_f, respectively) upon heating, as well as that at which austenite transforms into martensite (M_s) upon cooling are listed in **Table 5.1**. While for $Cu_{50}Zr_{50}$ alloy, A_s, A_f and M_s are 258.3 ^oC, 327.7 ^oC, and 58.3 ^oC, respectively, the addition of 1 at. % of Ni shifts all transformation temperatures to higher values, especially A_f, which increases to 363.8^oC. These temperatures are far lower than 400 ^oC, at which the recovery ratio was calculated (**Fig. 5.5**), ensuring that the stress-induced martensite can fully transform back into austenite. The increase in A_f was shown to be indicative of the promotion of martensitic transformation, as observed by Zhou et al. [152]. On the other hand, the addition to 1 at. % Co shifts the transformation temperatures to lower values, suggesting a decline in the martensitic transformation [199]. For the composition of $Cu_{49}Zr_{50}$-$Co_{0.5}Ni_{0.5}$ at %, A_s, A_f and M_s were measured about 247.2 ^oC, 283.3 ^oC and 62.5 ^oC, respectively, approximately intermediate to those of $Cu_{49}Zr_{50}Co_1$ and $Cu_{49}Zr_{50}Ni_1$ alloys and similar to $Cu_{50}Zr_{50}$.

Although M_s is usually used to assess the efficiency of the martensitic transformation of an alloy, A_s and A_f do follow a similar trend and, therefore, can be equally used for that purpose [3]. Microstructural changes upon compression of the samples (19.2 KN for 5 min) were investigated by XRD (**Fig. 5.7**). The XRD patterns of as-cast (**Fig. 5.7a**) and compressed (**Fig. 5.7b**) $Cu_{50}Zr_{50}$, $Cu_{49}Zr_{50}Co_1$, $Cu_{49}Zr_{50}Ni_1$ and $Cu_{49}Zr_{50}Co_{0.5}Ni_{0.5}$ at. % samples show the presence of peaks associated to the same crystalline phases, with varying relative intensity, depending on their composition. The phases detected consist of orthorhombic $Cu_{10}Zr_7$ (a = 0.9347 nm, b = 0.9347 nm, c = 1.2675 nm), orthorhombic Cu_8Zr_3 (a = 0.78686 nm, b = 0.81467 nm, c = 0.9977 nm), austenite B2 CuZr (a = 3.2562 nm, b = 3.2562 nm, c = 3.2562 nm) and monoclinic martensite B19' CuZr (a = 0.3237 nm, b = 0.4138 nm, c = 0.5449 nm). The intensity of the peak associated with austenite, at about 39º, decreases while the intensity of the peaks associated with martensite, especially the one at about 27.5º, increase after compression. Therefore, the results suggest that austenite transforms into martensite upon compression. While a reduction in the intensity of the XRD peak associated with martensite, at about 28º, was observed for the alloy containing 1 at. % Co, a significant increase was measured for the alloy containing 1 at. % Ni, in comparison to the $Cu_{50}Zr_{50}$ parent alloy. Regarding the alloy containing 0.5 at. % Co and 0.5 at. % Ni, the intensity was found to be comparable to the parent alloy. It was therefore concluded that Ni promotes martensitic transformation of the parent B2 CuZr phase, while Co obstructs the transformation, at least when incorporated to 1 at. %. In the case of the alloy containing 0.5 at. % Co and 0.5 at. % Ni, the two microalloying elements seemed to have compensating effect on the martensitic transformation. The efficiency of the stress-induced martensitic process seems to be composition dependent, which is in good agreement with previous observations [200].

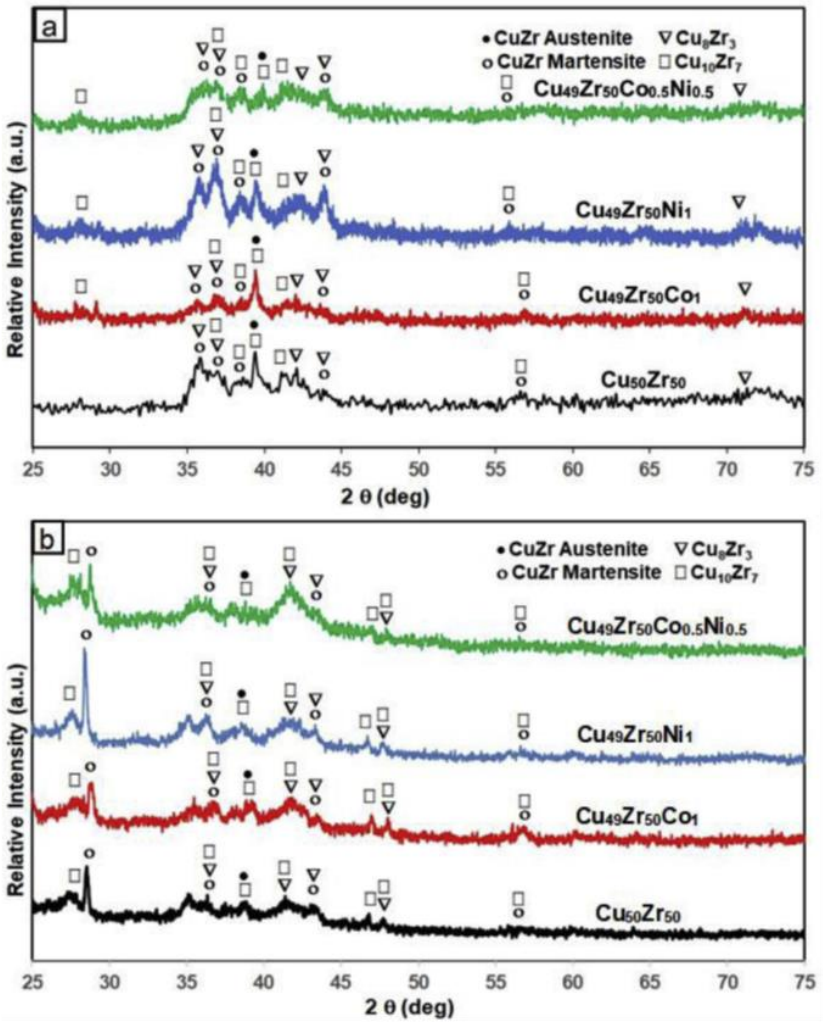

Fig. 5. 7. XRD diagrams of the different alloy compositions, a) before and b) after compression.

It was previously reported that 0.5 at. % Co addition promotes the martensitic transformation of B2-CuZr by decreasing the stacking fault energy of the (011)[100] slip system from 381 mJm^{-2} to 75 mJm^{-2} [151]. Further addition of Co atoms to about 12.5 and 50 at. % decreased the stacking fault energy to 281 and 75 $mJ\text{-}m^{-2}$, respectively [152]. However, for an intermediate concentration in Co of 1 at. %, the stacking fault energy seems to increase as can be deduced from the decrease in the effectiveness for the stress-induced martensitic transformation as proven from the XRD and DSC results. On the other hand, addition of 1 at. % Ni appears to promote the martensitic transformation of the parent B2-CuZr alloy, which is consistent with the increase of M_s (**Fig. 5.6**), as compared to $Cu_{50}Zr_{50}$. Smaller Ni additions (i.e., 0.5 at. %) was also reported to promote the martensitic transformation due to the decrease in the stacking fault energy.

However, the value of the stacking fault energy remains higher than for 0.5 at. % of Co, which implies that the martensitic transformation should be less effective [151, 152].

Table 5. 1. Transformation temperatures for all the CuZr alloys obtained from DSC scans.

Composition (at.%)	A_s (ºC)	A_f (ºC)	M_s (ºC)
$Cu_{50}Zr_{50}$	258.3	327.7	58.3
$Cu_{49}Zr_{50}Co_1$	211.1	252.8	<40
$Cu_{49}Zr_{50}Ni1$	291.7	363.8	88.8
$Cu_{49}Zr_{50}Co_{0.5}Ni_{0.5}$	247.2	283.3	62.5

5.4. Conclusions

The effect of microalloying with Co or Ni individually or combined (i.e., co-microalloying) on the twinning propensity of $Cu_{50}Zr_{50}$ at. % was investigated at the nano- and macroscale level. This enabled to assess the strategy of improving the shape memory performance of CuZr alloys through microalloying and, therefore, to develop cost-effective CuZr SMA actuators that could replace costly Ni-Ti SMAs. Partial replacement of Cu by 1 at. % Ni from the parent $Cu_{50}Zr_{50}$ alloy, enabled to improve the recovery ratio after annealing at 400 ºC for 5 min, from 15.6% to 19.5%. Better twinning propensity of B2-austenite was observed, favouring the formation of martensite.

Co-microalloying using equal concentrations of Co and Ni did not have a significant effect on the mechanical and thermal behaviour of $Cu_{50}Zr_{50}$ alloy due to the effect of Co in suppressing the formation of martensite. This works shows that proper selection of microalloying element/s, in optimum concentration, can promote twinning and, therefore, represent a new strategy to enhance the stress sensitivity in CuZr SMA sensors. This research opens up the possibility to explore novel compositions and concentrations to develop cost-effective CuZr SMAs that can achieve, in the future, similar performance to that of NiTi SMAs.

Chapter 6 – Modelling and experimental approach in selecting microalloying elements in $Cu_{50}Zr_{50}$ at.% SMA

Overview

It is understood from chapters 4 and 5 that minor addition of certain elements (Co in chapter 4) and (Ni in chapter 5) in place of Cu in CuZr SMAs can enhance work hardening. Therefore, it is important to implement a technique that can help highlight and predict potential performance of chosen elements that can lower SFE of B2 CuZr and therefore enhance wear performance. This screening method is introduced through density-based function calculations. This screening method (CASTEP electronic structure and materials properties package) allows for investigation of the nature and concentration of microalloying element effect on CuZr SMA, these findings have been analysed and compared to practical **wear tests** to investigate the **validity of results**.

In **Fig. 4.1**, Fe, Co, and Ni were the three elements that lowered SFE of B2 CuZr the most, giving these three elements the highest potential in accelerated martensitic transformation and therefore enhanced wear resistance when doped as microalloying elements in CuZr SMAs. Common factor between the three elements is their position in the **periodic table suggesting that atomic number may be a factor in deciding the most effective doping element**. Therefore, in this chapter, **Mn** (atomic number 25) is screened with CASTEP then investigated in wear tests as a microalloying element that could be added to the list of potential microalloying elements to enhance CuZr SMAs. Results obtained from microalloying with Mn is analysed with parent alloy as well as microalloying with Fe as it has not been investigated in this thesis yet. $Cu_{50}Zr_{50}$, $Cu_{49.5}Zr_{50}Fe_{0.5}$, $Cu_{49}Zr_{50}Fe_{1}$, $Cu_{49.5}Zr_{50}Mn_{0.5}$, $Cu_{49}Zr_{50}Mn_{1}$ and $Cu_{49}Zr_{50}Fe_{0.5}Mn_{0.5}$ alloys of 2mm diameter size were obtained by suction casting.

6.1. Modelling for Stacking Fault Energy predictions

The lowest energy slip plane of CuZr in the B2 structure is in the [011] plane sliding in the {100} direction (and given the system is cubic, [101]{010} and [110]{001} are also equivalent slip systems). A schematic of this is shown in **Fig. 6.1**. A supercell is constructed containing 40 monolayers of CuZr normal to [011] and half of the atoms

slipped in steps of 1/10 of the lattice parameter, forming 2 slip planes (forced by the periodicity of the system). This supercell was determined by converging total energies as a function of supercell size until the stacking fault energy was converged to better than 0.002 J/m^2. The total energy of the system is calculated as the plane slides a distance of a whole unit cell. We have performed calculations of the system with “defect” atoms on the slip plane replacing a Cu atom with a range of various other species, to search for lower SFEs and also at two concentrations.

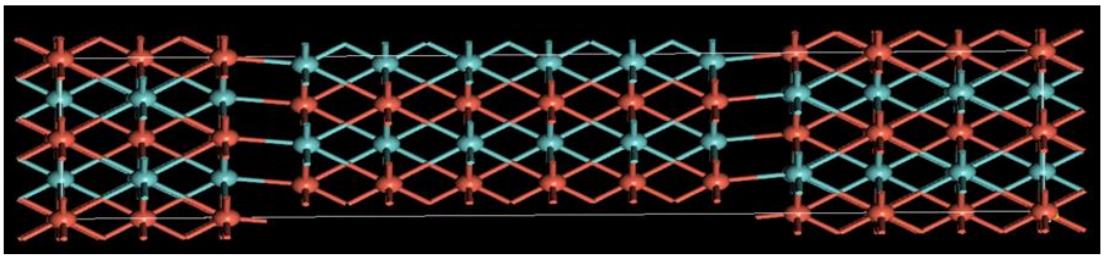

Fig. 6. 1. Model of B2 CuZr showing the position of the atomic structure, Cu (brown) and Zr (blue) in the [011] plane and {100} direction.

Fig. 6.2 (a) shows the slip plane energies for the [001], [011] and [111] planes in various orthogonal slip directions, confirming that [011]{001} is the lowest energy, while in (b) the relative total energies are shown for the parent alloy (i.e., base) containing no substitutional atoms and also for Fe and Mn substitutions as well as the co-microalloy with a mixed substitution of Fe/Mn. All Fe and Mn alloys cause a significant decrease of the SFE, however, we do not observe the huge energy reductions shown in [151] including a 3-fold decrease in stacking fault energy with Fe substitution. The $Fe_{0.5}$ plot does not lie between Fe_1 and Fe_0 because partial replacement of Cu in B2 CuZr by 0.5 at. % Fe decreases the stacking fault energy (SFE) of Fe_0 (base) the largest (i.e., minimum energy (J/m^2)). However, partial replacement by 1 at. % Fe (Fe_1) is not so effective decreasing the SFE of the base Fe_0 alloy, for this reason their values are relatively close to each other. The addition of Fe as microalloying element replacing Cu in B2 CuZr was reported by Wu et al. [151] to reduce the SFE. However, they solely studied the effect for a concentration in microalloying element in solid solution of 0.5 at. %. In this study we have expanded this by investigating the effect of microalloying with

1 at. % Fe and also the effect of the element Mn on the tribological performance of B2 CuZr using pin-on-disc experiments.

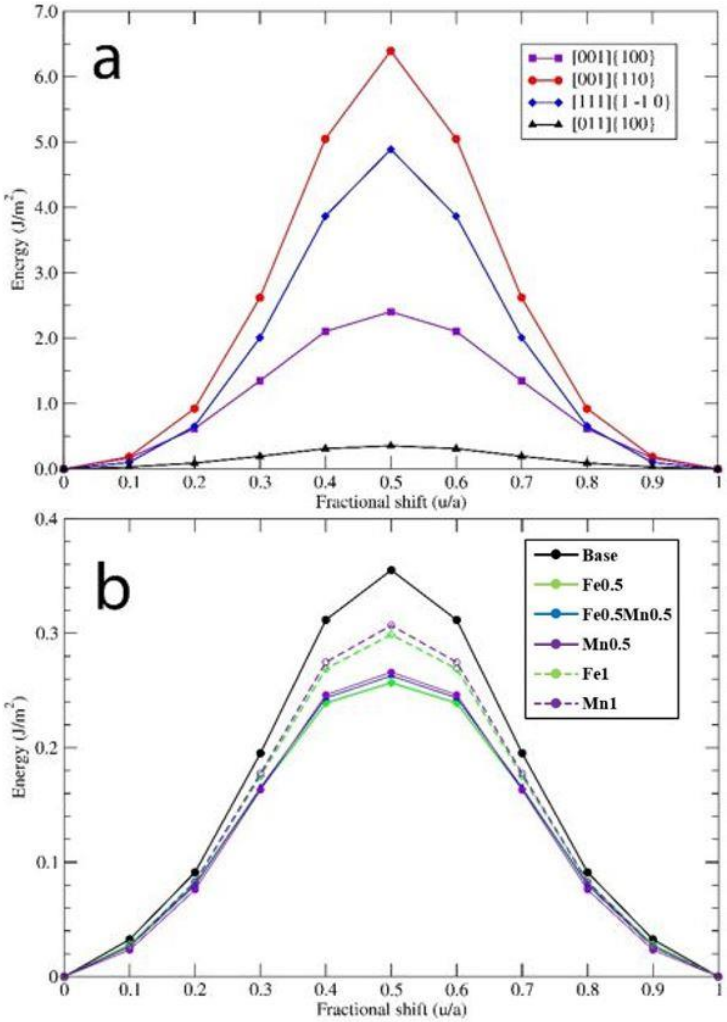

Fig. 6. 2. (a) Various stacking fault energies of slip planes in the B2 phase of CuZr. (b) Stacking fault energy on the lowest energy [011]{100} slip system of the B2 CuZr phase with half Cu on the slip plane substituted by Fe and Mn (solid line) and similarly for a doubled concentration (dashed).

6.2. Structural characterisation of the as-cast alloys

The experimental results of **Fig. 6.3** show the backscattered SEM images of as-cast $Cu_{50}Zr_{50}$ (**Fig. 6.3a**), $Cu_{49}Zr_{50}Fe_1$ (**Fig. 6.3c**) and $Cu_{49}Zr_{50}Mn_1$ (**Fig. 6.3e**) alloys and the corresponding EDX scans from the dendrites (see arrows) (**Fig. 6.3b, 3d and 3f**).

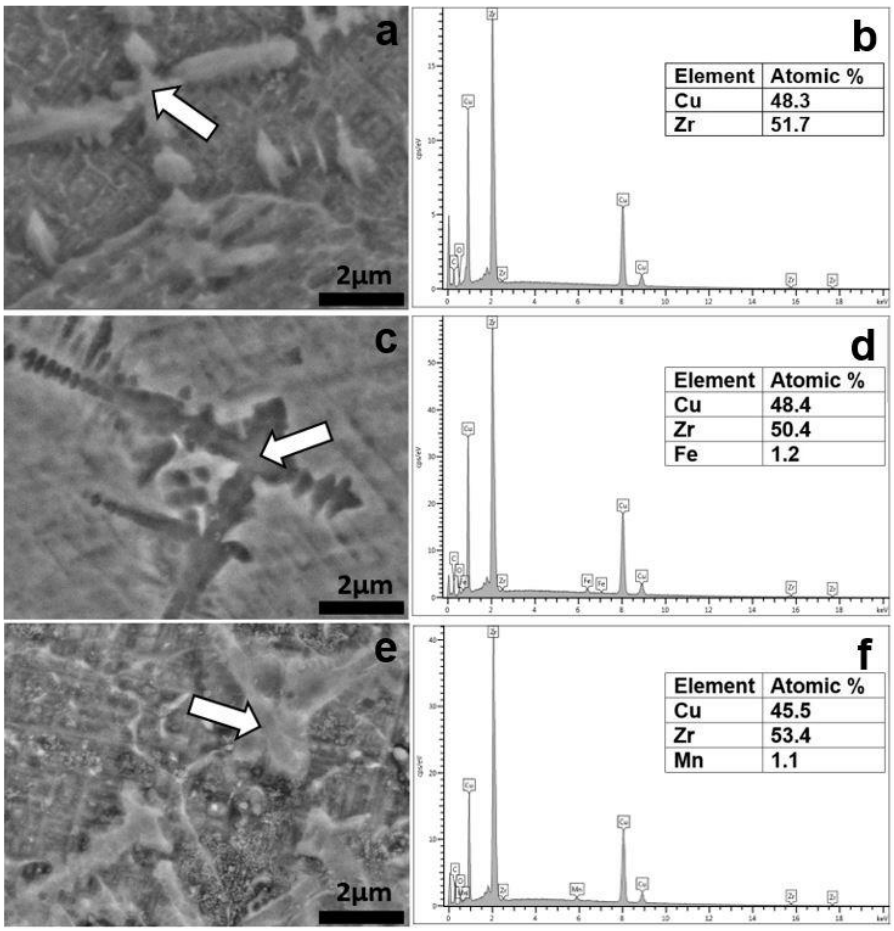

Fig. 6. 3. Backscattered SEM images of as-cast (a) $Cu_{50}Zr_{50}$, (c) $Cu_{49}Zr_{50}Fe_1$ (e) $Cu_{49}Zr_{50}Mn_1$ alloys and corresponding EDX scans of the dendrites indicated with an arrow (b), (d) and (f), respectively.

The microstructural differences among the three compositions are relatively small, as could be expected considering their similar composition. For all of them, the microstructure basically consists of dendrites from 2 µm to 10 µm in length, embedded in a fine crystalline matrix. To understand the nature of the as-cast samples, compositional EDX analysis and crystallographic analysis by XRD have been performed. Considering that for a microalloying element to have an effect on the twinning propensity of austenite it should be present in solid solution inside the crystalline lattice [151], their presence has been investigated by SEM-EDX. This analysis has been carried out from the dendrites located at approximately the centre of the samples, where the cooling rate is the lowest and thus the elements are more prone to segregation (i.e., if there is no segregation in the centre, then it will not occur close to the border where the cooling rate is faster). To get an average composition value of the dendrites, EDX analysis was carried out on more

than 3 dendrites per composition and the ones shown in **Fig. 6.3** are the most representative ones. For $Cu_{50}Zr_{50}$ (**Fig. 6.3a**), EDX analysis shown in **Fig. 6.3b** indicates that the composition is 48.3 at.% Cu and 51.7 at. % Zr. For $Cu_{49}Zr_{50}Fe_1$ (**Fig. 6.3c**) the composition is 48.39 at.% Cu, 50.42 at.% Zr and 1.19 at.% Fe (**Fig. 6.3d**). Similar results have been obtained for the $Cu_{49}Zr_{50}Mn_1$ at. % alloy (**Fig. 6.3e**) for which the composition of the dendrites is 45.47 at.% Cu, 53.43 at.% Zr and 1.10 at.% Mn (**Fig. 6.3f**). All results are listed in **Table 6.1**. The results show that concentration of microalloying element in the crystalline phase is close to the nominal composition, 1 at. % Fe and 1 at. % Mn respectively and thus confirms the presence of microalloying elements in solid solution inside the crystalline phase.

Table 6. 1. Composition in at. % of the dendrites indicated with arrows (Fig. 6.3).

Composition (at.%)	Cu	Zr	Fe	Mn
Fig. 3a ($Cu_{50}Zr_{50}$) dendrite	48.30	51.70	-	-
Fig. 3c ($Cu_{49}Zr_{50}Fe_1$) dendrite	48.39	50.42	1.19	-
Fig. 3e ($Cu_{49}Zr_{50}Mn_1$) dendrite	45.47	53.43	-	1.10

6.3. Thermal and thermomechanical behaviour

In order to understand the thermal and thermomechanical behaviour of the as-cast $Cu_{50}Zr_{50}$, $Cu_{49.5}Zr_{50}Fe_{0.5}$, $Cu_{49}Zr_{50}Fe_1$, $Cu_{49.5}Zr_{50}Mn_{0.5}$, $Cu_{49}Zr_{50}Mn_1$ and $Cu_{49}Zr_{50}Fe_{0.5}Mn_{0.5}$ alloys, they have been studied upon heating (**Figs. 6.4A**) and upon cooling (**Figs. 6.4B**) by DSC and DMA (**Fig. 6.4C**).

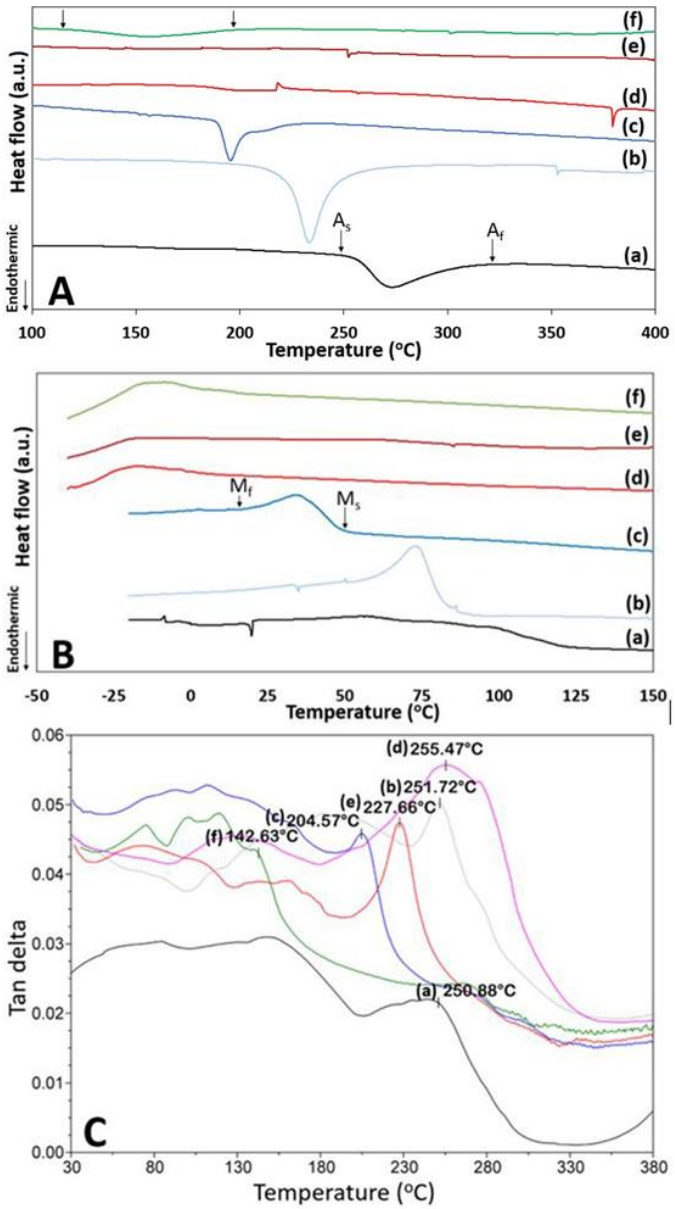

Fig. 6. 4. DSC scans upon (A) heating and (B) cooling and (C) DMA scans upon heating for (a) $Cu_{50}Zr_{50}$, (b) $Cu_{49.5}Zr_{50}Fe_{0.5}$, (c) $Cu_{49}Zr_{50}Fe_1$, (d) $Cu_{49.5}Zr_{50}Mn_{0.5}$, (e) $Cu_{49}Zr_{50}Mn_1$ and (f) $Cu_{49}Zr_{50}Fe_{0.5}Mn_{0.5}$.

The transformation temperatures have been summarized in **Table 6.2**, which shows A_s, A_f and martensite start (M_s) temperatures obtained from DSC (**Fig. 6.4A** and **5.4B**), as well as the austenite peak (A_p) obtained from DMA (**Fig. 6.4C**). For the parent $Cu_{50}Zr_{50}$ alloy and the Fe-containing alloys, a relatively large endothermic peak is observed associated to the transformation of martensite into austenite, where A_s and A_f are austenite start temperature and austenite finish temperature, respectively. For $Cu_{50}Zr_{50}$, the austenite phase starts the transformation (A_s) at around 250°C, and it is completed

(A_f) at around 323ºC. For $Cu_{49.5}Zr_{50}Fe_{0.5}$ the transformation temperatures are A_s = 205ºC and A_f = 273ºC while for $Cu_{49}Zr_{50}Fe_1$ they are A_s = 188ºC and A_f = 222ºC. These results clearly show that increasing addition of Fe progressively shifts the transformation temperatures to lower values. However, for the Mn-containing alloys, i.e. $Cu_{49.5}Zr_{50}Mn_{0.5}$ and $Cu_{49}Zr_{50}Mn_1$, the austenitic transformation peak is not detected. For $Cu_{49}Zr_{50}Mn_{0.5}Fe_{0.5}$ the intensity of the peak is very small and broad, with A_s = 115ºC and A_f =197ºC, and this is consistent with intermediate behaviour between that of the alloys with only Fe (showing peak) or with only Mn (no peak). This would not be possible to explain in terms of differences in volume fraction of martensite and austenite present upon rapid cooling for the different compositions since the XRD scans show that their relative intensity is similar (see section 6.5).

Table 6. 2. Transformation temperatures A_s, A_f and Ms from DSC scans, Ap from DMA scans for all alloys.

Composition (at.%)	A_s (ºC)	A_f (ºC)	M_s (ºC)	A_p (ºC)
$Cu_{50}Zr_{50}$	250	323	124	251
$Cu_{49.5}Zr_{50}Fe_{0.5}$	205	273	91	252
$Cu_{49}Zr_{50}Fe_1$	188	222	54	205
$Cu_{49.5}Zr_{50}Mn_{0.5}$	-	-	-	255
$Cu_{49}Zr_{50}Mn_1$	-	-	-	228
$Cu_{49}Zr_{50}Fe_{0.5}Mn_{0.5}$	115	197	4	143

To further investigate this, DMA measurements have been conducted and plotted as tan delta versus temperature (**Fig. 6.4C**). The presence of transformation peaks not only for Fe-containing alloys but also for those containing Mn, proves that DMA is able to detect transformations that could not be detected by DSC, since DMA measures the thermomechanical response rather than only the thermal behaviour of the alloys [201, 202]. The detection of more irregular curves consisting of small peaks from about 50 to 200 °C are attributed to the elimination of internal defects for the alloys containing Mn when compared to those containing Fe. This is in agreement with previous observations for which the amount of lattice defects present in SMAs can affect the 'intensity' of the

observed peaks in DSC analysis. The DMA curves of **Fig. 6.4C** show a high intensity peak attributed to the transformation of martensite into austenite. Moreover, the transformation peaks shift to lower temperatures with increasing concentration of Fe, which is in agreement with the DSC curves and the shift is similar for the Mn-containing alloys.

6.4. Wear tests

To study the effect of the microalloying elements Fe and Mn on the mechanical performance of B2 austenite, wear tests have been performed. **Fig. 6.5** shows the evolution of the mass loss (g) (**Fig. 6.5a**) and specific wear rate (mm^3/Nm) (**Fig. 6.5b**) for all the samples tested for 1h at room temperature (RT) at loads of 5, 10 and 15 N.

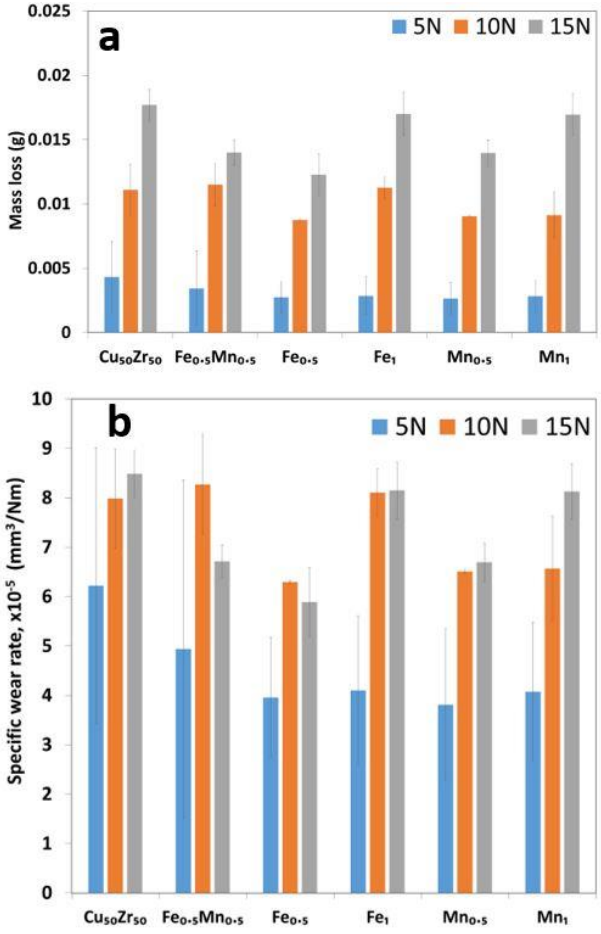

Fig. 6. 5. (a) Evolution of mass loss and (b) evolution of specific wear rate for the different alloys (code in parenthesis): $Cu_{50}Zr_{50}$, $Cu_{49}Zr_{50}Fe_{0.5}Mn_{0.5}$ ($Fe_{0.5}Mn_{0.5}$), $Cu_{49.5}Zr_{50}Fe_{0.5}$.

For all the compositions, the mass loss (**Fig. 6.5a**) increases with load increase. For the $Cu_{50}Zr_{50}$ alloy, the mass loss for a 5N load is 0.00255 g, increasing to 0.0111g and 0.0177g for 10 N and 15 N, respectively. However, the trend is different when Cu is replaced by Fe or Mn. Among all the compositions, the lowest mass loss values at 10 N (0.00875 g) and 15 N (0.0123 g) are observed when Cu is partly replaced by 0.5 at. % Fe. However, for 5 N load, the mass loss is similar (i.e., within the error range) for all the compositions tested. This suggests that for 15 N load, the alloy that exhibits the most effective work-hardening upon twinning is the one containing 0.5 at. % Fe. This is consistent with the fact that for this composition the stacking fault energy is the smallest (0.26 J/m^2, see **Fig. 6.2**) and therefore stress-induced twinning is promoted the most [31, 165]. **Fig. 6.5b** shows the specific wear rate in (mm^3/Nm) which can be calculated from the following equation:

$$W = V/L\ F \qquad (6.1)$$

where W corresponds to specific wear rates (mm^3/Nm), V is the wear volume (mm^3), L is the sliding distance (m), and F is the applied load (N). The sliding distance and applied load (i.e., 5, 10 and 15 N) for all the tested samples is the same. Therefore, the only difference in wear rate is due to the differences in wear volume. From **Fig. 6.5b** it is observed that $Fe_{0.5}$ has the lowest wear volume and therefore lowest specific wear rate, around 5.9 mm^3/Nm, compared to 8.5 for mm^3/Nm for $Cu_{50}Zr_{50}$ at 15 N load, which agrees with the lowest mass loss value (**Fig. 6.5a**). That can be attributed to the accelerated martensitic transformation and work-hardening, which is highest for the alloy containing 0.5 at. % Fe. Despite all pins have a flat surface before testing to ensure maximum contact between pin and disc, a complete surface contact between the two bodies (pin and disc) throughout the test (1h) can only be guaranteed when testing at 10 and 15 N. This explains the high uncertainty values for 5N compared to 10 and 15N. Moreover, only for 10 and 15 N load the stress is high enough to transform austenite into martensite. There is a general inverse correlation between the total wear debris produced and the alloy hardness through Archard's equation [203]. For this reason, higher hardness involves higher wear resistance. The hardness of the as cast $Cu_{50}Zr_{50}$ alloy is 2.82 ± 0.43 GPa and does not exhibit significant change after testing at 15N. However, the hardness

of the as cast $Cu_{49.5}Zr_{50}Fe_{0.5}$ alloy increases from 3.39±0.36 GPa to 3.65±0.2 GPa after testing at 15 N load. These values are similar to those previously reported [204]. The work-hardening effect upon loading with 15 N is attributed to partial transformation from austenite into martensite, a harder phase, as can be deduced from the change in relative intensity of the XRD peaks and the TEM images in section 6.5. However, the appropriate concentration of microalloying element is also an important factor when tailoring the SFE. In fact, for Fe_1 addition, the mass loss values for 10 N (0.011 g) and 15 N (0.017 g) are higher than for $Fe_{0.5}$. The higher mass loss indicates that the alloy does not work-harden so effectively as the one with $Fe_{0.5}$ due to the fact that the SFE for Fe_1 (0.3 J/m^2) is higher than for $Fe_{0.5}$ (0.26 J/m^2) as shown in **Fig. 6.2**.

The effect of Mn addition on the wear resistance is similar but not so remarkable as that of Fe as shown in **Fig. 6.5a and 6.5b**. The addition of $Mn_{0.5}$ as a microalloying element also enhances the wear performance as the mass loss increases to only 0.014 g at 15N compared to 0.017g for $Cu_{50}Zr_{50}$. This suggests that Mn also promotes stress-induced martensitic transformation during the wear test, but less efficiently than $Fe_{0.5}$. The slightly higher SFE (**Fig. 6.2**) for $Mn_{0.5}$ (0.27 J/m^2) than for $Fe_{0.5}$ (0.26 J/m^2) confirms these results.

For the Mn_1 alloy, the mass loss values for 15 N are very similar and within the error range of the $Cu_{50}Zr_{50}$ and Fe_1 alloys. This is in accordance with the similar SFE for Mn_1 (0.31 J/m^2) and Fe_1 (0.3 J/m^2) but smaller than that of $Cu_{50}Zr_{50}$ (0.36 J/m^2). This slight mismatch is attributed to the relatively large experimental error values of mass loss at 15 N load. For the $Fe_{0.5}Mn_{0.5}$ co-microalloyed alloy, the mass loss values at 15 N are intermediate between that of $Fe_{0.5}$ and $Mn_{0.5}$ and agree with the intermediate SFE values (**Fig. 6.2**), between 0.27 J/m^2 for $Mn_{0.5}$, and 0.26 J/m^2 for $Fe_{0.5}$. These results confirm the good agreement between our experiments and the model. The results also indicate that when testing at 15 N, the wear resistance is maximum when Cu is partly replaced by 0.5 at. % Fe, followed by 0.5 at. % Mn, thus resulting in a lifetime enhancement of the parent alloy of about 30.5 % and 21 %, respectively.

Analysis of wear tracks and wear debris on the pin and the SS304 counterbody was investigated using SEM and EDX. **Fig. 6.6** shows SEM images and EDX scans from the worn surface of the $Cu_{49.5}Zr_{50}Fe_{0.5}$ pin tested at 15 N load.

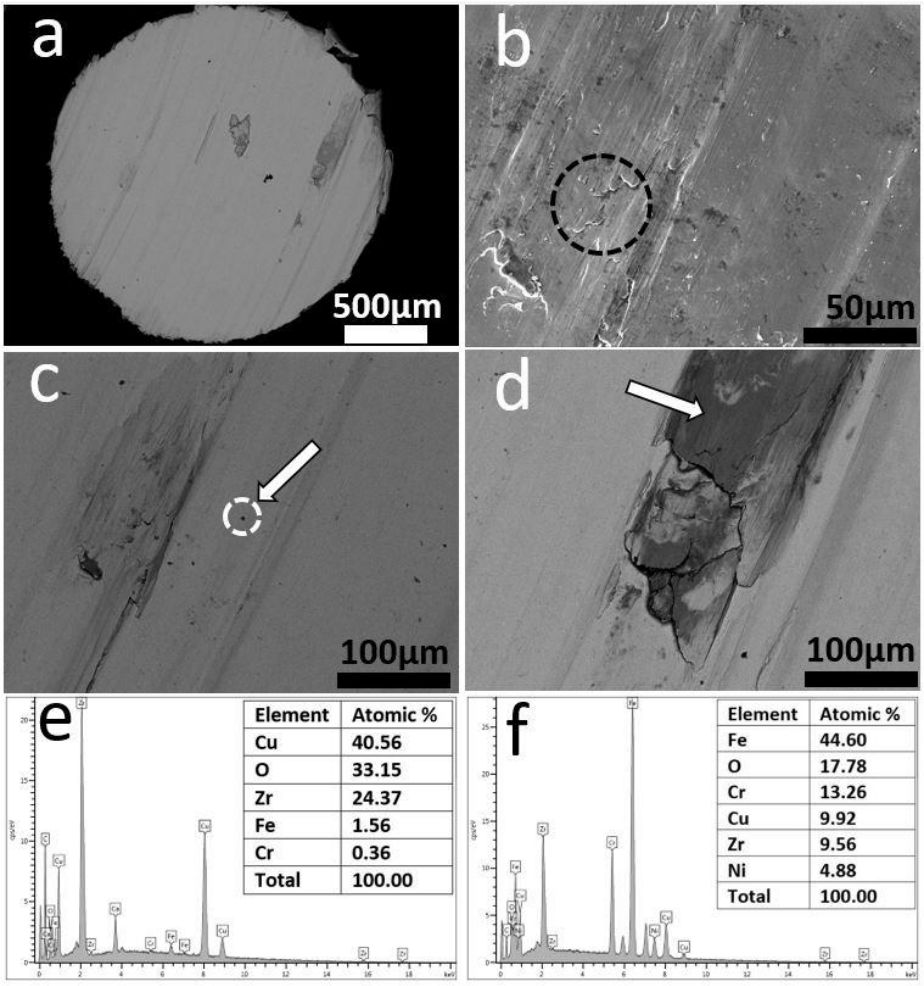

Fig. 6. 6. SEM images from the 2 mm diameter $Cu_{49.5}Zr_{50}Fe_{0.5}$ pin tested at 15N load. (a) General and detailed images showing (b) wear scars (circle) (c) dark particles (arrow) and (d) patches (arrow) and corresponding EDX scans, respectively.

This composition is of interest since it exhibits the highest wear resistance among all the studied the alloys (**Fig. 6.5**). The general image **Fig. 6.6a** shows the presence of long continuous grooves caused by ploughing, which is a common mechanism of abrasive wear [186, 205]. From the pin surface, different features can be observed. Among them, wear scars, which are signs of delamination generated by shear forces acting on the pin upon sliding. When testing at 15 N load, the surface of the pin deforms plastically and

subsurface cracks nucleate and propagate leading to formation of sheet-like wear features (see circle on **Fig. 6.6b**) [206]. This wear mechanism is responsible for the plastic deformation thus resulting in partial transformation from austenite into martensite. This can be proven from the increase in intensity of the XRD peaks associated to martensite and decrease of those associated to austenite after wear tests as shown in section 6.5. In addition, two distinctive features can be seen, small debris particles distributed across the surface (**Fig. 6.6c**) and smeared patches (**Fig. 6.6d**) along the wear direction. EDX microanalysis of the small particles of dark tonality indicate that these particles are rich in oxygen (33.2 at.% O, 1.6 at.% Fe, 0.36 at.% Cr, 40.6 at.% Cu, 24.4 at.% Zr) and have slightly higher concentration in Cu than Zr. These particles therefore they may correspond to $Cu_{10}Zr_7$ oxides. This is consistent with the detection of XRD peaks associated to $Cu_{10}Zr_7$ (see **Fig. 6.11**). These dragged hard third body particles plough through the surface and form grooves (**Fig. 6.6a**). In addition, the surface of the worn pin exhibits long smeared patches of up to 250 μm, which are oriented along the direction of grooves. EDX microanalysis indicate that these patches have a composition of 17.8 at.% O, 13.3 at.% Cr, 44.6 at.% Fe, 4.9 at.% Ni, 9.9 at.% Cu and 9.6 at.% Zr. The high percentage of Fe and presence of Ni and Cr indicates that these smeared patches are coming from the counterbody (SS304) as transferred material. This transference can be described by the mechanism of adhesive wear [207].

These results have been compared to the reference material, the $Cu_{50}Zr_{50}$ pin tested at the same conditions (15 N load) as shown in the SEM images and EDX scans of **Fig. 6.7**.

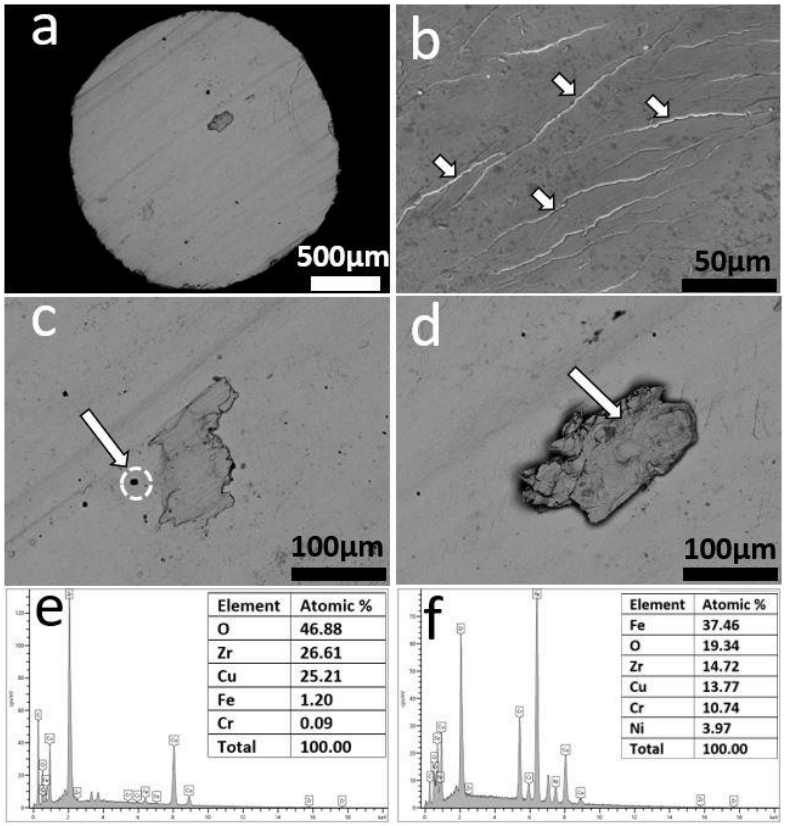

Fig. 6. 7. SEM images from the 2 mm diameter $Cu_{50}Zr_{50}$ pin tested at 15N load. (a) General and detailed images showing (b) wear scars (small arrows) (c) dark particles (arrow) and (d) patches (arrow) and corresponding EDX scans, respectively.

This composition is of interest since it exhibits the lowest wear resistance among all the studied alloys (**Fig. 6.5**). The general image **Fig. 6.7a** shows the presence of long continuous grooves indicative of abrasive wear, which are similar to those observed for $Fe_{0.5}$ at. % but they are more distinct and abundant for $Cu_{50}Zr_{50}$. Furthermore, longer, and more abundant continuous subsurface cracks that propagate towards the surface are seen in $Cu_{50}Zr_{50}$ (**Fig. 6.7b**). These subsurface cracks are associated to delamination wear and their morphology is consistent with observations from different authors including Li et al. [208] In order to identify the nature of the small particles of dark tonality shown in **Fig. 6.7c**, EDX microanalysis has been conducted. The results (46.9 at.% O, 1.2 at.% Fe, 0.09 at.% Cr, 25.3 at.% Cu, 26.6 at.% Zr) indicate that these particles are rich in oxygen and have similar concentration in Cu and Zr. These oxide particles are similar in terms of shape, size, and concentration in O to those reported for Fe0.5 at. % in **Fig. 6.6c.** Additionally, **Fig. 6.7d** shows the surface of the worn pin exhibiting long smeared patches

of around 150 μm length oriented along the direction of the grooves. EDX microanalysis indicate that these patches have a composition of 19.3 at.% O, 13.8 at.% Cr, 37.5 at.% Fe, 3.9 at.% Ni, 13.8 at.% Cu and 14.7 at.% Zr. The high percentage of Fe and presence of Ni and Cr indicates that these smeared patches are coming from the counterbody (SS304) as transferred material which is a common feature of adhesive wear. Both, the composition and morphology of the oxide particles and smeared patches are similar to those detected for the $Fe_{0.5}$ at. % alloy (**Fig. 6.6**) while the main difference is the presence of more profuse and well-defined grooves for the $Cu_{50}Zr_{50}$ pin. This has been studied in more detail in **Fig. 6.10**. In sliding wear, the performance of the entire tribosystem counts. For this reason, the surface of the SS304 counterbody (**Fig. 6.8**) after the wear tests for the $Fe_{0.5}$ (**Fig. 6.8a and b**) and $Cu_{50}Zr_{50}$ pin (**Fig. 6.8c and d**) at 15 N load have been also studied.

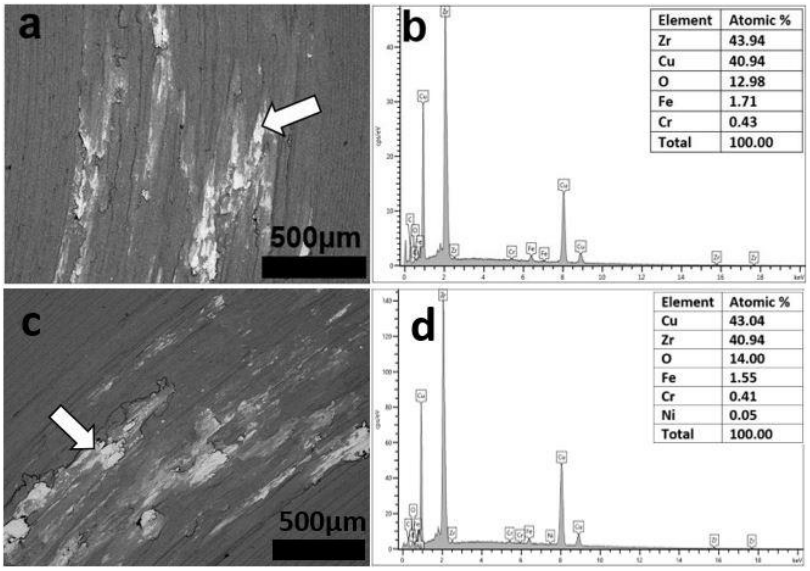

Fig. 6. 8. SEM backscattered images of SS304 counterbody worn surfaces after wear testing at 15 N (a) the $Fe_{0.5}$ and (c) the $Cu_{50}Zr_{50}$ pins and corresponding b) and d) SEM-EDX scans from the transferred material (see arrow), respectively.

The backscattered SEM image of **Fig. 6.8a** shows some patches (i.e., attached wear debris) of clear tonality heterogeneously attached to the wear track of the SS304 counterbody. The bright colour of the patches indicates the presence of heavier elements than those of the SS304 disc (grey background) and therefore they might be associated to material detached from the pin. This process of metal removal occurs by adhesion of

the material from the pin surface onto the SS304 counterbody [207]. This can be proven from EDX (**Fig. 6.8b**) as the content of Cu and Zr at.% roughly makes up 84% of the highlighted wear track (13 at.% O, 0.4 at.% Cr, 1.7 at.% Fe, 40.9 at.% Cu, 43.9 at.% Zr). For the $Cu_{50}Zr_{50}$ sample (**Fig. 6.8c**) the amount of material attached onto the SS304 counterbody is more abundant and of larger size, up to about 400 µm compared to about 200 µm for the $Fe_{0.5}$ alloy. This is consistent with the higher mass loss and wear rate (**Fig. 6.5**) and the more abundant grooves (**Fig. 6.6 and 6.7**) for $Cu_{50}Zr_{50}$ compared to the $Fe_{0.5}$ alloy. The morphology of these patches is similar to those observed by other authors [209] but they are not so elongated for our materials probably because the presence of brittle intermetallic phases makes the patches more hard and brittle and therefore more difficult to spread. EDX analysis of these patches (see arrow in **Fig. 6.8d**) indicate that the chemical composition is 14 at.% O, 0.4 at.% Cr, 1.55 at.% Fe, 43 at.% Cu and 40.9 at.% Zr, very similar to those for Fe0.5 but slightly poorer in Fe as could be expected considering that the $Cu_{50}Zr_{50}$ alloy does not contain Fe. Another important parameter to investigate the wear behaviour [86] is the coefficient of friction, i.e., the resistance encountered when moving one object over another. A small friction coefficient indicates high wear resistance [210]. The coefficient of friction generally exhibits two stages during the duration of the wear test, the first stage is a short period at the start of the test with a rapid increase of coefficient of friction followed by stabilization of the coefficient of friction throughout the rest of the test, also called the steady-state stage [32, 86, 210]. **Fig. 6.9** shows the coefficient of friction (COF) as a function of the testing time from 0 to 3,600 seconds.

The average values of the COF are 0.48±0.05, 0.49±0.04, 0.51±0.04, 0.54±0.03, 0.55±0.04 and 0.59±0.04 for the $Fe_{0.5}$, $Fe_{0.5}Mn_{0.5}$, $Mn_{0.5}$, Fe_1, $Cu_{50}Zr_{50}$ and Mn_1 alloys, respectively. The lowest value for the $Fe_{0.5}$ alloy is consistent with the lowest mass loss and specific wear rate (**Fig. 6.5**) and therefore this alloy exhibits the highest wear resistance. These values are not far from those reported in the literature, from about 0.4 to 0.6 for $Cu_{60}Zr_{30}Ti_{10}$ at. % [211] and about 0.35 to 0.45 for a Cu-BMG (bulk metallic glass) of similar composition to the alloys of this work, when sliding against EN26 steel [205].

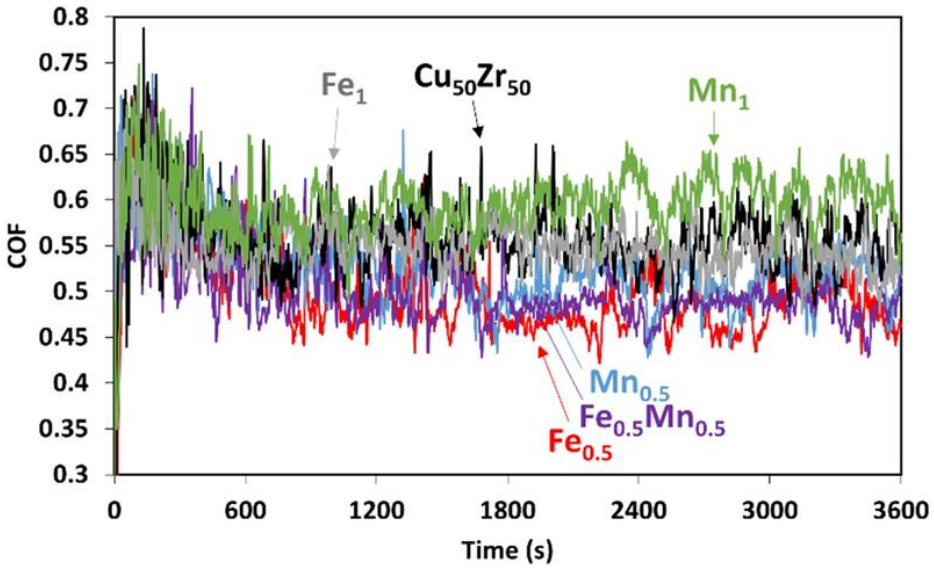

Fig. 6. 9. The coefficient of friction as a function of the testing time.

To analyse the differences in wear behaviour of all the compositions in more detail, the worn surfaces of the samples tested at 15 N load have been observed under the profilometer. This loading condition has been selected since maximum differences in mass loss among all the compositions are obtained for 15 N load (**Fig. 6.5**) and therefore, maximum differences of the worn surfaces are expected. In order to quantify the roughness of all the alloys wear tested at 15 N load for 1 hour, representative surfaces of each worn pin surface (square of 360mm^2 size) were analysed using a profilometer (**Fig. 6.10**).

Parallel grooves on the worn surface of all samples after sliding are observed. It was found that the average roughness values measured perpendicular to the grinding direction (R_a) for $Cu_{50}Zr_{50}$, Fe_1 and Mn_1 were 0.415±0.026, 0.375±0.004 and 0.356±0.021 µm, respectively. These values of R_a were higher than those for $Mn_{0.5}$ and $Fe_{0.5}Mn_{0.5}$, 0.301±0.003 and 0.247±0.010 µm, respectively. These results are in agreement with the values of mass loss (**Fig. 6.5**) and COF (**Fig. 6.9**). The worn surface of the $Fe_{0.5}$ alloy tested at 15 N exhibits a minimum roughness of 0.200±0.013 µm and the COF is the lowest.

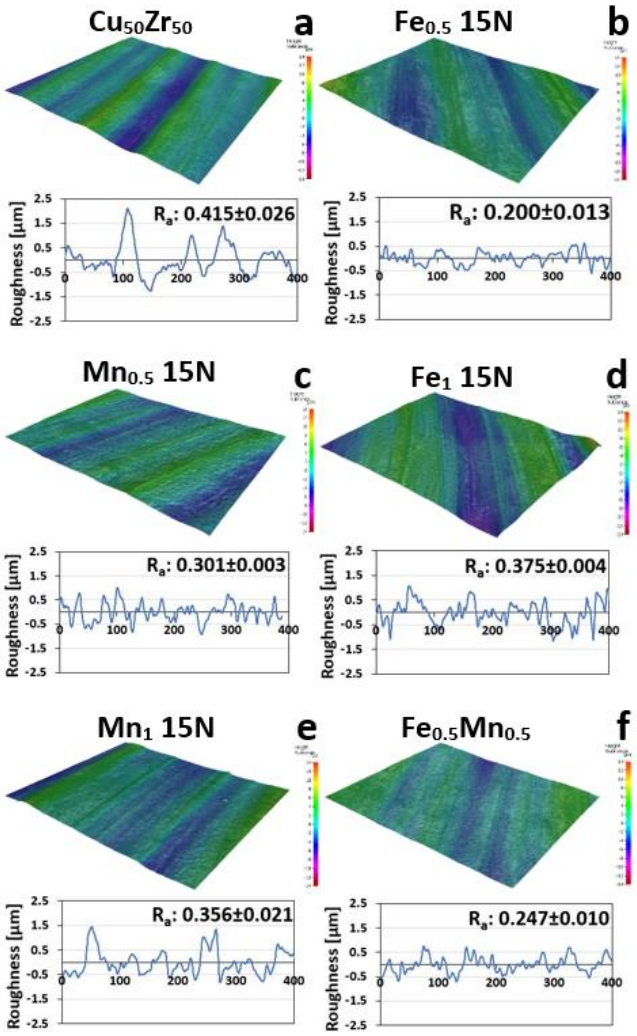

Fig. 6. 10. Surface topography for the different compositions after wear tests at 15 N load for 1 hour.

The compositions with higher roughness exhibit deeper grooves because more material is ploughed out from the surface while the sample with lowest roughness ($Fe_{0.5}$) exhibits the shallowest grooves. This type of wear is called abrasive wear since ploughing results in the removal of a certain volume of material thus resulting in the formation of abrasive grooves on the weaker surface of two surfaces in contact [212].

These results cannot be compared with the literature since, to the authors knowledge, this is the first attempt to link wear volume to surface roughness. However, a clear trend is observed, and the results are consistent with those obtained from our other experiments. It is important to point out that the wear mechanism is the same (i.e., combination of abrasion, adhesion, and delamination) for all the compositions. If the wear

mechanism for the tested samples was different, it might not be possible to correlate the wear volume and surface roughness, and this is something we aim to study in the future.

6.5. Structural characterization after wear tests

To better understand the microstructural changes that take place in the alloys during the wear tests after 1 hour and 15 N load, XRD scans have been done before and after the wear tests. **Fig. 6.11** shows the XRD patterns for $Cu_{50}Zr_{50}$, $Cu_{49.5}Zr_{50}Fe_{0.5}$, $Cu_{49}Zr_{50}Fe_{1}$, $Cu49.5Zr_{50}Mn_{0.5}$, $Cu_{49}Zr_{50}Mn_{1}$ and $Cu_{49}Zr_{50}Fe_{0.5}Mn_{0.5}$ at. % alloys in the as-cast condition (i.e., AC) and the after the wear tests (i.e., AT).

The XRD scans for the six compositions show peaks at similar angles associated to the following phases: austenite B2 CuZr (a= 3.2562 nm, b = 3.2562 nm, c = 3.2562 nm), monoclinic martensite B19′ CuZr (a = 0.3237 nm, b = 0.4138 nm, c= 0.5449 nm), orthorhombic $Cu_{10}Zr_{7}$ (a = 0.9347 nm, b = 0.9347 nm, c = 1.2675 nm), orthorhombic $Cu_{8}Zr_{3}$ (a = 0.78686 nm, b = 0.81467 nm, c = 0.9977 nm) and tetragonal $CuZr_{2}$ (a = 0.3220 nm, b = 0.3220 nm, c= 1.1183 nm). The intensity of the peaks associated to austenite decreases after the wear tests while the intensity of the peaks corresponding to martensite increase. This indicates that a martensitic transformation has taken place during the wear tests. For all as-cast and tested samples, peaks associated with B2 CuZr austenite are detected at around 39.4º and 70.8°. In addition, martensite peaks at around 27.4°, 35.9º, 43.7° and 56.5º are detected along with peaks associated to the intermetallic phases $CuZr_{2}$, $Cu_{8}Zr_{3}$ and $Cu_{10}Zr_{7}$.

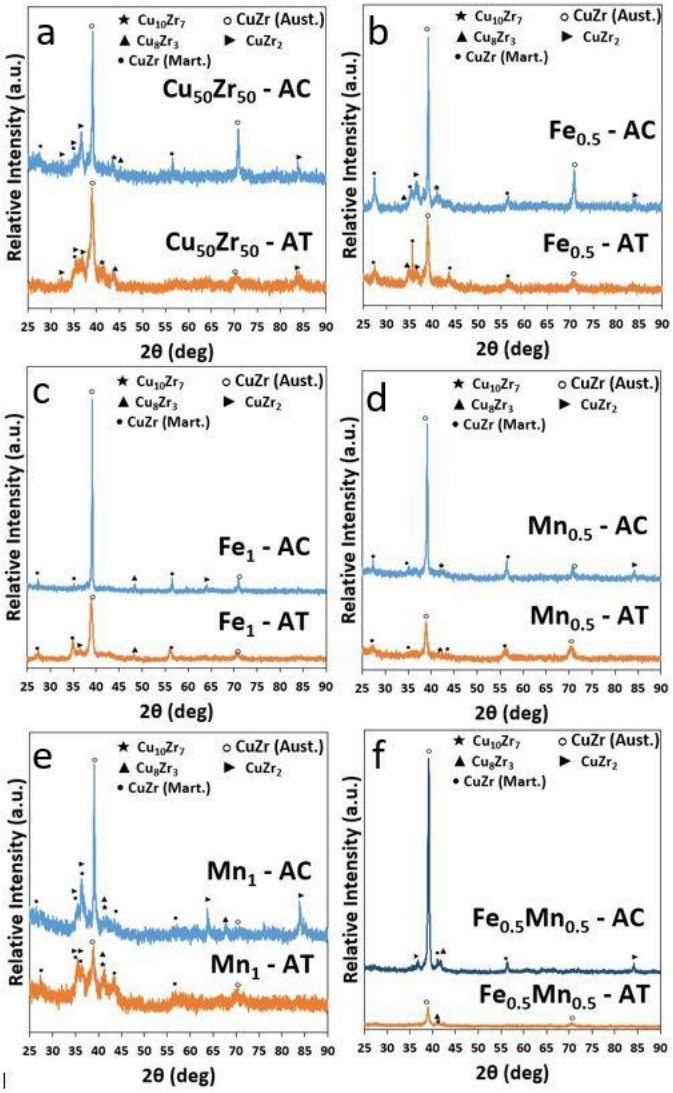

Fig. 6. 11. XRD scan of 2 mm diameter as-cast (AC) and after wear tested (AT) alloys with 15 N load for (a) $Cu_{50}Zr_{50}$, (b) $Cu_{49.5}Zr_{50}Fe_{0.5}$, (c) $Cu_{49}Zr_{50}Fe_1$, (d) $Cu_{49.5}Zr_{50}Mn_{0.5}$ and (e) $Cu_{49}Zr_{50}Mn_1$ and (f) $Cu_{49}Zr_{50}Fe_{0.5}Mn_{0.5}$.

The wear tested $Cu_{50}Zr_{50}$ alloy (**Fig. 6.11a**) shows a slight decrease in intensity of XRD peaks at 39.4º and 71.1º associated to austenite, while the peak at 35.9° associated to martensite increases in magnitude compared to the as cast (non-tested) alloy. This suggests that austenite has partly transformed into martensite. The intensity of XRD peaks of austenite for $Cu_{50}Zr_{50}$ decreased by about 28% after testing while for martensite the intensity increased by about 10%. Peaks associated to other intermetallics such as $CuZr_2$, Cu_8Zr_3 and $Cu_{10}Zr_7$ have also been detected. Microalloying with $Fe_{0.5}$ (**Fig. 6.11b**) results in large decrease in intensity of the austenite peak (58% decrement after test) and a large intensity increase of martensite peak (50% increase after test). These changes

are clearly more noticeable than for $Cu_{50}Zr_{50}$ (**Fig. 6.11a**) and Fe_1 (**Fig. 6.11c**) alloys and the effect of microalloying with Fe_1 seems to have an intermediate effect between the base alloy and $Fe_{0.5}$.

These results suggest that the stress-induced martensitic transformation is most effective for the $Fe_{0.5}$ alloy and it is consistent not only with the SFE (**Fig. 6.2**), 0.26 J/m^2, but also with the mass loss (**Fig. 6.5a**), 0.0123 g at 15 N load, both of which are the smallest among all the compositions. Although for $Mn_{0.5}$ alloy (**Fig. 6.11d**) the intensity of austenite decreased by 62% after the wear test, the intensity of the peaks associated to martensite do not seem to increase, especially when compared to the alloy with $Fe_{0.5}$. However, from the relative intensity of XRD peaks it can be deduced that the volume fraction of intermetallic phases ($CuZr_2$ and $Cu_{10}Zr_7$) increased by about 10% after testing. Considering that these intermetallics are hard, they could have also contributed towards the higher wear resistance. This is consistent with the higher SFE (**Fig. 6.2**) for $Mn_{0.5}$ (0.27 J/m^2) compared to that for $Fe_{0.5}$ (0.26 J/m^2) and therefore the lower ability for the Mn-containing alloy to transform into martensite. In fact, the mass loss (**Fig. 6.5a**) of $Mn_{0.5}$ (0.014 g) is slightly higher than that of Fe0.5 (0.0123 g). The microstructural changes for $Mn_{0.5}$ are very similar to those observed in the $Fe_{0.5}Mn_{0.5}$ alloy (**Fig. 6.11f**) as can be deduced from the similar XRD scans before and after the wear tests. For the alloy containing Mn_1 (**Fig. 6.11e**) after the wear test, the peak associated to austenite at about 39.4º, decreases in intensity by about 60%, while for martensite it increases after the test by 26%. The peaks associated to martensite overlap with broad peaks associated to different phases. The formation of these peaks may suggest that dynamic recrystallization has taken place, something that was previously observed for wear tested copper [213]. To understand the effect of the microalloying elements on the wear behaviour of CuZr-based SMAs, TEM analysis has been performed. The nominal composition of as-cast $Cu_{50}Zr_{50}$ was studied by TEM in order to have a reference parent sample (i.e., without microalloying or load applied). The results from TEM have been compared with those from XRD since the former gives local information while the latter provides average information from the microstructure. The XRD scan of **Fig. 6.11a** for as-cast $Cu_{50}Zr_{50}$ indicates the presence of multiple intermetallic phases whose peaks overlap at certain angles, for example, at 37.2º peaks associated to $Cu_{10}Zr_7$ and $CuZr_2$ are detected. To

corroborate the presence of intermetallic phases, the microstructure has been studied by TEM. A bright field TEM image (**Fig. 6.12a**) of a representative microstructure of the as-cast $Cu_{50}Zr_{50}$ sample is shown.

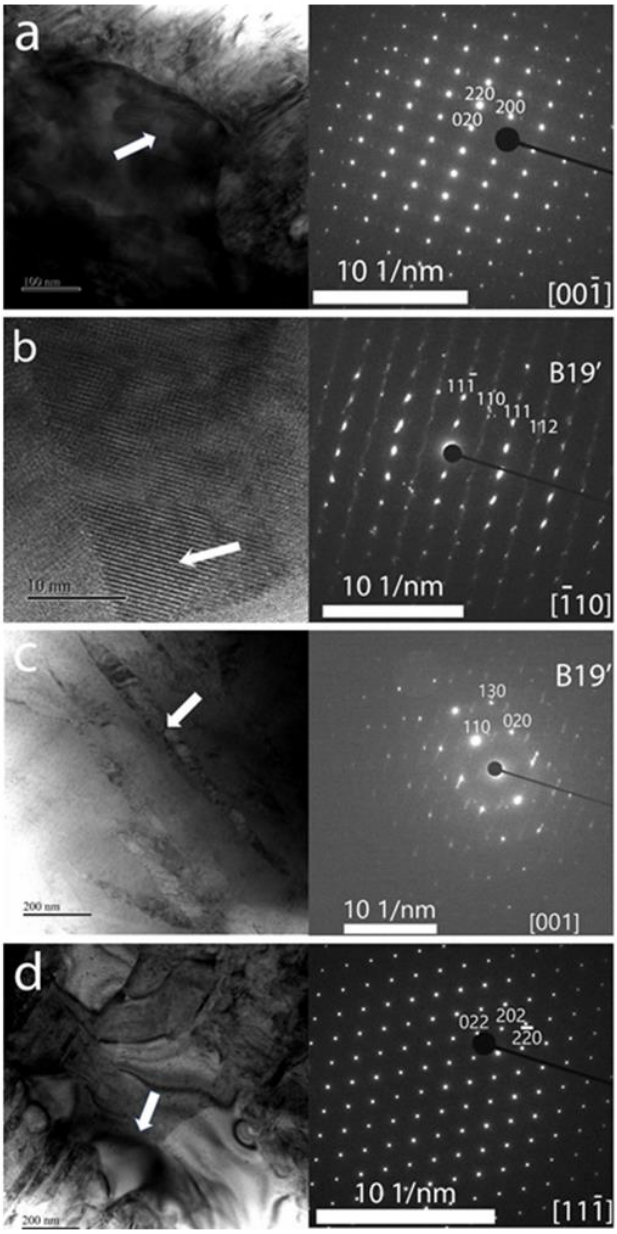

Fig. 6. 12. Bright field TEM images after wear tests at 15 N load and corresponding SAED pattern with zone axis B for (a) as-cast $Cu_{50}Zr_{50}$ alloy (B = [00-1]), (b) $Cu_{49.5}Zr_{50}Fe_{0.5}$ alloy (B = [-110]) and spots for B19' martensite twinned phase, (c) $Cu_{49}Zr_{50}Mn_{0.5}$ alloy (B = [001]) and spots for the B19' martensite twinned phase and (d) $Cu_{49}Zr_{50}Mn_1$ alloy (B = [11-1]).

The arrow in the TEM image of **Fig. 6.12a** points towards a crystalline phase from where a Selected Area Electron Diffraction Pattern (SAED) pattern was taken (image on the

right of **Fig. 6.12a**). The crystalline phase has a concentration in Cu of (53.56 at. %) and Zr of (46.44 at. %) according to EDX and thus would correspond to $Cu_{10}Zr_7$. The SAED pattern taken along the zone axis [00-1] confirms the formation of a crystalline phase with orthorhombic structure $Cu_{10}Zr_7$. As previously commented in section 6.4, the $Cu_{49.5}Zr_{50}Fe_{0.5}$ alloy exhibited the highest relative wear resistance (**Fig. 6.5**), especially at 15 N load, which was attributed to deformation twinning [31]. To investigate this in detail, the $Cu_{49.5}Zr_{50}Fe_{0.5}$ sample wear tested at 15 N load has been analysed by TEM. The bright field TEM image of a twinned structure (see arrow) of the $Cu_{49.5}Zr_{50}Fe_{0.5}$ sample wear tested with 15 N load is shown in **Fig. 6.12b** along with the corresponding SAED pattern taken along zone axis [-110]. This pattern indicates that the twinned structure corresponds to the monoclinic structure (P21/m, space group 11) of B19' CuZr (i.e., martensite). The presence of martensite in this Fe-containing alloy suggests that the martensitic transformation is promoted, and this agrees with our first principles simulations (see **Fig. 6.2**) and the XRD scans (**Fig. 6.11b**) since the peak intensity ratio of martensite to austenite increases after the wear tests. EDX analysis indicated that the composition of this phase is Cu (52.18 at. %), Zr (46.92 at. %) and Fe (0.9 at. %) and thus it would correspond to CuZr with Fe present in solid solution. Although the concentration of Fe in solid solution seems to be slightly higher than that of the nominal composition, one has to take into consideration that TEM is a very local technique. This means that the concentration of Fe might not be the same across all the grains, but the average value is close to the nominal composition as detected by SEM-EDX (**Fig. 6.3**).-**Fig. 6.12c** shows a bright field TEM image of $Cu_{49.5}Zr_{50}Mn_{0.5}$ at. % alloy tested at 15 N. The corresponding SAED pattern indexed along the [001] zone axis also shows the presence of a monoclinic structure (P21/m, space group 11) corresponding to B19' CuZr. The detection of martensite suggests that the addition of 0.5 at. % Mn also promotes the martensitic transformation but less efficiently than for 0.5 at. % Fe as the first principles simulations in **Fig. 6.2** suggest. These results are also in agreement with the XRD results of **Fig. 6.11d** as the intensity of the austenite peak significantly decreased after testing and volume fraction of martensite increased. The phase composition is Cu (39.32 at. %), Zr (60.04 at. %) and Mn (0.64 at. %) and thus it would correspond to CuZr with Mn in solid solution. To investigate in detail the microstructure of the as-cast $Cu_{49}Zr_{50}Mn_1$ at. % alloy,

whose overall microstructure was studied before (**Fig. 6.3f**), TEM study is done. Bright field TEM image of **Fig. 6.12d** shows the microstructure consisting of small phases of up to 200 nm long. For one of the crystalline phases (see arrow in **Fig. 6.12d**) a SAED pattern was obtained from the zone axis [11-1] and this pattern would correspond to an orthorhombic structure $Cu_{10}Zr_7$ (Aba2, space group 41). This crystalline phase has a chemical composition of $Cu_{61.34}Zr_{38.66}$ at. % and therefore, from the ratio of the elements, this phase would correspond to the intermetallic $Cu_{10}Zr_7$ phase.

6.6. Conclusions

The following conclusions can be drawn:

-Changes in the Stacking Fault Energy of B2 CuZr austenite upon partial replacement of Cu by a microalloying element has been analysed from first principles calculations to predict the ability of austenite to transform into martensite upon wear testing. This has been done in the present work to select the microalloying elements (Fe and Mn) and their concentrations (0.5 and 1 at. %) for maximum wear resistance,

-For pin-on-disc wear tests at 10 N load, the mass loss values are similar for all compositions, ranging from 0.00875 to 0.011 g, and become more similar, values around 0.00255 g, as the load decreases to 5 N. This indicates that the stress-induced martensitic transformation upon twinning becomes less relevant as the load decreases.

-For 15 N load wear tests, differences in mass loss are larger than for 5 and 10 N, ranging from a minimum of 0.0123 g for 0.5 at. % Fe to a maximum of 0.0177 g for $Cu_{50}Zr_{50}$ alloy. The lowest wear volume and therefore lowest specific wear rate, around 5.9 mm^3/Nm is attained by 0.5 at. % Fe, compared to 8.5 for mm^3/Nm for $Cu_{50}Zr_{50}$ at 15 N load, which agrees with the lowest mass loss value. The low mass loss and specific wear rate values are attributed to the promotion of the transformation from austenite into the harder and therefore more wear resistant stress-induced B19’ martensite as proven from TEM and XRD results. The more wear resistant samples exhibit not only lower friction coefficient but also more shallow abrasive groves, indicating the lowest wear volume and lowest wear rate.

-From the cross section of the pins after sliding wear tests, wear mechanisms of abrasion, adhesion and delamination have been identified. This can be deduced from the presence of long continuous grooves, the removal of material onto the disc and presence of subsurface cracks respectively.

-For 15 N load, partial replacement of Cu from the $Cu_{50}Zr_{50}$ shape memory alloy (SMA) by 0.5 at. % Fe, results in a lifetime enhancement of the $Cu_{50}Zr_{50}$ alloy of about 30.5 % while for 0.5 at. % Mn the lifetime enhancement is about 21 %. Microalloying is therefore an efficient strategy to develop Cu-Zr-based shape memory alloys as temperature adaptive shaft seals for engines. The shaft is generally made out of stainless steel and the contact surface and force between the shaft and the seal are of the same order of magnitude as those investigated in this PhD research. The ability to enhance the wear resistance of $Cu_{50}Zr_{50}$ austenite via optimum microalloying is promising to develop wear resistant shaft seals with enhanced lifetime.

Chapter 7 – Synergistic effect of cooling rate control and composition change on wear performance of CuZr SMAs

Overview

It is understood that addition of Co 0.5 at.% enhances wear performance of CuZr SMAs through lowering SFE and promotion of martensitic transformation (chapter 4), similarly, Ni 1 at.% significantly promotes martensitic transformation for CuZr SMA (chapter 5).

It is clear that concentration of microalloying element entering B2 CuZr phase in solid solution plays a major role in acceleration martensitic transformation and therefore improving mechanical properties. Therefore, chapter 6 highlighted other potential microalloying elements such as Mn and its role in promoting martensitic transformation as well as experimenting on smaller diameter pins (2mm) in comparison to chapter 4 and chapter 5 where samples were of (3mm) diameter.

Considering chapter 6 only investigated the mechanical performance of 2mm diameter samples, the role of cooling rate was not investigated despite its important role on the tribological and mechanical performance of CuZr SMAs. Chapter 7 is focusing on the synergistic effect of composition change as well as cooling rate control on wear performance of CuZr SMAs as it is a very important factor that influences the microstructure of CuZr SMAs.

7.1. Microstructural characterization of as-cast pins

The combined effect of the cooling rate and microalloying on the microstructure has been studied by suction casting samples of 2 mm and 4 mm diameter of $Cu_{50}Zr_{50}$, $Cu_{49.5}Zr_{50}Fe_{0.5}$ and $Cu_{49}Zr_{50}Fe_{1}$ (at. %). The cooling rate, $\dot{T}$, can be estimated from the relationship [84]:

$$\dot{T}\left(\frac{K}{s}\right) = \frac{10}{R^2}\left(\frac{1}{cm^2}\right) \qquad (18)$$

where R is the sample radius; hence for the 2 mm sample the cooling rate is ~1000 K/s while for 4 mm it is ~250 K/s. **Fig. 7.1** shows the backscattered SEM images from a

representative area from the sample centre and XRD scans for the 2 mm and 4 mm diameter $Cu_{50}Zr_{50}$, $Cu_{49.5}Zr_{50}Fe_{0.5}$, $Cu_{49}Zr_{50}Fe_1$ SMAs.

The microstructures of the high cooling rate as-cast $Cu_{50}Zr_{50}$ (**Fig. 7.1a**), $Cu_{49.5}Zr_{50}Fe_{0.5}$ (**Fig. 7.1c**) and $Cu_{49}Zr_{50}Fe_1$ (**Fig. 7.1e**) SMAs are very similar and basically consist of dendrites embedded in a fine matrix. To identify the nature of the phases present, XRD scans for the $Cu_{50}Zr_{50}$, $Cu_{49.5}Zr_{50}Fe_{0.5}$ and $Cu_{49}Zr_{50}Fe_1$ SMAs have been performed and are shown as insets in **Fig. 7.1a**. They consist of large intensity peaks at 39.4° and 70.8° attributed to cubic B2 CuZr austenite, smaller intensity peaks corresponding to monoclinic B19' and multiple small peaks for the intermetallics Cu_8Zr_3 and $CuZr_2$. This indicates that for the high cooling rate of ~1000 K/s, the retained metastable austenite is the dominant phase.

From EDX studies of the intermetallic phases, Fe was not detected the element but was detected inside the austenite/martensite dendrites, thus suggesting that Fe is present in solid solution as will be discussed later.

The backscattered SEM images and XRD scans for the low cooling rate $Cu_{50}Zr_{50}$ (**Fig. 7.1b**), $Cu_{49.5}Zr_{50}Fe_{0.5}$ (**Fig. 7.1d**), and $Cu_{49}Zr_{50}Fe_1$ (**Fig. 7.1f**) alloys were also obtained for comparison. The microstructure from the middle of the as-cast samples is similar for all the compositions and consists of a combination of dendrites embedded in a matrix of fine microstructure. Compared to the higher cooling rate sample, XRD scan shows much higher intensity peaks from the Cu_8Zr_3 and $CuZr_2$ intermetallic phases and the B19' CuZr phase (a = 3.2961 Å, b = 4.1937 Å, c = 5.2122 Å), and lower intensity peaks from the B2 CuZr phase (a = 3.2706 Å, b = 3.2706 Å, c = 3.2706 Å) as well as new peaks corresponding to the intermetallic $Cu_{10}Zr_7$ and B33 CuZr martensite (a = 3.2573 Å, b = 4.1143 Å, c = 10.3765 Å). Therefore, when the cooling rate decreases from 1000 K/s to 250 K/s, a microstructure is produced at closer to equilibrium conditions with the formation of more stable phases. The finding of the more stable B33 phase with the Cmcm space group rather than the B2 phase is consistent with the observations of other authors [54].

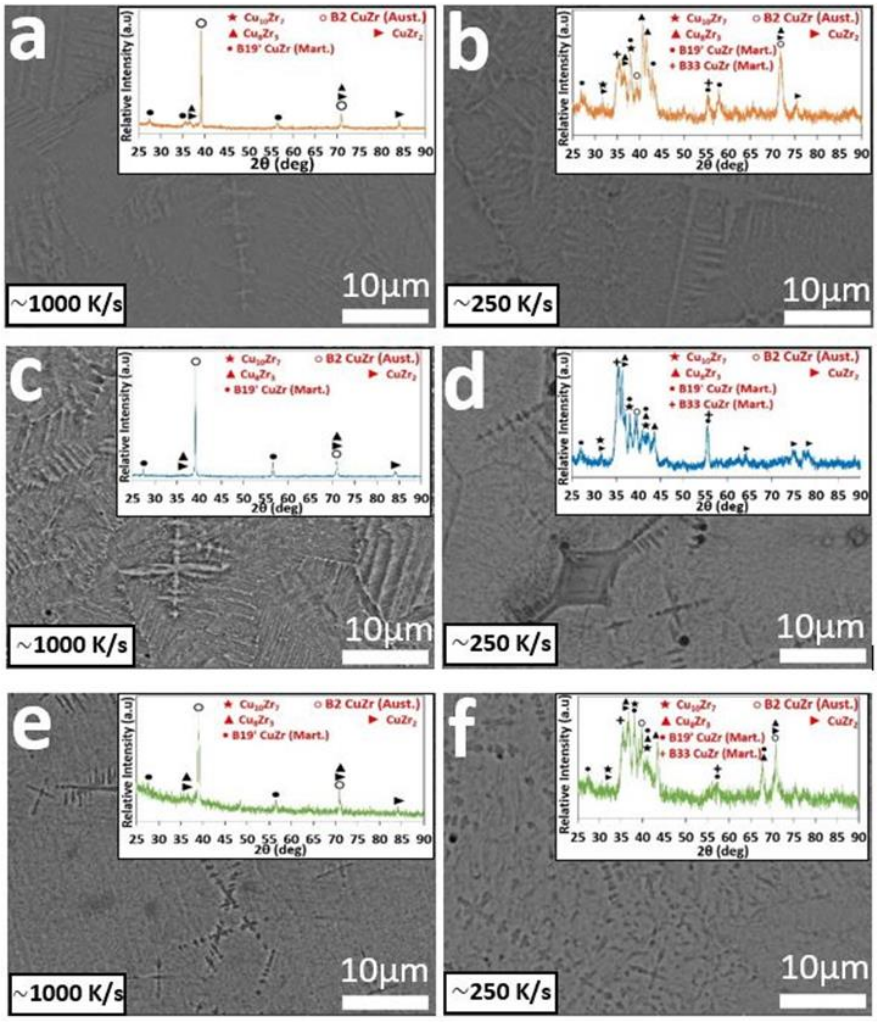

Fig. 7. 1. Backscattered SEM images for 2 mm (~1000 K/s) and 4 mm diameter (~250 K/s) as-cast: (a) and (b) $Cu_{50}Zr_{50}$; (c) and (d) $Cu_{49.5}Zr_{50}Fe_{0.5}$; (e) and (f) $Cu_{49}Zr_{50}Fe_1$ samples. The insets show the corresponding general XRD scans from the full cross-section of the sample. Note: The SEM images are taken from the middle radius to be representative.

Despite the microstructural similarities between the $Cu_{50}Zr_{50}$, $Cu_{49.5}Zr_{50}Fe_{0.5}$ and $Cu_{49}Zr_{50}Fe_1$ compositions, some slight differences are noted for $Cu_{49.5}Zr_{50}Fe_{0.5}$. For this intermediate composition, the relative intensity of the XRD peaks at 36.1° and 55.6° (associated with stable B33 martensite) is about twice that of the other two compositions while the intensity of XRD peaks for B19' practically does not change. This indicates that the formation of the B33 phase is synergistically stabilized by the combined effect of reducing the cooling rate and adding 0.5 at. % Fe. Moreover, no peaks from crystalline phase(s) containing Fe are detected, even when the concentration is as high as 1 at. % Fe, thus suggesting the element Fe remains in solid solution even for the lowest cooling

rate. These results provide information about the crystallization sequence upon cooling, with retention of the initial metastable B2 austenite at the high cooling rate while at lower cooling rate martensite and intermetallic phases are formed and grow. One should note that the solidification process does not follow the equilibrium diagram [214] especially when the highest cooling rate is achieved since practically no equilibrium intermetallic phases are present.

Since the presence of Fe in solid solution and its concentration is key in the formation of a stress-induced phase, the retention of this element upon cooling in the dendrites of the samples cooled at ~1000 k/s and ~250 K/s has been studied. Backscattered SEM images and EDX scans have been obtained from the dendrites close to the centre of the sample (i.e., where the cooling rate is the slowest and thus dendrites are prone to highest segregation). The dendrites for the high cooling rate $Cu_{50}Zr_{50}$, $Cu_{49.5}Zr_{50}Fe_{0.5}$ and $Cu_{49}Zr_{50}Fe_{1}$ samples and corresponding EDX scans from the centre of each dendrite (i.e., point indicated by the red arrow) are shown **in Fig. 7.2a**, **Fig. 7.2c** and **Fig. 7.2e**, respectively. Similarly, for the low cooling rate sample, EDX scans have been taken from the inner part of the dendrites as indicated in **Fig. 7.2b**, **Fig. 7.2d** and **Fig. 7.2f**. The red arrows point towards a region close to centre of each dendrite from where the EDX results were taken and summarized in the inset table for each panel. For the three compositions, the concentration of Cu and Zr are relatively similar, thus confirming that the dendrites correspond to austenite B2 CuZr and B19' martensite. The clear halo around the dendrites suggest that this area is rich in the element of higher atomic weight, Zr (91.224), thus leaving the dendrites slightly richer in the element of lower atomic weight, Cu (63.546). These differences in intensity agree with the EDX results. The composition profile of the dendrite/matrix interface is associated with the classical nucleation and growth mechanism for which the solute is transported down a composition gradient toward the dendrite [215]. EDX results indicate that the concentration of the Fe microalloying element inside the dendrites is 0.3 at. % for $Cu_{49.5}Zr_{50}Fe_{0.5}$ and 0.9 at. % for $Cu_{49}Zr_{50}Fe_{1}$, which are very close to the nominal composition of the alloys thus suggesting that Fe remains in solid solution. In fact, Fe is retained even for the slowest cooling rate, i.e., at the centre of the 4 mm diameter sample, the concentration of Fe

measured by EDX is 0.5 and 1 at. % for $Cu_{49.5}Zr_{50}Fe_{0.5}$ and $Cu_{49}Zr_{50}Fe_1$ alloys, respectively.

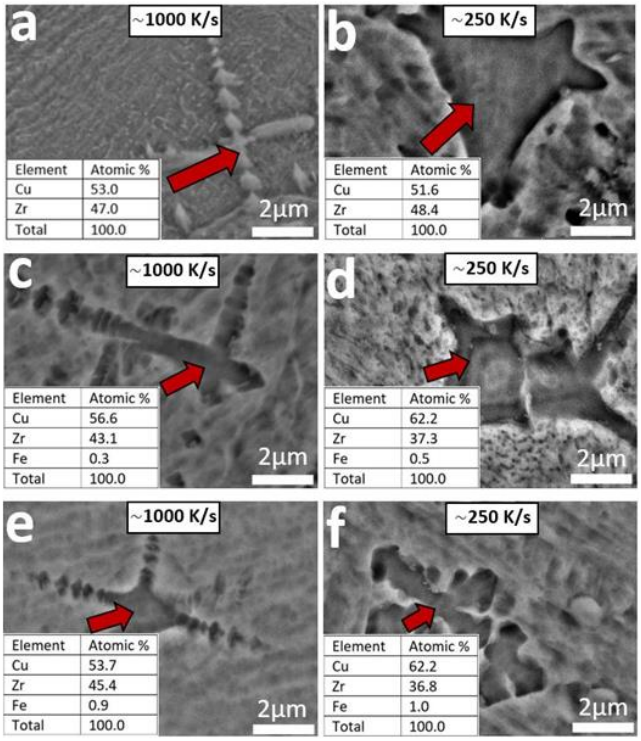

Fig. 7. 2. Magnified Backscattered SEM images from the dendrites located in the centre of 2 mm (~1000 k/s) and 4 (~250 k/s) mm samples: (a) and (b) $Cu_{50}Zr_{50}$; (c) and (d) $Cu_{49.5}Zr_{50}Fe_{0.5}$; (e) and (f) $Cu_{49}Zr_{50}Fe_1$ samples. The red arrows show the point at the centre.

In order to investigate the nano-matrix of the casted alloys, TEM images have been obtained for $Cu_{50}Zr_{50}$ of 2 and 4mm samples as shown in **Fig. 7.3**. Despite investigating the dendrites of 2 and 4mm samples in **Fig. 7.2**, it is not possible to assess the size of grains embedded in the crystalline matrix using SEM, therefore TEM images were taken. **Fig. 7.3a** shows a representative area of as cast 2mm $Cu_{50}Zr_{50}$ with grains embedded in the crystalline matrix, the arrows pointed towards grains that may reach 70nm in size. Similarly, **Fig. 7.3b** shows a representative area of as cast 4mm $Cu_{50}Zr_{50}$ where size of grains visibly distinguished by colour tonality difference are larger than that reported for 2mm sample.

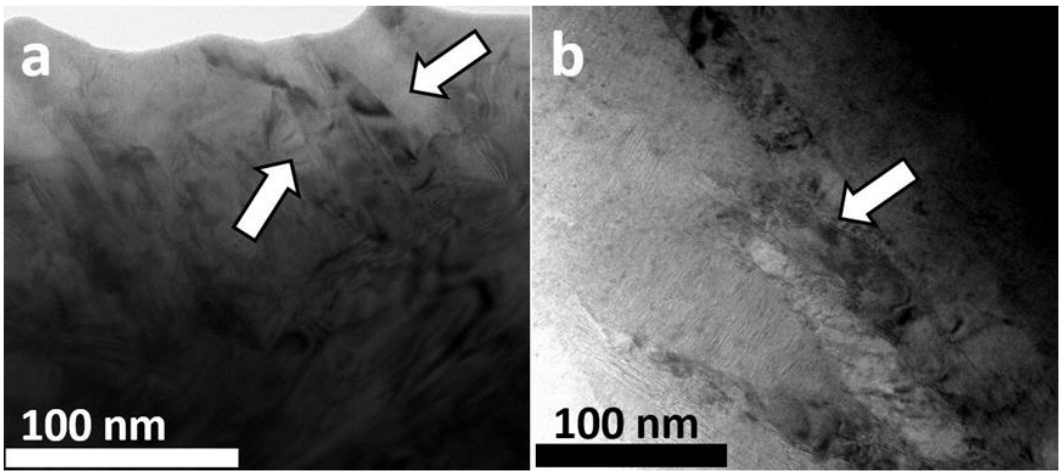

Fig. 7. 3. Bright field TEM image of (a) as-cast 2 mm (~1000 k/s) $Cu_{50}Zr_{50}$ and (b) as-cast 4 mm (~250 k/s) $Cu_{50}Zr_{50}$. The white arrows points towards grains embedded in crystalline matrix.

7.2. Wear behaviour

7.2.1. Pin-on-disc test

To investigate the combined effect of cooling rate and microalloying on the wear performance, pin-on-disc tests have been performed. **Fig. 7.4** shows the wear expressed as pin length loss for the three different compositions $Cu_{50}Zr_{50}$, $Cu_{49.5}Zr_{50}Fe_{0.5}$ and $Cu_{49}Zr_{50}Fe_1$ and diameters of 2 mm (~1000 k/s) and 4 mm (~250 k/s) when tested at 5, 10 and 15 N applied for 1 hour and also 40 N for the 4 mm sample. The 40 N test is performed to achieve the same pin-disc normal contact pressure (P = 3.2 MPa) as in the 2 mm sample under 10 N load. When the high cooling rate sample is subjected to a testing load of 15 N, a normal contact pressure of 4.8 MPa is achieved.

The pin length loss for the high cooling rate samples is very similar for all compositions when a load of 5 N is applied. However, when 10 and 15 N load are applied, the length loss depends on the composition. The lowest value is achieved at both loads for the $Cu_{49.5}Zr_{50}Fe_{0.5}$ alloy but is similar for the other compositions (i.e., $Cu_{50}Zr_{50}$ and $Cu_{49}Zr_{50}Fe_{1)}$. This indicates that addition of 0.5 at. % Fe enhances the wear resistance of the $Cu_{50}Zr_{50}$ alloy but only when the load is at least of 10 N thus suggesting that a stress sensitive mechanism is responsible for this behaviour. The wear resistance enhancement is attributed to the work hardening that B2 austenite experiences when it is transformed into martensite upon loading [165].

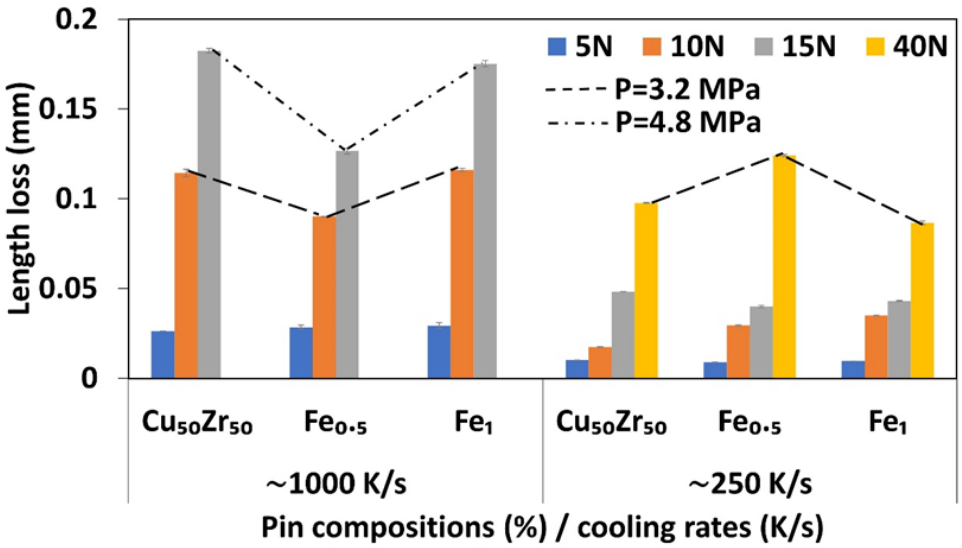

Fig. 7. 4. Evolution of pin length loss for 2 mm (~1000 k/s) and 4 mm (~250 k/s) for the different alloys: $Cu_{50}Zr_{50}$, $Cu_{49.5}Zr_{50}Fe_{0.5}$ and $Cu_{49}Zr_{50}Fe_1$ for 5, 10 and 15 N loads applied for 1 h. Results for 40 N is also included.

When the 2 mm pin is subjected to 10 N load, the pin-disc contact pressure is about 3.2 MPa. This is estimated to be the minimum pressure required to transform B2 austenite into B19' martensite. This transformation is promoted by the presence of 0.5 at. % Fe in solid solution (**Fig. 7.2**), which is consistent with observations from Wu et al. [151]. According to these authors, partial replacement of Cu from B2-CuZr phase by 0.5 at. % Fe decreases the SFE from 381 mJ/m^2 to ~125 mJ/m^2. However, further addition of Fe to 1 at. % does not seem to promote the martensitic transformation of CuZr austenite since the wear resistance is the same as that of the $Cu_{50}Zr_{50}$ alloy. For the low cooling rate samples (**Fig. 7.4**), the pin length loss for 15N is similar for all compositions. This is expected to be due to not only to microstructural differences resulting from the lower cooling rate but also to the lower pin-disc contact pressure leading to reduced stress-induced transformation; the cross-section area, (50.26 mm^2), is larger than for the 2 mm samples (12.56 mm^2). To achieve the same pressure as on the 2 mm pin subjected to 10 N load with the 4 mm sample, a 40 N load is required and therefore wear tests at this pressure for 1 hour have been also conducted (**Fig. 7.4**). For the low cooling rate samples under 40 N load, the length loss for $Cu_{50}Zr_{50}$ and $Cu_{49}Zr_{50}Fe_1$ are similar, 0.097 mm and 0.086 mm respectively, while for $Cu_{49.5}Zr_{50}Fe_{0.5}$ it is the highest, i.e., 0.124 mm, i.e., lowest wear resistance. This behaviour is therefore opposite to that observed in the high

cooling rate samples and could be explained by the microstructural differences. A high volume fraction of hard and therefore wear resistant intermetallic phases are present in $Cu_{50}Zr_{50}$ and $Cu_{49}Zr_{50}Fe_1$ alloys (**Fig. 7.1b and 7.1f**) [216]. However, for the low cooling rate $Cu_{49.5}Zr_{50}Fe_{0.5}$ alloy, in addition to these intermetallic phases, a high concentration of the B33 CuZr martensite phase is also present, which is different from the stress-induced martensite B19' produced by twinning in the high cooling rate sample. These results suggest that B33 CuZr is a low wear resistance phase. The reason for this behaviour will be investigated in more detail in the future.

The contact pressure measured in this study in **Fig. 7.4** ranges from 3.2 to 4.8 MPa which are of a similar order of magnitude to those previously reported by Phinney et al. [217]. Additionally, our values also match those reported by Ng et al. [218] where contact pressure was 2 MPa for near-equiatomic NiTi alloy.

7.2.2. **Hardness test**

To better understand the combined effect of cooling rate and microalloying on the wear performance, hardness tests have been performed. It is well known that the total wear volume produced is expected to be inversely proportional to the hardness (for a given material system) as indicated by Archard's equation [203]:

$$Q = \frac{KLD}{H} \qquad (7.1)$$

where Q is the volume of wear debris produced (volumetric loss), K is the wear coefficient, a dimensionless constant taken as 6.23×10^{-4} for CuZr alloys in this case according to calculation of K [219], L the load normal to the surface, D the sliding distance and H the hardness of the softer material of the contacting surfaces. For this reason and in order to corroborate our wear tests results, hardness measurements were made at high enough load (3 N) do that the plastic zone around the indentation would include all the crystalline phases to get a representative value for the microstructure as a whole. Measurements were done along the radius of the 2 and 4 mm samples for the 3 compositions as shown in the schematic in **Fig. 7.5** from the centre to the edge. The effect of the composition and distance from the centre is small, ranging from about 2.30 to 3 GPa for the 2 mm sample while for the 4 mm sample it ranges from about 3 to 3.74 GPa. This suggests that the

difference in cooling rate due to a change in diameter has much higher effect on the hardness. To better highlight this, the hardness versus the variation in the concentration of Fe added for both diameters has been plotted. While for the 2 mm sample highest hardness of about 3 GPa is attained for the $Cu_{49.5}Zr_{50}Fe_{0.5}$ alloy, the 4 mm sample shows the lowest value, about 3.46 GPa. These values are similar to those previously reported for CuZr-based alloys [220]. The hardness is consistent with the wear test values (**Fig. 7.4**) since the pin length loss for the 2 mm diameter samples is the smallest for $Cu_{49.5}Zr_{50}Fe_{0.5}$ while for the 4 mm diameter samples it is the highest. The results also agree with the XRD scans and SEM images (**Fig. 7.1 and Fig. 7.2**) for which mostly hard intermetallic phases ($Cu_{10}Zr_7$, Cu_8Zr_3 and $CuZr_2$) are detected for the low cooling rate samples while for the high cooling rate samples the microstructure is dominated by relatively soft B2 CuZr austenite dendrites.

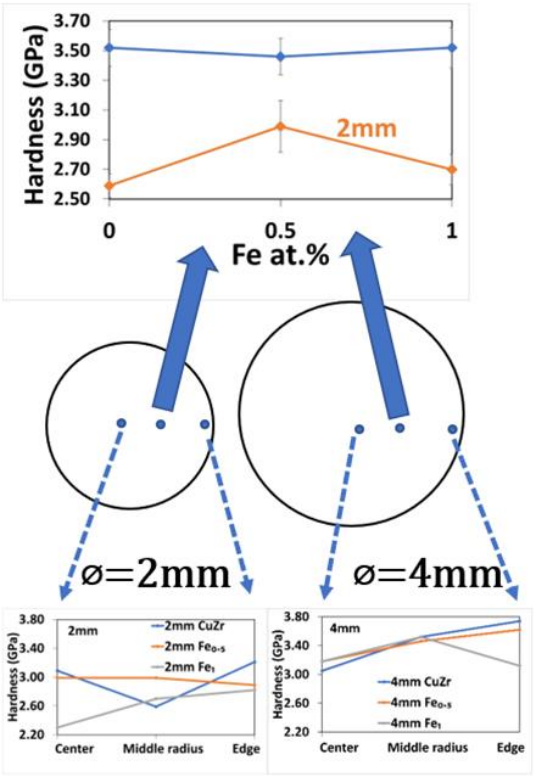

Fig. 7. 5. Schematic showing the 2 mm (~1000 k/s) and 4 mm (~250 k/s) cross section rod samples and locations from where hardness was measured (centre, middle radius, and edge, with centre as origin of the distance) as shown in the plots. The hardness values measured in the middle radius of the 2 mm and 4 mm samples versus the concentration in Fe are also shown.

This is the first time that the effect of the cooling rate on the hardness of the CuZr system has been reported as far as the authors are aware. These results are consistent with the evolution of the hardness with the cooling rate observed by Motemani et al. [221] in NiTi alloys.

It is important to also highlight that from a tribological point of view, the wear resistance of a material can be obtained indirectly from elastic strain to failure (H/Er) [222] and resistance to plastic deformation which is proportional to (H^3/Er^2) [223]. It was found that the values of H/Er and H^3/Er^2 which relate to hardness and wear relationship can be impacted by other factors such as air-annealing process [184].

7.2.3. **Morphological analysis after wear tests**

To investigate the effect of the cooling rate on the wear performance in more detail, the worn surface of the $Cu_{49.5}Zr_{50}Fe_{0.5}$ pin of 2 mm diameter (~1000 k/s) tested at 15 N (**Figs. 7.6a, 7.6b, 7.6c and 7.6d**), and the 4 mm diameter (~250 k/s) of the same composition tested at 15 N (**Figs. 7.6e, 7.6f, 7.6g and 7.6h**) and at 40 N load (**Figs. 7.6i, 7.6j, 7.6k and 7.6l**) for 1 h has been characterised. In addition, the debris generated upon wear testing that is attached onto the pin surface has been studied. This composition was selected since it exhibits the highest wear resistance among the 2 mm diameter samples and is a good basis of comparison for the 4 mm diameter samples.

The general images for the high cooling rate (**Fig. 7.6a**) and low cooling rate samples (**Fig. 7.6e and 7.6i**) show continuous grooves throughout the cross-section of the samples caused by ploughing, indicating an abrasive wear mechanism [205]. A load increase from 15 N to 40 N for the low cooling rate samples increases the groove depth; the average roughness increases from R_a= 0.462 µm (**Fig. 7.6f**) at 15 N to R_a= 0.533 µm (**Fig. 7.6j**) at 40 N. These values are much higher than the R_a= 0.200 µm for the 2 mm sample tested at 15 N (**Fig. 7.6b**). This can be attributed to the relatively high content of hard abrasive $Cu_{10}Zr_7$, Cu_8Zr_3 and $CuZr_2$ intermetallic phases present in the wear debris for the low cooling rate sample compared to the high cooling rate sample (SEM and XRD from **Fig. 7.1**). This wear debris is rich is oxygen, with concentrations ranging from about 32 to 34 at. % and is therefore significantly oxidised during dry wear. The degree of oxidation does not seem to depend on the load. The Zr to Cu ratio of the wear debris is

around 1.15, close to the nominal composition of the $Cu_{50}Zr_{50}$, $Cu_{49.5}Zr_{50}Fe_{0.5}$ and $Cu_{49}Zr_{50}Fe_1$ SMAs and this suggests that the material has not been systematically removed from any single phase but from all phases in the cross-section. This wear debris generates abrasive damage as it slides across the pin surface (**Fig. 7.6e**).

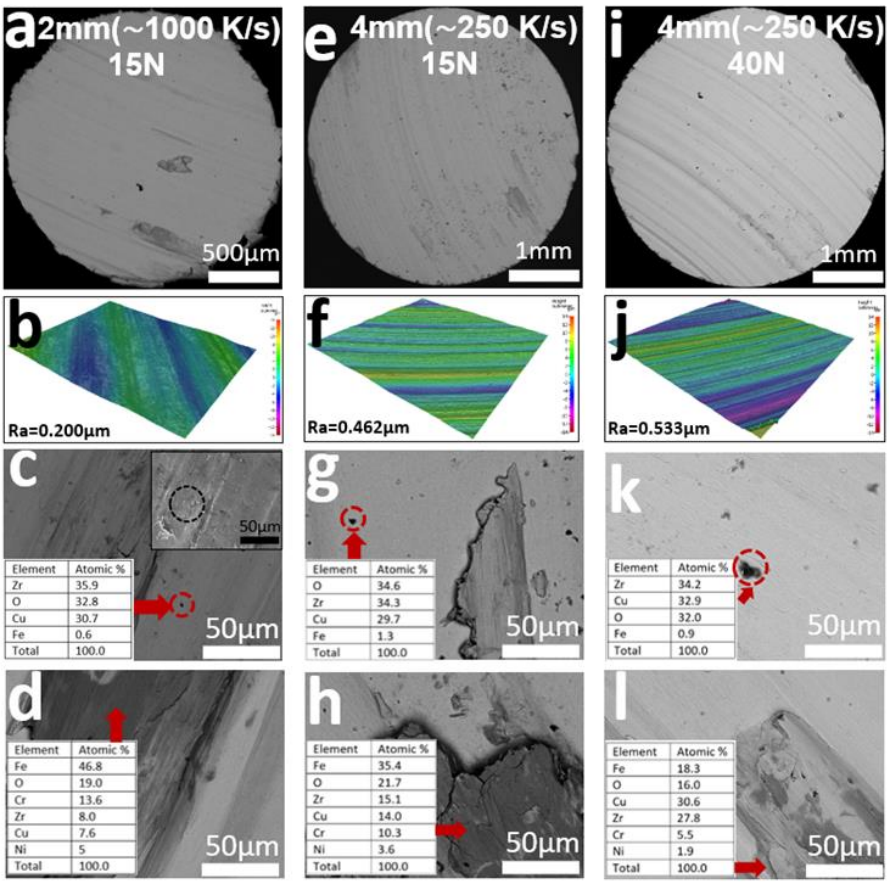

Fig. 7. 6. SEM images from $Cu_{49.5}Zr_{50}Fe_{0.5}$ pin: (a) General image for 2 mm and 15 N load; (b) and (c) details showing dark particles and smeared patches respectively; (d) General image for 4 mm and 15 N load; (e) and (f) details showing dark particles and smeared patches respectively; (g) General image for 4 mm and 40 N load; (h) and (i) details showing dark particles and smeared patches respectively.

However, for the high cooling rate sample, the surface is smoother and free of significant debris (**Fig. 7.6a**), thus suggesting lower presence and release of abrasive intermetallic particles, which is consistent with the XRD scans (**Fig. 7.1a, c and e**). In general, for two materials with the same phase composition one could expect higher hardness (i.e., higher yield strength) and hence room temperature wear resistance for the sample cooled faster, i.e., 2 mm diameter, due to microstructural refinement. However, differences in cooling

rate not only have an effect in the nature but also in the volume fraction of the phases formed. The larger volume fraction of intermetallic crystallites for the 4 mm diameter samples, which are harder than B2 CuZr austenite or B19' and B33 CuZr martensites are responsible for the enhanced wear resistance. Another important difference is that while for the high cooling rate samples subsurface cracks are present (inset of **Fig. 7.6c**), no such features are observed for the low cooling rate samples. The presence of these cracks is associated with plastic deformation (as well as surface fatigue) and therefore the contact stress is high enough to transform austenite into martensite. In addition, the subsurface cracks propagate under surface fatigue loading and lead to delamination (i.e., lamellar wear particles) [206] as previously observed in alloys of similar composition (e.g., $Cu_{45.5}Zr_{51}Al_{3.5}$ at. % alloy [32]). This delamination is responsible for the large amount of material loss displayed by the 2 mm diameter sample (**Fig. 7.4**) since in the delamination process larger wear particles are removed compared to in abrasive wear. However, for the low cooling rate samples, no signs of plastic deformation are observed, and this is associated to the presence of abundant hard and brittle intermetallic phases. Additional features are the wear debris particles (see arrows for **Fig. 7.6c, Fig. 7.6g and Fig. 7.6k**) and smear patches (evidence of plastic deformation dominated adhesive wear - see arrows for **Fig. 7.6c, Fig. 7.6f and Fig. 7.6i**) detected on the surface of both samples. These patches are associated with the transfer of SS304 steel from the counterbody disc to the pins and therefore are indicative of adhesive wear of the counterface. The general images from the worn surfaces of the low cooling rate pin tested at 15 N (**Fig. 7.6e**) and 40 N (**Fig. 7.6i**) show similar features but for 40 N load the roughness is higher and the presence of smeared SS304 steel patches transferred from the disc counterface are rare. Both surfaces exhibit oxides (**Fig. 7.6g and 7.6k**) from the oxidation of the intermetallic particles released but they do not exbibit the subsurface cracks detected in the high cooling rate samples, thus suggesting that the wear mechanism for the low cooling rate samples is predominantly abrasion rather than delamination, additionally, the abundant presence of hard abrasive intermetallic particles such as $Cu_{10}Zr_7$, Cu_8Zr_3 and $CuZr_2$ contribute greatly towards abrasion being the dominant wear mechanism for low cooling rate samples. When testing at 40 N, the steel transfer patches attached to the pin are about 3 times richer in Cu and Zr (see EDX from **Fig. 7.6l**) than when testing at 15 N (see

EDX from **Fig. 7.6h**). The Cu and Zr originates from the $Cu_{49.5}Zr_{50}Fe_{0.5}$ pin, which wears out about 3 times more at 40 N than at 15 N load (see length loss in **Fig. 7.4**). However, the intermixing of stainless steel with Cu and Zr during transfer is not homogeneous as can be deduced from the areas of different grey colouration of the patch shown in the backscattered SEM image of **Fig. 7.6l**. This steel patch contains mostly light grey areas which is due to a high content of elements with relatively high atomic number, Cu (30.6 at. %) and Zr (27.8 %) that mix during the wear test thus turning these patches into a composite of stainless steel with Cu and Zr. The patch also contains some isolated darker areas which are richer in chromium and iron, elements of lower atomic number present in the stainless steel, and poorer in Cu and Zr. The low number of patches on the pin surface when testing at 40 N is attributed to the lower ability of these composite patches to attach and spread because they should be more stiff and less ductile than the more Fe-rich patches attached when testing at 15 N load. The reason is that, according to the rule of mixtures, the properties of the composite patches approach to those of the CuZr intermetallic phases as they get richer in intermetallic phases.

An important parameter to assess the tribological performance is the coefficient of friction (COF) since it provides information about the resistance encountered when moving one object over another [86]. In many cases, a small value of the COF suggests high wear resistance, i.e., small material loss [210]. During the wear test experiments, the evolution of the COF exhibits two stages. The first stage is unstable and is characterized by a rapid increase of COF for a short time at the start of the test and is associated with establishing the transfer layer and the surface roughness, followed by a second steady state stage which represents most of the duration of the test. **Fig. 7.7** shows the comparison of evolution of COF over time, from 600 to 3600 s, for $Cu_{50}Zr_{50}$, $Cu_{49.5}Zr_{50}Fe_{0.5}$ and $Cu_{49}Zr_{50}Fe_{1}$ when tested at 15 N load for the 2 mm diameter samples (**Fig. 7.7a**) and for the 4 mm diameter samples tested at 15 N (**Fig. 7.7b**) and 40 N (**Fig. 7.7c**) load.

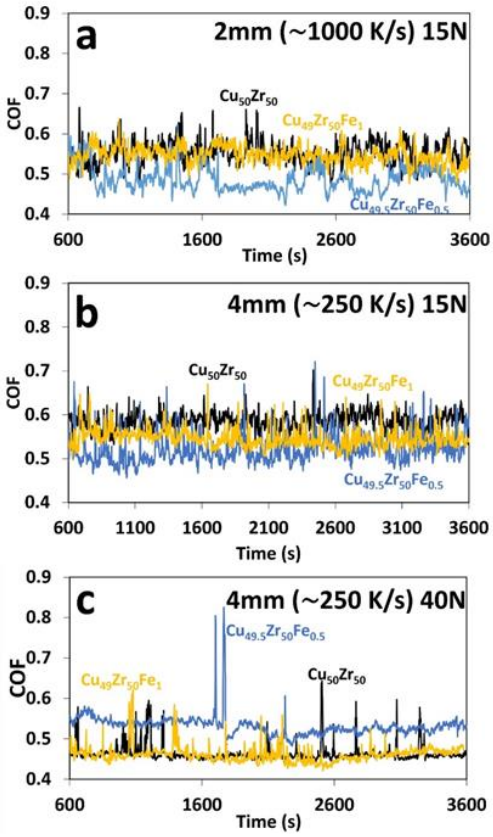

Fig. 7. 7. The COF as a function as a function of the wear time, from 600 to 3600 seconds during the steady-stage state for the 2 mm (~1000 K/s) and 4 mm (~250 K/s) samples.

For high cooling rate samples at 15 N load, the lowest COF is 0.47 and corresponds to the $Cu_{49.5}Zr_{50}Fe_{0.5}$ alloy. This is attributed to the work-hardening effect of the martensitic transformation of B2 CuZr austenite promoted by the presence of Fe in solid solution. For the 4 mm diameter sample at 15 N load (**Fig. 7.7b**) the values of the COF are practically the same, which is consistent with the similar wear rate data (**Fig. 7.4**). Finally, for the low cooling rate samples tested at 40 N, the $Cu_{49.5}Zr_{50}Fe_{0.5}$ exhibits the highest COF, around 0.53 compared to about 0.48 for $Cu_{50}Zr_{50}$ and $Cu_{49}Zr_{50}Fe_1$. The difference in COF is because when the load increases, the effect of deformation of the microstructure becomes more significant. Since the $Cu_{49.5}Zr_{50}Fe_{0.5}$ alloy contains less intermetallic phases and more easily deformable as-cast B33 martensite than $Cu_{50}Zr_{50}$ and $Cu_{49}Zr_{50}Fe_1$, its COF is higher, i.e., 0.53, and its wear rate (pin length loss, i.e., 0.128 mm) is the highest (**Fig. 7.4**). These COF values are close to those reported in the literature, from about 0.4 to 0.6 for $Cu_{60}Zr30Ti_{10}$ at. % [211] and about 0.35 to 0.45 for a

Cu-BMG (bulk metallic glass), of similar composition to the alloys of this work, when sliding against EN26 steel [205].

The correlation between the microstructure and the mechanical performance (wear and hardness) are discussed in more detail here. Typically, faster cooling rate results in a refined microstructure and therefore in an enhancement of the yield strength [224]. At the same time, an increase of the yield strength results in a hardness increase, estimated from Tabor's relationship σ_y = H/3 and therefore enhancement of the wear resistance. However, this trend is not followed for the $Cu_{50}Zr_{50}$ alloy for three reasons, first because at high cooling rate abundant ductile austenite metastable B2 phase is retained, second because not all materials contain a stress-induced martensite phase associated with work-hardening that can be tuned by microalloying and third because a small decrease of the cooling rate to 250 K/s results in the formation of wear resistant intermetallic phases. After wear testing at 15N, high cooling rate samples containing 0.5% Fe exhibit work-hardening and martensitic transformation as explained in Fig. 4. The relatively small wear rate of high cooling rate samples of this composition compared to other alloys is attributed to the effect of martensitic transformation. This can be seen from **Fig. 7.8a** where an increase in intensity of the XRD peak associated to B19' martensite (at angle 35.6º) after the wear test is observed compared to the intensity of the same peak in the as-cast condition, before wear testing (**Fig. 7.1c**).

XRD scans provide an overall analysis of the microstructure, however, for greater in-depth analysis, TEM has been performed for 2mm $Fe_{0.5}$ after testing at 15 N load. A bright field TEM image and corresponding Selected Area Electron Diffraction (SAED) pattern from the phase indicated by the arrow show the presence of twinned B19' CuZr martensite. The increase in volume fraction of this phase is responsible for the hardness increase (**Fig. 7.5**) and enhanced wear resistance (**Fig. 7.4**). In the case of the 4mm diameter sample with 0.5% Fe, the wear resistance is relatively low due to presence of the B33 martensite phase (at angle 36.1º) in the as-cast condition (**Fig. 7.1d**). This can also be observed after testing at 15N (see XRD of **Fig. 7.8b**) where high-volume fraction of B33 and intermetallic phases are present in the worn sample. These results agree with

the TEM analysis (inset **Fig. 7.8b**) where the $Cu_{10}Zr_7$ intermetallic is detected and indexed.

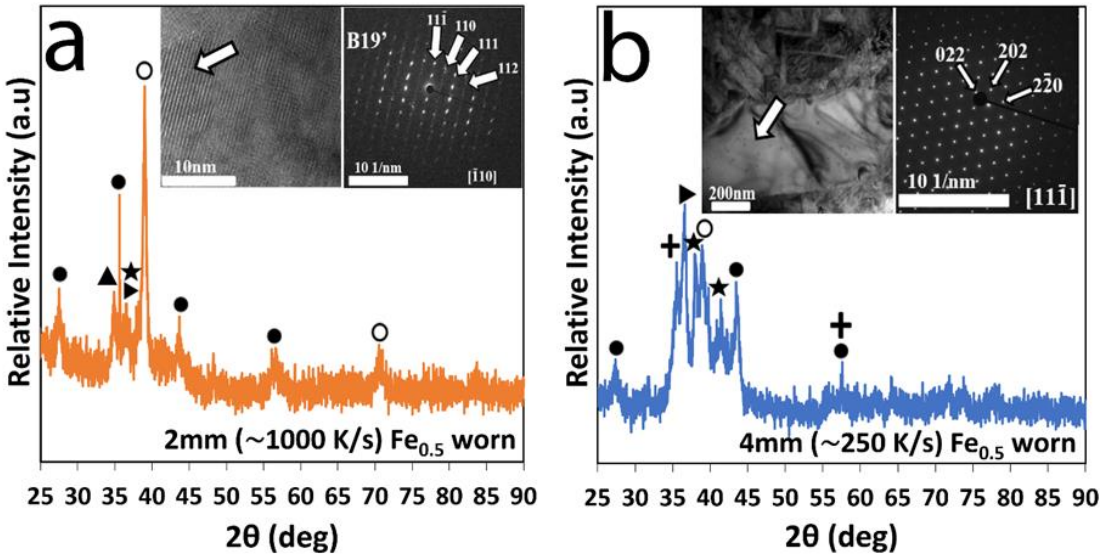

Fig. 7. 8. XRD scan of: (a) 2mm (~1000K/s); (b) 4 mm diameter (~250K/s) $Fe_{0.5}$ sample after being wear tested at 15N. Insets show bright field TEM image of a representative area (see arrow) and corresponding SAED pattern: (a) B19' phase with zone axis [-110]; (b) $Cu_{10}Zr_7$ phase with zone axis [11-1]. Symbols: ★$Cu_{10}Zr_7$,○B2 CuZr (Aust.), ▲Cu_8Zr_3, ►$CuZr_2$, •B19' CuZr (Mart.), + B33 CuZr (Mart.).

The B33 martensite phase was previously detected in CuZr alloys by Zhou and Napolitano [54] and they assigned to it a new superstructure (S) with space group Cmcm. However, the effect of B33 phase on the wear and mechanical performance has not been studied before. Our results indicate that when the cooling rate is ~1000 K/s (2mm diameter pins), no XRD peaks associated to B33 where detected (see **Fig. 7.1a, c and e**). On the other hand, when cooling rate drops to ~250 K/s (4mm diameter pins), XRD peaks of B33 appear in the as-cast condition as can be seen in (**Fig. 7.1b, d and f**). This agrees with the observation from Yue et al. [225] where it was found that B33 tends to form and stabilise after structural relaxation, meaning that when cooling rate drops from 1000 K/s to 250 K/s, the chances of formation and stabilisation of the B33 phase dramatically increases. The presence of B33 plays an important role in the wear performance of CuZr SMAs. For example, when the pressure on the pin is equivalent for both diameter sizes (i.e., 3.2 MPa) as can be seen in **Fig. 7.4**, the pin length loss for 2 mm diameter samples containing 0.5% Fe is 0.09 mm while for 4mm samples of the same

composition is 0.12 mm. The small length loss for the 2 mm samples is attributed to the transformation to the B19' martensite as can be seen in XRD after testing (see **Fig. 7.8a**). Meanwhile, the high pin length loss (0.12 mm) for the 4 mm sample is attributed to the presence of B33 martensite (see **Fig. 7.8b**). This is a significant finding since for 4 mm diameter $Cu_{50}Zr_{50}$ and Fe_1 the wear resistance was smaller than for the other two compositions of 2 mm diameter due to the higher volume fraction of the hard intermetallic multiphase. There is also an agreement between the COF and the wear resistance. The $Cu_{50}Zr_{50}$, $Cu_{49.5}Zr_{50}Fe_{0.5}$, and $Cu_{49}Zr_{50}Fe_1$ alloys of **Fig. 7.7** show a clear decrease in COF with increase in hardness (**Fig. 7.5**) and wear resistance (**Fig. 7.4**). Zhao et al. [226] have investigated the relationship of between wear resistance of NiTi SMAs and COF. It was found that samples that exhibited better wear resistance also exhibited the lowest COF, which agrees with our results. Other researchers [227, 228] have also observed the same trend. The correlation between the hardness and wear resistance observed for $Cu_{50}Zr_{50}$, $Cu_{49.5}Zr_{50}Fe_{0.5}$, and $Cu_{49}Zr_{50}Fe_1$ alloys are consistent with Archard's equation [203].

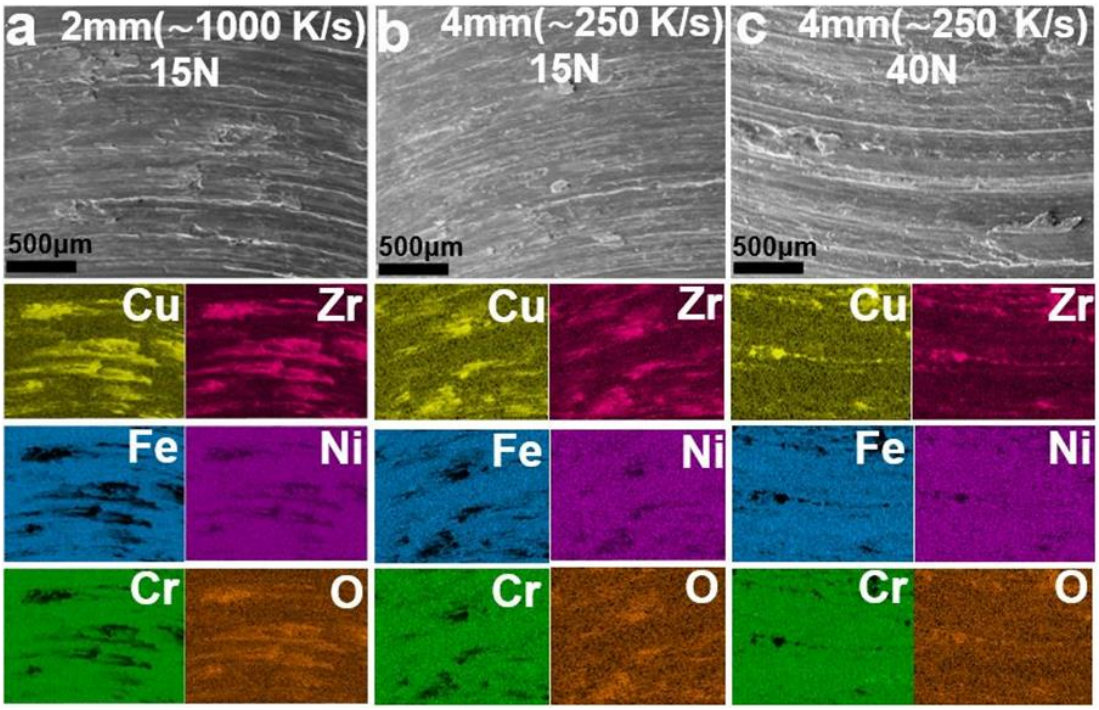

Fig. 7. 9. SEM backscattered image of SS304 counterbody worn disc after testing the $Cu_{49.5}Zr_{50}Fe_{0.5}$ alloy at the following conditions: (a) 2 mm (~1000 K/s) sample at 15 N; (b) 4 mm (~250 K/s) at 15 N; (c) 4 mm (~250 K/s) at 40 N load for 1 hour. In addition, the corresponding compositional X-ray mappings for Cu, Zr, Fe, Ni Cr and O are shown.

Considering that in sliding wear it is important to analyse the performance of the entire tribosystem, the surfaces of the SS304 counterbody after the wear tests with $Cu_{49.5}Zr_{50}Fe_{0.5}$ have been analysed (**Fig. 7.9**).

For the high cooling rate sample tested at 15 N load for 1 h (**Fig. 7.9a**) the general image (**Fig. 7.9a**) shows a homogeneous distribution of transfer patches across the track width that according to the mapping contain Cu and Zr. This confirms full contact between the pin surface and the disc and therefore the validity of the wear test results. When comparing the surface morphology of the 2 mm samples tested at 15 N (**Fig. 7.9a**) with the low cooling rate samples tested at 40 N (**Fig. 7.9c**) for $Cu_{49.5}Zr_{50}Fe_{0.5}$, there are larger patches oriented along the track direction at the lower load. These CuZr patches originate mostly from the B2 CuZr austenite and B19' CuZr martensite dendrites and therefore they are relatively ductile compared to the intermetallic phases and therefore can be easily smeared along the track. For the low cooling rate samples, the higher volume fraction of hard and brittle $Cu_{10}Zr_7$, Cu_8Zr_3 and $CuZr_2$ intermetallic phases make transfer of the CuZr more difficult and reduce its spread on the steel disc thus resulting in more discontinuous round transfer patches at 40 N load than for high cooling rate sample at 15 N test load. The volume fraction of phases in the 2 and 4mm diameter samples will be further discussed in section 7.4. The morphology of the disc after testing with the 4 mm diameter pin at 15 N (**Fig. 7.9b**) exhibits intermediate features between those of the 2 mm sample at 15 N and 4 mm sample at 40 N.

The results show that microalloying as a strategy to enhance the wear resistance of CuZr shape memory alloys is only useful when the cooling rate is fast enough (~1000 K/s) to attain a microstructure consisting mostly of retained austenite. This microstructure can be useful to develop shape memory components such as microactuators. However, fabrication of these components at a slower cooling rate (250 K/s) would lead to the formation of crystalline phases such as intermetallics that do not show the shape memory effect, and therefore are not useful for microactuator applications. In this work it has been shown that 0.5 at. % Fe addition is useful to enhance the wear resistance of the CuZr SMA obtained at a cooling rate of ~1000 K/s by promoting the transformation of the B2 CuZr austenite into stress-induced B19' CuZr martensite leading to work-hardening.

However, partial replacement of Cu by 0.5 at. % Fe has a detrimental effect on the wear resistance when the alloy is obtained at a slower cooling rate of about 250 K/s since in this case the 0. 5 at. % Fe promotes the formation of B33 CuZr martensite upon casting, i.e., a phase which is much softer than the stress-induced martensite formed at higher cooling rates.

7.3. Effect of the cooling rate and microalloying on the nature and volume fraction of crystalline phases

To understand the combined effect of the cooling rate and microalloying on the mechanical performance of CuZr based SMAs, **Fig. 7.10** presents in a simple schematic the microstructures formed upon cooling at ~1000K/s (2 mm) and ~250K/s (4mm). This schematic illustrates the volume fraction and nature of the formed crystalline phases upon cooling at different rates.

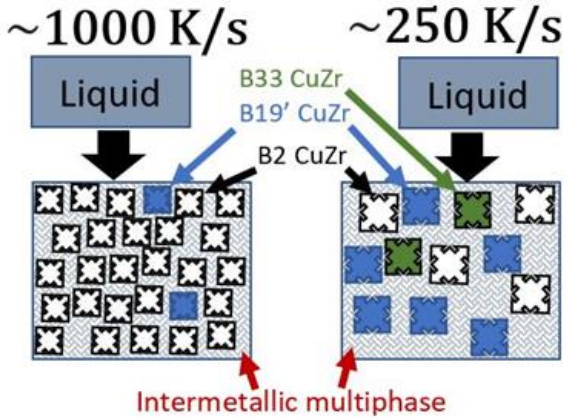

Fig. 7. 10. Schematic of the microstructure for the two different cooling rates for the 2 mm (~1000K/s) and 4 mm (~250K/s) diameter samples.

When the molten material solidifies at ~1000K/s, the metastable B2 CuZr phase is mostly retained, as previously reported [229] but this cooling rate is not fast enough to prevent the crystallization of the more stable phases B19' and the intermetallic multiphase as proven in XRD scans shown in **Fig. 7.1a, c and e**. However, at a cooling rate of ~250K/s the stable intermetallic multiphase dominates the microstructure followed by B19' and B33 martensites, although the more metastable B2 CuZr is still present, this is also proven in the XRD scans of the as cast samples in **Fig. 7.1b, d and f**. The volume fractions of these phases, estimated from XRD results are summarized in **Fig. 7.11**, where the volume fraction of B2 CuZr phase is in the range 69-89 % vol. for the 2 mm diameter

sample while for the 4 mm diameter samples about 62-69 % of the volume is the intermetallic multiphase [149, 229] with some B2 CuZr austenite, from 13 to 18 %, retained. In addition, the alloy with 0.5 % Fe contains about 25 % martensite by volume, most of which corresponds to the B33 phase, being responsible for the relatively low wear resistance of this alloy.

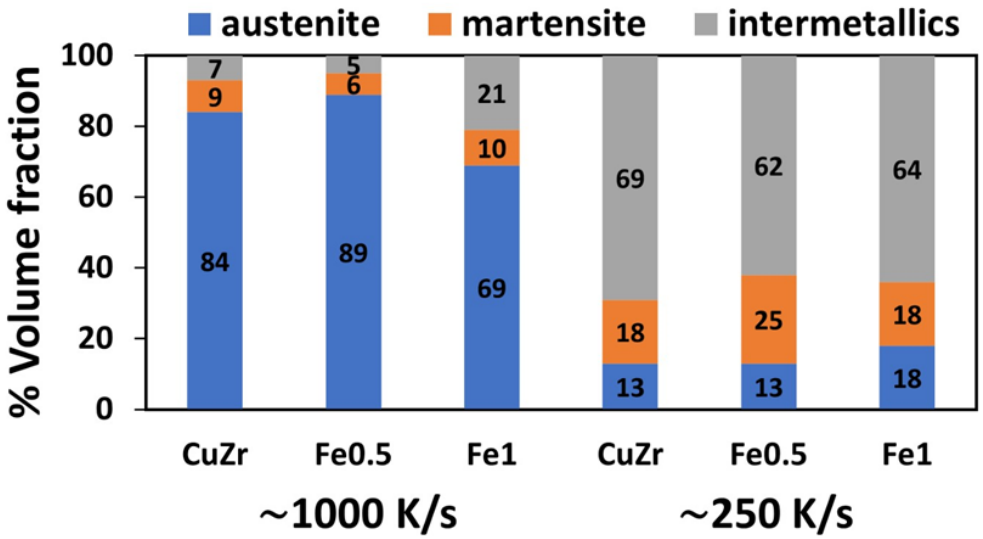

Fig. 7. 11. Volume fraction of austenite, martensite (B19' and/or B33) and intermetallic phases for 2 mm (~1000K/s) and 4 mm diameter (~250 K/s) as cast $Cu_{50}Zr_{50}$, $Cu_{49.5}Zr_{50}Fe_{0.5}$, $Cu_{49}Zr_{50}Fe_1$ alloys.

7.4. Conclusions

The following conclusions can be drawn:

1. The combined effect of cooling rate (i.e., 2 mm and 4 mm diameter samples: ~1000 K/s and: ~250 K/s respectively) and microalloying with Fe (i.e., $Cu_{50}Zr_{50}$, $Cu_{49.5}Zr_{50}Fe_{0.5}$ and $Cu_{49}Zr_{50}Fe_1$) results in microstructural differences. For the highest cooling rate sample, the microstructure consists mostly of retained B2 austenite (from 68 to 89 %) and microalloying does not have an appreciable effect on the microstructure. For the slowest cooling rate, the 4 mm diameter sample, the dominant phase is the intermetallic multiphase $Cu_{10}Zr_7$, Cu_8Zr_3 and $CuZr_2$ (from 64 to 69 %) and addition of 0.5 at. % Fe promotes the formation of the more stable B33 CuZr phase.

2. The combined effect of cooling rate and microalloying affects the wear performance of $Cu_{50}Zr_{50}$, not only because of the differences in microstructure but also because Fe can enter into solid solution in the metastable B2 CuZr phase. For example, for the high cooling rate samples, despite the microstructure being basically the same for all compositions, the fact that 0.5 at. % Fe decreases the SFE of B2 phase and thus promotes the formation of B19' martensite upon wear testing, improves the wear resistance of the alloy. However, for the low cooling rate samples, microalloying with 0.5 at. % Fe results in a large increase in volume fraction of B33 phase that decreases the wear resistance of the alloy. It is interesting to observe that there is no linear trend between the concentration in Fe and the stabilization of the B33 phase since for $Cu_{50}Zr_{50}$, and $Cu_{49}Zr_{50}Fe_1$ alloys the concentration of B33 phase is similar thus resulting in similar wear resistance.

3. Some differences in the wear mechanism are observed for 2 mm and 4 mm diameter samples. Although for both sample diameters it is observed that there are long continuous grooves induced by ploughing, a common feature of abrasive wear, but there are some differences. For the high cooling rate samples at 15 N load the signs of abrasive wear are relatively small while additional features consisting of subsurface cracks are observed. These features indicate that the wear mechanism is delamination characterized by the formation of lamellar wear debris. This is consistent with the relative low roughness of the wear surface, R_a = 0.200 μm, compared to the roughness for the low cooling rate samples for which only signs of abrasive wear are detected. This is especially true at the highest load of 40 N for which R_a = 0.533 μm since the presence of abundant $Cu_{10}Zr_7$, Cu_8Zr_3 and $CuZr_2$ hard intermetallic phases can form deep groves when they are dragged along the track.

4. From an engineering point of view, this chapter demonstrates that proper selection of a microalloying element, its nature and concentration, is not enough to enhance the wear resistance of $Cu_{50}Zr_{50}$ SMA. Proper selection of the cooling rate upon casting is needed to guarantee success. Not only the cooling rate has to be fast enough to retain the microalloying element in solid solution, which also occurs in the 4 mm sample, but to prevent growth of undesirable phases. For example, as shown in this

work, microalloying with 0.5 at. % Fe enhances the wear resistance when the cooling rate is ~1,000 K/s but diminishes the wear resistance of the parent $Cu_{50}Zr_{50}$ alloy when the cooling rate is ~250 K/s. In this case, microalloying with the same element and concentration has a detrimental effect. Therefore, this should be taken into consideration at industrial scale during the fabrication process by using a suitable cooling system.

Chapter 8 – Summary and future directions

NiTi SMAs have been widely used for various engineering applications due to their remarkable stability, practicability, high recovery ratio and superior thermo-mechanical performance. However, researchers have started to investigate other alloy systems to replace NiTi due to its high cost and inability to operate at high temperature environment. Various alloy systems with relatively cheaper elements have been investigated by researchers over the years such as…, however high temperature SMA CuZr has not been investigated with different microalloying elements that can enhance its mediocre performance.

The prime aim of this thesis was to assess the improved CuZr based SMAs after microalloying and tuning of cooling rate control in terms of wear performance. The scares research in the field of wear and tribological performance of CuZr SMAs made it difficult to examine the results against previous literature, however, with the use of material characterisation techniques and post testing analysis (XRD, SEM, EDX, DSC, TEM, etc…) it was possible to compare the change of newly obtained CuZr based SMAs compared to nominal composition $Cu_{50}Zr_{50}$.

In summary, the following points are studied in this **thesis to fill a gap in knowledge**

- The possibility of addition of Co as microalloying element at certain atomic % in order to lower SFE (i.e. 0.5 at.%) of B2 CuZr.
- Addition of Co as a microalloying element at different concentration (i.e., 1 at.%) does not have similar effect to 0.5 at.% in terms of lowering SFE and therefore promoting martensitic transformation.
- Wear performance of CuZr and CuZr based SMAs at RT and high temperature (above austenitic transformation temperature) in order to validate the operating temperature range of high temperature CuZr SMAs.
- CuZr SMAs are considered high temperature alloys, however, the austenitic transformation is responsible for transforming hard martensite into soft austenite. This thesis highlights that a relatively low temperature of 100^{o}C can be enough to

transform martensite into austenite, therefore the benefit of microalloying at 100^{o}C is disregarded.

- Introduction of low-cost Fe 0.5 at.% as a microalloying element enhances the wear performance of CuZr SMAs.
- Proper selection of a microalloying element, its nature and concentration, is not enough to enhance the wear resistance of $Cu_{50}Zr_{50}$ SMA, cooling rate control is also crucial. For example, cooling $Cu_{49.5}Zr_{50}Fe_{0.5}$ rapidly (i.e., 2mm diameter rods) enhances wear performance through promoting martensitic transformation as well as preventing growth of undesirable phases. However, when obtaining 4mm diameter rods of the same composition, the undesirable phases, namely B33, contribute towards lowering wear performance.

Future work recommendations:

- The investigation of corrosion behaviour of high temperature CuZr and possibility of enhancing it as well as understanding the effect of temperature on corrosion performance.
- The role of Fe to CuZr in corrosive environment and whether its presence in enhancing martensitic transformation outweighs its issues in corrosive environment.
- In depth comparisons of other HTSMA alloy systems and their ability to outperform CuZr SMAs considering the operating temperature range largely limits the ability to use SMAs at high temperature.
- Possibility of using relatively lower cost CuZr based SMAs for medical applications (i.e., implants) and an investigation of their antimicrobial behaviour.
- The principle used to enhance tribological performance of CuZr based SMAs comes from lowering SFE, this principle is not applied to Fe based SMAs. It is important to understand if lowering SFE of Fe based SMAs can enhance mechanical performance considering the low cost of Fe.

Presentation and publications

Publications

- Younes, A., Nnamchi, P., Medina, J., Pérez, P., Villapún, V.M., Badimuro, F., Kamnis, S., Jimenez-Melero, E. and Gonzalez, S., 2020. Wear rate at RT and 100° C and operating temperature range of microalloyed $Cu_{50}Zr_{50}$ shape memory alloy. *Journal of Alloys and Compounds*, *817*, p.153330.
- Younes, A., De la Flor, S., Clark, S.J., Nutter, J., Birkett, M., Watson, J.O., Unthank, M. and Gonzalez, S., 2021. Tribological Behavior of Microalloyed $Cu_{50}Zr_{50}$ Alloy. *Journal of Tribology*, *144*(2), p.021706.
- Nnamchi, P., Younes, A. and González, S., 2019. A review on shape memory metallic alloys and their critical stress for twinning. *Intermetallics*, *105*, pp.61-78.
- De Luca, F., Nnamchi, P., Younes, A., Fry, A.T. and González, S., 2019. Stress-induced martensitic transformation of $Cu_{50}Zr_{50}$ shape memory alloy optimized through microalloying and co-microalloying. *Journal of Alloys and Compounds*, *781*, pp.337-343.
- Unravelling the combined effect of cooling rate and microalloying on the microstructure and tribological performance of $Cu_{50}Zr_{50}$ – “Under review”

Presentations

Oral presentation: Webinar on “Materials Science and Nanotechnology” held in March 24-25, 2021. Title of the presentation: “Wear Rate of Microalloyed $Cu_{50}Zr_{50}$ Shape Memory Alloy at RT and 100^{o}C”

Oral presentation: Webinar on “5th International Conference on Materials Research and Nanotechnology” in March 7-8. 2022. Title of the presentation: “Tuning the tribological performance of $Cu_{50}Zr_{50}$ through microalloying”

Poster presentation: F. De Luca, P. Nnamchi, A. Younes, A.T. Fry, S. González. “Stress-induced martensitic transformation of $Cu_{50}Zr_{50}$ shape memory alloy through microalloying and co-microalloying”. Boston, US, MRS Fall Meeting 2018, November 25-30.

References:

1. Mehta, K. and K. Gupta, *Fabrication and processing of shape memory alloys*. 2019: Springer.
2. Duerig, T.W., K. Melton, and D. Stöckel, *Engineering aspects of shape memory alloys*. 2013: Butterworth-Heinemann.
3. Duerig, T.W., et al., *Engineering aspects of shape memory alloys*. 1st ed. 1990, London: Butterworth-Heinemann.
4. Lecce, L., *Shape memory alloy engineering: for aerospace, structural and biomedical applications*. 2014: Elsevier.
5. Ölander, A., *An electrochemical investigation of solid cadmium-gold alloys.* Journal of the American Chemical Society, 1932. **54**(10): p. 3819-3833.
6. Greninger, A.B. and A.R. Troiano, *Orientation habit of martensite.* Nature, 1938. **141**(3557): p. 38-38.
7. Chang, L. and T. Read, *Plastic deformation and diffusionless phase changes in metals—The gold-cadmium beta phase.* JOM, 1951. **3**(1): p. 47-52.
8. Basinski, Z. and J. Christian, *Experiments on the martensitic transformation in single crystals of indium-thallium alloys.* Acta metallurgica, 1954. **2**(1): p. 148-166.
9. Buehler, W.J. and R.C. Wiley, *Nickel-Base Alloys*. 1965, DEPARTMENT OF THE NAVY WASHINGTON DC.
10. Han, D., et al., *A good strength-ductility match in Cu-Mn alloys with high stacking fault energies: Determinant effect of short range ordering.* Scripta Materialia, 2017. **133**: p. 59-64.
11. Liu, R., et al., *Extremely-low-cycle fatigue behaviors of Cu and Cu–Al alloys: Damage mechanisms and life prediction.* Acta Materialia, 2015. **83**: p. 341-356.
12. Asgari, S., et al., *Strain hardening regimes and microstructural evolution during large strain compression of low stacking fault energy fcc alloys that form deformation twins.* Metallurgical and Materials Transactions A, 1997. **28**(9): p. 1781-1795.
13. Wayman, C.M., *On memory effects related to martensitic transformations and observations in β-brass and Fe3Pt.* Scripta Metallurgica, 1971. **5**(6): p. 489-492.
14. Elahinia, M.H., *Shape memory alloy actuators: design, fabrication, and experimental evaluation*. 2016: John Wiley & Sons.
15. Maruyama, T. and H. Kubo, *12 - Ferrous (Fe-based) shape memory alloys (SMAs): properties, processing and applications*, in *Shape Memory and Superelastic Alloys*, K. Yamauchi, et al., Editors. 2011, Woodhead Publishing. p. 141-159.
16. Hong, K., et al., *Evaluation of Fe-Based Shape Memory Alloy (Fe-SMA) as Strengthening Material for Reinforced Concrete Structures.* Applied Sciences, 2018. **8**(5): p. 730.
17. Hong, K.-N., et al., *Recovery Behavior of Fe-Based Shape Memory Alloys under Different Restraints.* Applied Sciences, 2020. **10**(10): p. 3441.
18. Kauffman, G.B. and I. Mayo, *The Story of Nitinol: The Serendipitous Discovery of the Memory Metal and Its Applications.* The Chemical Educator, 1997. **2**(2): p. 1-21.
19. Safranski, D., K. Dupont, and K. Gall, *Pseudoelastic NiTiNOL in Orthopaedic Applications.* Shape Memory and Superelasticity, 2020. **6**(3): p. 332-341.
20. Facts, C.E.; Available from: https://www.chemicool.com/elements/copper.html.
21. Lenntech. Available from: https://www.lenntech.com/periodic-chart-elements/melting-point.htm.
22. Kumar, P. and D. Lagoudas, *Introduction to shape memory alloys*, in *Shape memory alloys*. 2008, Springer. p. 1-51.

23. López, G.A., *Shape Memory Alloys 2020.* Metals, 2021. **11**(10): p. 1618.
24. Kim, Y.-S., et al., *Effect of composition and cooling rate on microstructure and tensile properties of Sn–Zn–Bi alloys.* Journal of Alloys and Compounds, 2003. **352**(1): p. 237-245.
25. Wang, H., *Synthesis, microstructure and mechanical behaviour of CuZr-based bulk metallic glass composites*. 2019, University of Sheffield.
26. Otsuka, K. and C.M. Wayman, *Shape memory materials*. 1999: Cambridge university press.
27. Reyes-Morel, P.E. and I.-W. Chen, *Stress-Biased Anisotropic Microcracking in Zirconia Polycrystals.* Journal of the American Ceramic Society, 1990. **73**(4): p. 1026-1033.
28. Pauly, S., *Phase formation and mechanical properties of metastable Cu-Zr-based alloys.* 2010.
29. Zanaboni, E., F. Auricchio, and V. Massarotti, *One Way and Two Way–Shape Memory Effect: Thermo–Mechanical Characterization of Ni–Ti wires*, in *Department of Structural Mechanics*. 2008, University of Pavia: Pavia, Italy. p. 29.
30. Jani, J.M., et al., *A review of shape memory alloy research, applications and opportunities.* Materials & Design (1980-2015), 2014. **56**: p. 1078-1113.
31. Younes, A., et al., *Wear rate at RT and 100 °C and operating temperature range of microalloyed Cu50Zr50 shape memory alloy.* Journal of Alloys and Compounds, 2020. **817**: p. 153330.
32. Villapún, V.M., et al., *Strategy for preventing excessive wear rate at high loads in bulk metallic glass composites.* Materials & Design, 2017. **135**: p. 300-308.
33. Laureanda, C., *One Way and Two Way–Shape Memory Effect: Thermo–Mechanical Characterization of Ni–Ti wires*. 2008, Ph. D. thesis, Universitá degli Studi di Pavia.
34. Antonopoulos, J.G., et al., *Dislocation movements and deformation twinning in zinc.* Acta Metallurgica, 1988. **36**(9): p. 2493-2502.
35. *Slip and twinning*. Available from: https://www.slideshare.net/GopinathGuru3/slip-and-twiniing.
36. Wang, L., et al., *The effect of twinning and detwinning on the mechanical property of AZ31 extruded magnesium alloy during strain-path changes.* Materials & Design, 2014. **63**: p. 177-184.
37. Rogers, C. and H. Robertshaw, *Shape memory alloy reinforced composites.* Engineering Science Preprints, 1988. **25**: p. 20-22.
38. Ashby, M.F., *Boundary defects, and atomistic aspects of boundary sliding and diffusional creep.* Surface Science, 1972. **31**: p. 498-542.
39. Nnamchi, P., A. Younes, and S. González, *A review on shape memory metallic alloys and their critical stress for twinning.* Intermetallics, 2019. **105**: p. 61-78.
40. Yan, H., et al., *Variant organization and mechanical detwinning of modulated martensite in Ni–Mn–In metamagnetic shape-memory alloys.* Acta Materialia, 2016. **111**: p. 75-84.
41. Pauly, S., et al., *Transformation-mediated ductility in CuZr-based bulk metallic glasses.* Nature Materials, 2010. **9**(6): p. 473-477.
42. Blewitt, T., R. Coltman, and J. Redman, *Low ‐temperature deformation of copper single crystals.* Journal of Applied Physics, 1957. **28**(6): p. 651-660.
43. Suzuki, H. and C. Barrett, *Deformation twinning in silver-gold alloys.* Acta metallurgica, 1958. **6**(3): p. 156-165.
44. Haasen, P., *Plastic deformation of nickel single crystals at low temperatures.* Philosophical Magazine, 1958. **3**(28): p. 384-418.
45. Gray Iii, G., *Deformation twinning in Al-4.8 wt% Mg.* Acta Metallurgica, 1988. **36**(7): p. 1745-1754.
46. Paxton, A. and A. Entwisle, *Deformation twinning in the intermetallic compound Cu2Sb.* Philosophical Magazine A, 1985. **52**(4): p. 573-579.
47. Pirouz, P., *Deformation mode in silicon, slip or twinning?* Scripta metallurgica, 1987. **21**(11): p. 1463-1468.

48. Androussi, Y., G. Vanderschaeve, and A. Lefebvre, *Slip and twinning in high-stress-deformed GaAs and the influence of doping.* Philosophical Magazine A, 1989. **59**(6): p. 1189-1204.
49. Allan, P., E. Crellin, and M. Bevis, *Stress-induced twinning and phase transformations in polyethylene single crystals.* Philosophical Magazine, 1973. **27**(1): p. 127-145.
50. Zhang, D., et al., *Deformation twinning (update).* Ref. Modul. Mater. Sci. Eng, 2016: p. 1-24.
51. Christian, J.W. and S. Mahajan, *Deformation twinning.* Progress in materials science, 1995. **39**(1-2): p. 1-157.
52. Abbaschian, R. and R.E. Reed-Hill, *Physical Metallurgy Principles-SI Version*. 2009: Nelson Education.
53. Nicholls, A.W., I.R. Harris, and W. Mangen, *Identification of phases resulting from the transformation of the intermetallic phase ZrCu.* Journal of Materials Science Letters, 1986. **5**(2): p. 217-220.
54. Zhou, S.H. and R.E. Napolitano, *Identification of the B33 martensite phase in Cu–Zr using first-principles and X-ray diffraction.* Scripta Materialia, 2008. **59**(10): p. 1143-1146.
55. Koval, Y.N., G.S. Firstov, and A.V. Kotko, *Martensitic transformation and shape memory effect in ZrCu intermetallic compound.* Scripta Metallurgica et Materialia, 1992. **27**(11): p. 1611-1616.
56. Seo, J.W. and D. Schryvers, *TEM investigation of the microstructure and defects of CuZr martensite. Part I: Morphology and twin systems.* Acta Materialia, 1998. **46**(4): p. 1165-1175.
57. Javid, F.A., N. Mattern, and J. Eckert, *Phase formation and martensitic transformation of cast Cu-Zr-Co alloys.* Verhandlungen der Deutschen Physikalischen Gesellschaft, 2011(Dresde2011issue): p. 1.
58. Dorin, T., A. Vahid, and J. Lamb, *Chapter 11 - Aluminium Lithium Alloys*, in *Fundamentals of Aluminium Metallurgy*, R.N. Lumley, Editor. 2018, Woodhead Publishing. p. 387-438.
59. Ciftci, N., et al., *Novel Cooling Rate Correlations in Molten Metal Gas Atomization.* Metallurgical and Materials Transactions B, 2019. **50**(2): p. 666-677.
60. Okamoto, H., *Journal of Phase Equilibria and Diffusion.* Section III: Supplemental Literature Review Al− B (Aluminum-Boron) Volume, 2007. **27**: p. 195-196.
61. Sato, Y., et al., *Predictive modeling of Time-Temperature-Transformation diagram of metallic glasses based on atomistically-informed classical nucleation theory.* Scientific Reports, 2017. **7**(1): p. 7194.
62. Wang, D., et al., *Bulk metallic glass formation in the binary Cu–Zr system.* Applied Physics Letters, 2004. **84**(20): p. 4029-4031.
63. Biffi, C., A. Figini, and A. Tuissi, *Influence of compositional ratio on microstructure and martensitic transformation of CuZr shape memory alloys.* Intermetallics, 2014. **46**: p. 4-11.
64. El-Eskandarany, M.S., *Mechanical Alloying: Nanotechnology, Materials Science and Powder Metallurgy*. 2015: Elsevier Science.
65. Klement, W., R.H. Willens, and P.O.L. Duwez, *Non-crystalline Structure in Solidified Gold–Silicon Alloys.* Nature, 1960. **187**(4740): p. 869-870.
66. Johnson, W.L., *Bulk Glass-Forming Metallic Alloys: Science and Technology.* MRS Bulletin, 1999. **24**(10): p. 42-56.
67. Inoue, A., B. Shen, and N. Nishiyama, *Development and applications of late transition metal bulk metallic glasses.* Bulk metallic glasses, 2008: p. 1-25.
68. Qin, C., W. Zhao, and A. Inoue, *Glass Formation, Chemical Properties and Surface Analysis of Cu-Based Bulk Metallic Glasses.* International Journal of Molecular Sciences, 2011. **12**(4): p. 2275-2293.
69. Suryanarayana, C. and A. Inoue, *Bulk metallic glasses*. 2017: CRC press.
70. Cahn, R.W., P. Haasen, and E.J. Kramer, *Materials science and technology—a comprehensive treatment.* International Journal of Materials Research, 1993. **84**(2): p. 90-90.

71. Zhang, Y.-h., et al., *An investigation on hydrogen storage kinetics of nanocrystalline and amorphous Mg2Ni1−xCox (x=0–0.4) alloy prepared by melt spinning.* Journal of Alloys and Compounds, 2011. **509**(6): p. 2808-2814.
72. Shechtman, D., et al., *Metallic Phase with Long-Range Orientational Order and No Translational Symmetry.* Physical Review Letters, 1984. **53**(20): p. 1951-1953.
73. Antonione, C., L. Battezzati, and F. Marino, *Quasi-crystalline and amorphous phases as products of the rapid solidification of Al80−xMn20Six alloys.* Journal of the Less Common Metals, 1988. **145**: p. 421-428.
74. Dong, Z.F., K. Lu, and Z.Q. Hu, *Formation and stability of a supersaturated solid solution phase formed during a melt-spinning process.* Nanostructured Materials, 1999. **11**(3): p. 351-360.
75. Kramer, M.J., et al., *Rapid solidification and metallic glass formation – Experimental and theoretical limits.* Journal of Non-Crystalline Solids, 2007. **353**(32): p. 3633-3639.
76. Gillen, A.G. and B. Cantor, *Photocalorimetric cooling rate measurements on a Ni-5 wt% A1 alloy rapidly solidified by melt spinning.* Acta Metallurgica, 1985. **33**(10): p. 1813-1825.
77. Jones, H., *Cooling rates during rapid solidification from a chill surface.* Materials Letters, 1996. **26**(3): p. 133-136.
78. Wang, G.X. and E.F. Matthys, *Experimental determination of the interfacial heat transfer during cooling and solidification of molten metal droplets impacting on a metallic substrate: effect of roughness and superheat.* International Journal of Heat and Mass Transfer, 2002. **45**(25): p. 4967-4981.
79. Christopher, N., K. Anand, and N. Singh, *Influence of cooling rate on the magnetic properties of Hf–Co–Fe–B melt-spun alloy.* Applied Physics A, 2020. **126**(8): p. 621.
80. Ashgriz, N., *Handbook of atomization and sprays: theory and applications*. 2011: Springer Science & Business Media.
81. Zheng, B., et al., *Gas atomization of amorphous aluminum powder: Part II. Experimental investigation.* Metallurgical and Materials Transactions B, 2009. **40**(6): p. 995.
82. Srivatsan, T.S., *Processing and fabrication of advanced materials, XVII: Volume One*. 2009: I.K. International Publishing House.
83. Yazici, Z.O., et al., *Effects of minor Cu and Si additions on glass forming ability and mechanical properties of Co-Fe-Ta-B Bulk metallic glass.* Metals and Materials International, 2016. **22**(1): p. 50-57.
84. Lin, X. and W. Johnson, *Formation of Ti–Zr–Cu–Ni bulk metallic glasses.* Journal of Applied Physics, 1995. **78**(11): p. 6514-6519.
85. Vitek, J.M., A. Dasgupta, and S.A. David, *Microstructural modification of austenitic stainless steels by rapid solidification.* Metallurgical Transactions A, 1983. **14**(9): p. 1833-1841.
86. Huang, Y., et al., *The effect of cooling rate on the wear performance of a ZrCuAlAg bulk metallic glass.* Materials & Design, 2014. **58**: p. 284-289.
87. Huang, W., *On the selection of shape memory alloys for actuators.* Materials & Design, 2002. **23**(1): p. 11-19.
88. Özkul, İ., E. Kalay, and C. Aksu Canbay, *The investigation of shape memory recovery loss in NiTi alloy.* Materials Research Express, 2019. **6**(8): p. 0865a5.
89. Cederström, J. and J. Van Humbeeck, *Relationship between shape memory material properties and applications.* Le Journal de Physique IV, 1995. **5**(C2): p. C2-335-C2-341.
90. Nishida, M., C.M. Wayman, and T. Honma, *Phase transformations in a Ti50Ni47.5Fe2.5 shape memory alloy.* Metallography, 1986. **19**(1): p. 99-113.
91. Zhang, Z., et al., *Orientation relationship between TiC carbides and B2 phase in as-cast and heat-treated NiTi shape memory alloys.* Materials Science and Engineering: A, 2006. **438-440**: p. 879-882.

92. Bastin, G.F. and G.D. Rieck, *Diffusion in the titanium-nickel system: I. occurrence and growth of the various intermetallic compounds.* Metallurgical Transactions, 1974. **5**(8): p. 1817-1826.
93. Khalil-Allafi, J., A. Dlouhy, and G. Eggeler, *Ni4Ti3-precipitation during aging of NiTi shape memory alloys and its influence on martensitic phase transformations.* Acta Materialia, 2002. **50**(17): p. 4255-4274.
94. Tang, W., et al., *New modelling of the B2 phase and its associated martensitic transformation in the Ti–Ni system.* Acta Materialia, 1999. **47**(12): p. 3457-3468.
95. Frenzel, J., et al., *Influence of Ni on martensitic phase transformations in NiTi shape memory alloys.* Acta Materialia, 2010. **58**(9): p. 3444-3458.
96. Tong, H.C. and C.M. Wayman, *Characteristic temperatures and other properties of thermoelastic martensites.* Acta Metallurgica, 1974. **22**(7): p. 887-896.
97. Lee, W.J., et al., *Phase transformation behavior under uniaxial deformation of an Fe–Mn–Si–Cr–Ni–VC shape memory alloy.* Materials Science and Engineering: A, 2013. **581**: p. 1-7.
98. Czaderski, C., et al., *Feasibility of iron-based shape memory alloy strips for prestressed strengthening of concrete structures.* Construction and Building Materials, 2014. **56**: p. 94-105.
99. Janke, L., et al., *Applications of shape memory alloys in civil engineering structures—Overview, limits and new ideas.* Materials and Structures, 2005. **38**(5): p. 578-592.
100. Sawaguchi, T., et al., *Vibration mitigation by the reversible fcc/hcp martensitic transformation during cyclic tension–compression loading of an Fe–Mn–Si-based shape memory alloy.* Scripta Materialia, 2006. **54**(11): p. 1885-1890.
101. Yang, J.H. and C.M. Wayman, *Development of Fe-based shape memory alloys associated with face-centered cubic-hexagonal close-packed martensitic transformations: Part III. microstructures.* Metallurgical Transactions A, 1992. **23**(5): p. 1445-1454.
102. Otsuka, H., et al., *Effects of alloying additions on Fe-Mn-Si shape memory alloys.* ISIJ international, 1990. **30**(8): p. 674-679.
103. Rong, L., et al., *Improvement of shape memory effect in Fe-Mn-Si alloy by Cr and Ni addition.* Scripta metallurgica et materialia, 1995. **32**(12).
104. Wang, Z., et al., *Effect of thermomechanical treatment on the two-way shape memory effect of NiTi alloy spring.* Materials Letters, 2002. **54**(1): p. 55-61.
105. Czaderski, C., et al. *Iron-based shape memory alloys (Fe-SMA)-a new material for prestressing concrete structures*. in *Conference paper*. 2015.
106. Wilkes, K.E. and P.K. Liaw, *The fatigue behavior of shape-memory alloys.* Jom, 2000. **52**(10): p. 45-51.
107. Gu, Q., et al., *Effect of amount of deformation on the martensitic transformation and shape memory effect in Fe-Mn-Si based shape memory steel.* Le Journal de Physique IV, 1995. **5**(C2): p. C2-311-C2-315.
108. Rojob, H. and R. El-Hacha, *Self-prestressing using iron-based shape memory alloy for flexural strengthening of reinforced concrete beams.* ACI Structural Journal, 2017. **114**(2): p. 523.
109. KAJIWARA, S., et al., *Remarkable improvement of shape memory effect in Fe-Mn-Si based shape memory alloys by producing NbC precipitates.* Scripta materialia, 2001. **44**(12): p. 2809-2814.
110. Farjami, S., K. Hiraga, and H. Kubo, *Shape memory effect and crystallographic investigation in VN containing Fe-Mn-Si-Cr Alloys.* Materials Transactions, 2004. **45**(3): p. 930-935.
111. Dong, Z., et al., *A Novel Fe-Mn-Si Shape Memory Alloy With Improved Shape Recovery Properties by VC Precipitation.* Advanced Engineering Materials, 2009. **11**(1‐2): p. 40-44.
112. Leinenbach, C., et al., *Thermo-Mechanical Properties of an Fe–Mn–Si–Cr–Ni–VC Shape Memory Alloy with Low Transformation Temperature.* Advanced Engineering Materials, 2012. **14**(1‐2): p. 62-67.

113. Hsu, T.Y. and X. Zuyao, *Martensitic transformation in Fe-Mn-Si based alloys.* Materials Science and Engineering: A, 1999. **273-275**: p. 494-497.
114. Lagoudas, D.C., *Shape memory alloys: Modeling and engineering applications*. 1 ed. 2008, US: Springer -Verlag.
115. Watanabe, Y., Y. Mori, and A. Sato, *Training effect in Fe-Mn-Si shape-memory alloys.* Journal of Materials Science, 1993. **28**(6): p. 1509-1514.
116. Maji, A.K. and I. Negret, *Smart Prestressing with Shape-Memory Alloy.* Journal of Engineering Mechanics, 1998. **124**(10): p. 1121-1128.
117. Neven, K.-O. and E.N. Antoine, *Self-Stressing Fiber Composites.* ACI Structural Journal. **97**(2).
118. Deng, Z., Q. Li, and H. Sun, *Behavior of concrete beam with embedded shape memory alloy wires.* Engineering Structures, 2006. **28**(12): p. 1691-1697.
119. Genevray, R.M., *The martensitic transformation in muntz metal*. 1953, Massachusetts Institute of Technology.
120. Suoninen, E.J., *Investigation of the martensitic transformation in metastable beta brass*. 1954, Massachusetts Institute of Technology.
121. Wayman, C.M., *Some Applications of Shape-Memory Alloys.* JOM, 1980. **32**(6): p. 129-137.
122. Wu, M. and C. Wayman. *Isothermal Ageing of Martensite in a Cu-Zn-Al Shape Memory Alloy*. in *Materials Science Forum*. 1990. Trans Tech Publ.
123. Wei, Z.G., et al., *Reverse transformations in CuAlNiMnTi alloy at elevated temperatures.* Acta Materialia, 1996. **44**(3): p. 1189-1199.
124. Kennon, N.F., D.P. Dunne, and L.A. Middleton, *Metallographic method for manganese-copper alloys.* Metallography, 1981. **14**(4): p. 329-334.
125. Bolcich, J. and R. Rapacioli, *Energy conversion using pseudoelastic cuznal alloys-a prototype heat engine.* Le Journal de Physique Colloques, 1982. **43**(C4): p. C4-831-C4-832.
126. Witting, P. and F.A. Cozzarelli, *Shape memory structural dampers: material properties, design and seismic testing*. 1992: National Center for Earthquake Engineering Research.
127. Gillet, Y., E. Patoor, and M. Berveiller, *Structure calculations applied to shape memory alloys.* Le Journal de Physique IV, 1995. **5**(C2): p. C2-343-C2-348.
128. Casciati, F., L. Faravelli, and L. Petrini, *Energy Dissipation in Shape Memory Alloy Devices.* Computer-Aided Civil and Infrastructure Engineering, 1998. **13**(6): p. 433-442.
129. Dejonghe, W., et al., *Temperature- and amplitude-dependence of internal friction in Cu-Zn-Al alloys.* Metal Science, 1977. **11**(11): p. 523-530.
130. Perkins, J. and W.E. Muesing, *Martensitic transformation cycling effects in Cu-Zn-Al shape memory alloys.* Metallurgical Transactions A, 1983. **14**(1): p. 33-36.
131. Perkins, J. and R.O. Sponholz, *Stress-Induced Martensitic Transformation Cycling and Two-Way Shape Memory Training in Cu-Zn-Al Alloys.* Metallurgical Transactions A, 1984. **15**(2): p. 313-321.
132. Ahlers, M., *Martensite and equilibrium phases in Cu Zn and Cu Zn Al alloys.* Progress in Materials Science, 1986. **30**(3): p. 135-186.
133. Saule, F. and M. Ahlers, *Stability, stabilization and lattice parameters in Cu Zn Al martensites.* Acta Metallurgica et Materialia, 1995. **43**(6): p. 2373-2384.
134. Qader, I.N., et al., *Mechanical and Thermal Behavior of Cu84−xAl13Ni3Hfx Shape Memory Alloys.* Iranian Journal of Science and Technology, Transactions A: Science, 2021. **45**(1): p. 343-349.
135. Alkan, S., et al., *Transformation stress of shape memory alloy CuZnAl: Non-Schmid behavior.* Acta Materialia, 2018. **149**: p. 220-234.
136. Dasgupta, R., *A look into Cu-based shape memory alloys: Present scenario and future prospects.* Journal of Materials Research, 2014. **29**(16): p. 1681-1698.
137. Ma, J., I. Karaman, and R.D. Noebe, *High temperature shape memory alloys.* International Materials Reviews, 2010. **55**(5): p. 257-315.

138. Firstov, G.S., J. Van Humbeeck, and Y.N. Koval, *High-temperature shape memory alloys: Some recent developments.* Materials Science and Engineering: A, 2004. **378**(1): p. 2-10.
139. Manjaiah, M., S. Narendranath, and S. Basavarajappa, *Review on non-conventional machining of shape memory alloys.* Transactions of Nonferrous Metals Society of China, 2014. **24**(1): p. 12-21.
140. Meng, X.L., et al., *Phase transformation and precipitation in aged Ti–Ni–Hf high-temperature shape memory alloys.* Materials Science and Engineering: A, 2006. **438-440**: p. 666-670.
141. Gao, W.-h., et al., *Effects of Co and Al addition on martensitic transformation and microstructure in ZrCu-based shape memory alloys.* Transactions of Nonferrous Metals Society of China, 2015. **25**(3): p. 850-855.
142. Van Humbeeck, J., *Shape memory alloys with high transformation temperatures.* Materials Research Bulletin, 2012. **47**(10): p. 2966-2968.
143. Ma, W.-J., et al., *Microstructure and mechanical properties of Zr-Cu-Al bulk metallic glasses.* Transactions of Nonferrous Metals Society of China, 2007. **17**(5): p. 929-933.
144. Hofmann, D.C., *Shape Memory Bulk Metallic Glass Composites.* Science, 2010. **329**(5997): p. 1294-1295.
145. Pauly, S., et al., *Microstructural heterogeneities governing the deformation of Cu47.5Zr47.5Al5 bulk metallic glass composites.* Acta Materialia, 2009. **57**(18): p. 5445-5453.
146. Wu, Y., et al., *Bulk Metallic Glass Composites with Transformation-Mediated Work-Hardening and Ductility.* Advanced Materials, 2010. **22**(25): p. 2770-2773.
147. Zhang, Q., et al., *Glass-Forming Ability and Mechanical Properties of the Ternary Cu-Zr-Al and Quaternary Cu-Zr-Al-Ag Bulk Metallic Glasses.* MATERIALS TRANSACTIONS, 2007. **advpub**: p. 0706180019-0706180019.
148. Zhang, W., et al., *Effects of additional Ag on the thermal stability and glass-forming ability of Cu–Zr binary glassy alloys.* Materials Science and Engineering: A, 2007. **459**(1): p. 330-336.
149. Cui, X., et al., *Study of the reversible intermetallic phase: B2-type CuZr.* Intermetallics, 2013. **36**: p. 21-24.
150. Biffi, C.A., et al., *Effect of Al Addition on Martensitic Transformation Stability and Microstructural and Mechanical Properties of CuZr Based Shape Memory Alloys.* Metals, 2021. **11**(7): p. 1141.
151. Wu, Y., et al., *Ductilizing Bulk Metallic Glass Composite by Tailoring Stacking Fault Energy.* Physical Review Letters, 2012. **109**(24): p. 245506-1-245506-12.
152. Zhou, D.Q., et al., *Alloying effects on mechanical properties of the Cu–Zr–Al bulk metallic glass composites.* Computational Materials Science, 2013. **79**: p. 187-192.
153. Pops, H., *Stress-induced pseudoelasticity in ternary Cu-Zn based beta prime phase alloys.* Metallurgical Transactions, 1970. **1**(1): p. 251-258.
154. Casciati, S. and A. Marzi, *Experimental studies on the fatigue life of shape memory alloy bars.* Smart Structures and Systems, 2010. **6**(1): p. 73-85.
155. Wen, Y.H., et al., *Large recovery strain in Fe-Mn-Si-based shape memory steels obtained by engineering annealing twin boundaries.* Nature Communications, 2014. **5**(1): p. 4964.
156. Kahn, H., M.A. Huff, and A.H. Heuer, *The TiNi shape-memory alloy and its applications for MEMS.* Journal of Micromechanics and Microengineering, 1998. **8**(3): p. 213-221.
157. Busch, J.D. and A.D. Johnson. *Prototype micro-valve actuator*. in *IEEE Proceedings on Micro Electro Mechanical Systems, An Investigation of Micro Structures, Sensors, Actuators, Machines and Robots.* 1990.
158. Van Humbeeck, J., *High Temperature Shape Memory Alloys.* Journal of Engineering Materials and Technology, 1999. **121**(1): p. 98-101.
159. Liu, Y., et al., *A TiNiPd thin film microvalve for high temperature applications.* Materials Science and Engineering: A, 2004. **378**(1): p. 205-209.

160. Stachiv, I., E. Alarcon, and M. Lamac, *Shape Memory Alloys and Polymers for MEMS/NEMS Applications: Review on Recent Findings and Challenges in Design, Preparation, and Characterization.* Metals, 2021. **11**(3): p. 415.
161. Askari-Naeini, F.G., et al., *On the microstructure and mechanical properties of a two-way shape memory NiTi/NiTiCu bi-layer diaphragm.* Materials & Design, 2020. **188**: p. 108464.
162. *Shape memory alloys market report coverage*. 2018; Available from: https://www.gminsights.com/industry-analysis/shape-memory-alloys-market?utm_source=GoogleAds&utm_medium=Adwords&utm_campaign=Polymer-PPC&gclid=CjwKCAjwlcaRBhBYEiwAK341jRLTi1MTDgcsb_UBt5PRLvmCDwqWYzfkOFNPUd3SMyL8DsHFYuIY9BoCu78QAvD_BwE.
163. *Road Haulage Services*. [cited 2022 5 May]; Available from: https://www.roadhaulageservices.com/haulage-rates.
164. Zipperian, D.C., *Metallographic specimen preparation basics.* Pace technology, 2001.
165. De Luca, F., et al., *Stress-induced martensitic transformation of Cu50Zr50 shape memory alloy optimized through microalloying and co-microalloying.* Journal of Alloys and Compounds, 2019. **781**: p. 337-343.
166. Jiang, Q.K., et al., *Glass formability, thermal stability and mechanical properties of La-based bulk metallic glasses.* Journal of Alloys and Compounds, 2006. **424**(1): p. 183-186.
167. Nishiyama, N., K. Amiya, and A. Inoue, *Novel applications of bulk metallic glass for industrial products.* Journal of Non-Crystalline Solids, 2007. **353**(32): p. 3615-3621.
168. Wu, Y., et al., *Formation of Cu–Zr–Al bulk metallic glass composites with improved tensile properties.* Acta Materialia, 2011. **59**(8): p. 2928-2936.
169. Bhushan, B., *Modern tribology handbook, two volume set*. 2000: CRC press.
170. Wei, Y.X., et al., *Erbium- and cerium-based bulk metallic glasses.* Scripta Materialia, 2006. **54**(4): p. 599-602.
171. Mills, K.C., *Recommended Values of Thermophysical Properties for Selected Commercial Alloys*. 2002: Woodhead Publishing. 73-134.
172. Fink, J.K. and L. Leibowitz, *Thermal conductivity of zirconium.* Journal of Nuclear Materials, 1995. **226**(1): p. 44-50.
173. Valencia, J.J. and P.N. Quested, *Thermophysical properties.* ASM Handbook, 2008. **15**: p. 468-481.
174. Samsonov, G.V., *Handbook of the Physicochemical Properties of the Elements*. 1st ed. 1968: Springer US. 395-396.
175. Harvey, P.D. and A.S.f. Metals, *Engineering properties of steel*. 1982: American Society for Metals. 259-270.
176. Courtney, T.H., *Mechanical Behavior of Materials*. 2nd ed. 2005: Waveland Press. 50-59.
177. Spittel, T. and M. Spittel, *Ferrous Alloys*. 1st ed. Vol. 2. 2009: Springer-Verlag Berlin Heidelberg. 1-3.
178. Touloukian, Y.S., *Thermal Conductivity-Metallic Elements and Alloys*. Thermophysical Properties of Matter. Vol. 1. 1970: IFI/Plenum. 985-987.
179. Yamasaki, M., S. Kagao, and Y. Kawamura, *Thermal diffusivity and conductivity of Zr55Al10Ni5Cu30 bulk metallic glass.* Scripta Materialia, 2005. **53**(1): p. 63-67.
180. Boer, F.R.d., et al., *Cohesion in metals*. 1988, Netherlands: North-Holland. 751-755.
181. Zhao, Y.-Y., E. Ma, and J. Xu, *Reliability of compressive fracture strength of Mg–Zn–Ca bulk metallic glasses: Flaw sensitivity and Weibull statistics.* Scripta Materialia, 2008. **58**(6): p. 496-499.
182. Zberg, B., et al., *Tensile properties of glassy MgZnCa wires and reliability analysis using Weibull statistics.* Acta Materialia, 2009. **57**(11): p. 3223-3231.

183. Ji, X., S.H. Alavi, and S.P. Harimkar, *High-Temperature Sliding Wear Behavior of Zr-Based Bulk Amorphous Alloys.* JOM, 2015. **67**(7): p. 1578-1584.
184. González, S., et al., *Effect of thermally-induced surface oxidation on the mechanical properties and corrosion resistance of Zr 60 Cu 25 Al 10 Fe 5 bulk metallic glass.* Science of Advanced Materials, 2014. **6**(1): p. 27-36.
185. William, B.A., C. Margam, and L.N. Lam, *Materials Degradation And Its Control By Surface Engineering*. 2nd ed. 2003: World Scientific Publishing Company. 119-126.
186. Liu, Y., et al., *Wear behavior of a Zr-based bulk metallic glass and its composites.* Journal of Alloys and Compounds, 2010. **503**(1): p. 138-144.
187. He, B.B., et al., *Nanoindentation investigation on the mechanical stability of individual austenite grains in a medium-Mn transformation-induced plasticity steel.* Scripta Materialia, 2013. **69**(3): p. 215-218.
188. Sekido, K., et al., *Nanoindentation/atomic force microscopy analyses of ε-martensitic transformation and shape memory effect in Fe–28Mn–6Si–5Cr alloy.* Scripta Materialia, 2011. **65**(11): p. 942-945.
189. Ahn, T.H., et al., *Investigation of strain-induced martensitic transformation in metastable austenite using nanoindentation.* Scripta Materialia, 2010. **63**(5): p. 540-543.
190. Fornell, J., et al., *The Influence of Deformation-Induced Martensitic Transformations on the Mechanical Properties of Nanocomposite Cu-Zr-(Al) Systems.* Advanced Engineering Materials, 2011. **13**(1‐2): p. 57-63.
191. Kaya, A.A., *2 - Physical metallurgy of magnesium*, in *Fundamentals of Magnesium Alloy Metallurgy*, M.O. Pekguleryuz, K.U. Kainer, and A. Arslan Kaya, Editors. 2013, Woodhead Publishing. p. 33-84.
192. Laplanche, G., J. Pfetzing-Micklich, and G. Eggeler, *Sudden stress-induced transformation events during nanoindentation of NiTi shape memory alloys.* Acta Materialia, 2014. **78**: p. 144-160.
193. Sun, J.-y. and J. Tong, *Fracture toughness properties of three different biomaterials measured by nanoindentation.* Journal of Bionic Engineering, 2007. **4**(1): p. 11-17.
194. Chung, Y.-w., *Introduction to materials science and engineering, CRC*. 2007, Taylor & Francis, Boca Raton.
195. Beake, B.D., et al., *Coating optimisation for high speed machining with advanced nanomechanical test methods.* Surface and Coatings Technology, 2009. **203**(13): p. 1919-1925.
196. Fox-Rabinovich, G., et al., *Nanocrystalline coating design for extreme applications based on the concept of complex adaptive behavior.* Journal of Applied Physics, 2008. **103**(8): p. 083510.
197. Zhang, S., *Nanostructured thin films and coatings*. 2010, Boca Raton: CRC Press.
198. Ni, W., Y.-T. Cheng, and D.S. Grummon, *Recovery of microindents in a nickel–titanium shape-memory alloy: a "self-healing" effect.* Applied physics letters, 2002. **80**(18): p. 3310-3312.
199. Biffi, C.A., M. Coduri, and A. Tuissi, *CuZr Based Shape Memory Alloys: Effect of Co on the Martensitic Transformation and the Microstructure.* Materials Today: Proceedings, 2015. **2**: p. S797-S800.
200. González, S., et al., *Drastic influence of minor Fe or Co additions on the glass forming ability, martensitic transformations and mechanical properties of shape memory Zr–Cu–Al bulk metallic glass composites.* Science and Technology of Advanced Materials, 2014. **15**(3): p. 035015.
201. Foreman, J., S. Sauerbrunn, and C. Marcozzi, *Exploring the sensitivity of thermal analysis techniques to the glass transition.* TA Instruments: Thermal Analysis & Rheology, 2006.
202. Fabregat-Sanjuan, A., et al., *Identifying the effects of heat treatment temperatures on the Ti50Ni45Cu5 alloy using dynamic mechanical analysis combined with microstructural analysis.* Materials Science and Engineering: A, 2018. **712**: p. 281-291.

203. Archard, J.F., *Contact and Rubbing of Flat Surfaces.* Journal of Applied Physics, 1953. **24**(8): p. 981-988.
204. Pan, X.F., et al., *Vickers hardness and compressive properties of bulk metallic glasses and nanostructure-dendrite composites.* Journal of Materials Research, 2005. **20**(10): p. 2632-2638.
205. Rahaman, M.L., et al., *Surface roughness effect on the friction and wear of bulk metallic glasses.* Wear, 2015. **332-333**: p. 1231-1237.
206. Suh, N., *Tribophysics*. 1986: Englewood Cliffs, NJ, Prentice Hall.
207. Zum Gahr, K.-H., *Microstructure and wear of materials*. Tribology series. Vol. 10. 1987, Amesterdam: Elsevier.
208. Li, Y.-C., et al., *Design of Fe-Based Bulk Metallic Glasses with Improved Wear Resistance.* ACS Applied Materials & Interfaces, 2018. **10**(49): p. 43144-43155.
209. Madhu, H., et al., *Fabrication of Wear-Resistant Ti 3 AlC 2/Al 3 Ti Hybrid Aluminum Composites by Friction Stir Processing.* Metallurgical and Materials Transactions A, 2020. **51**: p. 4086-4099.
210. Blau, P.J. and R. Komanduri, *Friction and Wear Transitions of Materials: Break-in, Run-in, and Wear-in.* Journal of Engineering Materials and Technology, 1990. **112**(2): p. 254-254.
211. Bhatt, J., et al., *Tribological behaviour of Cu60Zr30Ti10 bulk metallic glass.* Materials Science and Engineering: A, 2007. **458**(1): p. 290-294.
212. Kato, K. and K. Adachi, *Wear mechanisms*, in *Modern Tribology Handbook*. 2000, CRC Press. p. 273-300.
213. Yao, B., Z. Han, and K. Lu, *Correlation between wear resistance and subsurface recrystallization structure in copper.* Wear, 2012. **294-295**: p. 438-445.
214. Baker, H., *Alloy phase diagrams.* ASM handbook, 1992. **3**: p. 2-80.
215. Verhoeven, J.D., *Fundamentals of physical metallurgy*. 1975: Wiley.
216. Villapún, V.M., et al., *Tuning the Mechanical and Antimicrobial Performance of a Cu-Based Metallic Glass Composite through Cooling Rate Control and Annealing.* Materials, 2017. **10**(5): p. 506.
217. Phinney, L.M., et al., *Effects of mechanical stress on thermal microactuator performance.* Journal of Micromechanics and Microengineering, 2010. **20**(9): p. 095011.
218. Ng, C.H., et al., *NiTi shape memory alloy with enhanced wear performance by laser selective area nitriding for orthopaedic applications.* Surface and Coatings Technology, 2017. **309**: p. 1015-1022.
219. Yang, L.J., *A test methodology for the determination of wear coefficient.* Wear, 2005. **259**(7): p. 1453-1461.
220. Limbach, R., et al., *Serrated flow of CuZr-based bulk metallic glasses probed by nanoindentation: Role of the activation barrier, size and distribution of shear transformation zones.* Journal of Non-Crystalline Solids, 2017. **459**: p. 130-141.
221. Motemani, Y., et al., *Effect of cooling rate on the phase transformation behavior and mechanical properties of Ni-rich NiTi shape memory alloy.* Journal of Alloys and Compounds, 2009. **469**(1): p. 164-168.
222. Leyland, A. and A. Matthews, *On the significance of the H/E ratio in wear control: a nanocomposite coating approach to optimised tribological behaviour.* Wear, 2000. **246**(1): p. 1-11.
223. Musil, J., et al., *Relationships between hardness, Young's modulus and elastic recovery in hard nanocomposite coatings.* Surface and Coatings Technology, 2002. **154**(2): p. 304-313.
224. Hall, E., *The deformation and ageing of mild steel: III discussion of results.* Proceedings of the Physical Society. Section B, 1951. **64**(9): p. 747-753.
225. Yue, Y., et al., *Stress-induced phase stabilization and transformation in equiatomic CuZr B19' martensite: A DFT study.* Journal of Alloys and Compounds, 2021. **860**: p. 157906.

226. Zhao, T., et al., *Nano-hardness, wear resistance and pseudoelasticity of hafnium implanted NiTi shape memory alloy.* Journal of the Mechanical Behavior of Biomedical Materials, 2012. **13**: p. 174-184.
227. Li, Y., et al., *Enhanced wear resistance of NiTi alloy by surface modification with Nb ion implantation.* Rare Metals, 2014. **33**(3): p. 244-248.
228. Waqar, S., et al., *Effects of Ni and Cr addition on the wear performance of NiTi alloy.* The International Journal of Advanced Manufacturing Technology, 2020. **108**: p. 625-634.
229. Javid, F.A., et al., *Phase formation of Cu50−xCoxZr50 (x=0–20at.%) alloys: Influence of cooling rate.* Journal of Alloys and Compounds, 2014. **590**: p. 428-434.